18 January 2013 | $10

Science

MESSENGER
Mercury's North Pole

AAAS

NEW ENGLAND BioLabs® Inc.
enabling technologies in the life sciences

Make ends meet.

Gibson Assembly™ Cloning Kit

New England Biolabs has revolutionized your laboratory's standard cloning methodology. The Gibson Assembly Cloning Kit combines the power of the Gibson Assembly Master Mix with NEB 5-alpha Competent *E. coli*, enabling fragment assembly and transformation in just under two hours. Save time, without sacrificing efficiency.

Making ends meet is now quicker and easier than ever before, with the Gibson Assembly Cloning Kit from NEB.

NEBuilder™ for Gibson Assembly

Visit **NEBGibson.com** to view the latest tutorials and to try our primer design tool.

Gibson Assembly Cloning Kit provides robust transformation efficiencies

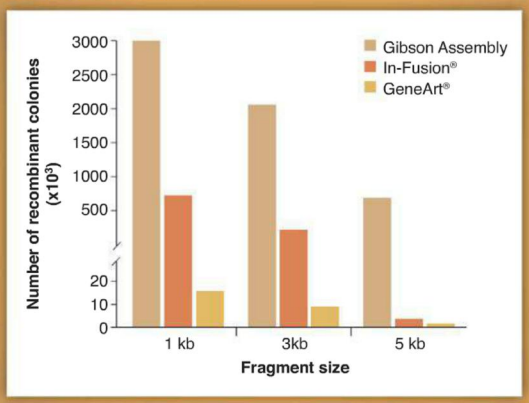

Assembly reactions containing 25 ng of linear pUC19 vector and 0.04 pmol of each fragment were performed following individual suppliers' recommended protocols and using the competent cells provided with the kit. The total number of recombinant colonies was calculated per 25 ng of linear pUC19 vector added to the assembly reaction.

EDITORIAL

250 The Basics of Translation
Huda Y. Zoghbi

NEWS OF THE WEEK

256 A roundup of the week's top stories

NEWS & ANALYSIS

259 Killings Force Rethinking of Pakistan's Anti-Polio Drive

260 For $60, a Peek Inside Your Dog's Mind

262 Genealogy Databases Enable Naming of Anonymous DNA Donors
>> *Policy Forum p. 275; Report p. 321*

263 Performance of Nanowire Solar Cells on the Rise
>> Science *Express Report by J. Wallentin* et al.

NEWS FOCUS

264 Who Will Step Up to Exascale?

267 The Promise and Perils of Oxytocin
>> Science *Podcast*

LETTERS

270 Exploitation in Northeast India
S. Dalvi et al.

Sharing Future Conservation Costs
D. Sheil et al.

Response
S. H. M. Butchart et al.

271 CORRECTIONS AND CLARIFICATIONS

271 TECHNICAL COMMENT ABSTRACTS

BOOKS *ET AL.*

273 What Did the Romans Know?
D. Lehoux, reviewed by P. Pesic

274 The Fractalist
B. B. Mandelbrot, reviewed by B. Finegold

POLICY FORUMS

275 The Complexities of Genomic Identifiability
L. L. Rodriguez et al.
>> *News story p. 262; Report p. 321*

277 Essential Biodiversity Variables
H. M. Pereira et al.

PERSPECTIVES

279 Hormones and the Social Brain
B. S. McEwen
>> *Reports pp. 332 and 335*

280 The Closing Door of Climate Targets
T. F. Stocker

282 A Wet and Volatile Mercury
P. G. Lucey
>> *Reports pp. 292, 296, and 300*

283 Re-Engineering Nature's Catalysts
A. R. H. Narayan and D. H. Sherman
>> *Report p. 307*

284 Polymer Rigidity Improves Microporous Membranes
M. D. Guiver and Y. M. Lee
>> *Report p. 303*

CONTENTS continued >>

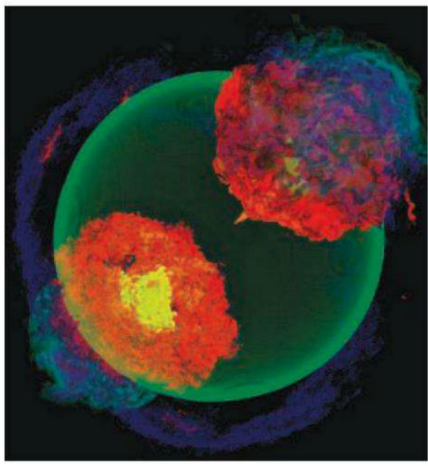

page 264

pages 262, 275, & 321

Explore our rich online offerings, including multimedia, news, and our two research journals—*Science Signaling* and *Science Translational Medicine*—at www.sciencemag.org

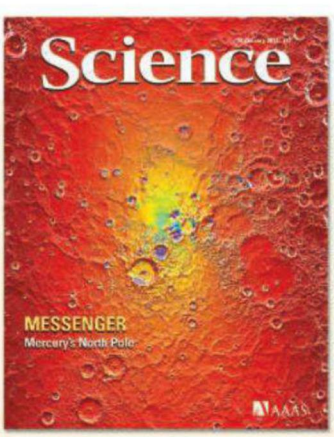

COVER

Map of highest surface temperature in the north polar region of Mercury superimposed on topography measured by the MESSENGER spacecraft. Red areas surrounding the pole (center) reach temperatures above 450 K. Blue and purple areas inside polar impact craters never exceed 100 K and are sufficiently cold to harbor water ice and frozen organic compounds. The largest ice-containing crater near the center of the image is ~112 km in diameter and 2.7 km deep. See pages 282, 292, 296, and 300. For the story behind the cover, go to http://scim.ag/cov6117.

Image: NASA/Johns Hopkins University Applied Physics Laboratory/ Carnegie Institution of Washington/UCLA/David Paige

DEPARTMENTS

249 This Week in *Science*
251 Editors' Choice
254 *Science* Staff
353 New Products
354 *Science* Careers

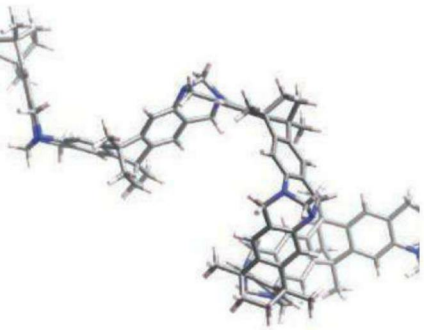

pages 284 & 303

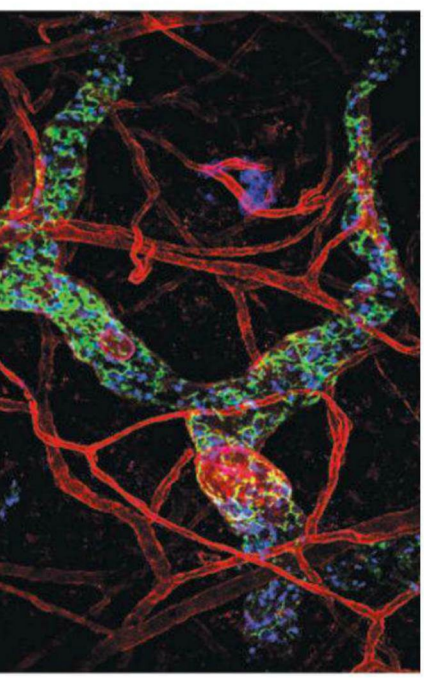

page 328

REVIEW

286 Neutralizing Tumor-Promoting Chronic Inflammation: A Magic Bullet?
L. M. Coussens et al.

REPORTS

292 Evidence for Water Ice Near Mercury's North Pole from MESSENGER Neutron Spectrometer Measurements
D. J. Lawrence et al.

296 Bright and Dark Polar Deposits on Mercury: Evidence for Surface Volatiles
G. A. Neumann et al.

300 Thermal Stability of Volatiles in the North Polar Region of Mercury
D. A. Paige et al.
Spacecraft data and a thermal model show that water ice and organic volatiles are present at Mercury's north pole.
>> *Perspective p. 282*

303 An Efficient Polymer Molecular Sieve for Membrane Gas Separations
M. Carta et al.
Intrinsically porous polymers made using reactions associated with Tröger's base manifested enhanced membrane properties.
>> *Perspective p. 284*

307 Olefin Cyclopropanation via Carbene Transfer Catalyzed by Engineered Cytochrome P450 Enzymes
P. S. Coelho et al.
An oxidative enzyme has been engineered to transfer carbon to synthetic substrates in place of oxygen.
>> *Perspective p. 283*

310 Metamaterial Apertures for Computational Imaging
J. Hunt et al.
Metamaterial-based sensors can be used for compressive image reconstruction.
>> Science *Podcast*

313 Climate Events Synchronize the Dynamics of a Resident Vertebrate Community in the High Arctic
B. B. Hansen et al.
Reindeer, ptarmigan, vole, and fox populations on Svalbard respond together to extreme weather.

316 Invasive Plants Have Scale-Dependent Effects on Diversity by Altering Species-Area Relationships
K. I. Powell et al.
In three different biomes, invasive plant species cause larger declines in common species than in rare species.

318 Structure of Histone mRNA Stem-Loop, Human Stem-Loop Binding Protein, and 3′hExo Ternary Complex
D. Tan et al.
Two RNA binding proteins recognize their target RNA through shape, rather than sequence.

321 Identifying Personal Genomes by Surname Inference
M. Gymrek et al.
Anonymity of male personal genome data sets can be compromised by means of publicly available data.
>> *News story p. 262; Policy Forum p. 275;* Science *Podcast*

324 GDE2 Promotes Neurogenesis by Glycosylphosphatidylinositol-Anchor Cleavage of RECK
S. Park et al.
A molecular mechanism to inhibit Delta-Notch signaling and initiate neurogenesis is elucidated.

328 Interstitial Dendritic Cell Guidance by Haptotactic Chemokine Gradients
M. Weber et al.
In mouse skin, immune cells migrate toward lymphatic vessels along an immobilized chemokine gradient.

332 Chronic Stress Triggers Social Aversion via Glucocorticoid Receptor in Dopaminoceptive Neurons
J. Barik et al.
Aggressive defeat stress in mice causes glucocorticoid release and increased activity in the dopamine system.

335 Adolescent Stress–Induced Epigenetic Control of Dopaminergic Neurons via Glucocorticoids
M. Niwa et al.
Genetically susceptible mice isolated during adolescence can subsequently present schizophrenia-like symptoms.
>> *Perspective p. 279*

CREDIT: (BOTTOM) MICHELE WEBER AND MICHAEL SIXT/IST AUSTRIA

SCIENCE (ISSN 0036-8075) is published weekly on Friday, except the last week in December, by the American Association for the Advancement of Science, 1200 New York Avenue, NW, Washington, DC 20005. Periodicals Mail postage (publication No. 484460) paid at Washington, DC, and additional mailing offices. Domestic individual membership and subscription (51 issues): $149 ($74 allocated to subscription). Domestic institutional subscription (51 issues): $990; Foreign postage extra: Mexico, Caribbean (surface mail) $55; other countries (air assist delivery) $85. First class, airmail, student, and emeritus rates on request. Canadian rates with GST available upon request, GST #1254 88122. Publications Mail Agreement Number 1069624. **Printed in the U.S.A.**

Change of address: Allow 4 weeks, giving old and new addresses and 8-digit account number. **Postmaster:** Send change of address to AAAS, P.O. Box 96178, Washington, DC 20090–6178. **Single-copy sales:** $10.00 current issue, $15.00 back issue prepaid includes surface postage; bulk rates on request. *Science* is indexed in the *Reader's Guide to Periodical Literature* and in several specialized indexes.

EDITED BY STELLA HURTLEY

CREDITS (TOP TO BOTTOM): NICOLAS LECOMTE/NORWEGIAN POLAR INSTITUTE; HUNT *ET AL.*

All Together Now

Environmental drivers, such as extreme weather events, impact population dynamics and can synchronize such dynamics across populations within a species. Given that many species depend on similar resources, such events might also be expected to synchronize dynamics across species, but the complexity of multispecies communities makes it difficult to reveal potential drivers in common. **Hansen *et al.*** (p. 313) took advantage of the simplicity of the year-round community on the high-arctic island of Spitsbergen to test for the presence of synchrony. Population fluctuations were synchronized across the three herbivore species (Svalbard reindeer, Svalbard rock ptarmigan, and sibling vole) and the single resident predator, the arctic fox, was in lagged synchrony. The driver of these fluctuations appears to be extreme winter rain-on-snow events that reduce the availability of winter forage due to ice cover.

Putting a C in Cytochrome

Cytochrome P450 enzymes oxidize hydrocarbons using a highly reactive iron oxo intermediate. Much research has focused on tuning the protein structure to broaden the range of hydrocarbons that can be functionalized. **Coelho *et al.*** (p. 307, published online 20 December; see the Perspective by **Narayan and Sherman**) substituted a carbene source for the oxygen to make a P450 mutant a cyclopropanation catalyst whereby a carbon fragment is transferred in place of oxygen. Though carbene activation by iron is chemically analogous to the native oxygen activation pathway, the overall reaction is completely different from any known enzymatic transformation.

Wet Mercury

Radar observations of Mercury's poles in the 1990s revealed regions of high backscatter that were interpreted as indicative of thick deposits of water ice; however, other explanations have also been proposed (see the Perspective by **Lucey**). MESSENGER neutron data reported by **Lawrence *et al.*** (p. 292, published online 29 November) in conjunction with thermal modeling by **Paige *et al.*** (p. 300, published online 29 November) now confirm that the primary component of radar-reflective material at Mercury's north pole is water ice. **Neumann *et al.*** (p. 296, published online 29 November) analyzed surface reflectance measurements from the Mercury Laser Altimeter onboard MESSENGER and found that while some areas of high radar backscatter coincide with optically bright regions, consistent with water ice exposed at the surface, some radar-reflective areas correlate with optically dark regions, indicative of organic sublimation lag deposits overlying the ice. Dark areas that fall outside regions of high radio backscatter suggest that water ice was once more widespread.

A Well-Defined Path

Although chemokines have long been thought to direct immune cell movements within tissues, a formal in vivo demonstration and detailed understanding are lacking. By tracking dendritic cell movements in the ears of mice, **Weber *et al.*** (p. 328) were able to provide both. Endogenous gradients of the chemokine CCL21 were observed in ear tissue and, at distances of up 90 μm, dendritic cells were able to use these gradients to migrate directionally toward lymphatic vessels. The CCL21 gradient was immobilized on heparan sulfates and disruption of the gradient inhibited dendritic cell migration.

Defeat, Distress, and Glucocorticoids

Understanding how individuals control emotions and cope with stressful events is a major clinical concern and of importance for the treatment of psychiatric illnesses (see the Perspective by **McEwen**). **Barik *et al.*** (p. 332) discovered that aggressive defeat stress in mice caused glucocortioid release and increased activity in the dopamine system. Deleting the glucocorticoid receptors in dopaminoceptive neurons completely prevented the social avoidance that usually follows aggressive defeat. How the combination of genetic factors and environmental stressors during adolescence determines adult behavior and how their disturbance results in neuropsychiatric disorders is poorly understood. **Niwa *et al.*** (p. 335) found that isolation stress during adolescence, which does not cause any long-lasting changes in wild-type mice, induced significant neurochemical and behavioral alterations in mutant mice expressing a dominant-negative variant of the *disrupted in schizophrenia 1* gene under the control of the prion protein promoter. These deficits could be reversed by a glucocorticoid receptor antagonist.

Compressed Sampling

It is often said that a picture is worth a thousand words. But images often contain a lot of redundant information—effectively creating huge data files of meaningless information. While algorithms can compress the size of a file without loss of information, such processing is done after the picture has been taken. **Hunt *et al.*** (p. 310) used a metamaterial sensor to compress the sampled scene directly, obviating the need for postprocessing. Tuning the response of the metamaterial allowed imaging of a scene with a 40:1 compression ratio, which may mean that finding that needle in a haystack may be much easier using a metamaterial camera.

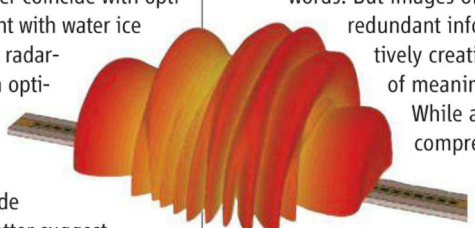

The Basics of Translation

Huda Y. Zoghbi is an investigator with the Howard Hughes Medical Institute; professor of Pediatrics, Molecular and Human Genetics, and Neuroscience at Baylor College of Medicine; and director of the Jan and Dan Duncan Neurological Research Institute at Texas Children's Hospital in Houston, TX. E-mail: hzoghbi@bcm.edu.

THE PAST 20 YEARS HAVE WITNESSED GREAT ADVANCES IN UNDERSTANDING THE CAUSES OF MANY medical disorders, while also revealing how complex their pathogenesis can be. Hypertension, autism, and Alzheimer's disease have each proven to be a collection of disorders with multiple causes. Although the dream of personalized treatments has been realized for a few disorders, particularly in the field of cancer, the translation of scientific discoveries into effective treatments for other diseases has been much slower than expected. There are two main reasons for this fact: the complexity of human physiology, and our limited understanding of how the vast majority of genes, proteins, and RNAs work, irrespective of whether they are disease-associated or not.

Traditionally, such fundamental knowledge has come from untargeted, discovery-driven basic research. In recent years, however, the pressure to develop treatments at an ever more rapid pace has attenuated enthusiasm for deciphering the language of life. Science, like most human endeavors, is susceptible to fads and fashions driven by money and status; and today many highly qualified basic scientists feel compelled to jump on the "translational medicine" bandwagon. For quite some time, it has been apparent that biomedical research in the United States is more likely to get funded if it is tied to a practical outcome, such as a step toward a cure for some disorder. There is no doubt that such targeted and in-depth disease-oriented research is sorely needed. But it is at least as important to support investigators dedicated to discovery-driven basic research.

Specific outcomes from discovery-driven research are hard to predict, but they often surprise and delight us with their applicability in unexpected contexts. Who, for example, would have predicted that an apparently trivial notched-wing phenotype in the fruit fly would yield a gene that is important for so many developmental processes in humans and so many ills, ranging from cancer to stroke?* Or that trying to trace how the brain develops the capacity for proprioception would suggest a potential therapy for deafness?† When basic research is made to seem silly in public discourse, and when its usefulness is questioned during key points in federal budget cycles, scientists should not yield to the bullying. We should instead educate the public about how scientific knowledge actually grows. Not everything worthwhile can be justified by its market value; what is most meaningful may have no apparent practical impact. Yet we can be sure that human imagination will find applications for knowledge, if we are allowed to develop that knowledge in the first place.

The task of translational research is not unlike the act of translating a book from one language into another. Fluency in both languages is a given; beyond that, there must be a talent, a feel, for those concepts unique to one language or culture that cannot be directly translated but must somehow still be conveyed. The challenge in translational medicine is that scientists are trying to translate a text with the sophistication and depth of Shakespeare using a first-grader's vocabulary and experience, because our knowledge about the functions of most pathways in various cell types, during different developmental stages, and under normal physiological conditions, is still rudimentary and piecemeal.

To better translate recent discoveries into benefits for human health, we must admit the limitations of our knowledge of this language and invest in learning it in full. There is no doubt that studying human patients and the functions of disease-associated molecules will provide a rich lexicon for the language of life, but so will many molecules, organisms, and physiological processes that are not (currently) linked to any disease. The best way to promote discovery is to invest in talented researchers driven by curiosity and passion, whether for disease-oriented questions or the more obscure mysteries of nature. **– Huda Y. Zoghbi**

10.1126/science.1234799

*S. Artavanis-Tsakonas, M. A. Muskavitch, *Curr. Top. Dev. Biol.* **92,** 1 (2010). †S. Maricich, H. Y. Zoghbi, *Cell* **26**, 11 (2006).

ECOLOGY

Pulsing Populations of Jellies

One strand of evidence for the deterioration of Earth's oceans is the perception that the seas are becoming overwhelmed by jellyfish. In fact, there has been little global analysis of jellyfish populations and the jellyfish ocean perception as made on the basis of a few scattered reports. Condon *et al.* undertook a meta-analysis using linear and logistic mixed models and effect-size analysis on data ranging from 1790 to 2011. There are many limitations to the available data: The older records are sparse, and the majority of more recent data are from the North Atlantic and Mediterranean. Although strong 20-year oscillations were revealed by the analysis, in fact only a weak upward trend has been observed since 1970. The authors acknowledge that this could be a false negative, but unless more data are collected from more sites, the jury is still out on whether jellyfish will take over the increasingly anthropogenically affected oceans. — CA

Proc. Natl. Acad. Sci. U.S.A. 10.1073/pnas.1210920110 (2012).

PLANETARY SCIENCE

No Stellar Explosion Needed

The presence of the decay products of short-lived radioactive isotopes in meteorites provides clues to the astrophysical context of the formation of our solar system. Iron-60, for example, can only be produced in stellar explosions; given its half-life of 2.62 million years, a high abundance of this radioisotope in early solar system materials would imply that a star exploded in the vicinity of the newborn Sun. The abundance of ^{60}Fe, an extinct radioisotope, can be constrained by measuring isotopic variations in its decay product ^{60}Ni: a stable isotope of nickel. Previous estimates disagree, depending on the materials analyzed, which has been interpreted as reflecting heterogeneous distribution of ^{60}Fe among planetary bodies. Based on high-precision and high-accuracy ^{60}Ni and ^{58}Fe isotope measurements of a variety of meteorites, Tang and Dauphas now show that, contrary to previous results, the initial abundance of ^{60}Fe in the early solar system was uniformly low, precluding the need for a nearby stellar explosion around the time the solar system formed. Instead, ^{60}Fe may have been inherited from the interstellar medium as the result of the long-term chemical evolution of our galaxy. — MJC

Earth Planet. Sci. Lett. **359-360**, 248 (2012).

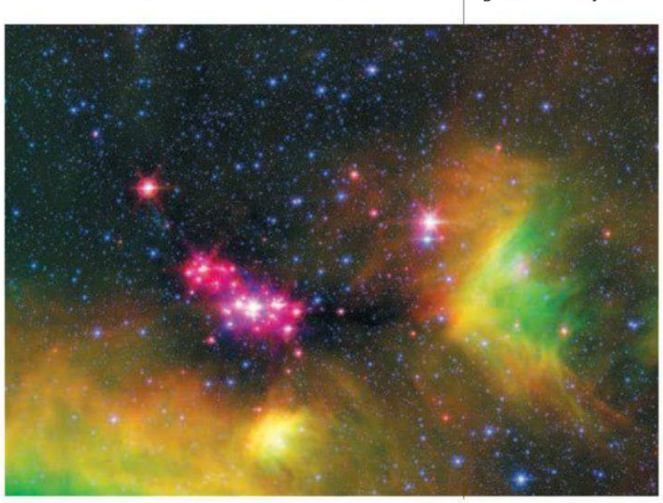

CREDITS (TOP TO BOTTOM): THINKSTOCK; NASA/JPL/UNIVERSITY OF ARIZONA

CELL BIOLOGY

Toxoplasma Invasion Revisited

Apicomplexan parasites actively invade their host cell. Invasion depends on an arsenal of secreted invasion factors and the ability of the parasite to glide. The Myosin A (MyoA) motor complex, also known as the glideosome, is a multisubunit complex localized beneath the plasma membrane of the parasite. It is thought to provide the necessary force to move the parasite forward and is essential for gliding motility in *Toxoplasma gondii* and *Plasmodium*. Gliding mutants, however, retain the ability to invade host cells, albeit at reduced efficiency. To establish whether background expression of the respective protein in the knockdown mutants might be sufficient to drive host cell invasion, Andenmatten *et al.* generated a conditional recombination system based on dimerizable Cre recombinase, which they used to generate complete knockouts of three proteins—MyoA, the micronemal protein MIC2, and actin—each thought to be essential for host cell invasion in *T. gondii*. Surprisingly, each of the complete knockout mutants could invade host cells, and the MyoA and MIC2 knockouts could be maintained and grown in vitro, suggesting that alternative invasion strategies exist. As expected, parasites lacking MyoA were not able to move by gliding motility and consequently were significantly impaired in host cell egress. — SMH

Nat. Meth. 10.1038/nmeth.2301 (2012).

EDUCATION

Assessing Literacy

Scientific literacy, a skill needed beyond the classroom, is being integrated into general education curriculums, resulting in a need to assess students as they develop scientific literacy skills. Gormally *et al.* describe the development of the Test of Scientific Literacy Skills (TOSLS) as a freely available, time-efficient, and psychometrically sound test for use in undergraduate introductory science courses. Using definitions of scientific literacy in education policy documents and survey results from general education faculty, the team identified two major skill categories as measurable outcomes, or TOSLS skills: recognizing and analyzing

Continued on page 253


NO ANTIBODY.
NO PROBLEM.
Breakthrough multiplex RNA *in situ* hybridization for any gene with RNAscope® technology.
Be Amazed.
Because up to 76% of protein-coding genes have no reliable antibody for immunohistochemistry (IHC), your research often comes to a screeching halt while you wait for a new antibody to be developed. We say forget your antibody problems. Choose RNAscope technology. With rapid probe design and universal assay workflows for any gene, RNAscope frees you from the hassles of antibody screening, saving you precious time and effort, while delivering publication quality data.
Learn more about RNAscope now at www.acdbio.com/no-antibody
Advanced Cell Diagnostics
ACD

Continued from page 251

the use of methods of inquiry, and organizing, analyzing, and interpreting quantitative data. An extensive pilot study that included testing students in a general biology course, individual student interviews, and several rounds of expert faculty evaluation suggested that the TOSLS is able to identify students' scientific literacy skill proficiency. Additionally, the TOSLS was sensitive enough to detect pre- to post-semester learning gains, suggesting that it will be valuable in future assessment efforts. — MM

CBE-Life Sci. Educ. **11**, 364 (2012).

IMMUNOLOGY

An Antiviral Sterol

After viral infection, the production of type I interferons (IFNs) induces an antiviral state through the induction of a large network of genes. How these different pathways induce viral control, however, is incompletely characterized. By using microarray analysis to look for genes induced in response to IFN treatment of mouse macrophages, Liu *et al.* identified *Ch25h*, which encodes cholesterol-25-hydroxylase, as an IFN-stimulated gene with antiviral activity. CH25H mediates these effects by catalyzing the oxidation of cholesterol to the soluble oxysterol 25-hydroxycholesterol (25HC). Pretreatment of cells with 25HC was able to protect these cells against infection with a variety of enveloped viruses, including HIV-1. Further characterization of the mechanism of inhibition revealed that 25HC blocked membrane fusion between the virus and host cells. Viral infection of *Ch25h*-deficient mice and treatment of HIV-1–infected humanized mice with 25HC confirmed the physiological relevance of the authors' findings. Similar findings were reported by Blanc *et al.*, who also revealed that the transcription factor Stat1 was required for IFN-dependent induction of 25HC. — KLM

Immunity 10.1016/j.immuni.2012.11.005; 10.1016/j.immuni.2012.11.004 (2012).

MICROBIOLOGY

Bacterial Reprogramming

Cell reprogramming is a phenomenon that occurs in vitro and in vivo. The former involves the introduction of proteins such as the four "Yamanaka factors" or more recent studies with small molecules, whereas in vivo reprogramming can be seen, for example, during gametogenesis. Masaki *et al.* report on another reprogramming event in nature, one that involves host/pathogen interaction. The leprosy-causing bacterium *Mycobacterium leprae* targets differentiated adult Schwann cells, which display considerable plasticity for regeneration after injury. Upon infection, *M. leprae* induced reprogramming of adult peripheral nerve mouse Schwann cells, converting the host cells to a stemlike fate with the ability to produce chemoattractants and trophic factors that promote macrophage recruitment, bacterial transfer, and survival of infected macrophages. This reprogramming occurred through direct differentiation of infected Schwann cells to mesenchymal cells and skeletal and smooth muscle cells, as well as through the formation of granuloma-like structures that released macrophages carrying bacteria. Perhaps by understanding the mechanism of bacterial spread via the exploitation of adult Schwann cell plasticity and the shutting down of Schwann cell gene expression, new therapies to prevent *M. leprae* infection can be developed. — BAP

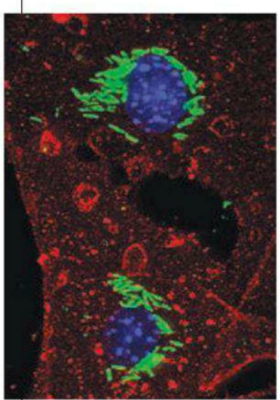

CREDIT: RAMBUKKANA LAB

Cell 10.1016/j.cell.2012.12.014 (2013).

GEOCHEMISTRY

Bombs Below

The political ramifications of clandestine underground nuclear tests are often severe. Therefore, methods must be developed to reliably verify when a test has been completed, without generating false positives. Radiogenic xenon (Xe) is one such tracer produced by nuclear explosions either directly as a fission product or indirectly from unstable iodine precursors; however, it is also generated by nuclear power plants and during the production of radioisotopes for medical use. These sources have different ratios of four Xe isotopes when measured in gas samples, so that there is a typical isotopic range assumed for a weapons test. By incorporating radioactive decay into subsurface transport modeling of the Nevada Test Site in the United States, Lowrey *et al.* suggest that this range may be too narrow. For example, some simulations showed that some signals could be produced by the decay of precursor radioiodine exclusively. More generally, differential transport caused by variations in atmospheric pressure can strongly influence Xe isotopic ratios. Based on their simulations, the 26 March 1992 test at Pahute Mesa within the Nevada Test Site would have been undetectable using Xe isotopes if measured at some site locations. — NW

Geophys. Res. Lett. 10.1029/2012GL053885 (2012).

www.sciencemag.org

Science

1200 New York Avenue, NW
Washington, DC 20005
Editorial: 202-326-6550, FAX 202-289-7562
News: 202-326-6581, FAX 202-371-9227
Bateman House, 82-88 Hills Road
Cambridge, UK CB2 1LQ
+44 (0) 1223 326500, FAX +44 (0) 1223 326501

Subscription Services For change of address, missing issues, new orders and renewals, and payment questions: 866-434-AAAS (2227) or 202-326-6417, FAX 202-842-1065. Mailing addresses: AAAS, P.O. Box 96178, Washington, DC 20090-6178 or AAAS Member Services, 1200 New York Avenue, NW, Washington, DC 20005

Institutional Site Licenses please call 202-326-6755 for any questions or information

Reprints: Author Inquiries 800-635-7181
Commercial Inquiries 803-359-4578

Permissions 202-326-7074, FAX 202-682-0816

Member Benefits AAAS Travels: Betchart Expeditions 800-252-4910; Apple Store www.store.apple.com/us/go/eppstore/aaas; NASA Federal, 1-888-NASA-FCU (1-888-627-2328) or www.nasafcu.com; Cold Spring Harbor Laboratory Press Publications www.cshlpress.com/affiliates/aaas.htm; GEICO Auto Insurance www.geico.com/landingpage/go51.htm?logo=17624; Hertz 800-654-2200 CDP#343457; Office Depot https://bsd.officedepot.com/portalLogin.do; Seabury & Smith Life Insurance 800-424-9883; Subaru VIP Program 202-326-6417; VIP Moving Services www.vipmayflower.com/domestic/index.html; Other Benefits: AAAS Member Services 202-326-6417 or www.aaasmember.org.

science_editors@aaas.org	(for general editorial queries)
science_letters@aaas.org	(for queries about letters)
science_reviews@aaas.org	(for returning manuscript reviews)
science_bookrevs@aaas.org	(for book review queries)

Published by the American Association for the Advancement of Science (AAAS), *Science* serves its readers as a forum for the presentation and discussion of important issues related to the advancement of science, including the presentation of minority or conflicting points of view, rather than by publishing only material on which a consensus has been reached. Accordingly, all articles published in *Science*—including editorials, news and comment, and book reviews—are signed and reflect the individual views of the authors and not official points of view adopted by AAAS or the institutions with which the authors are affiliated.

AAAS was founded in 1848 and incorporated in 1874. Its mission is to advance science, engineering, and innovation throughout the world for the benefit of all people. The goals of the association are to: enhance communication among scientists, engineers, and the public; promote and defend the integrity of science and its use; strengthen support for the science and technology enterprise; provide a voice for science on societal issues; promote the responsible use of science in public policy; strengthen and diversify the science and technology workforce; foster education in science and technology for everyone; increase public engagement with science and technology; and advance international cooperation in science.

Information for Authors
See pages 752 and 753 of the 10 February 2012 issue or access www.sciencemag.org/about/authors

EDITOR-IN-CHIEF **Bruce Alberts**
EXECUTIVE EDITOR **Monica M. Bradford**
NEWS EDITOR **Colin Norman**
MANAGING EDITOR, RESEARCH JOURNALS **Katrina L. Kelner**
DEPUTY EDITORS **R. Brooks Hanson, Barbara R. Jasny, Andrew M. Sugden, Valda J. Vinson**

Editorial senior editors/commentary Lisa D. Chong, Brad Wible; **senior editors** Gilbert J. Chin, Pamela J. Hines, Paula A. Kiberstis (Boston), Marc S. Lavine (Toronto), Beverly A. Purnell, L. Bryan Ray, Guy Riddihough, H. Jesse Smith, Phillip D. Szuromi (Tennessee), Jake S. Yeston, Laura M. Zahn (San Diego); **associate editors** Melissa R. McCartney (Education Projects), Kristen L. Mueller, Jelena Stajic, Sacha Vignieri (Oregon), Nicholas S. Wigginton; **book review editor** Sherman J. Suter; **associate letters editor** Jennifer Sills; **editorial manager** Cara Tate; **senior copy editors** Jeffrey E. Cook, Cynthia Howe, Harry Jach, Lauren Kmec, Barbara P. Ordway, Trista Wagoner; **copy editor** Chris Filiatreau; **senior editorial coordinators** Carolyn Kyle, Beverly Shields; **editorial coordinators** Joi S. Granger, Anita Wynn; **publications assistants** Ramatoulaye Diop, Aneera Dobbins, Jeffrey Hearn, Lisa Johnson, Dona Mathieu, Le-Toya Mayne Flood, Shannon McMahon, Scott Miller, Jerry Richardson, Teresa R. Sakon, Brian White; **editorial assistant** Patricia M. Moore; **executive editorial assistant** Yolanda O'Bannon (San Francisco); **executive assistant** Alison Crawford; **administrative support** Maryrose Madrid

Editorial director, web and new media Stewart Wills; **senior web editor** Sarah Crespi; **web editor** Kerry Klein; **web development manager** Martyn Green; **web developers** Corinna Cohn, Andrew Whitesell

News deputy news editors Robert Coontz, David Grimm (Online), Eliot Marshall, Jeffrey Mervis, Leslie Roberts, Richard Stone, John Travis; **contributing editors** Elizabeth Culotta, Polly Shulman; **news writers** Yudhijit Bhattacharjee, Adrian Cho, Jennifer Couzin-Frankel, Carolyn Gramling, Jocelyn Kaiser, Richard A. Kerr, David Malakoff, Elizabeth Pennisi, Robert F. Service (Pacific NW), Erik Stokstad, Emily Underwood; **web developer** Daniel Berger; **social media strategist** Meghna Sachdev; **intern** Lizzie Wade; **contributing correspondents** John Bohannon, Jon Cohen (San Diego, CA), Ann Gibbons, Sam Kean, Eli Kintisch, Andrew Lawler, Mitch Leslie, Charles C. Mann, Virginia Morell, Gary Taubes; **copy editors** Melissa Raimondi, Kara Estelle, Linda B. Felaco; **administrative support** Scherraine Mack; **bureaus** San Diego, CA: 760-942-3252, FAX 760-942-4979; Pacific Northwest: 503-963-1940

Production director Wendy K. Shank; **assistant manager** Rebecca Doshi; **senior specialists** Steve Forrester, Christopher Redwood, Anthony Rosen; **Preflight director** David M. Tompkins; **manager** Marcus Spiegler; **specialists** Jason Hillman, Tara Kelly

Art director Yael Fitzpatrick; **associate art director** Laura Creveling; **senior illustrators** Chris Bickel, Katharine Sutliff; **illustrator** Yana Hammond; **senior art associates** Holly Bishop, Preston Huey; **art associates** Kay Engman, Garvin Grullón, Chrystal Smith; **photo editor** Leslie Blizard

***Science* International**

Europe (science@science-int.co.uk) **editorial: international managing editor** Andrew M. Sugden; **senior editor/commentary** Julia Fahrenkamp-Uppenbrink; **senior editors** Caroline Ash, Stella M. Hurtley, Ian S. Osborne, Peter Stern; **associate editor** Maria Cruz; **contributing editor** Helen Pickersgill; **editorial support** Rachel Roberts, Alice Whaley; **administrative support** Janet Clements, Jenny Hinson, John Wood; **news: deputy news editor, u.k.** Daniel Clery; **contributing editor, europe** Martin Enserink; **contributing correspondents** Michael Balter (Paris), Kai Kupferschmidt (Berlin), Gretchen Vogel (Berlin)

Asia Japan Office: Asca Corporation, Tomoko Furusawa, Rustic Bldg. 7F, 77 Tenjin-cho, Shinjuku-ku, Tokyo 162-0808, Japan; +81 3 6802 4616, FAX +81 3 6802 4615, inquiry@sciencemag.jp; **contributing correspondents** Dennis Normile [Japan: +81 (0) 3 3391 0630, FAX +81 (0) 3 5936 3531; dnormile@gol.com]; Hao Xin [China: cindyhao@gmail.com]; Mara Hvistendahl [China: mhvisten@aaas.org]; Pallava Bagla [South Asia: +91 (0) 11 2271 2896; pbagla@vsnl.com]

EXECUTIVE PUBLISHER **Alan I. Leshner**
PUBLISHER **Beth Rosner**

Fulfillment Systems and Operations (membership@aaas.org); **customer service supervisor** Pat Butler; **specialists** LaToya Casteel, Michelle Ofordire, April Marshall; **manager, data entry** Mickie Napoleoni; **data entry specialists** Tarrika Hill, JJ Regan, Eva Mae Campbell

Business Operations and Administration director Deborah Rivera-Wienhold; **business systems and financial analysis director** Randy Yi; **manager, fulfillment systems** Frits Buninghi; **systems analyst** Nicole Mehmedovich; **manager, business analysis** Eric Knott; **manager, business operations** Jessica Tierney; **business analysts** Cory Lipman, Celeste Troxler; Christine Wehrli; **financial analyst** Julia Nguyen; **rights and permissions: administrator** Emilie David; **associate** Elizabeth Sandler; **marketing director** Ian King; **marketing managers** Allison Pritchard, Alison Chandler, Julianne Wielga, Samantha Smith; **marketing associates** Aimee Aponte, Mary Ellen Crowley, Elizabeth Sattler, Rebecca Riffkin; **senior marketing executive** Jennifer Reeves; **director, site licensing** Tom Ryan; **director, corporate relations** Eileen Bernadette Moran; **senior publisher relations specialist** Kiki Forsythe; **publisher relations manager** Catherine Holland; **publisher relations, eastern region** Keith Layson; **publisher relations, western region** Ryan Rexroth; **customer relations manager** Iquo Edim; **marketing manager** Christina Schlecht; **marketing associates** Paulina Curto, Mitchell Edmund; **customer relations associate:** Joe Horn; **electronic media: director** Lizabeth Harman; **assistant manager** Lisa Stanford; **production specialists** Antoinette Hodal, Nichele Johnston, Lori Murphy, Kimberly Oster; **web and new media: senior project manager** Trista Smith, **project leader** Luke Johnson **computer specialists** Walter Jones, Kai Zhang, **web developer** Jeremy Bates; **program director, aaas member central** Peggy Mihelich

director, global collaboration, custom publications, advertising Bill Moran
editor, custom publishing Sean Sanders: 202-326-6430
assistant editor, custom publishing Tianna Hicklin 202-326-6463
associate director, collaboration, custom publications/china/taiwan/korea/singapore Ruolei Wu +86-1367-101-5294

Product (science_advertising@aaas.org); **midwest** Rick Bongiovanni: 330-405-7080, FAX 330-405-7081; **east coast/e. canada** Laurie Faraday: 508-747-9395, FAX 617-507-8189; **west coast/w. canada** Lynne Stickrod: 415-931-9782, FAX 415-520-6940; **uk europe/asia** Roger Goncalves: TEL/FAX +41 43 243 1358; **japan,** Makiko Hara: +81 (0) 3 6802 4616, FAX +81 (0) 3 6802 4615; ads@sciencemag.jp; **china/taiwan** Ruolei Wu: +86 1367 1015 294 rwu@aaas.org
worldwide associate director of *Science* Careers Tracy Holmes: +44 (0) 1223 326525, FAX +44 (0) 1223 326532

Classified (advertise@sciencecareers.org); **u.s.: east coast/west coast/south central/south america** Tina Burks: 202-326-6577; **midwest/canada/industry** Allyson Rosen: 202-326-6578; **sales administrator** Marci Gallun; **europe/row sales** Benjamin Asfaha, Lucy Nelson; **sales assistant** Kelly Grace; **japan** Yuri Kobayashi +81 (6) 6627-9250; careerads@sciencemag.jp; **china/taiwan** Ruolei Wu: +86 1367 1015 294 rwu@aaas.org; **advertising support manager** Karen Foote: 202-326-6740; **advertising production operations manager** Deborah Tompkins; **senior production specialist/graphic designer** Amy Hardcastle; **production specialist** Yuse Lajiminmuhip; **senior traffic associate** Christine Hall; **sales coordinator** Shirley Young

AAAS Board of Directors retiring president, chair Nina V. Fedoroff; **president** William H. Press; **president-elect** Phillip A. Sharp; **treasurer** David E. Shaw; **chief executive officer** Alan I. Leshner; **board** May R. Berenbaum, Bonnie L. Bassler, Stephen L. Mayo, Raymond Orbach, Julia M. Phillips, Sue V. Rosser, David D. Sabatini, Inder M. Verma

AAAS
ADVANCING SCIENCE, SERVING SOCIETY

“WE’RE PROVIDING THE TOOLS TO ADVANCE

a new wave of cancer research

UNIMAGINABLE FIVE YEARS AGO.

The XF^e Analyzer makes real-time, kinetic measures of the Warburg Effect, glucose and glutamine metabolism, and fatty acid oxidation of cancer cells in a microplate. Amazing!”

— *Min Wu, PhD,*
Director of Biology
Seahorse Bioscience

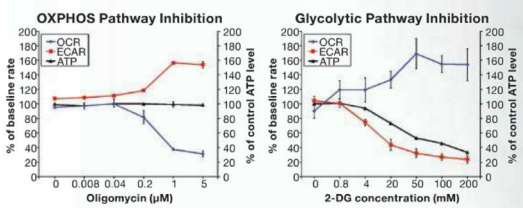

The Seahorse XF^e Extracellular Flux Analyzer

Measurements of cellular glycolysis are essential to understanding cancer, immune response, stem cell differentiation, aging, and cardiovascular and neurodegenerative diseases. The XF Glycolysis Stress Test Kit makes it easy to measure the three key parameters of cellular glycolysis in a microplate: glycolysis, glycolytic capacity, and glycolytic reserve, revealing critical information not evident in mitochondrial respiration measurements alone.

See what’s possible.

Scan this QR code to view videos and see what the XF Analyzer can achieve. Visit **www.seahorsebio.com/science** for more information!

Seahorse *Bioscience*

AROUND THE WORLD

Tasmania, Australia **1**

Bushfires Rage Across Tasmania

Australia welcomed the New Year with raging fires and a record-breaking heat wave. On 7 January, the average highest daily temperature hit 40.33°C, beating the previous record of 40.17°C set in 1972. The first 2 weeks of January were "the hottest 13-day period in Australian history," says the Australian Bureau of Meteorology's David Jones.

Scorching. Fires blazed near Hobart, Tasmania, on 5 January.

The extreme heat forced the bureau to top-up its color-coded weather map to accommodate temperatures up to 54°C. Trains were halted in the state of Queensland amid fears that tracks might buckle. As *Science* went to press, Tasmania continues to battle two major bushfires triggered on 4 January by what the state fire service classified as "catastrophic" weather conditions. Hundreds of grass- and bushfires are burning across the country, with the most severe in Victoria and New South Wales, where 33 homes were lost, as well as facilities at the Siding Spring Observatory.

A report released on 12 January by Australia's Climate Commission says that the heat wave and bushfires were "exacerbated" by global warming. It concludes: "The length, extent and severity of the current heatwave are unprecedented in the measurement record."

Washington, D.C. **2**

Appeal to Restore U.S. Gun Violence Research

More than 100 academic leaders signed a letter asking the Obama administration to lift a virtual ban on U.S.-funded gun violence research. The 10 January letter, organized by the University of Chicago's social science group, the Crime Lab, was sent to Vice President Joseph Biden, head of the White House's new Gun Violence Commission. The letter says that "politically-motivated constraints" sought by pro-gun lobbies and adopted by Congress in the mid-1990s have cut short a promising area of study. After 1997, funding from the Centers for Disease Control and Prevention and the National Institutes of Health dried up. "Right now the research community is hampered in its ability to inform policymakers about the expected benefits and costs of different policy approaches because of politically-motivated limits on data access, and substantial federal under-funding of research on gun violence," writes Crime Lab Director Jens Ludwig, a co-author of the letter, in an e-mail to Science. The Biden panel is weighing new policies in response to the December mass shooting of schoolchildren in Newtown, Connecticut; its recommendations are due this week. **http://scim.ag/gunviol**

Targeting guns. A panel led by Joe Biden (*right*) considers new measures on gun violence.

Collected. The team that drilled down to Lake Vostok last year now has an ice core.

Lake Vostok, Antarctica **3**

Russian Team Retrieves First Sample From Lake Vostok

A long-running Antarctic drilling effort finally yielded an ice core, when a team of Russian scientists successfully retrieved its first sample this week from Antarctica's 20-million-year-old Lake Vostok, which is buried under nearly 4000 meters of ice. The team, from Russia's Arctic and Antarctic Research Institute, had completed drilling to the surface of the lake in February 2012. To prevent contamination during sampling, the scientists devised a plan to drill just to the lake's surface, but then allow the pressurized lake water to rise into the borehole and freeze there. They returned this Antarctic summer to retrieve the frozen core—and on 10 January, the team told RIA Novosti, the researchers collected their prize. "The first core of transparent lake ice, 2 meters long, was obtained on January 10 at a depth of 3,406 meters," declared the Arctic and Antarctic Research Institute in a statement. "Inside it was a vertical channel filled with white bubble-rich ice." Next up: Analysis of the core itself, which many hope will contain evidence of microbial life.

Washington, D.C. **4**

Biologists Accuse Bureau Of Fishy Behavior

Managers at the U.S. Bureau of Reclamation (BOR) committed scientific misconduct when they sought to shut down the agency's research division last year after it produced controversial studies about endangered fish populations, according to a complaint filed earlier this month on behalf of seven fisheries

Science LIVE

Join us on Thursday, 24 January, at 3 p.m. EST for a live chat about **the next big step in supercomputing**—and which country might choose to take it. **http://scim.ag/science-live**

biologists working in southern Oregon.

The complaint alleges that BOR area office manager Jason Phillips called for scrapping the agency's Fisheries Resources Branch (FRB), in part because some FRB results conflicted with research results from the National Oceanic and Atmospheric Administration and the U.S. Fish and Wildlife Service (FWS). In one case, an FRB study found a stable population of endangered suckers in Lake Ewauna, where a previous FWS study had deemed the lake habitat of poor water quality. Phillips had stated in an 8 November memorandum that "[t]here's a concern that … in some cases we are simply carrying out studies to contradict the science of other agencies." The scrapping of FRB "will have a chilling effect of suppressing future scientific findings," the complaint states. BOR spokesperson Pete Lucero says the decision to close FRB was an attempt to make the agency more efficient.

Washington, D.C. **5**

A New Look for House Science Panel

The congressional committee that pays the most attention to U.S. science policy has three new subcommittee chairs.

Last week, the House of Representatives' Committee on Science, Space, and Technology announced that second-term legislator Representative Larry Bucshon (R–IN), a cardiothoracic surgeon who is a deep skeptic of climate change science, would head its research subcommittee. Bucshon replaces Representative Mo Brooks (R–AL), who in his first term impressed the community with his understanding of the government's role in funding basic research.

Bucshon

Lummis

The new chair of the full committee, Representative Lamar Smith (R–TX), has split the environment and energy portfolio and given energy to a new member of the committee: Representative Cynthia Lummis (R–WY). A lawyer and career politician, she's a strong advocate of the fossil fuel industry and doesn't believe that humans are contributing to climate change.

Finally, the new chair of the technology panel is freshman Representative Thomas Massie (R–KY). A Massachusetts Institute of Technology–trained mechanical engineer and entrepreneur who developed pioneering human-computer interface software, Massie is an acolyte of Tea Party favorite Senator Rand Paul (R–KY).

http://scim.ag/scisub

Washington, D.C. **6**

NOAA: 2012 Hottest Year On Record for U.S.

Last year saw the warmest average temperatures on record—at least for the contiguous United States, according to a report released last week by the National Oceanic and Atmospheric Administration (NOAA). The average temperature was 13°C, compared with a 20th century average of 11.2°C. (The previous record-holder, 1998, saw average temperatures of 12.4°C). The year consisted of "a record warm spring, the second warmest summer, the fourth warmest winter, and a warmer than average autumn," said climate scientist Jake Crouch, of NOAA's National Climatic Data Center, in a press conference on 8 January. The data do not address global temperatures, however.

Meanwhile, a draft of another climate-related report—the U.S. Global Change Research Program's National Climate Assessment on the impact of global warming in the United States, released every 4 years—was published on 11 January. It points to stronger evidence that the climate is changing rapidly, and primarily as a result of human activities, including the burning of fossil fuels—and notes that there will be increasing impacts on crops and fresh water supplies. The report, written by a group of 240 scientists, will now undergo a 3-month period of public comment and review.

THEY SAID IT

"The Administration does not support blowing up planets."

—Paul Shawcross, chief of the Science and Space Branch at the White House Office of Management and Budget, rejecting an online petition to build the Death Star, the orbiting weapons system from *Star Wars*.

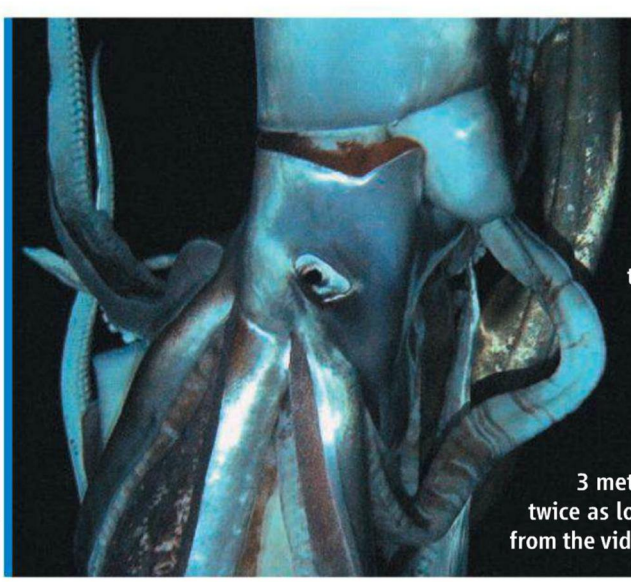

Denizen of the Deep, Caught on Film

In 2004, the first still photographs of the giant squid roaming its deep-water habitat wowed the world. But this year, scientists have gone one better: They have video. The ghostly white creature was spied by a three-person team, led by Japanese zoologist Tsunemi Kubodera, in a submersible in waters 600 meters deep about 1000 kilometers south of Tokyo. The team included scientists and filmmakers from Japan's National Museum of Nature and Science, the Discovery Channel, and Japanese broadcaster NHK, which has made it a 10-year mission to capture images of the creature in its habitat. For hundreds of hours last summer, the team searched for signs of the sea creatures with the aid of chemical attractants, bioluminescent lures, and ultrasensitive cameras that used only infrared light. The lucky dive came in July 2012: The team spied a giant squid about 3 meters long—which is still small for the species; the largest ever caught was twice as long—and followed it to a depth of about 900 meters. NHK aired footage from the video in Japan on 13 January; the Discovery Channel will air it on 27 January.

CREDITS (LEFT TO RIGHT): USFWS/TIMOTHY KNEPP; NHK/NEP/DISCOVERY CHANNEL; UNITED STATES CONGRESS/ERIC CONNOLLY; OFFICE OF CONGRESSMAN CYNTHIA LUMMIS

FINDINGS

Building a Better Burrow

Genetically speaking, it might not take much to evolve some new complex behaviors—such as how a wild mouse expands its burrow. Burrowing behavior varies between species: Deer mice make simple, one-tunnel burrows, whereas a close relative, the oldfield mouse, goes for a long, two-tunnel design that includes an escape passage. To assess the genetic basis of burrow building, Harvard University evolutionary biologist Hopi Hoekstra and her colleagues bred oldfield mice with deer mice, mated the offspring again with deer mice, and then assessed tunnel characteristics in both generations. Different genes control different components of burrow building, Hoekstra and her colleagues reported this week in *Nature*. Three gene regions underlie tunnel length, but just one determines whether escape tunnels are made. That region could contain only one gene—suggesting that very little genetic change is needed to evolve the two-tunnel burrow (a dominant trait). "The paper provides a nice empirical example of how a complex behavior evolves on a genetic level," says Catherine Peichel, an evolutionary biologist at the Fred Hutchinson Cancer Research Center in Seattle, Washington.
http://scim.ag/burrowers

Dig in. Genetics drives this oldfield mouse to build a two-tunnel burrow.

Rethinking Barnacle Reproduction

Scientists continue to marvel at the length of the barnacle's penis—up to eight times its body length in some species. That endowment has long been thought to explain how the immobile creatures manage to reproduce (barring a few self-fertilizing species). But a study published this week in the *Proceedings of the Royal Society B* suggests that at least one species, *Pollicipes polymerus,* has a different approach—possibly a compensation for its relatively short penis. *P. polymerus* delivers sperm through copulation when close enough to reach its neighbor, but it also casts sperm out into the water column, trusting that distant mates will capture them. Apparently, the scattershot approach works: The researchers found that most fertilized barnacle eggs contained DNA from distant barnacles. But the finding may make some scientists cringe, says Joseph Pawlik, a marine biologist at the University of North Carolina, Wilmington, who was not involved in the study. Previous studies have assumed that barnacles reproduce only with their near neighbors, he says—so "I suspect that some people will need to go back and look at the studies they've been doing."
http://scim.ag/barnre

Long shot. *P. polymerus* shoots sperm into the water via its long penis (*top, above feeding legs*).

Frankensteinish Flight of the Bumblebee

Bumblebees seem to have subpar wings when it comes to wear and tear—at least, compared with their cousins the yellow jackets. But how does a more fragile wing benefit the bumblebee? Harvard University biomechanist Andrew Mountcastle took an unusual approach to the question: He glued yellow jacket wings to a bumblebee—and found that what's good for the wasp isn't necessarily best for the bee.

While examining insect wing adaptations, Mountcastle had noticed that, unlike the bee's wing, the wasp's wing has a joint that makes it flexible and possibly more resilient in crashes. Subjected to repeated collisions with a leaf, the bumblebee wing wore down 1.5 times faster than the yellow jacket wing, Mountcastle reported last week at the annual meeting of the Society for Integrative and Comparative Biology in San Francisco.

Wing change. Gluing a yellow jacket wing to a bumblebee (*right*) tests the wing's performance.

But bumblebees beat their wings much more rapidly than do yellow jackets. And after attaching the yellow jacket wing, he says, he found that the quicktime beat caused the wasp wing to flex all the time, possibly lowering flight efficiency.

Bumblebees have their own way of coping with collisions, too. The scaffolding veins on their wings are concentrated close to the body, leaving the tip less rigid and likely better able than the rest of the wing to withstand wear and tear. These findings could help the development of insect-sized aerial robots: "The more we know about biodesign, the better we will be able to emulate it with technology," says Robert Dudley, a physiologist at the University of California, Berkeley.

NOTED

>Gastrointestinal disease–causing *Clostridium difficile* is the scourge of hospitals; scientists have explored ways to introduce healthy gut bacteria to the afflicted via a controversial and somewhat unpalatable treatment called "fecal transplant" (http://scim.ag/GutBacteria). Enter RePOOPulate, a synthetic poop product made from purified intestinal bacterial cultures that can combat *C. difficile*—and, says its creator, microbiologist Emma Allen-Vercoe of the University of Guelph in Canada, it offers a "less icky" alternative to fecal bacteriotherapy.

NEWS & ANALYSIS

CREDIT: MOHAMMAD SAJJAD/AP

DISEASE ERADICATION

Killings Force Rethinking of Pakistan's Anti-Polio Drive

Mourning. Pakistani villagers attend the funeral of a polio worker killed near Peshawar in December.

Of all the messy, dangerous places that he has fought to eradicate polio—Somalia, Sudan, Yemen—Elias Durry says that nothing has prepared him for what he faces now in Pakistan: the targeted assassination of nine polio workers over 3 days in December. Seven more aid workers were killed on New Year's Day in what might be related attacks.

Over the years, polio workers have been killed in conflict zones, but never in such numbers or in such deliberate attacks. "This is unprecedented in all accounts. To have health workers targeted and not know who [is behind it] or why, it is a first," says a clearly shaken Durry, an Ethiopian-born epidemiologist who now heads the World Health Organization's (WHO) team in Pakistan as part of the Global Polio Eradication Initiative (GPEI).

Durry and his colleagues in the government are grappling with two questions: Can the government safeguard its legions of vaccinators and still reach enough kids to keep the poliovirus in check? And if not and the virus regains steam, how big a setback will that be to the global initiative, which, 13 years after it was due to be finished, is finally close to success (*Science*, 3 August 2012, p. 514)? Pakistan is one of just three countries where the poliovirus remains entrenched, and global cases are at an all-time low.

The attacks came in waves. On Monday, 17 December, one polio worker was shot and killed in Gadap Town in Karachi, at the southern tip of the country, where two polio workers were killed in July. The next day, in three carefully orchestrated attacks, four campaign workers were killed in drive-by shootings, again in the slums of Karachi. Another was killed in Peshawar in the northwestern province of Khyber Pakhtunkhwa (KP). On the 19th, another three vaccinators were gunned down in KP. Six of the nine victims were women, as were six of the seven killed 2 weeks later. A nurse was killed on her way to work on 13 January.

"The first reaction for a lot of us was despair," says Hamid Jafari, a physician and epidemiologist who directs GPEI from WHO in Geneva, Switzerland. "It is reprehensible … 17- and 18-year-old young women getting shot in the head." The country temporarily suspended vaccination activities, and the United Nations ordered its staff members off the streets.

But despair was quickly followed by resolve as the government vowed not to quit with the end finally in sight, Jafari says. In 2012, polio cases in Pakistan dropped to 58 from 198 the year before, and the virus is increasingly cornered in three small pockets of the country—not coincidentally, hotbeds of violence and mistrust of the government and all things Western (*Science*, 3 August 2012, p. 517). "I could smell finishing the job by April/June," Durry says. "Everything was going in the right direction. And we were in full gear to take advantage of the 'last low season,'" when transmission ebbs and the virus is at its weakest. "Now it is the most dangerous season, which can have a chilling effect not only on Pakistan but the globe."

As the country resumes limited vaccinations under tight security, investigators are trying to figure out who is behind the attacks, and why. People close to the program don't see the attacks as directed at polio vaccination per se. Jafari thinks the perpetrators are likely "some element trying to disrupt the government," perhaps before the upcoming general elections, or otherwise "jockeying for some advantage." He suspects the high-profile polio program is just "an easy target." He, Durry, and others do not see the events as necessarily part of an ideological war with the Taliban over polio vaccination, as some factions support the eradication effort in Pakistan and Afghanistan. Nor do they think the shootings are a direct response to the fake hepatitis B vaccination campaign that the U.S. Central

Intelligence Agency used to try to track down Osama bin Laden, as has been widely alleged. David Heymann, the former assistant director general of WHO in charge of polio and health security who is now at the United Kingdom's Health Protection Agency, agrees. He and others suspect that the shootings are part of a broader assault on women's education and development, especially since the aid workers killed on New Year's Day were not directly involved in polio vaccination. "It's a political issue that will require a political resolution," says Jafari, who adds that the program needs to work with all parties and Islamic leaders.

Until the culprits are identified, "We will try to do what we can without making a big noise," Durry says. "Security is the priority." For now, the widely publicized 3-day national campaigns, when vaccinators fan out across the country in an attempt to reach some 30 million kids with polio drops, seem off the table. "We can't constantly provide protection to 250,000 vaccinators," Durry says. "But we can be surgical," protecting workers in discreet campaigns in the areas where viral circulation is rampant. Equally important, he says, will be the ability to respond rapidly should the virus break out of its known reservoirs. Going forward, "we will play it by ear," says Jafari, who declines to give specifics for security reasons.

Everyone's worst fear is a repeat of Nigeria, Durry says, where several northern states banned polio vaccination in 2003 and 2004, and virus from Nigeria reinfected some 20 countries, setting back the global initiative for years.

There are reasons to think the fallout won't be as bad, says Mark Pallansch, a virologist and epidemiologist who tracks the virus at the U.S. Centers for Disease Control and Prevention in Atlanta. Historically, the Pakistan virus hasn't traveled far, except for its frequent forays into Afghanistan across the porous border. And unlike in Nigeria, many countries surrounding Pakistan, including India and China, have strong polio immunization programs and thus present a "wall of immunity" that the virus will find difficult to penetrate. That's the hope, at least.

Amid the uncertainties, what is clear is that working in Pakistan, never easy, just got a whole lot harder. Durry says he remains optimistic. Still, he adds, today's crisis "makes the problems we were worrying about 6 months ago seem like 'child's play.' "

–LESLIE ROBERTS

ANIMAL BEHAVIOR

For $60, a Peek Inside Your Dog's Mind

Is your dog a deep thinker? A keen reader of emotions? Liable to wolf down a meatloaf when it thinks you aren't looking? Evolutionary anthropologist Brian Hare of Duke University in Durham, North Carolina, is helping to launch a new company that claims to offer dog owners answers to these pivotal questions and more. Dognition is currently in beta testing, and more than 2000 dogs in almost 40 countries have participated in the series of exercises provided to their owners on its Web site. It's slated to open to all on 5 February, timed with the release of a new book by Hare and his wife, author and researcher Vanessa Woods, called *The Genius of Dogs: How Dogs Are Smarter Than You Think*. The testing costs $59.95.

Dognition parallels Hare's academic life: He runs the Duke Canine Cognition Center (www.dukedogs.com), described online as having the "cheapest tuition and highest acceptance rate at Duke." Enthusiastic dog owners bring their pets to the university for a battery of games that aims to elucidate animal cognition. The Dognition exercises were drawn partly from games that the center administers to identify promising service dogs and bomb detection dogs.

In addition to tapping into a large and lucrative market of dog lovers, Hare and his scientific advisory board will use the Dognition data to formulate new research questions and help answer existing ones. This might be a bit tricky. "These are not professional scientists running the tests," says Zsófia Virányi, a canine behavior researcher at the University of Veterinary Medicine, Vienna. Hare is taking care to find simple games that are least prone to user error—although, he and others admit, the data generated will be far from ironclad. And who knows what might distract the animal when it's tested in its home environment. Virányi says: "Was the dog listening to the grandmother preparing dinner in the kitchen?"

Science spoke with Hare last week. The interview was edited for brevity and clarity.

–JENNIFER COUZIN-FRANKEL

Q: How did you come up with the idea for Dognition?

B.H.: I went to a conference called The Association of Pet Dog Trainers [in October 2009]. I gave my keynote lecture … [describing his studies of dog cognition]. Everybody kept saying over and over again, "We want to know how to do these tests; we want to do these tests with our clients."

People said while I was there: "You should really start a company." I was like: "That's ridiculous." I knocked around the idea for a couple years. I went to the Duke Business School and gave an elevator pitch—I had 3 minutes to explain my idea to a room of a couple hundred people. … A bunch of business professors came up to me afterwards and said: "You have to do this."

I ended up meeting our CEO [Kip Frey] who is in charge of the entrepreneurship program at the [Duke] law school. He is a serial entrepreneur. … We met, he loved the idea, he basically said, "I want to be your CEO." … He said, "Let's do this," and a week later he'd raised a million dollars. … We currently are a company of around 25, 30 people depending on how you count it. This is not a joke.

Q: So tell me how this all works. I sit down in front of the computer with Fido and then what?

B.H.: We've had the Canine Cognition Center since 2009. … [People] drive their dog to Duke, then they're met by some undergraduates who play games with their dogs. … From this experience what became clear is that there's a real hunger for people to learn more about how their dogs think, … [and] some of these things aren't that hard to do.

You go to the Web site; you sign up your dog and tell us a little bit about your dog. You get a personality questionnaire, things you've observed your dog do and not do. … Then the fun, interesting new part comes, the CAT—the Canine Assessment Toolkit. … It's 10 games. … There will be a video that gives you detailed instructions on how to play the game with your dog.

Q: Like what?
B.H.: One of the first tests is, for instance, you yawn. You yawn five times within a minute, then you watch for 2 minutes to see if your dog yawns. That's literally the game. It's not that complicated.

Q: And what does this tell you about your dog?
B.H.: It's a measure of contagion. Contagion, some people have argued, is a precursor to empathy. … You go through all 10 tests. … We're looking at how empathic is your dog, how communicative is your dog, how reliant on their memory is your dog, does your dog use reasoning to solve some problems, and also how cunning is your dog—it's a nice way of saying how deceptive is your dog.

Q: And how do you measure how deceptive a dog is?
B.H.: All the games are based on published studies. … We didn't just make up a game and cross our fingers that it would work. … There are actually several studies showing if you face your dog and you say, "Don't eat that food," versus you say, "Don't eat that food" and close your eyes—there are many dogs that pick up on the fact your eyes are closed and will eat the food if your eyes are closed, but won't eat the food if your eyes are open. They're actually taking into account whether they can get away with things and making a cost-benefit analysis.

In each dimension we're going to tell you how your dog performs relative to all the other dogs in the [Dognition] database. But the key thing to understand, it's not about, "Your dog is the best!" … like a GRE or an SAT [score]. … In the communication dimension, you can be a highly communicative dog. Or maybe you're an independent problem solver. If you ignore my gesture maybe you're a little more independent. I don't know if you've ever been around a chow chow …

Q: So it's about making the dogs—or maybe more accurately their owners—feel good about themselves?
B.H.: You can say it that way, absolutely, and it's true. But at the same time it's really trying to help people understand that the way that we talk about intelligence, it doesn't play out when you start thinking about evolution. There are different strategies, you can be dependent on one or you can be dependent on the other [to thrive]. We're [the company] assuming the dog is a genius—the question is which strategy is a dog using to feed that genius

Q: You're charging people $59.95, but are you also collecting these data for research purposes?
B.H.: Yes, absolutely. … There are questions that you just can't answer without big data, … meaning tens of thousands of people participating, maybe even hundreds of thousands of people. That's what I'm after.

Q: Is there any kind of conflict there, in asking people to pay to be part of a research project?
B.H.: I don't know, I don't know. This may sound lame, but people are already paying for this at Duke—not in money, but in opportunity costs. We've had people drive from different states. We have people stay in hotels for a week to have their dog tested. People really, really want this.

Unraveling doggie thoughts. Anthropologist Brian Hare, with his dog, Tasmania, hopes to recruit hundreds of thousands of dogs to his database.

Q: Who can access the data that's collected?
B.H.: That is currently undecided. The idea would be that certainly the scientific board [could]. We are still in discussions about how to govern ourselves. The hope is that whatever we do, it's not going to be, "Ha ha ha, this is all my data."

Q: Let's say my dog is deemed a weaker communicator—can I do anything to change that or is this like an IQ test where you're stuck with the results?
B.H.: That question has often come up [from the business side of Dognition]. The answer is I have no idea. … That's why we're partnering with some really wonderful well-known trainers … [who] will give you some advice.

Q: Do you think Dognition will change how people relate to or think about their dogs?
B.H.: I sure hope so. I think it can only make people's relationships richer. … If we're profitable, or I should say when we are profitable, one of the goals of the company would be to reinvest some of the profit into the work we do—noninvasive animal behavior research. We could become a major funder of research.

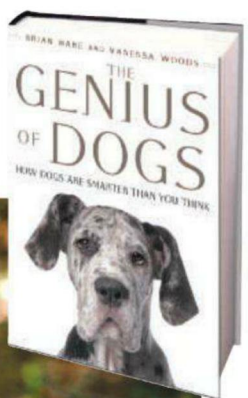

Q: It looks like you're going all out promoting Dognition on a blog, Facebook, Twitter and other social media. Do you have a goal for how many dogs you want to recruit in the first few months?
B.H.: I think we would hope we'd have somewhere near 100,000 in the first year. That may sound ridiculous, but it is a tiny, tiny piece of the market. The eighth largest industry in the U.S. is the pet industry. There are 70 million dogs just in the United States.

CREDITS (TOP TO BOTTOM): COURTESY OF DUTTON, PENGUIN GROUP; GRETCHEN MATHISON

GENETICS

Genealogy Databases Enable Naming Of Anonymous DNA Donors

CAMBRIDGE, MASSACHUSETTS—One afternoon in March last year, Yaniv Erlich sat down at his computer to do an experiment. Before he became a geneticist here at the Whitehead Institute for Biomedical Research, Erlich was a white hat: a hacker hired by banks and credit card companies to break into their computer systems and identify weaknesses. Now he was about to do something similar with genome databases. With little more than the Internet, Erlich wondered, is it possible to identify people who anonymously donate their DNA for research? In other words, could he hack someone's name from their genome data?

Hunched over the computer with him was Massachusetts Institute of Technology undergraduate (and now Ph.D.) student Melissa Gymrek who had helped develop an algorithm to extract genetic markers from DNA sequences. By applying the algorithm to an anonymized genome from a research database and doing some online sleuthing with popular genealogy sites, they came up with a guess for the name of the DNA donor and information about his family. But was it correct?

Erlich and Gymrek did a quick search with the man's name and state of residence using Google, and a family Web site popped right up. Every single detail that they had guessed about an anonymous DNA donor matched up with this man living in Utah. "I kept looking at my notepad to see if we missed anything," says Erlich, who was so shocked that he had to go for a walk.

On page 321 of this issue, Erlich and his collaborators report that they were ultimately able to expose the identity of 50 individuals whose DNA was donated anonymously for scientific study through consortiums such as the 1000 Genomes Project. Those revelations have prompted the National Institutes of Health (NIH) to hide certain data associated with anonymized DNA sequences that it makes public for researchers. "The scientific community needs to have an open discussion about this," says Laura Rodriguez, director of policy, communications, and education at the National Human Genome Research Institute in Bethesda, Maryland, and a co-author of an NIH response to Erlich's study on page 275.

Privacy concerns have been raised about publicly accessible genome data before. A study 5 years ago showed that individuals whose genomes were in seemingly anonymous pools of DNA data could be identified by certain genetic markers, known as single nucleotide polymorphisms, or SNPs (*Science*, 5 September 2008, p. 1278). But this is the first time that people have been identified without needing a sample of their DNA as a reference.

Erlich's team exploited two tricks. The first is that metadata about anonymous DNA donors, such as age at the time of donation and state of residence, is often included with their sequences. Erlich started with the genomes of 32 men of northern and western European ancestry collected in a public database as part of the International HapMap Project (*Science*, 26 May 2006, p. 1131). Based on the metadata, he knew the men's ages and that each resided in Utah when they donated their DNA. But that only narrowed the search down to approximately 10,000 men.

For the next step in Erlich's hack, he turned to a few dozen SNPs on the Y chromosome called Y-STR markers. These are almost certain to remain unchanged between father and son. Taken together, Y-STR markers are like a family crest that distinguishes one patrilineal pedigree from another. That's a powerful tool if you want to know whether a man is a member of a particular family.

That is where the second trick comes in. Cheap DNA-sequencing has made it possible for people to share their genetic markers in databases on recreational genealogy Web sites. To ferret out the donors' identities, Erlich used the two most popular, which provide free access to databases containing nearly 40,000 records matching Y-STR to surnames.

When he plugged the 10 genomes with the most recoverable Y-STR markers into those genealogy databases, eight strongly matched to surnames of Mormon families in Utah. Ultimately, he was confident of his guesses for the surnames of five of the genome donors.

Erlich then gathered more information on each one using online resources such as public record search engines and obituaries. He hit the jackpot with metadata in records from Coriell Cell Repositories, a facility in New Jersey that provides cells from the 1000 Genomes Project donors to researchers. With that, he identified family members who had donated their own genomes to the same project, including women.

"I was surprised but not flabbergasted," Rodriguez says. The managers of the 1000 Genomes Project were aware of the risks posed by the metadata and genealogy Web sites, but, she says, "We didn't realize how easy it was to access this information." They immediately removed donors' ages from the publicly available metadata—critical for Erlich's method—but Rodriguez admits that this is only a short-term fix.

This has "huge implications" for the way that consent is obtained from DNA donors, says George Church, a geneticist at Harvard Medical School in Boston. Church founded the Personal Genome Project, which has a consent form for donors that is "very explicit that their DNA and trait data are identifiable." By contrast, Church points to a phrase from the consent form of the 1000 Genomes project: "… it will be hard for anyone to find out anything about you personally from any of this research."

Deanonymizing genomes could have consequences for DNA donors, Rodriguez says. Federal law prohibits health insurance companies from using a person's genetic data, "but many people worry that the law does not go far enough," she says. For example, there is nothing stopping companies from using genetic data to determine policies for life insurance and long-term disability care.

As genealogy databases and other resources improve, "the reidentification of existing data sets will become easier," Church says. But he and Rodriguez hope that the scientific community will not react by clamping down. "There are enormous benefits to sharing research data," Rodriguez says.

–JOHN BOHANNON

CREDIT: G. GRULLÓN/*SCIENCE*

SOLAR ENERGY

Performance of Nanowire Solar Cells on the Rise

There's no shortage of ways to convert sunlight into electricity. Solar cells made from silicon, thin semiconductor alloy films, and even plastics are all commercial technologies. About 10 years ago, researchers began to consider a new alternative: using arrays of tiny, semiconducting nanowires to harvest light and produce power. Because they use so little semiconductor material and can potentially be produced very cheaply, nanowire solar cells had the look of a solar upstart with plenty of upside. But for years their performance lagged far behind other technologies: Even when the nanowires converted the sun's photons to electrical charges, they had trouble getting those charges out of the cell and putting them to work.

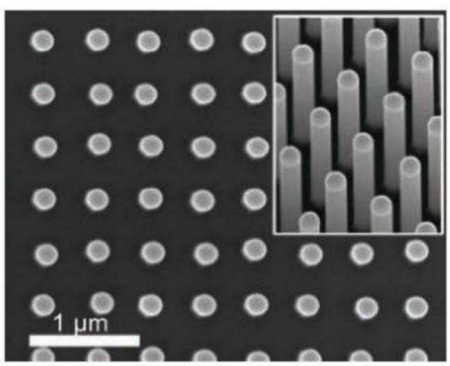

Big gains. Vertically aligned nanowires are the heart of increasingly efficient array-based solar cells.

Now, nanowire photovoltaics are on the ascent. In a paper published online this week in *Science*, researchers from Sweden, Germany, and China report creating nanowire solar cells that convert 13.8% of the energy in sunlight into electricity. And several other groups are also hot on the trail. At the fall meeting of the Materials Research Society in November in Boston, researchers led by Jung-Ho Lee, a chemical engineer at Hanyang University, Ansan, in South Korea, reported wire array solar cells made with high-grade crystalline silicon wires that are 12.8% efficient. And in the 12 December 2012 issue of *Nano Letters*, researchers led by Xiang Zhang of the University of California, Berkeley, reported similar cells made from cheap "metallurgical" silicon. All of these devices still trail the 15% to 22% efficiency of commercial silicon solar cells. But according to several solar cell experts, the nanowire solar cells are improving fast and have plenty of room for further growth.

"From a science and technological point of view, the new results are exciting," says Paul Alivisatos, a chemist and director of the Lawrence Berkeley National Laboratory in California who isn't affiliated with any of the teams behind the recent results. The improvements in controlling the nanostructure of the materials needed to produce the higher efficiency are "a big development," Alivisatos says. However, he adds, "they still have a ways to go beyond this" to have a shot at making a commercial impact.

Compared with other solar technologies, they've already come a long way very quickly. It has taken nearly 40 years for some of the early thin-film technologies to improve from about 5% to 17% efficiency. And over just the past few years, nanowire cells have leapfrogged other decades-old technologies, such as amorphous silicon cells, plastic cells, and dye-sensitized solar cells.

In each case, the improved results of current wire array solar cells came about in part by overcoming the major efficiency killer: electrical charges giving up their energy before they're collected. Light absorbed in a solar cell excites electrons and gives them enough energy to hop from atom to atom through the wire to an electrode. The big advantage of nanowire cells is that electrons have a direct path to the point where they are collected, which reduces the amount of semiconductor needed by as much as 90%. But as electrons make these jumps they leave behind electron vacancies, called holes. If an electron happens to fall into one of these holes, it gives up its extra energy as light or heat, and the efficiency of the cell drops.

The downside of wire array cells is that the wires have a high ratio of surface area to volume, and electrons and holes tend to pair more readily at the crystalline imperfections found at surfaces. Each of the recent advances used tight control of growth techniques to minimize the number of such recombinations. The Swedish-led group, for example, used indium phosphide for its 13.8%-efficient cells because it tends to have slower electron-hole recombination, says Magnus Borgström, a physicist at Lund University in Sweden who directed the research effort. The team also used a newly developed refinement of a growth method known as MOCVD to grow arrays of pristine nanowires. The Korean- and American-led teams grew silicon-based wires using different array designs and growth techniques, but they also managed to minimize recombination losses. And all three teams say they expect this improving nanoscale control to bring even better results soon.

But despite such advances, Alivisatos notes, all new solar technologies face fierce competition from crystalline silicon cells, the dominant technology on the market. The efficiency of silicon cells has barely improved in decades. But since 1980, the cost of silicon modules, the finished packages of cells that are put in service, has fallen by 90% (see figure). That drop in price has accelerated in recent years as China has become the dominant manufacturer of the technology. Over the past 3 years, the price drop has been so sharp that in some countries the cost of installing new solar capacity is now on par with that of building conventional power plants. That's still not the case in the United States, which already has an electric power infrastructure in place and where the installation costs of solar power remain high. But the upshot, Alivisatos notes, is that the market for conventional silicon solar cells is exploding, growing 65% a year. "In a few years we could be looking at a terawatt-[1 trillion watts]-a-year market instead of the tens of gigawatts [billions of watts] now," Alivisatos says. So even though wire array cells are improving fast, the bar is rising. And that's a good thing for the growth of clean energy.

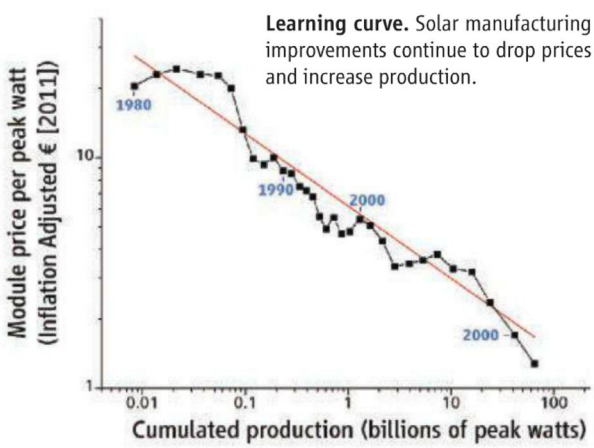

Learning curve. Solar manufacturing improvements continue to drop prices and increase production.

–ROBERT F. SERVICE

CREDITS (LEFT TO RIGHT): WALLENTIN *ET AL.*, *SCIENCE*; FRAUNHOFER INSTITUTE FOR SOLAR ENERGY SYSTEMS, *PHOTOVOLTAICS REPORT*, 22 JUNE 2012

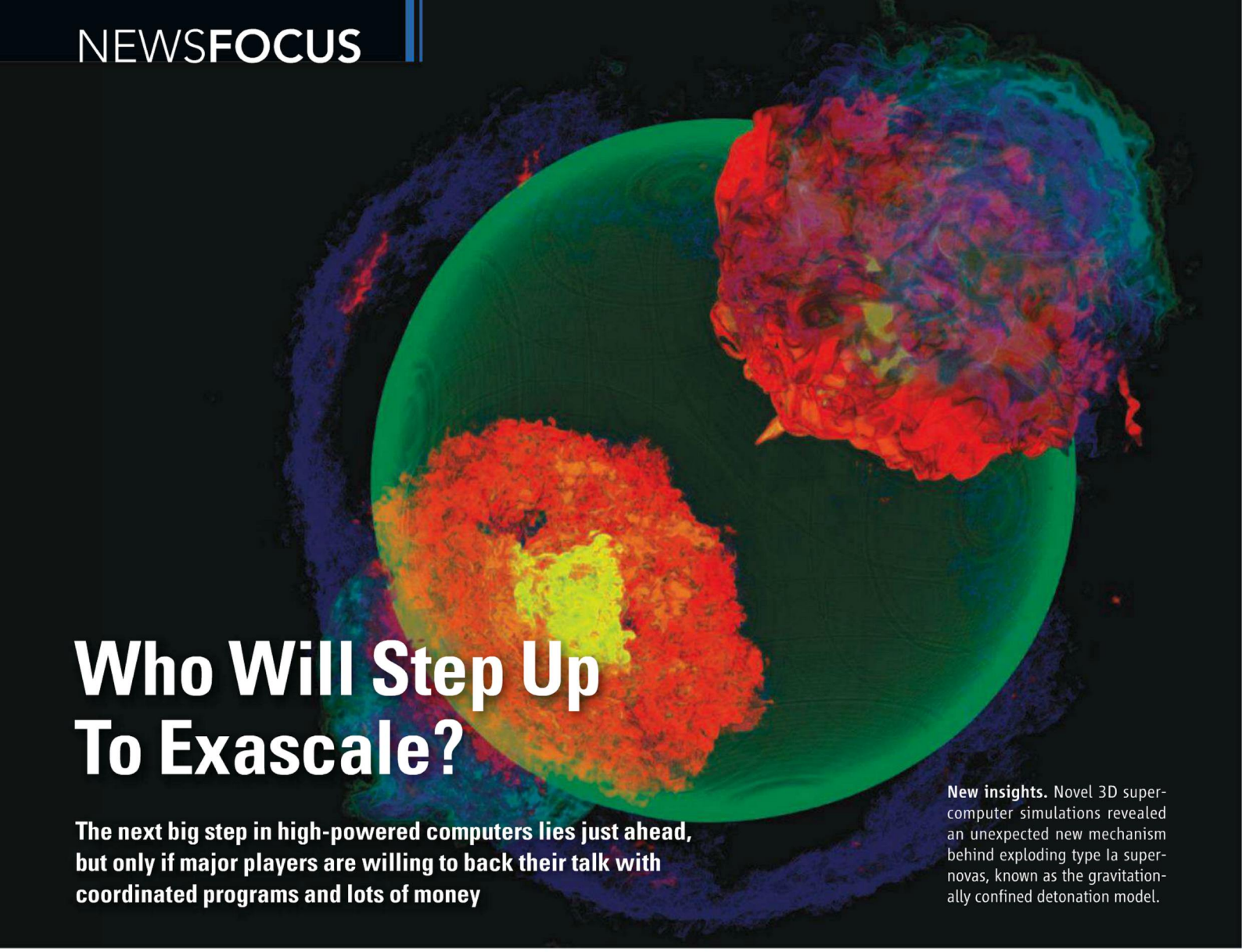

Who Will Step Up To Exascale?

The next big step in high-powered computers lies just ahead, but only if major players are willing to back their talk with coordinated programs and lots of money

New insights. Novel 3D supercomputer simulations revealed an unexpected new mechanism behind exploding type Ia supernovas, known as the gravitationally confined detonation model.

CREDIT: FLASH CENTER FOR COMPUTATIONAL SCIENCE, UNIVERSITY OF CHICAGO

HORST SIMON DOESN'T OFTEN BET AGAINST progress. But several months ago, the supercomputer expert and deputy director of Lawrence Berkeley National Laboratory (LBNL) in California did just that. He bet Thomas Lippert—a German colleague—$2000 that supercomputer makers wouldn't create an exascale computer by the beginning of 2020. If built, this next major milestone in supercomputing will be capable of carrying out 10^{18} floating-point operations per second, or an exaflop. That's 57 times as fast as today's fastest supercomputer, Oak Ridge National Laboratory's Titan, which runs at 17.6 petaflops (10^{15} flops). Such intense computing power could vastly improve everything from climate models to the engineering of engines to work with advanced biofuels.

A quick glance at supercomputing trends would suggest that Simon's bet is a bad one. The improvement of high-performance computers (HPC) has been on an unvarying upward trajectory. The industry marched from the first teraflop (10^{12} flops) machine to the first petaflop machine in just 12 years. Extrapolate this steady rate of progress, and supercomputers should reach exascale computing in 2018.

But troubles are brewing. Supercomputer experts agree that scaling up existing technology won't get supercomputers to the exascale level. Intel, IBM, and other hardware makers say they won't pursue exascale computers without government backing. The United States, China, Japan, Russia, India, and the European Union are all flirting with exascale plans. But to date, governments have balked at committing the hundreds of millions to billions of research dollars likely to be needed to create the new technology.

Just a year ago, supercomputer experts were confident that the industry would cross the exascale threshold between 2018 and 2020 (*Science*, 27 January 2012, p. 394). Now, that confidence is slipping. "There was a fair amount of traction with exascale," says Jack Dongarra, a supercomputing expert at the University of Tennessee, Knoxville, who closely tracks international supercomputing trends. "Some of that is gone now. That's a big disappointment," Dongarra says. John Hengeveld, the HPC segment marketing director for Intel in Hillsboro, Oregon, is more upbeat: "I don't think there has been any setback on the path to exascale." However, he adds, "there is a question about national will."

For Dongarra, Hengeveld, and many others, the key question is which country will step up to create the first exascale computer. The answer will determine more than who gets bragging rights for leading high-performance computing technology into the future. Because the effort is expected to revolutionize the design of everything from computer logic and memory to the interconnections and software that make them all run, the race could determine which country's high-tech firms are likely to dominate computer technology in the decades ahead. And because scientists

who take advantage of the world's top computers tend to be leaders in their own fields, the race to exascale could also affect which nation's researchers will drive developments in disciplines including materials science, alternative energy production, and climate research. "Exascale [computing] is going to have a tremendous impact on our future," says William Harrod, a division director at the U.S. Department of Energy (DOE)'s Office of Advanced Scientific Computing Research.

Radical departures

By all accounts, the transition from current petascale computers to exascale will be difficult. But this isn't the first time supercomputer makers have needed to radically shift technology to keep moving forward. In the 1980s, supercomputer designers switched designs from computers run by single central processing units to parallel computers containing multiple CPUs coupled together. More recently, they began making hybrid supercomputers that added in graphics processing units (GPUs) capable of carrying out some types of calculations faster. Titan, for example, contains 18,688 CPUs (each with 16 processors) and the same number of GPUs. Despite these fundamentally different architectures, the supercomputing performance has roughly doubled each year for 2 decades, a nearly exponential growth rate, according to Erich Strohmaier, a high-performance computing expert at LBNL, who helps run the TOP500 supercomputer Web site, which tracks trends in the industry.

But unless things change quickly, this rate of progress may not continue. "There are great challenges ahead as we scale towards exascale," Dongarra says. Chief among them, Dongarra and others say, is power. Titan, today's top machine, already uses 8.2 megawatts of power, or a watt for every 2 gigaflops. That's a marked efficiency improvement over the previous generation of supercomputers. But if an exascale machine were to run at the same efficiency, it would require 466 MW, enough energy to power nearly half a million homes. To be viable, HPC leaders say an exascale machine must aim to use no more than 20 MW, which means researchers will need to improve the energy efficiency of their machines 23-fold.

That's only the beginning. Researchers will also need to learn how to design massively parallel machines capable of executing a billion computational threads simultaneously. They'll need to redesign computer memory to be faster and more efficient. They'll need to design machines that won't crash when one operation runs into trouble or stalls. And along with these demands and many others, they'll need to design a machine that costs somewhere between $100 million and $200 million. The upshot, Harrod says: "We really need to change the design of the system itself."

That change is complicated by the fact that academic researchers don't build supercomputers: Computer companies such as IBM, HP, and Fujitsu do. But those companies are driven by commercial markets for technology found in desktops, laptops, tablets, and smartphones. And according to Harrod, the gulf between commercial computer technology and the technology at the heart of supercomputers is widening. In 1996, for example, Intel built ASCI Red, the first supercomputer made with off-the-shelf CPUs. By contrast, the custom-built designs that integrate large numbers of CPUs and GPUs in today's high-end machines have no counterparts in lower end machines. What's more, because the commercial chip market dwarfs the HPC market, there is little incentive for chip makers to sink massive investments into a technology that will likely net them only a handful of sales.

To make matters worse, many computer giants are shifting the focus of their business to the emerging field of Big Data, where they help other industries mine vast amounts of data to better target and serve their customers. "To be honest, that market segment has better [profit] margins than HPC," says IBM's Ed Seminaro, the chief architect of the IBM POWER7 supercomputer technology. "We haven't given up on [exascale] technology," Seminaro says. However, he adds, the company has not yet committed to being a leader in the field. In fact, in 2011 IBM backed out of building Blue Waters, a 1 petaflop supercomputer being built at the University of Illinois, Urbana-Champaign, citing high costs (*Science*, 25 November 2011, p. 1044).

Intel's Hengeveld agrees that it's up to government funding agencies to take the lead. "Unless they step up, it isn't going to happen," Hengeveld says. Harrod says he has no illusions otherwise: "Industry is not going to develop exascale systems for the technology alone. It's not going to happen without the federal government."

Who and where?

The question is, whose government? If mere talk is any indication, there could be plenty of competitors. The Russian and Indian governments have both said that they're interested, but neither has announced formal plans yet. The European Union has backed several modest scale research efforts, including PRACE, the Partnership for Advanced Computing in Europe, a $67 million effort of 25 member countries to advance supercomputing software and hardware in Europe. PRACE isn't explicitly an exascale research effort, and its funds are due to end in 2014. But it could be extended if it is included in Europe's 8th Framework Programme (FP8), which coordinates research funding across member countries. According to Dietmar Erwin, a computer scientist at the Jülich Supercomputing Centre in Germany, the PRACE countries will likely be asked to have PRACE funds increased by 50% for the 2014 to 2020 FP8 session. But other infrastructure programs could up that number considerably.

Erwin notes that in Europe, "at the moment there is no plan in place to purchase an exascale computer." And others doubt that Europe will be the first out of the blocks. Not only are European governments grappling with their worst economic tumult in decades, but they

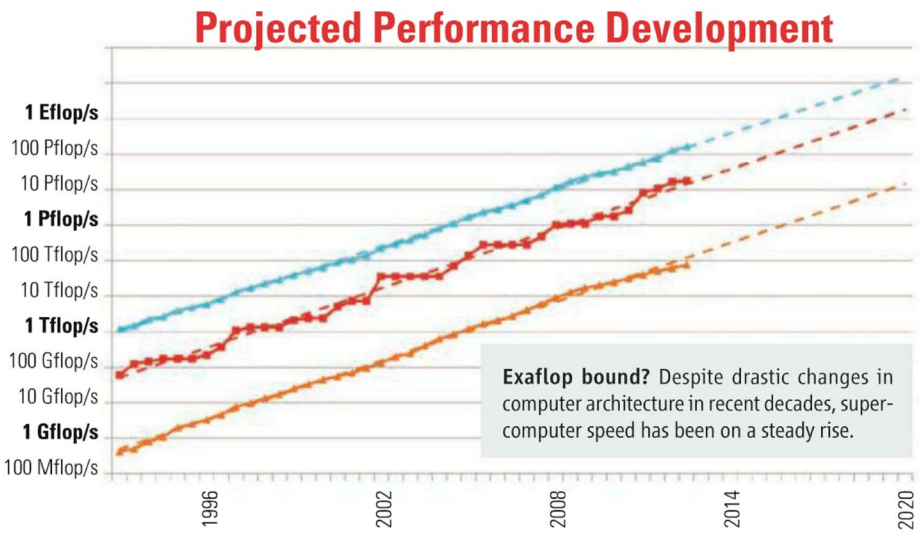

Exaflop bound? Despite drastic changes in computer architecture in recent decades, supercomputer speed has been on a steady rise.

CREDIT: TOP500 PROJECT/WWW.TOP500.ORG

Top spot. To reach exascale, researchers need to design a supercomputer that's 57 times faster than today's best machine.

also have few hardware vendors like Intel and other computer chip makers that they'd have to rely on to build the machine. "Europe cannot actually do it unless they want to create something new," Simon says.

Japan is in a better position. The country recently spent nearly $1 billion to construct the K computer, a 10-petaflop machine that topped the TOP500 list in 2011. Fujitsu built that machine using its own internal technology. Toshiyuki Shimizu, who directs Fujitsu's System Development Division in Kawasaki, says that Japan's Ministry of Education, Culture, Sports, Science and Technology (MEXT) is currently conducting a feasibility study outlining possible technological paths to reach exascale. That study is expected to be completed in March 2014, at which time MEXT is likely to spell out its goals for its next-generation supercomputer, Shimizu says. Shimizu says he believes its "likely" that government officials will back a move toward exacale. However, he adds, "we don't know when."

Thus far, China's plans are perhaps furthest along. The country has already committed 600 million yuan ($96 million) to building a 100-petaflop machine by 2015 as part of the nation's current 5-year plan. China has also developed its own domestic processing chip technology. But so far there's been no word on exascale. At the SC12 supercomputing conference, held last November in Salt Lake City, Depei Qian, a supercomputer expert at Beihang University in Beijing, said that despite its recent rapid progress in supercomputing technology, China remains 3 to 5 years behind the United States and other supercomputing powers. Qian estimates that China won't build its first exascale computer until between 2022 and 2025.

Simon says he isn't sure China is that far behind. Tianhe-1, China's 2.5-petaflop machine that topped the TOP500 list in 2010, as well as the nation's commitment to a 100-petaflop machine, proves that China has caught up with international supercomputing standards. However, he adds: "I don't know if they are willing to make the investment to create the breakthroughs needed to go beyond that." David Kahaner, who closely follows supercomputing advances in Asia as director of the Asian Technology Information Program, which is headquartered in Albuquerque, New Mexico, agrees. "Everybody is looking to the U.S. for intellectual leadership," he says.

Until recently, the United States seemed be on track to produce an exascale supercomputer by the end of this decade. Over the past 2 years, the U.S. Congress made an initial exascale investment by funding more than $200 million in advanced hardware and software research. In its 2012 budget, Congress also asked DOE officials to submit a report detailing an exascale program's components, funding needs, and research benchmarks. That report was due on 10 February 2012. But almost a year later, there's still no sign of it.

On 12 October, senators Dianne Feinstein (D–CA) and Lamar Alexander (R–TN), who lead the Senate Appropriations subcommittee on energy and water development, wrote a letter to DOE Secretary Steven Chu and Jeffrey Zients, deputy director of the Office of Management and Budget, asking again for the report and calling it "critically important to help us evaluate funding needs in fiscal years 2013 and 2014." Harrod says the report is still in the works, but has been delayed by the complexity of the problem and the task of coming up with an acceptable budget. DOE leaders, Harrod says, "are trying to determine what level of funding to go for."

Even though DOE's exascale program has yet to be officially released, at SC12 Harrod spelled out many of the likely key components if an exascale computing initiative is eventually approved. For starters, Harrod says, any exascale initiative would include both hardware and software research; construction of a prototype, probably between 2019 and 2022, followed by an exascale machine; and support for the scientific applications that would run on any such machine. As part of this effort, Harrod says it's critical that any U.S. effort support supercomputing companies to create a technology that is commercially viable, and not useful for merely building a one-off machine.

But just how fast any DOE effort can produce that remains up in the air as Congress struggles with bitter negotiations over the nation's finances. Congress and DOE must also sort out how exascale computing fits among other high-ticket DOE priorities such as supporting ITER, the international fusion program, and the Facility for Rare Isotope Beams, a nuclear research lab being designed at Michigan State University. "The biggest problem is the budget," Harrod says. "Until I have the budget, I don't know what I'm doing."

The best-case scenario, Harrod adds, is that exascale computing initiative funding would start in fiscal year 2014, which begins in October 2013. That gives any U.S. effort only 7 years to build an exascale machine by 2020. Given the financial hurdles and technical challenges of doing so, Simon's bet is looking better every day.

–ROBERT F. SERVICE

CREDITS (LEFT TO RIGHT): OAK RIDGE LEADERSHIP COMPUTING FACILITY (OLCF)/OAK RIDGE NATIONAL LABORATORY; NCSA/UNIVERSITY OF ILLINOIS

NEUROSCIENCE

The Promise and Perils of Oxytocin

Is oxytocin the next revolution in psychiatric medicine—or an overhyped hormone that could make some patients worse?

Few substances produced by the human body have inspired as much hoopla as oxytocin. Recent newspaper articles have credited this hormone with promoting the kind of teamwork that wins World Cup soccer championships and suggested that supplements of the peptide could have prevented the dalliances and subsequent downfall of a certain high-ranking U.S intelligence official. Although the breathless media coverage often goes too far, it reflects a genuine and infectious excitement among many scientists about the hormone's role in social behavior. First studied by biologists for its role in childbirth and lactation, oxytocin has more recently captivated neuroscientists and psychologists who have found that it can promote trust and cooperation and make people more attuned to social cues.

Now psychiatrists have caught oxytocin fever. Dozens of clinical trials are under way, or will be soon, to investigate the hormone's potential benefits for a wide range of psychiatric disorders. The interest isn't hard to understand. Many psychiatric conditions have social symptoms, such as the characteristic lack of empathy in autism, the attachment anxiety of borderline personality disorder, and the paranoia of schizophrenia. Yet no drugs currently approved for psychiatric use directly target social behavior.

For autism in particular, hopes for oxytocin run high. A large trial of the hormone on 300 affected children is expected to begin this spring. Meanwhile, thousands of impatient parents of autistic children have persuaded physicians to prescribe oxytocin nasal spray, which can be obtained from compounding pharmacies.

At first glance, oxytocin might seem like just what the doctor should be ordering. But as researchers have continued to explore the hormone's effect on human behavior, a darker side has emerged. Oxytocin seems to promote aggression or other antisocial behavior in some circumstances. Its effects also appear to vary depending on a person's genetic makeup and psychological status. And no one knows what long-term oxytocin treatment does to the developing human brain. Disconcertingly, one recent study found that male voles treated for several weeks with oxytocin nasal spray around the time of adolescence later exhibited impaired social bonding with females. "The more we know, the more complicated it's getting," says Sue Carter, a behavioral neuroendocrinologist and a pioneer of research on oxytocin's role in social behavior now based at RTI International in Research Triangle Park, North Carolina.

> "What worries me, and should worry others, is that so much of the basic background is missing."
>
> —SUE CARTER, RTI INTERNATIONAL

Carter is particularly worried about giving oxytocin to children before more is known about the hormone's developmental effects. "I think there probably is a place for oxytocin in several aspects of medicine," she says. "But what worries me, and should worry others, is that so much of the basic background is missing."

At the same time, those leading the trials say that the scientific rationale for using oxytocin is already strong enough, especially given the lack of better options. "This could be the first drug to address the core symptoms of autism," says Geraldine Dawson, a developmental and child clinical psychologist and chief science officer of Autism Speaks, which has funded some of the early pilot studies. At the heart of the debate is the tension between scientific caution and the desperation of patients and families living with disruptive disorders day in, day out.

From bonding to bedside

The hypothalamus, an evolutionarily ancient part of the mammalian brain, makes oxytocin. Released into the bloodstream by the nearby pituitary gland, it signals the uterus to contract during childbirth and stimulates the release of milk for nursing. The hormone was the first peptide to be synthesized in the laboratory, a feat that earned American biochemist Vincent du Vigneaud the 1955 Nobel Prize in chemistry.

Given the hormone's known roles, researchers soon wondered whether it also played a role in reproductive behavior. In the late 1970s and early 1980s, work with rats and sheep found that oxytocin enhances mother-infant bonding. In the '90s, Carter and others established its role in fostering pair bonding in prairie voles. Unlike most rodents, these furry inhabitants of the North American plains form lifelong bonds and share the work of raising offspring (although trysts are not uncommon). In 2000, Larry Young and colleagues at Emory University in Atlanta reported that genetically engineered mice lacking oxytocin are unable to recognize other individuals, pointing to an even broader role for the hormone in nonreproductive social behavior.

Although much of this work has been written into textbooks, the more recent oxytocin research in humans has frequently found its way into tabloids. In one of the first eye-catching studies, neuroeconomist Ernst Fehr of the University of Zurich in Switzerland and colleagues gave oxytocin nasal spray or a saline spray placebo to university students before a game in which they had to decide how much money to entrust to a stranger. (The more money a player entrusts, the larger the potential gains and potential losses.) Those who got oxytocin were more trusting, the researchers reported in *Nature* in 2005. A torrent of studies followed, suggesting that oxytocin not only increases trust and cooperation, but also boosts social perceptiveness, such as face recognition and the ability to read what's on someone's mind from the look in their eyes.

Online

sciencemag.org

Podcast interview with author Greg Miller (http://scim.ag/pod_6117).

These findings quickly led to speculation about clinical applications. The first published study in which oxytocin was given to autistic children appeared online in *Biological Psychiatry* in late 2009. In an experiment conducted by Adam Guastella, a clinical psychologist at the University of Sydney in Australia, and colleagues, 16 autistic boys between 12 and 19 years old received a single dose of oxytocin nasal spray or a placebo in one session, and the alternative in another. (Neither the boys nor the researchers evaluating them knew which time they'd gotten the hormone.) On oxytocin, the boys performed better on a common test of social cognition that involves looking at photographs of faces cropped to show just the eyes and reporting what emotion the person is most likely experiencing. The improvement was modest: from about 45% to 49% correct on average. People without autism typically get more than 70% correct.

Studies in adults with autism have also demonstrated improvements on standard lab tests of social cognition. But the vast majority of published work on oxytocin to date has looked at the effects of a single dose over the course of an hour or so in the lab. The real question is whether the hormone can restore normal behavior in real life.

To find out, Guastella and others are conducting trials in which people with autism take daily sniffs of oxytocin for several weeks or months. These pilot studies are in various stages and several researchers told *Science* that it's too soon to talk about the findings in detail. "Interesting things are coming out of these studies," Guastella says of his group's work. "At the same time, we're not seeing a ginormous result that makes us think this is a cure for autism."

A far larger trial scheduled to get under way this spring should help clarify things. It will be led by psychiatrist Linmarie Sikich at the University of North Carolina (UNC), Chapel Hill, who received a $12.6 million Autism Centers of Excellence grant from the National Institutes of Health in September for this trial. Her team plans to enroll 300 autistic children between the ages of 3 and 17, half of whom will receive oxytocin nasal spray twice daily for 6 months in a placebo-controlled, double-blind trial, and all of whom will receive the hormone for 6 months in a subsequent open-label extension of the trial. Researchers will look for any adverse side effects and monitor the kids with various checklist measures of social behavior filled out by a clinician or parent.

Autism is hardly the only disease being investigated. Out of 44 neuropsychiatric trials of oxytocin listed on clinicaltrials.gov, roughly three-quarters are for other disorders. Pilot studies in people with schizophrenia, who often suffer from paranoia and difficulty reading social cues, suggest that oxytocin can reduce psychotic symptoms and improve social cognition. The benefits are modest, but encouraging, says Cort Pedersen, a psychiatrist and behavioral neurobiologist at UNC Chapel Hill.

Pedersen's work in the 1970s established the role of oxytocin in mother-infant bonding, but more recently his interest has turned to the hormone's clinical potential. "One of the real deficits in psychiatry research is a complete lack of appreciation of evolution," Pedersen says. "The human brain evolved to evaluate and maneuver in very complex social environments." Pedersen argues that the role of the brain's social circuitry in psychopathology is too often ignored. And that's what makes oxytocin so exciting in his view. "One of the really cool things about oxytocin is that it probably plays a central role in the social brain," he says.

Caring family. Prairie vole parents share the work of raising offspring, but a recent study suggests long-term oxytocin treatment can disrupt bonding between partners.

CREDIT: KAREN BALES/UNIVERSITY OF CALIFORNIA, DAVIS

Cause for concern

The explosion of clinical trials with oxytocin, particularly those in children, troubles Karen Bales, a behavioral neuroscientist at the University of California, Davis. "There's been this quick leap from looking at a single dose of oxytocin in healthy adults to trying to give it to children with autism whose brains are still developing," she says. Bales says that she looked and couldn't find a single published study on the long-term behavioral effects of multiple doses of oxytocin in developing animals. "It seemed to me that we were really skipping a step."

From work she did as a postdoctoral fellow with Carter, Bales knew that even a single dose of oxytocin can have long-lasting effects. In a series of studies published in the 2000s, they found that prairie vole pups treated with oxytocin on the day of birth exhibited abnormal pair bonding and parental behavior as adults. The effects were messy—treated animals grew up to be more social or less social than normal, depending on their sex and the dose they received. "The clearest message was that any exposure to oxytocin can cause long-term behavioral and neuroendocrine effects," Bales says. In one study, Bales found that males given a single dose of oxytocin at birth had reproductive difficulties as adults: They deposited sperm in the female reproductive tract in only 50% of mating attempts, for example.

More recently, Bales and colleagues tried to better mimic the type of oxytocin treatment now in clinical trials for autism, giving young prairie voles daily squirts of oxytocin in the nose for 3 weeks. In developmental terms, Bales says that the voles were roughly equivalent to 12- to 17-year-old children, the target group for several trials. In the short term, oxytocin made the voles more social, as expected: After a dose, they spent more time in close contact with a cage mate. As adults, however, treated males had abnormal relationships with their partners, the researchers reported online on 15 October 2012 in *Biological Psychiatry*.

The standard test of pair bonding in voles, Bales explains, is to put a male in an empty chamber connected to two other chambers: one containing his mate, and another containing an unfamiliar female. "A normal male prairie vole will run around and check everything out and then go hang out with his partner," Bales says. But males that had gotten a daily dose of oxytocin comparable to that being given to autistic children—or an even lower dose—were more likely to spurn their partner in favor of the stranger. To Bales, the findings raise the troubling possibility that repeated use of oxytocin nasal spray may cause long-term changes in the brain that negate or even reverse the hormone's benefits, perhaps by tricking the brain into making less oxytocin of its own.

Other signs that there's more to oxytocin than cuddles and hugs have emerged from human experiments. In 2010, psychologist Carsten De Dreu and colleagues at the University of Amsterdam gave oxytocin nasal

spray to men before they played a computer game in which small teams competed for money. Compared with men who got a saline spray, those who sniffed oxytocin behaved more altruistically to members of their own team—but at the same time, they were more likely to preemptively punish competitors, the team reported in *Science*. In a 2011 study in the *Proceedings of the National Academy of Sciences*, De Dreu's team found that oxytocin increased favoritism toward subjects' own ethnic group (native Dutch men) on a series of tasks and thought experiments done on a computer, and in some situations the treated men exhibited more prejudice against other groups (Germans and Middle Easterners, in this case).

To some researchers, this suggests that oxytocin is a double-edged sword: promoting bonds with familiar individuals, but promoting unfriendly behavior toward strangers. "In the beginning, everyone thought it would have very robust prosocial effects, but it seems to depend on how you interpret the term prosocial," says René Hurlemann, a psychiatrist at the University of Bonn in Germany. In a study published on 14 November 2012 in *The Journal of Neuroscience*, his team reported that when men who reported being in a stable heterosexual relationship took oxytocin, they put a bit more distance between themselves and an attractive female experimenter who entered the room. To Hurlemann, these findings, like De Dreu's, suggest that oxytocin promotes bonding within an established pair (or group) at the expense of outsiders. That makes sense from an evolutionary perspective, he says, but may not be ideal for a prosocial drug. Though optimistic that oxytocin can help some people with psychiatric disorders, Hurlemann cautions that it might not have the same benefits for all patients.

An illustration of just that comes from work by Jennifer Bartz, a social psychologist at McGill University in Montreal, Canada. Encouraged by the reports that oxytocin increases trust, Bartz thought it might help people with borderline personality disorder (BPD), who are plagued by fears of abandonment and separation, and have profound difficulties with relationships as a result. But when she and colleagues gave a single dose of oxytocin nasal spray to people with BPD, they became less trusting and less likely to cooperate with a partner in a social dilemma game, the researchers reported in 2011 in *Social Cognitive and Affective Neuroscience*. This effect was strongest in those with BPD who scored highest on self-report measures of relationship anxiety and fear of rejection.

CREDIT: TONY GUTIERREZ/AP

Social studies. New clinical trials seek to determine if oxytocin can boost social behavior in children with autism.

One possibility, Bartz says, is that oxytocin increases the desire to connect and heightens attention to social cues. That may backfire in people with BPD, who are already hyperattentive and anxious in social situations. "The picture that's now emerging is that it's not this global social panacea," Bartz says. "In many cases it depends on the situation in which it's given or the person to whom it's given."

A risk worth taking?

Going forward, the success or failure of oxytocin as a psychiatric drug may hinge on figuring out which disorders and which people respond positively to the hormone—there's evidence that people with variants of the oxytocin receptor gene respond differently—and in what context. "In my view, the best benefit from stimulating the oxytocin system is going to be to combine it with a controlled behavioral therapy," Emory's Young says. He believes that oxytocin's main effect is to make people more sensitive to social cues. In a therapist's office, children could be assured of receiving positive, reinforcing social cues while under the hormone's sway. Not so if they simply take the hormone and went about their day. "Say you give it to a kid and then he goes to school and gets bullied. That's not going to have a positive impact, and it may even make things worse," Young says.

A better handle on the basic biology of intranasal oxytocin, such as how it enters the brain and which receptors it hits, might enable researchers to develop more effective drugs, Young adds. "If we want to move beyond this initial investigatory era and get more sophisticated and potent effects, we need to understand the mechanisms."

Despite the unknowns, Sikich and others insist that the clinical trials are justified. "A lot of people in this country, probably a few thousand, are going to compounding pharmacies and having them put together preparations of oxytocin," Sikich says. "We feel like it's really important, for something that's being used in this unregulated way, to get some data on how safe it is … and figure out does it work or does it not work."

For Dawson, the lack of better options is a powerful motivator. Only two drugs are currently approved for autism, she notes: Both are antipsychotic medications prescribed to cut down on tantrums, aggression, and self-injury. These drugs don't directly address the social deficits at the core of the disorder, and they have potentially dangerous side effects, not to mention unknown effects on brain development. Behavioral interventions such as the Early Start Denver Model, which Dawson co-developed, have proven successful in improving social behavior, but they require 25 hours or more a week of intensive one-on-one therapy and can cost $25,000 to $50,000 a year. In contrast, a year's supply of oxytocin, which is currently only available in a proprietary synthetic version, costs roughly $5000. And it could get much cheaper if a generic version becomes available.

Among parents of autistic kids, there's long been a willingness to try experimental treatments, even before they're fully vetted by researchers, Guastella says. A driving factor, he says, is frustration that science has let them down by moving too slowly. At the same time, researchers such as Carter and Bales hope that science won't let these families down again by rushing too quickly into clinical trials with a hormone whose effects aren't adequately understood. **–GREG MILLER**

LETTERS

edited by Jennifer Sills

Exploitation in Northeast India

LITTLE STUDIED AND LITTLE VISITED, NORTHEAST INDIA IS THOUGHT TO be second only to the northern Andes in terrestrial species density (*1*). Because of its distance from Delhi and its predominantly tribal culture, minimal regulation protects biodiversity in the region. As a result, there has been a transition over the past two decades from sustainable harvesting of wildlife to, in many places, empty forests (*2*).

The Amur Falcon, *Falco amurensis*, recently joined the list of relatively abundant species that are heavily exploited (*3*). Birdlife International estimates that, worldwide, the population of these birds is more than 1 million (*4*). In just one location in the state of Nagaland, more than 120,000 of them are harvested annually during their stopover on migration from northeast Asia to their winter quarters in southern Africa. The main reason for high exploitation appears to be market forces, with trappers selling birds at the rate of two per U.S. dollar. Carcasses are piled into pickup trucks, whose destination is currently unknown (*3*).

Captured Amur Falcon.

We draw attention to this phenomenon for three reasons. First, although overexploitation is a problem globally (*5*), India has a strong legal framework for species protection and a good record of enforcement in other areas of the country. India recently hosted the 11th Conference of the Parties to the United Nations Convention on Biological Diversity, at which it committed $50 million to the biodiversity targets agreed upon at the previous meeting in Nagoya, Japan. Second, researchers and tourists alike need to be aware that this magnificent area is now relatively easy to access, and not only to developers. Research is essential. Third, time is of the essence. The next few decades will be critical. Relatively few well-protected areas may conserve a large fraction of the region's biodiversity. Alternatively, local communities can become rapidly engaged in wildlife conservation, given the right incentives (*6*).

SHASHANK DALVI,[1] RAMKI SREENIVASAN,[2] TREVOR PRICE[3,4]*

[1]Postgraduate Program in Wildlife Biology and Conservation, Wildlife Conservation Society, India, National Centre for Biological Sciences, Bangalore 560065, India. [2]Centre for Wildlife Studies, Bangalore 560001, India. [3]Conservation India, Bangalore, Karnataka 560038, India. [4]Department of Ecology and Evolution, University of Chicago, IL 60637, USA.

*To whom correspondence should be addressed. E-mail: pricet@uchicago.edu

References

1. R. Grenyer *et al.*, *Nature* **444**, 93 (2006).
2. A. Datta, M. O. Anand, R. Naniwadekar, *Biol. Conserv.* **141**, 1429 (2008).
3. S. Dalvi, R. Sreenivasan, Shocking Amur Falcon massacre in Nagaland (www.conservationindia.org/campaigns/amur-massacre).
4. BirdLife International, Species, Amur Falcon *Falco amurensis* (www.birdlife.org/datazone/speciesfactsheet.php?id=3604).
5. J. S. Brashares, C. D. Golden, K. Z. Weinbaum, C. B. Barrett, G. V. Okello, *Proc. Natl. Acad. Sci. U.S.A.* **108**, 13931 (2011).
6. D. Mohan, R. Athreya, *Int. J. Innovation Sci.* **3**, 23 (2011).

Sharing Future Conservation Costs

IN THEIR REPORT "FINANCIAL COSTS OF MEETing global biodiversity conservation targets: Current spending and unmet needs" (16 November, p. 946), D. P. McCarthy *et al.* estimate the financial costs required for conservation of terrestrial species as US$76.1 billion annually. They highlight the need for increased spending while noting that these costs are small relative to the value provided by biodiversity. However, when budgeting current and future funds, we should factor in necessary changes to our conservation approach.

McCarthy *et al.*'s expert-derived expenditure estimates assume a "more of the same" approach to conservation, focusing on the immediate financial costs of rearguard efforts to prevent extinctions. This approach ignores the potential of relatively inexpensive reforms such as regulatory measures to prevent conversion of production forest and the removal of perverse subsidies. It also ignores the need to build a society in which conservation goals are widely acceptable. Critically, it neglects local opportunity costs (i.e., forgone incomes).

McCarthy *et al.*'s cost assessments highlight the expectation that the wider economic benefits resulting from such conservation activities surpass their associated costs (i.e., expenditures). These aggregate comparisons avoid the pertinent question of which biodiversity provides what values (and costs) to whom, and confound the opportunity costs imposed upon poor stakeholders with the values accruing to the global community.

For many, the benefits associated with conservation interventions do not outweigh the costs. Much conservation expenditure ensues from the resulting conflicts (*1*). Yet local people are often sympathetic to conservation, and would accept, and even support, specific actions performed in a transparent and equitable manner and with adequate compensation. Conservation gains will only be secured once

CREDIT: SHASHANK DALVI/CONSERVATIONINDIA.ORG

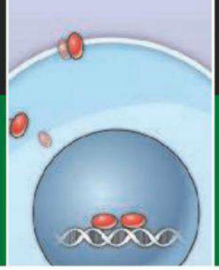

Stress hormones and behavior

279

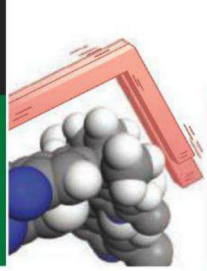

Stiffening microporous membranes

284

we reduce the burden on those people who bear unreasonable costs and conservation efforts earn the legitimacy of local democratic accountability.

DOUGLAS SHEIL,[1,2,3]* ERIK MEIJAARD,[3] ARILD ANGELSEN,[3,4] JEFF SAYER,[5] JEROME VANCLAY[1]

[1]School of Environment, Science and Engineering, Southern Cross University, Lismore, NSW 2480, Australia. [2]Institute of Tropical Forest Conservation (ITFC), Post Office Box 44, Kabale, Uganda. [3]Center for International Forestry Research, Bogor, Indonesia. [4]School of Economics and Business, Norwegian University of Life Sciences (UMB), 1432 Ås, Norway. [5]Center for Tropical Environmental and Sustainability Science, School of Earth and Environmental Sciences, James Cook University, Smithfield, QLD 4878, Australia.

*To whom correspondence should be addressed. E-mail: Douglas.Sheil@scu.edu.au

Reference

1. K. M. A. Chan *et al.*, *Conserv. Biol.* **21**, 59 (2007).

Response

IN THEIR LETTER, SHEIL *ET AL.* APPEAR TO HAVE misinterpreted several key points. Far from ignoring local opportunity costs, we assumed that for reasons of fairness and effectiveness, establishing new protected areas "will require the full opportunity costs of conservation to be paid" (Supplementary Materials to our Report), as implied in the Convention on Biological Diversity (CBD)'s target (*1*). Such costs were reflected in our estimate of the sum required for protecting and managing important terrestrial sites for biodiversity globally. Moreover, at least 13% of our estimate of the total costs of preventing extinctions and improving species' conservation status was for actions relating to education, awareness-raising, improving local livelihoods, and ensuring local participation in (and benefits from) conservation so that "conservation efforts earn the legitimacy of local democratic accountability," as called for by Sheil *et al.*

We agree with Sheil *et al.* that the benefits and costs of conservation are often inequitably distributed and that this issue needs addressing. However, a global cost-benefit analysis was not the topic of our paper. Instead, we focused on providing the information needed by the CBD Parties on the financial costs of meeting the biodiversity conservation targets that they have adopted. Our analysis informed their decision in October 2012 to "double total biodiversity-related international financial resource flows to developing countries" by 2015 (*2*). It will be essential to invest these resources in ways that address the unequal distributions of conservation costs and benefits (*3*).

We did not assume a "more of the same" approach to conservation, as Sheil *et al.* sug-

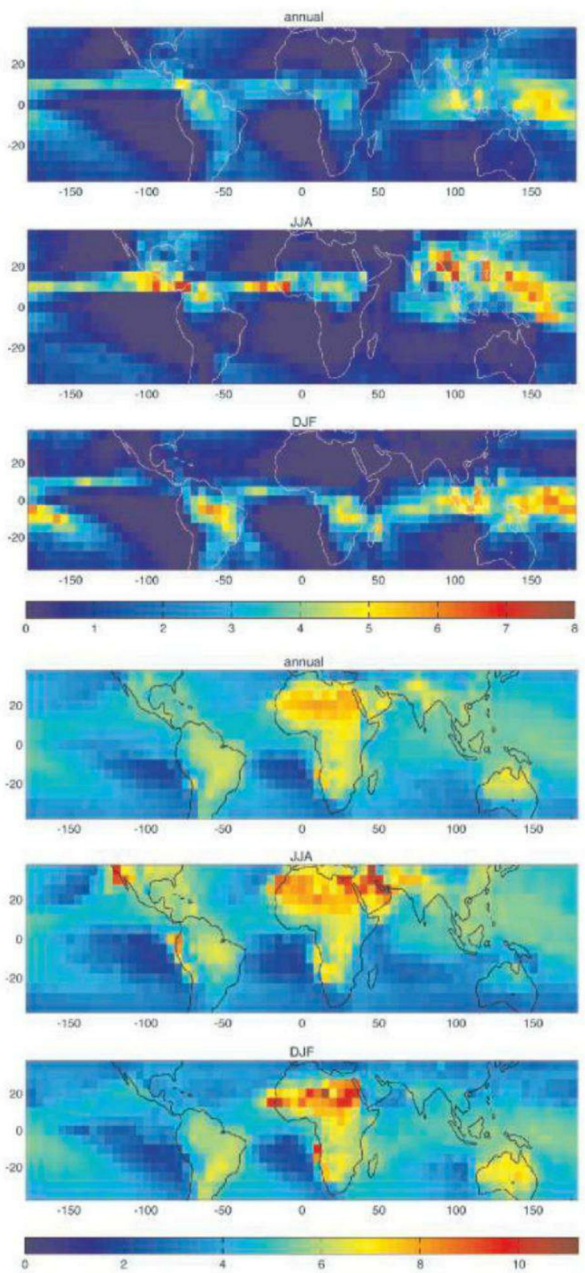

CORRECTIONS AND CLARIFICATIONS

Reports: "Satellite estimates of precipitation-induced dissipation in the atmosphere," by O. Pauluis and J. Dias (24 February 2012, p. 953). The authors inadvertently used a "rectangular" method for the integration rather a "trapezoidal" method. This led to an overestimation of the integral and the dissipation rate by about 20%. In the published paper, the dissipation rate is said to be about 1.8 W/m^2. The new calculations yield 1.5 W/m^2. The corrected Figs. 1 and 3 are shown here (right). The authors thank A. Makarieva, V. Gorshkov, A. Nefiodov, D. Sheil, A. Nobre, P. Bunyard, and B.-L. Li for bringing this problem to their attention.

TECHNICAL COMMENT ABSTRACTS

Comment on "Extinction Debt and Windows of Conservation Opportunity in the Brazilian Amazon"

John M. Halley, Yoh Iwasa, Despoina Vokou

A paper by Wearn *et al.* (Reports, 13 July 2012, p. 228) yields new insights on extinction debt. However, it leaves out the area dependence of the relaxation process. We show that this is not warranted on theoretical or observational grounds and that it may lead to erroneous conservation recommendations.

Full text at http://dx.doi.org/10.1126/science.1231438

Response to Comment on "Extinction Debt and Windows of Conservation Opportunity in the Brazilian Amazon"

Oliver R. Wearn, Daniel C. Reuman, Robert M. Ewers

Halley *et al.* purport to show a power-law relationship between fragment size and relaxation rates. We use a much more extensive data set to show that area dependence of relaxation rates exists only for very small fragment sizes (<60 hectares), which has limited relevance for our analyses conducted using 250,000-hectare grid squares. We also show that the example of Halley *et al.* is based on an unrealistic fragmentation model with an infinite number of fragments that have an average size of zero hectares. A more realistic formulation of the model shows that relaxation is much less dependent on fragmentation than Halley *et al.* present.

Full text at http://dx.doi.org/10.1126/science.1231618

gest; we imposed no restrictions when asking respondents to estimate the cost of the actions necessary to improve species' status and to protect and manage important sites. This allowed respondents to include innovative approaches where appropriate, including compensation schemes, conservation easements, integrated livelihoods, community-conserved areas, and other measures to rebalance inequities resulting from the cost and benefit flows from biodiversity conservation.

Sheil *et al.* comment that we ignored the potentially cheaper options of regulatory measures to prevent conversion, and the removal of perverse subsidies. However, our estimates do include these options where appropriate, at a local scale and feasible within the time frame of the CBD 2020 targets. Many experts have recognized that simple enforcement of regulations may be less effective than more collaborative approaches. More broadly, these options are mostly about reducing future threats to avoid further habitat conversion, and are addressed by separate CBD targets. Estimating conservation costs beyond 2020 under hypothetical future regulatory regimes would be fraught with difficulty.

Finally, although it was not the topic of our paper, we concur with Sheil *et al.* that existing resources need to be better targeted and spent more effectively [e.g., (*4*, *5*)]. However, even with increased efficiency, the financial shortfall for biodiversity conservation shown by our analysis is so great that substantially increased investment will be essential to meet the CBD Aichi Targets.

STUART H. M. BUTCHART,[1]* DONAL P. MCCARTHY,[2] ANDREW BALMFORD,[3] LEON A. BENNUN,[1] GRAEME M. BUCHANAN,[2] NEIL D. BURGESS,[4,5,6] PAUL F. DONALD,[2] LINCOLN D. C. FISHPOOL,[1] STEPHEN T. GARNETT,[7] DAVID L. LEONARD,[8] RICHARD F. MALONEY,[9] H. MARTIN SCHAEFER,[10] JÖRN P. W. SCHARLEMANN,[11] ANDY SYMES,[1] DAVID A. WIEDENFELD[12]

[1]BirdLife International, Wellbrook Court, Cambridge CB3 0NA, UK. [2]RSPB, The Lodge, Sandy, Bedfordshire SG19 2DL, UK. [3]Department of Zoology, University of Cambridge, Downing Street, Cambridge CB2 3EJ, UK. [4]United Nations Environment Programme World Conservation Monitoring Centre, 219 Huntingdon Road, Cambridge CB3 0DL, UK. [5]Center for Macroecology, Evolution and Climate, Department of Biology, University of Copenhagen, DK-2100 Copenhagen, Denmark. [6]Conservation Science Program, World Wildlife Fund, Washington, DC 20037, USA. [7]Research Institute for the Environment and Livelihoods, Charles Darwin University, Darwin, NT 0909, Australia. [8]U.S. Fish and Wildlife Service, Portland, OR 97232, USA. [9]Science and Technical Group, Department of Conservation, Christchurch, New Zealand. [10]University of Freiburg, Faculty of Biology, Hauptstrasse 1, D-79104 Freiburg, Germany. [11]School of Life Sciences, University of Sussex, Falmer, Brighton, BN1 9QG, UK. [12]Warrenton, VA 20186, USA.

*To whom correspondence should be addressed. E-mail: stuart.butchart@birdlife.org

References

1. Convention on Biological Diversity, Conference of the Parties Decision X/2: Strategic Plan for Biodiversity 2011–2020 (2011); www.cbd.int/decision/cop/?id=12268.
2. Convention on Biological Diversity, Conference of the Parties Decision XI/4: Review of Implementation of the Strategy for Resource Mobilization, Including the Establishment of Targets (2012); www.cbd.int/cop/cop-11/doc/2012-10-24-advanced-unedited-cop-11-decisions-en.pdf.
3. A. Balmford, T. Whitten, *Oryx* **37**, 238 (2003).
4. M. R. W. Rands *et al.*, *Science* **331**, 31 (2011).
5. S. H. M. Butchart *et al.*, *PLoS ONE* **7**, e32529 (2012).

Letters to the Editor

Letters (~300 words) discuss material published in *Science* in the past 3 months or matters of general interest. Letters are not acknowledged upon receipt. Whether published in full or in part, Letters are subject to editing for clarity and space. Letters submitted, published, or posted elsewhere, in print or online, will be disqualified. To submit a Letter, go to www.submit2science.org.

HISTORY OF SCIENCE

What the Romans Really Knew

Peter Pesic

Many thoughtful readers might wonder what Roman science really amounted to. Unquestionably the Romans were great engineers—witness their aqueducts, bridges, and buildings—but scientists? Didn't they just copy the Greeks? We are reminded of the Roman soldier killing Archimedes, the absent-minded Greek too busy thinking about his circles to pay attention to the conqueror.

Even the Romans worried about their reputation. In the central scene of Virgil's epic, Aeneas's father tells him that though they may not be as good as "others" at oratory, sculpture, and astronomy, Roman "arts" shall be "to pacify, to spare the conquered, to subdue the proud"—to rule the world. Yet Cicero held that "we Romans found out everything for ourselves more wisely than the Greeks did, or else improved the things we got from the Greeks."

Daryn Lehoux (a classicist at Queen's University, Kingston, Ontario) seeks to understand this claim. He begins by correcting a long-standing view that the concept of "laws of nature" only originated in the 16th century, when that phrase became current. Lehoux helpfully discusses a number of important passages in which Latin (and Greek) versions of that expression were indeed used by ancient writers. Emphasizing that we should really look to the content of Roman views, rather than just the words they used, he invites us to consider whether the Pluto Platter really changed its essence in 1957, when its manufacturer renamed it "Frisbee."

Lehoux concentrates on the meaning of several emblematic Roman scientific ideas and, above all, on how the Romans "made" their world, shaped their views. He brings forward the religious, social, legal, rhetorical, and moral background he considers essential for Roman world-making. His emphasis on the foundational influence of Roman law is crucial, for "laws of nature" can scarcely be understood apart from the underpinnings of Roman law. His discussion of these issues was so rich and exciting that I wanted to hear much more about the detailed character of Roman law and how exactly we should read its implications for the imputation of law to nature.

Sometimes names are not merely conventional; I wish Lehoux had addressed the separation between the celestial and terrestrial realms, common to Greek and Roman natural philosophy. Though after Newton, laws of nature can span both realms, yet in ancient natural philosophy their sharp separation meant that mathematics could be applied to describe the changeless heavens but not the changeable Earth. Lehoux also indicates that the Roman *scientia* cannot be simply equated with our "science," though he decided to use our word to cover both. Perhaps it would have helped had he left *scientia* untranslated and helped us to assimilate its different meanings without the crutch (and distraction) of our word.

Rather than surveying a broad range of Roman natural philosophy, Lehoux concentrates on a few instances he considers emblematic, especially the "law" (recounted by Plutarch and others) that garlic annuls the effect of magnets. How could such practical people have accepted something so easily disproved? Lehoux offers a rich and complex response involving subtly competing concepts of truth, consistency, correspondence, and justifiability. Alongside his mastery in reading and interpreting classical texts, Lehoux shows great depth of understanding and sophistication in modern philosophy of science. More remarkably, he expresses these difficult distinctions in superbly clear and accessible, yet admirably precise, language.

Even so, I was, in the end, not really sure why the Romans held to the garlic-magnet connection, beyond a general notion of "effluvia," whether odoriferous or magnetic, streaming from both. Lehoux connects this with a general idea of affinity, "like connects with like." He also reminds us that, viewed from a thousand years in the future, some of our current scientific views might seem similarly bizarre. Fair enough, but Lehoux holds up the example of an anthropologist investigating sympathetically the beliefs of a tribe. In that spirit, I would have liked additional guidance from him to help us enter more deeply and in a more sustained way into the inner thought-world of the Romans, trying to share more fully the felt quality of their knowledge.

But that is a great deal to ask of such a brief book in which Lehoux already brings forward so many important insights. He seems to have chosen to spend more time on the philosophic underpinnings of what he calls "world-making," the ways in which the Romans (and we) fashion our worldviews, rather than on the contents of those views. [To be sure, Lehoux's earlier book (*1*) treated the specifics of astronomy, weather, and calendars in exhaustive detail, spanning Egypt, Mesopotamia, Greece, and Rome.] His philosophic and expository gifts help him present a thoughtful and persuasive argument for a pragmatic view of truth that remains open both to the Romans' ways of world-making and to ours. The heart of this book may be its sensitive reading of Cicero's "Dream of Scipio," which revisits the music of the spheres that Plato invoked unforgettably at the end of his *Republic*, now placed in the course of Cicero's own account of the ideal commonwealth. Reading Lehoux's

What Did the Romans Know?
An Inquiry into Science and Worldmaking
by Daryn Lehoux
University of Chicago Press, Chicago, 2012. 287 pp. $45, £29. ISBN 9780226471143.

CREDIT: WIKIMEDIA COMMONS

Pierre Henri de Valenciennes, *Cicero Discovering the Tomb of Archimedes* (1787).

The reviewer is at St. John's College, 1160 Camino de la Cruz Blanca, Santa Fe, NM 87505–4511, USA. E-mail: ppesic@mail.sjcsf.edu

eloquent analysis, one feels the quest for the hidden harmonies of the cosmos strongly animating the Romans' world-making, as it continues to figure in contemporary physical and cosmological speculation even today.

In this important, brilliant, and truly admirable book, Lehoux has laid the groundwork for a deeper and clearer understanding of Roman science, most of all that it was rich and significant. May he continue to help us enter still further into what the Romans really knew and ponder what that should mean, in turn, for us.

References

1. D. Lehoux, *Astronomy, Weather, and Calendars in the Ancient World: Parapegmata and Related Texts in Classical and Near Eastern Societies* (Cambridge Univ. Press, Cambridge, 2007).

10.1126/science.1232228

MATHEMATICS

From Simple Rules Repeated

Brie Finegold

Best known for discovering the set named after him, Benoit Mandelbrot's titles ranged from stable boy to IBM scientist, from apprentice toolmaker to eminent mathematician. The autobiography he finished near the end of his life, *The Fractalist*, puts his accomplishments in historical and mathematical perspective. In summary, he asks, "Does not the distribution of my personal experiences remind one of the central topic of my scientific work—namely, extreme fractal unevenness?" Just as a fractal, his experiences were indeed rough in nature and self-similar in quality.

As a child, Mandelbrot separated from his family and hid his Jewish heritage to survive World War II. Not one to follow advice, he wrote his thesis on an unpopular topic without an advisor. On this note, he quotes mathematician and family friend Jacques Hadamard, apparently complaining about a student who asked for a thesis topic, "Can you imagine that? If he has no topic of his own, he should not even think of a Ph.D.!" Mandelbrot's self-described "messy" thesis consisted of two seemingly unrelated parts: one on Zipf's universal power law concerning the frequency of words and one on statistical thermodynamics. Lacking an academic position in Europe, he went to work for IBM after a postdoc at Massachusetts Institute of Technology (MIT). Several universities subsequently invited him for long-term visits: Harvard (in economics), then MIT (in engineering), and finally Yale (in mathematics). But none offered him a full-time position. In 1940s academia, the interdisciplinary nature of his interests was not an asset as it might be today.

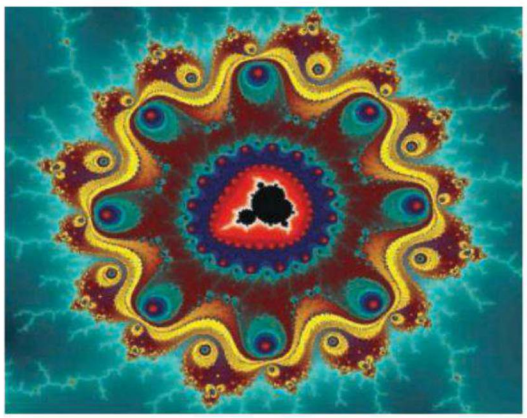

Deep into the Mandelbrot set.

Mandelbrot avoided overly technical language, noting that "Many scientific articles are completely flat because they are written for people who do not have to be convinced. … In my case, the fact that I write for an unknown public influences and shapes my style." Mandelbrot's account will inspire scientists because he writes about the general trajectory of his career and the origins of his thoughts. For example, the study of fractals has its roots in work from the 1910s by Pierre Fatou and Mandelbrot's teacher Gaston Julia. These works lingered in Mandelbrot's mind despite their not being the hot topics of his day. He writes "much of my work has consisted of bringing a medley of old issues back to life and triumphant evolution." In addition, his biggest breakthroughs came later in life. The Collège de France invited him back at age 49 to talk about his research and subsequently offered him the chance for a position there. Improvements in computer graphics as well as the freedom afforded to him by IBM helped showcase this stunning work.

Needing a title for the slim 1975 work (*1*) that he calls his "preview book," Mandelbrot coined the term "fractal" based on its similarity to "fractured." A fractal can be built by iterating one transformation of the complex plane and separating points according to characteristics of their orbit under this iteration. Despite the simple algorithms that generate them, fractals have unexpected properties, such as a noninteger Hausdorff dimension and growth that follows power laws. As his work took off, aided by his classic *The Fractal Geometry of Nature* (*2*), Mandelbrot saw his disorganization as his greatness weakness, claiming that it led him to publish work in journals that may not have been the most esteemed or appropriate. "Each partial success aroused some old expectation or some old hunger." Never feeling truly satisfied that his body of work was well presented or complete, he left many open doors for research to continue.

In the end, reliance on instincts for both basic and professional survival paid off. Learning trades and fighting for survival in his youth influenced him to focus on concrete geometry rather than abstract numerics. By assessing pictures qualitatively, he identified opportunities to collaborate where others detected no connection. Teaching, as he confessed, without a clear plan might have enriched his students' lives. He quotes one student from his "Topics in Applied Mathematics" course at Harvard: "I had been told that science was created by humans, but in all my other courses it seemed created by creaky machines. Your course made me watch science being created." Perhaps more students would have witnessed science in action had Mandelbrot been an academic.

Readers might balk at the author's tendency to tell them how to feel through headings such as "A Flawed Ph.D. Dissertation Well Ahead of Its Time" or "Firebrand Newcomer to Finance Advances a Revolutionary Development." But reading *The Fractalist*, one finds a man who is as self-critical as he is self-promoting. Also, the accounts of his collaborations with Noam Chomsky, Jean Piaget, "Johnny" von Neumann, Stephen Jay Gould, Robert Oppenheimer, and other visionaries indicate that Mandelbrot had little reason to be humble.

References

1. B. Mandelbrot, *Les objets fractals: Forme, hasard, et dimension* (Flammarion, Paris, 1975).
2. B. Mandelbrot, *The Fractal Geometry of Nature* (Freeman, San Francisco, 1982).

10.1126/science.1232229

The Fractalist
Memoir of a Scientific Maverick
by Benoit B. Mandelbrot
Pantheon, New York, 2012. 353 pp. $30, C$35, £18.74. ISBN 9780307377357.

The reviewer is at the Department of Mathematics, University of Arizona, 617 North Santa Rita Avenue, Tucson, AZ 85721, USA. E-mail: bfinegold@arizona.edu

CREDIT: COURTESY PANTHEON BOOKS

RESEARCH ETHICS

The Complexities of Genomic Identifiability

Recent work reveals the need to re-examine the current paradigms for managing the potential identifiability of genomic and other "omic"-type data.

Laura L. Rodriguez,[1] Lisa D. Brooks,[1] Judith H. Greenberg,[2] Eric D. Green[1*]

Sharing research data has long been fundamental to the advancement of science. In today's scientific culture, making research data available broadly and efficiently via the internet has become the standard for many data types, including genomic and some other "omic"-type data produced by high-throughput methods. The acceleration of research progress and the resulting public benefit achieved through such broad data-sharing have been transformative for the scientific enterprise (*1*–*3*). However, sharing data generated from human research participants must be done in a manner that appropriately protects participant interests.

Several recent studies have suggested that some analyses of high-dimensional molecular data can raise more risks to privacy than had been appreciated. For instance, it is possible to determine whether data from a person with a known genotype are in a gene-expression database (*4*) or in aggregated data sets of allele frequencies (*5*) or of phenotype regressions in genome-wide association studies (GWAS) (*6*). It has also been suggested that people may have a stable microbiome-variation profile (*7*), which, theoretically, could be matched to a sample from a known individual.

In this issue of *Science*, Gymrek *et al.* (*8*) describe how various public data sets developed for both research and nonresearch purposes can be analyzed to deduce the individual identity of some research participants by leveraging information pertaining to distant patrilineal relations. Specifically, Gymrek *et al.* attempted surname identification for 10 males in the Center for Study of Human Polymorphisms (CEPH) family collection whose genomes were sequenced as part of the 1000 Genomes Project (*9*). The researchers used sequence data for Y-chromosome short tandem repeats (STRs) and databases linking STRs to surname information, with the resulting information used to query public genealogy data and other available information [e.g., from the National Institute of General Medical Sciences (NIGMS) Human Genetic Cell Repository at the Coriell Institute, which distributes biological materials from the CEPH family collection, and obituary archives]. Using these steps, the authors were able to establish the identity of close to 50 of the CEPH participants (women as well as men). It is important to note that the authors do not reveal the names of the participants (or violate any known policies), but merely demonstrate their ability to identify them through the analysis of publicly available information.

Limitations and Broader Implications of the Study

The approach described by Gymrek *et al.* highlights vulnerabilities in efforts to protect the privacy of participants in genomics (and other 'omics) research. At this time, this methodology is particularly relevant to participants in the CEPH family collection because of the richness of publicly available research data and genealogic information derived from these individuals and their relatives (*10*, *11*). The CEPH participants whose samples were included in the HapMap Project (and then in the 1000 Genomes Project) underwent a process of re-consent to inform them about the plans for providing very broad and open access to the genomic data derived from their samples and for the in-depth genomic analyses that would be performed on those data. The inability to guarantee privacy and the possibility—then seen as remote—that individual identification might eventually become feasible were described explicitly. Despite this hypothetical and assumed low risk of identification, Gymrek *et al.* have now shown that it is possible to identify some participants of a genomics research study even in the absence of a second (matching) DNA sample.

Although additional studies are needed to assess more fully the generalizability of these findings to the broader population, this report—along with previous studies exposing other potential vulnerabilities in the current approach for protecting participant identity (*4*–*7*)—raises broader issues about how to protect participant privacy as more information becomes readily accessible to the public. These issues will become even more challenging in the future, as genomic technologies and information are used increasingly outside of research and health-care settings. It is thus prudent for the research community to reflect on the implications of these various studies (*4*, *6*) in considering how best to move forward.

The willingness of individuals and communities to assume some risk to participate in biomedical research depends on the scientific community's ability to maintain the public's trust. Indeed, it was this spirit that prompted the authors of the Gymrek *et al.* paper to contact staff at the National Institutes of Health (NIH) about their findings before publication. NIH staff, in turn, consulted with *Science* and the local institution for the CEPH study in

[1]National Human Genome Research Institute, National Institutes of Health (NIH), Bethesda, MD 20892, USA. [2]National Institute of General Medical Sciences, NIH, Bethesda, MD 20892, USA.

*Author for correspondence. E-mail: egreen@nhgri.nih.gov

Utah. In consultation with the authors, NIH staff acted swiftly to mitigate future risks by working with the NIGMS repository to shift age information, which had been available for some of the participants on the repository's public Web site, into controlled-access portions of the resource.

Shifting Concepts of Identifiability and Privacy

The recent set of papers exploring the potential for identifying individuals using genomic and other types of data, culminating with this latest report, calls into question whether the goal of complete deidentification of many types of human data is realistic in today's information-rich society. The ability to establish an acceptable threshold for "identifiability" has been debated vigorously since whole-genome analyses became feasible on a large scale with the introduction of GWAS (*12*–*14*). The approaches developed by Gymrek *et al*. and others call for reconsidering whether a simplistic distinction between identifiability and nonidentifiability remains adequate as a metric for describing expectations about participant protections. Some have suggested framing the risk of identifiability along a continuum (*13*, *15*) rather than as an absolute.

The general expectations of the public about privacy and confidentiality may be subtly shifting as well. In addition to social media outlets (e.g., Facebook) that have led to more pervasive sharing of personal details, patient-centric organizations (e.g., PatientsLikeMe) now provide the means to share in-depth information about health status and to identify research opportunities for motivated individuals (*16*). There are many perspectives about how to incorporate these potentially shifting norms into the systems for protecting research-participant interests in a manner that promotes maximum public benefit. Examples include an increasing number of "citizen science" initiatives [such as the Sage Bionetworks Commons (*17*) and Genomera (*18*)], which use informatics tools and social-media strategies to build research models for integrating participant preferences about privacy protection and future research use in an iterative and dynamic way. These initiatives can promote participants' long-term investment in and commitment to research, thereby gaining public trust through transparency and accountability (*19*). Although important questions remain regarding the scalability and feasibility of such approaches across populations and for various types of research projects, it is important for the research community to consider the options and potential advantages for the scientific enterprise as a whole.

From an oversight perspective, several bills proposing to convey various forms of property rights to genetic or genomic information have been introduced in U.S. state legislatures over the past few years (*20*). Such proposals should be considered in the face of an already inconsistent array of privacy protections at the state level that address access to or use of genetic/genomic information (*21*). The current patchwork of extant and potential legal standards for acquiring and managing such information adds more uncertainty to the considerations.

The Value of Broad Data Sharing

Gymrek *et al*. argue against placing barriers to accessing genomic and other high-density 'omic data derived from human participants. Substantial differences are seen in the use of data sets available through open-access versus controlled-access mechanisms. For example, the open-access HapMap and 1000 Genomes data sets of human genomic variation are used by many more researchers each year than related data sets in the controlled-access database of Genotypes and Phenotypes (dbGaP). In addition, recent NIH meetings on the scientific needs and opportunities for "big data" in stimulating basic and translational research recommended expanding open-access mechanisms for human research data with appropriate governance (*22*). Although the research community must be realistic and mindful of identifiability concerns, there are also ethical responsibilities to ensure that data contributed by participants for research are maximally utilized and that public research funding stimulates the greatest public good.

It is thus time for the research community to engage in a rigorous and open discussion about data identifiability and how to balance most effectively the benefits of broad data sharing and the imperative to respect and protect research participants. This dialogue should involve the full range of stakeholders, including participants, researchers, clinicians, database managers, advocacy groups, journal editors, and public representatives. Developing sustainable models that promote both continued willingness to participate in research and ongoing public trust will require a panoply of approaches.

Conclusion

We are at a crucial juncture brought about by the confluence of new technologies for data generation, bioinformatics, and information access on the one hand, which seem to create new risks to privacy, and the public's desire to benefit from these advances for a variety of personal and health reasons on the other hand. In light of this changing landscape, it is time to re-examine how to balance the protection of research participants (individuals, families, and groups) with the societal benefits likely to be gained through the enhanced research that broad data sharing facilitates. In doing so, we should consider whether there are alternative approaches that provide appropriate participant privacy and allow implementation across various research settings, including genomics and other emerging fields. The ultimate goal must be to develop a robust system that ensures the full societal benefits of biomedical research while respecting both individual needs and the communal good.

References and Notes

1. Batelle Technology Partnership Practice, *Economic Impact of the Human Genome Project* (2011); http://battelle.org/docs/default-document-library/economic_impact_of_the_human_genome_project.pdf.
2. E. Birney *et al*., *Nature* **461**, 168 (2009).
3. The Wellcome Trust, Sharing data from large-scale biological research projects: A system of tripartite responsibility, meeting, Fort Lauderdale, FL, 14 to 15 January 2003; www.wellcome.ac.uk/stellent/groups/corporatesite/@policy_communications/documents/web_document/wtd003207.pdf.
4. E. E. Schadt, S. Woo, K. Hao, *Nat. Genet.* **44**, 603 (2012).
5. N. Homer *et al*., *PLoS Genet.* **4**, e1000167 (2008).
6. H. K. Im, E. R. Gamazon, D. L. Nicolae, N. J. Cox, *Am. J. Hum. Genet.* **90**, 591 (2012).
7. S. Schloissnig *et al*., *Nature* **493**, 45 (2013).
8. M. Gymrek, A. L. McGuire, D. Golan, E. Halperin, Y. Erlich, *Science* **339**, xxx (2013).
9. 1000 Genomes Project Consortium, *Nature* **491**, 56 (2012).
10. Coriell Institute for Medical Research, Centre de'Etude du Polymorphism Humain (CEPH) Resources; www.ccr.coriell.org/Sections/Collections/NIGMS/CEPHResources.aspx?PgId=525&coll=GM.
11. Sorenson Molecular Genealogy Foundation, Overview of the Sorenson Database; www.smgf.org/pages/sorenson-database.jspx.
12. L. Curren *et al*., *Eur. J. Health Law* **17**, 329 (2010).
13. W. W. Lowrance, F. S. Collins, *Science* **317**, 600 (2007).
14. A. L. McGuire, R. A. Gibbs, *Science* **312**, 370 (2006).
15. C. Heeney, N. Hawkins, J. de Vries, P. Boddington, J. Kaye, *Public Health Genomics* **14**, 17 (2011).
16. PatientsLikeMe, www.patientslikeme.com.
17. Sage Bionetworks Commons, www.sagebase.org/commons/.
18. Genomera, http://genomera.com.
19. J. Kaye *et al*., *Nat. Rev. Genet.* **13**, 371 (2012).
20. J. K. Wagner, D. Vorhaus, On genetic rights and states: A look at South Dakota and around the U.S. *Genomics Law Rep.* (2012); www.genomicslawreport.com/index.php/2012/03/20/on-genetic-rights-and-states-a-look-at-south-dakota-and-around-the-u-s/.
21. Presidential Commission for the Study of Bioethical Issues, *Privacy and Progress in Whole Genome Sequencing* (Commission, Washington, DC, 2012); http://bioethics. gov/cms/sites/default/files/PrivacyProgress508.pdf.
22. Establishing a central resource of data from genome sequencing projects, NIH workshop, Rockville, MD, 5 and 6 June 2012; www.genome.gov/27549169.

Acknowledgments: The authors thank J. McEwen and M. Guyer for consultation and feedback, and A. Bailey for editorial assistance.

10.1126/science.1234593

ECOLOGY

Essential Biodiversity Variables

A global system of harmonized observations is needed to inform scientists and policy-makers.

H. M. Pereira,[1*†] S. Ferrier,[2] M. Walters,[3] G. N. Geller,[4] R. H. G. Jongman,[5] R. J. Scholes,[3] M. W. Bruford,[6] N. Brummitt,[7] S. H. M. Butchart,[8] A. C. Cardoso,[9] N. C. Coops,[10] E. Dulloo,[11] D. P. Faith,[12] J. Freyhof,[13] R. D. Gregory,[14] C. Heip,[15] R. Höft,[16] G. Hurtt,[17] W. Jetz,[18] D. S. Karp,[19] M. A. McGeoch,[20] D. Obura,[21] Y. Onoda,[22] N. Pettorelli,[23] B. Reyers,[24] R. Sayre,[25] J. P. W. Scharlemann,[26,27] S. N. Stuart,[28] E. Turak,[29] M. Walpole,[26] M. Wegmann[30]

Reducing the rate of biodiversity loss and averting dangerous biodiversity change are international goals, reasserted by the Aichi Targets for 2020 by Parties to the United Nations (UN) Convention on Biological Diversity (CBD) after failure to meet the 2010 target (*1*, *2*). However, there is no global, harmonized observation system for delivering regular, timely data on biodiversity change (*3*). With the first plenary meeting of the Intergovernmental Science-Policy Platform on Biodiversity and Ecosystem Services (IPBES) soon under way, partners from the Group on Earth Observations Biodiversity Observation Network (GEO BON) (*4*) are developing—and seeking consensus around—Essential Biodiversity Variables (EBVs) that could form the basis of monitoring programs worldwide.

Despite progress in digital mobilization of biodiversity records and data standards (*5*), there is insufficient consistent national or regional biodiversity monitoring and sharing of such information. Along with inadequate human and financial resources (*6*), a key obstacle is the lack of consensus about what to monitor. Many initiatives collect data that could be integrated into an EBV global observation network (see the table), though important gaps remain. Different organizations and projects adopt diverse measurements, with some important biodiversity dimensions, such as genetic diversity, often missing (*7*).

The EBV process is inspired by the Essential Climate Variables (ECVs) that guide implementation of the Global Climate Observing System (GCOS) by Parties to the UN Framework Convention on Climate Change (UNFCCC) (*8*). EBVs, whose development by GEO BON has been endorsed by the CBD (Decision XI/3), are relevant to derivation of biodiversity indicators for the Aichi Targets (*9*). Although CBD biodiversity indicators are designed to convey messages to policy-makers from existing biodiversity data (*1*), EBVs aim to help observation communities harmonize monitoring, by identifying how variables should be sampled and measured.

Given the complexity of biodiversity change (*3*), the challenge of developing a global observation system can appear insurmountable. Nearly 100 indicators have been proposed for the 2020 CBD targets (ongoing work seeks to identify a more limited subset) (*9*). Two-thirds of reports recently submitted by Parties to the CBD lacked evidence-based information on biodiversity change (*10*).

EBVs help prioritize by defining a minimum set of essential measurements to capture major dimensions of biodiversity change, complementary to one another and to other environmental change observation initiatives. EBVs also facilitate data integration by providing an intermediate abstraction layer between primary observations and indicators (fig. S1). An EBV estimating population abundances for a group of species at a location sits between raw observations (e.g., from different sampling events or methods) and an aggregated population trend indicator that averages multiple species and locations.

Essential Biodiversity Variables in Practice

We define an EBV as a measurement required for study, reporting, and management of biodiversity change. Hundreds of variables potentially fit this definition. We developed and tested a process, still ongoing, to identify the most essential (*11*). Dozens of biodiversity variables were screened to identify those that fulfill criteria on scalability, temporal sensitivity, feasibility, and relevance. These variables were scored for importance, checked for redundancy, and organized into six classes on the basis of commonalities, general enough for use across taxa and terrestrial, freshwater, and marine realms (see the table).

Often, it is not possible to generalize observations from point locations to the regional scale. Variables selected as EBVs harness remote sensing (RS) to measure continuously across space (e.g., habitat structure), or local sampling schemes that can be integrated to enable large-scale generalizations. For instance, citizen scientists contribute locally to species population monitoring across extensive regions (*12*). Ecosystem function or community composition variables often need intensive in situ measurements feasible only at a few locations, but models and proxies detectable by RS can be used to extrapolate from point locations to the regional scale (*13*, *14*). Such models are also important to predict the response of EBVs (e.g., species distributions) to environmental drivers (*15*), and can be used to develop scenarios exploring different policy options (*16*), a core activity of IPBES.

Many biodiversity assessments emphasize species inventories, e.g., identification of all species in a region, and there have been calls for redoubled efforts to describe all species in the world (*17*). The EBV framework instead emphasizes repeated measures for the same taxa at the same locations or regions mainly at short-term intervals (1 to 5 years), although a few may be medium term (10 to 50 years).

Key determinants of observation system feasibility are the number of variables that need monitoring and their measurability. Although determination of the 50 ECVs requires elaborate observation and modeling systems, the end result is often outwardly simple (e.g., air temperature or pressure) (*8*). This is also true of some EBVs, particularly those related to ecosystem structure and func-

[1]Centro de Biologia Ambiental, Faculdade de Ciências da Universidade de Lisboa, Portugal. [2]CSIRO Ecosystem Sciences, Australia. [3]CSIR Natural Resources and Environment, South Africa. [4]Jet Propulsion Laboratory, California Institute of Technology, USA. [5]Alterra, Wageningen UR, Netherlands. [6]Cardiff School of Biosciences, Cardiff University, UK. [7]Natural History Museum, UK. [8]BirdLife International, UK. [9]Joint Research Centre, Institute for Environment and Sustainability, Italy. [10]Department of Forest Resource Management, University of British Columbia, Canada. [11]Food and Agriculture Organization of the United Nations, Italy. [12]The Australian Museum, Australia. [13]BioFresh, The Leibniz Institute of Freshwater Ecology and Inland Fisheries, Germany. [14]The Royal Society for the Protection of Birds, UK. [15]Royal Netherlands Institute for Sea Research, Netherlands. [16]Secretariat of the Convention on Biological Diversity. [17]Department of Geographical Sciences, University of Maryland, USA. [18]Yale University, USA. [19]Center for Conservation Biology, Stanford University, USA. [20]School of Biological Sciences, Monash University, Australia. [21]CORDIO East Africa, Kenya. [22]Graduate School of Agriculture, Kyoto University, Japan. [23]Institute of Zoology, Zoological Society of London, UK. [24]CSIR Natural Resources and Environment, South Africa. [25]U.S. Geological Survey, USA. [26]United Nations Environment Programme World Conservation Monitoring Centre, UK. [27]School of Life Sciences, University of Sussex, UK. [28]IUCN Species Survival Commission, UK. [29]Office of Environment and Heritage, NSW, Australia. [30]Department for Geography and Geology, Würzburg University, Germany.

*For complete addresses, see supplementary materials. †Author for correspondence. E-mail: hpereira@fc.ul.pt

Examples of candidate Essential Biodiversity Variables

EBV class	EBV examples	Measurement and scalability	Temporal sensitivity	Feasibility	Relevance for CBD targets and indicators (*1*,*9*)
Genetic composition	Allelic diversity	Genotypes of selected species (e.g., endangered, domesticated) at representative locations.	Generation time	Data available for many species and for several locations, but little global systematic sampling.	Targets: 12, 13. Indicators: Trends in genetic diversity of selected species and of domesticated animals and cultivated plants; RLI.
Species populations	Abundances and distributions	Counts or presence surveys for groups of species easy to monitor or important for ES, over an extensive network of sites, complemented with incidental data.	1 to >10 years	Standardized counts under way for some taxa but geographically restricted. Presence data collected for more taxa. Ongoing data integration efforts (Global Biodiversity Information Facility, Map of Life).	Targets: 4, 5, 6, 7, 8, 9, 10, 11, 12, 14, 15. Indicators: LPI; WBI; RLI; population and extinction risk trends of target species, forest specialists in forests under restoration, and species that provide ES; trends in invasive alien species; trends in climatic impacts on populations.
Species traits	Phenology	Timing of leaf coloration by RS, with in situ validation.	1 year	Several ongoing initiatives (Phenological Eyes Network, PhenoCam, etc.)	Targets: 10, 15. Indicators: Trends in extent and rate of shifts of boundaries of vulnerable ecosystems.
Community composition	Taxonomic diversity	Consistent multitaxa surveys and metagenomics at select locations.	5 to >10 years	Ongoing at intensive monitoring sites (opportunities for expansion). Metagenomics and hyperspectral RS emerging.	Targets: 8, 10, 14. Indicators: Trends in condition and vulnerability of ecosystems; trends in climatic impacts on community composition.
Ecosystem structure	Habitat structure	RS of cover (or biomass) by height (or depth) globally or regionally.	1 to 5 years	Global terrestrial maps available with RS (e.g., Light Detection and Ranging). Marine and freshwater habitats mapped by combining RS and in situ data.	Targets: 5, 11, 14, 15. Indicators: Extent of forest and forest types; mangrove extent; seagrass extent; extent of habitats that provide carbon storage.
Ecosystem function	Nutrient retention	Nutrient output/input ratios measured at select locations. Combine with RS to model regionally.	1 year	Intensive monitoring sites exist for N saturation in acid-deposition areas and P retention in affected rivers.	Targets: 5, 8, 14. Indicators: Trends in delivery of multiple ES; trends in condition and vulnerability of ecosystems.

tion. However, EBVs relating to species populations or traits and to genetic or community composition require representative sampling across taxonomic groups or community types. These EBVs need to balance specificity and generality, enabling valid aggregation of data from multiple monitoring programs, while allowing for flexibility in the species or taxonomic groups addressed by these programs.

Variables selected as EBVs fill a niche not covered by global observation initiatives looking at environmental pressures [e.g., GCOS (*8*), Essential Ocean Variables (*18*)]. An EBV such as species abundance provides data for indicators such as the Living Planet, Wild Bird, and Red List indices (LPI, WBI, and RLI) (see the table). Assessing ecosystem services (ES) requires knowledge of changes in beneficial species, functional groups, or ecosystem processes; additional physical, social, and economic data (fig. S1) can be obtained from valuation studies, surveys, and national statistics (*19*). Complementary spatial information on responses implementation (e.g., coverage of protected areas) can inform indicators of the effectiveness of policy and management (fig. S1). This fundamental, but flexible, role of EBVs confers robustness to the system: EBVs are insulated from changing technologies at the observation level and from changing approaches at the indicator level.

Building Consensus and Capacity

Identification of EBVs and definition of sampling protocols are done by an open process that requires engagement of scientific, policy, and other communities. Major roles can be played by IPBES, national biodiversity authorities, space agencies, nongovernmental organizations, and citizen-science communities. Information on the EBV process is updated at (*11*); written contributions can be sent to GEO BON. Side events will be organized in scientific and policy meetings over the next year. This will refine the EBV list, which, once stable, will periodically be updated by GEO BON in a process similar to that used for ECVs (*8*).

Coordination of sampling schemes by GEO BON across countries and scales can minimize costs and improve spatial representativeness. Developing suitable financial mechanisms to share costs between developing countries, where most biodiversity occurs, and developed countries, which share in the benefits but drive many of the pressures (*20*), will play a key role in the development of a truly global system. We hope that EBVs will catalyze investment in biodiversity observations, as ECVs have done for climate.

References and Notes

1. S. H. M. Butchart *et al.*, *Science* **328**, 1164 (2010).
2. CBD, Decision X/2, The Strategic Plan for Biodiversity 2011–2020 and the Aichi Biodiversity Targets, Nagoya, Japan, 18 to 29 October 2010.
3. H. M. Pereira, L. M. Navarro, I. S. Martins, *Annu. Rev. Environ. Resour.* **37**, 25 (2012).
4. R. J. Scholes *et al.*, *Curr. Opin. Environ. Sustain.* **4**, 139 (2012).
5. R. P. Guralnick *et al.*, *Ecol. Lett.* **10**, 663 (2007).
6. L. J. Martin *et al.*, *Front. Ecol. Environ* **10**, 195 (2012).
7. C. K. Feld *et al.*, *Oikos* **118**, 1862 (2009).
8. GCOS, *Implementation Plan for the Global Observing System for Climate in Support of the UNFCCC (2010 Update)* (World Meteorological Organization, Geneva, 2010), p. 180.
9. Secretariat of the CBD, *Report of the Ad Hoc Technical Expert Group on indicators for the Strategic Plan for Biodiversity 2011–2020* (SCBD, Montreal, Canada, 2011).
10. P. Bubb *et al.*, *National Indicators, Monitoring and Reporting for the Strategic Plan for Biodiversity 2011–2020* (UNEP-WCMC, Cambridge, 2011).
11. GEO BON, EBVs; www.earthobservations.org/geobon_ebv.shtml.
12. R. D. Gregory *et al.*, *Philos. Trans. R. Soc. London Ser. B* **360**, 269 (2005).
13. D. P. Turner, *Front. Ecol. Environ* **9**, 111 (2011).
14. S. Ferrier, *Bioscience* **61**, 96 (2011).
15. W. Jetz *et al.*, *Trends Ecol. Evol.* **27**, 151 (2012).
16. H. M. Pereira *et al.*, *Science* **330**, 1496 (2010).
17. E. O. Wilson, *Science* **289**, 2279 (2000).
18. IOC, A framework for ocean observing—Consultative draft v.7 (UNESCO, Paris, 2011), p. 26.
19. H. Tallis *et al.*, *Bioscience* **62**, 977 (2012).
20. M. Lenzen *et al.*, *Nature* **486**, 109 (2012).

Acknowledgments: NASA, DIVERSITAS, GEO, ESA-ESRIN, and the Department of Science and Technology (South Africa) provided resources. H.M.P. was supported by FCT grant PTDC/AAC-AMB/114522/2009. M. Paganini helped organize a workshop. H.M.P., S.F., M. Walters, G.N.G., R.H.G.J., R.J.S., D.P.F., C.H., R.H., R.S., S.N.S., and M. Walpole are on the GEO BON steering committee. Abbreviations spelled out in SM.

Supplementary Materials

www.sciencemag.org/cgi/content/full/339/6117/277/DC1

10.1126/science.1229931

NEUROSCIENCE

Hormones and the Social Brain

Social stress can act through glucocorticoids on discrete dopamine-controlled neuronal pathways in the rodent brain to influence behavior.

Bruce S. McEwen

Glucocorticoids are steroid hormones that function in immune responses, metabolism, development, and a range of behaviors. On pages 332 and 335 in this issue, Barik *et al.* (*1*) and Niwa *et al.* (*2*), respectively, challenge our understanding of the sites and mechanisms of action of glucocorticoid "stress hormones" in the mammalian brain, revealing surprising neuroanatomical specificity and pointing to the participation of other regulatory factors and cellular interactions, as well as the importance of gene-environment interactions in the effects of glucocorticoids.

In the mammalian brain, glucocorticoid receptors in dopaminoceptive neurons (those that respond to the neurotransmitter dopamine) are required for the enhancement of addictive behavior that is triggered by stress (*3*). Barik *et al.* show that in adult mice, glucocorticoid receptor activation in dopaminoceptive neurons, but not in dopaminergic neurons (those that release dopamine), is required for inducing anxiety and social aversion after repeated exposure to aggression. Glucocorticoids released (by the adrenal gland) in a stress response activated the "ascending" dopamine system, which controls the motor system, reward system, and cognition. Specific inactivation of the gene encoding the glucocorticoid receptor in dopaminoceptive neurons prevented social aversion in response to the stressor, apparently by activating dopamine release through a positive feedback loop from the nucleus accumbens (NAc; functions in reward, addiction, aggression, and fear) to the ventral tegmental area (VTA; functions in cognition and addiction), where dopamine-producing neurons are located (see the figure). This loop could be arrested by a pharmacological inhibitor (RU486) of the glucocorticoid receptor, and also by stimulating D2 dopamine receptors on dopaminergic neurons, which suppresses their activity. Thus, it is not direct glucocorticoid regulation of dopaminergic activity from the VTA to NAc, but rather the action of glucocorticoids on neurons responding to dopamine (dopaminoceptive) that is responsible for this specific behavioral outcome of a social stress.

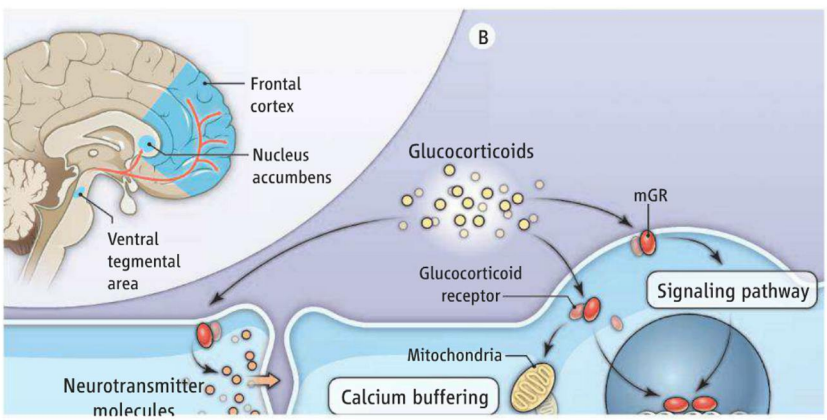

Glucocorticoids and brain circuitry. (**A**) Social stress acts, in a glucocorticoid-dependent manner, on two dopamine-dependent pathways—the ventral tegmental area–to–nucleus accumbens and ventral tegmental area–to–frontal cortex—in the rodent brain to influence behavior (human brain shown). (**B**) Glucocorticoid actions on neurons are direct genomic, indirect genomic, and nongenomic, affecting the release of signaling factors, calcium buffering, and structural plasticity. mGR, membrane-associated glucocorticoid receptor.

Niwa *et al.* report that the stress of isolation experienced by adolescent mice (from 5 to 8 weeks of age) produced a vulnerability that continued into adult life (until at least 20 weeks of age), as observed by increased immobility time in the forced swim test, for example. However, only mice bearing a risk allele for neuropsychiatric disorders—a faulty *DISC1* allele—exhibited this behavior. This dependence on a genetic predisposition reflects a gene-environment interaction. The authors determined that a dopaminergic pathway from the VTA to the frontal cortex (FC) was important. Here, the amounts of dopamine and tyrosine hydroxylase (involved in dopamine synthesis) were reduced, and the expression of D2 dopamine receptors in dopaminergic neurons increased. The gene encoding tyrosine hydroxylase in the dopaminergic neurons showed increased DNA methylation, underlying its reduced expression. Blocking the glucocorticoid receptor with RU486 during the 3-week isolation period prevented the molecular, neurochemical, and behavioral effects in the mice bearing the risk allele. These alterations were not observed in neuronal projections from the VTA to the NAc.

DNA methyltransferases are regulated by glucocorticoids both positively (*4*) and negatively (*5*), but the anatomically specific effects observed by Niwa *et al.* implied the involvement of other factors. That the authors found a genetic predisposition as a necessary condition to a behavioral outcome, along with the animal's developmental stage, suggests that alterations in developing neural architecture can make an individual vulnerable to a social stressor, with glucocorticoids participating in some manner. The amount of circulating glucocorticoid increased during behavioral testing in the mice with the aberrant *DISC* allele. Could that elevation maintain the altered neuronal state in which the VTA-NAc pathway is hyperactive while the VTA-FC pathway is not? Niwa *et al.* suggest that their gene-environment animal model could be useful in testing interventions for the contributions of glucocorticoids and dopaminergic activity to human psychotic depression (*6*).

Both Barik *et al.* and Niwa *et al.* show that glucocorticoid receptors function in specific neuroanatomical pathways in the dopaminergic system that underlie behaviors associated with social stress. Still, there is much about the mechanisms that remains to be uncovered. Glucocorticoid actions may be classified as direct genomic, indirect genomic, and nongenomic (*7*, *8*), all of which may be involved in the pathways studied by Barik *et al.* and Niwa *et al.* In addition, a key aspect of

Laboratory of Neuroendocrinology, Rockefeller University, New York, NY 10065 USA. mcewen@rockefeller.edu

the action of glucocorticoid and mineralocorticoid (a steroid hormone so-named because it controls fluid homeostasis) receptors in diverse functions is a dependence on other mediators and ongoing cellular processes. For example, activation of these receptors in the brain is associated with the release of the neurotransmitter glutamate (*8*–*10*) as well as the release of endocannabinoids, lipids that modulate appetite, mood, and memory (*11*, *12*). These hormones also act on receptors that translocate to the mitochondria to control calcium buffering (*13*). Glucocorticoids support neuronal synapses (*14*), dendritic growth (*15*), and neuronal plasticity (*16*), suggesting a role in maintaining a dynamic brain architecture. Moreover, glucocorticoid action on some processes involves concurrent activity of other mediator systems, such as oxytocin for neurogenesis (*17*) and adrenergic mechanisms for learning (*18*).

Clearly, our understanding of the complex and widespread actions of adrenal steroid hormones throughout the developing and adult nervous system is at an early stage. The finding that these hormones play a role in the discrete specification of neuronal circuits in the brain and behavioral outcomes point to potential therapeutic approaches that could intervene and restore normal behaviors.

References and Notes

1. J. Barik *et al.*, *Science* **339**, 332 (2013).
2. M. Niwa *et al.*, *Science* **339**, 335 (2013).
3. F. Ambroggi *et al.*, *Nat. Neurosci.* **12**, 247 (2009).
4. A. Crudo *et al.*, *Endocrinology* **153**, 3269 (2012).
5. X. Yang *et al.*, *Biochem. Biophys. Res. Commun.* **420**, 570 (2012).
6. A. F. Schatzberg, A. J. Rothschild, *Ann. N.Y. Acad. Sci.* **537**, 462 (1988).
7. K. R. Yamamoto, *Annu. Rev. Genet.* **19**, 209 (1985).
8. M. Popoli, Z. Yan, B. S. McEwen, G. Sanacora, *Nat. Rev. Neurosci.* **13**, 22 (2012).
9. H. Karst *et al.*, *Proc. Natl. Acad. Sci. U.S.A.* **102**, 19204 (2005).
10. E. M. Prager, L. R. Johnson, *Sci. Signal.* **2**, re5 (2009).
11. M. N. Hill, B. S. McEwen, *Prog. Neuropsychopharmacol. Biol. Psychiatry* **34**, 791 (2010).
12. J. G. Tasker, S. Di, R. Malcher-Lopes, *Endocrinology* **147**, 5549 (2006).
13. J. Du *et al.*, *Proc. Natl. Acad. Sci. U.S.A.* **106**, 3543 (2009).
14. C. Liston, W. B. Gan, *Proc. Natl. Acad. Sci. U.S.A.* **108**, 16074 (2011).
15. E. Gould, C. S. Woolley, B. S. McEwen, *Neuroscience* **37**, 367 (1990).
16. M. Spolidoro *et al.*, *Nat. Commun.* **2**, 320 (2011).
17. B. Leuner, J. M. Caponiti, E. Gould, *Hippocampus* **22**, 861 (2012).
18. S. Okuda, B. Roozendaal, J. L. McGaugh, *Proc. Natl. Acad. Sci. U.S.A.* **101**, 853 (2004).

10.1126/science.1233713

CLIMATE CHANGE

The Closing Door of Climate Targets

The linear relationship between cumulative carbon emissions and global climate warming implies that as mitigation is delayed, climate targets become unachievable.

Thomas F. Stocker

Robust evidence from a range of climate–carbon cycle models shows that the maximum warming relative to pre-industrial times caused by the emissions of carbon dioxide is nearly proportional to the total amount of emitted anthropogenic carbon (*1*, *2*). This proportionality is a reasonable approximation for simulations covering many emissions scenarios for the time frame 1750 to 2500 (*1*). This linear relationship is remarkable given the different complexities of the models and the wide range of emissions scenarios considered. It has direct implications for the possibility of achieving internationally agreed climate targets such as those mentioned in the Copenhagen Accord and the Cancun Agreements (*3*, *4*). Here I explain some of the implications of the linear relationship between peak warming and total cumulative carbon emissions.

The considerations presented here are based on the assumption of a generic set of carbon dioxide emissions scenarios that reasonably approximate what is presently observed and what needs to be done to limit warming below a specific global mean temperature increase. In these idealized and illustrative emissions scenarios (see the Box), emissions follow an exponential increase with a constant rate until a given year, after which the emissions decrease exponentially at a constant rate. The scenarios delineate the boundaries for any discussion and decision process for global measures limiting anthropogenic climate change.

Results from a large number of Earth system model simulations suggest that peak warming, ΔT, and cumulative CO_2 emissions, C_∞, are nearly linearly related via the parameter β, which is the peak response to cumulative emissions (see Eq. 3 in the Box).

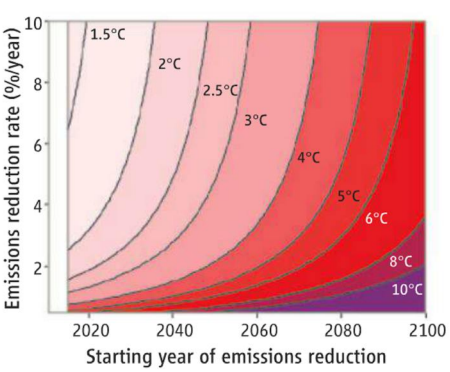

Contours of peak warming. Contours of peak CO_2-induced warming (as given by Eq. 3 in the Box) as a function of the starting date of the GMS and the implemented reduction rate of emissions. Parameters are $C_0 = 530$ GtC, $E_0 = 9.3$ GtC per year, $\beta = 2°C$ $(TtC)^{-1}$, and $r = 1.8\%$ per year. The later the GMS starts, the higher the required emissions reduction rate is for a given peak warming.

The value of β is estimated to be between 1.3° and 3.9°C per trillion metric tons of carbon (1 TtC = 10^{18} g carbon) (*1*). The uncertainty in β arises from the range of climate sensitivities and carbon cycle feedbacks in the models. More recent estimates of a closely related quantity, the transient climate response to cumulative emissions, take into account observational constraints and report 1.0° to 2.1°C $(TtC)^{-1}$ (*2*). However, this quantity is less useful here because warming can still continue when emissions stop. This warming is better captured by the peak response to cumulative emissions.

For a given β, the peak warming is determined by three quantities in these simple scenarios: the current rate of emissions increase, the starting time of the Global Mitigation Scheme (GMS), and the rate of emissions reduction realized by the GMS. The latter two depend on future choices and are therefore policy-relevant. As shown in the first figure, a delay in the start of the GMS results in a rapid increase in ΔT as a result of the continued exponential increase in emissions before the start of mitigation. Likewise, for a given starting date of mitigation, achieving a low climate target calls for very aggressive emission decreases. For example, under the present illustrative assumptions, keeping CO_2-induced global warming below 2°C would require emissions reductions of almost 3.2% per year from 2020 onward; this is more than

Climate and Environmental Physics, Physics Institute, and Oeschger Centre for Climate Change Research, University of Bern, 3012 Bern, Switzerland. E-mail: stocker@climate.unibe.ch

A set of simple analytic greenhouse gas emissions scenarios

For simplicity, we assume that past greenhouse gas emissions followed an exponential path, which is a reasonable approximation for historical emissions (*6*). To extract some essential characteristics and consequences of increasing emissions followed by sustained mitigation, we construct a simple emission path that consists of two exponentials,

$$E(t) = \begin{cases} E_0 \cdot e^{r\cdot(t-t_0)} & t_0 < t \le t_1 \\ E_0 \cdot e^{r\cdot(t_1-t_0)} \cdot e^{-s\cdot(t-t_1)} & t > t_1 \end{cases} \quad (1)$$

where $E(t)$ are the anthropogenic CO_2 emissions at time t, E_0 = 9.3 GtC year^{-1} is the emission at t_0, taken here as the year 2009 (*7*), and r is the rate of emissions increase per year until time t_1. The exact path of emissions before t_0 is not important here, because its effect can be taken into account by the cumulative emissions until t_0, C_0. We select C_0 = 530 GtC (*6*). A Global Mitigation Scheme (GMS) starts at time t_1 with emissions reductions at the constant rate of s. We take r = 1.8% per year, which is somewhat lower than a recent estimate of r (*6*) for the entire historical period, in order to be more consistent with the cumulative emission until 2009 as also estimated by (*6*). Similar peak-and-decline emissions trajectories represented by analytical functions were used recently (*8*), with a smooth transition path to sustained emissions reductions.

The scenario path for $t > t_1$ in Eq. 1 implies that negative emissions (active removal of carbon from the atmosphere) on a global scale will not be realized anytime in the future. This should be considered as a conservative, but likely realistic, assumption. The total cumulative emissions C_∞ follow from Eq. 1 and are given by

$$C_\infty = C_0 + \int_{t_0}^{+\infty} E(t)dt = C_0 + E_0 \cdot \left(\tfrac{1}{r} + \tfrac{1}{s}\right) \cdot e^{r\cdot(t_1-t_0)} - \tfrac{1}{r}E_0 \quad (2)$$

This simple scenario can be used to illustrate some fundamental and policy-relevant consequences of the robust linear relationship between peak warming and cumulative emissions. I consider implicitly only long-lived greenhouse gases, which is appropriate unless temperatures peak in the next few decades.

Simulations with many Earth system models (*1*, *2*) show a near-linear relationship between peak warming, ΔT, and cumulative CO_2 emissions, C_∞,

$$\Delta T = \beta \cdot C_\infty \quad (3)$$

where β is the factor of proportionality between cumulative emissions and peak warming and is referred to as the peak response to cumulative emissions.

By taking in Eq. 2, the limit of $s = \infty$, and using Eq. 3, one obtains

$$\Delta T_{min} = \beta \cdot \left(C_0 + \tfrac{1}{r}E_0 \cdot (e^{r\cdot(t_1-t_0)} - 1)\right) = \beta \cdot C_1 \quad (4)$$

which is the minimum peak warming resulting from the most aggressive GMS, that is, zero emissions from time t_1 onwards. Achievable climate targets are therefore determined by the cumulative emissions until time t_1, C_1.

doubled if GMS starts in 2032. Thus, every year counts; if mitigation actions are delayed, much larger emissions reductions are later required to maintain a selected target.

The simple emission pathway provides another important insight. If we assume that the most aggressive GMS is "zero emission" (that is, carbon will not be extracted actively from the atmosphere), the total amount of carbon emitted up to the start of GMS determines the lowest peak warming, or minimum climate target, ΔT_{min} (see Eq. 4 in the Box). An absolute limit then emerges in the climate system for the possibility of satisfying a climate target. Past cumulative emissions up to the time of sustained emissions reductions leave a legacy, or commitment, in the future, irrespective of any long-term mitigation efforts. As the starting time of GMS is delayed, the low climate targets are progressively lost. The door for these climate targets closes irreversibly (see the second figure, panel A).

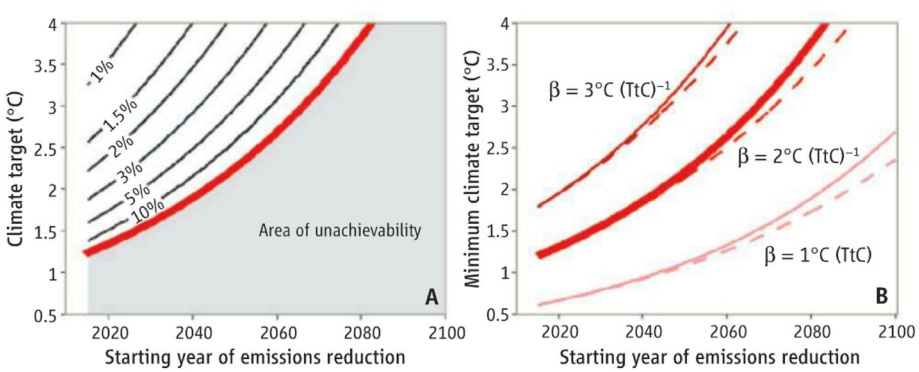

A closing door. (**A**) Contours of required emissions reduction rate s (% per year), derived from Eq. 3, as a function of the starting date of the GMS and the desired climate target. The red line indicates the achievable minimum climate target as a function of the starting date as given by Eq. 4. Climate targets increase exponentially with later starting years of the GMS and become unachievable in the gray shaded area. Parameters are as in the first figure. (**B**) Achievable minimum climate target for three values of the peak response to cumulative emissions, β, and the rate of emissions increase used in the first figure (solid curves, r = 1.8% per year), and a lower rate of emissions increase roughly representative of the past 10 years, r = 1.5% per year (dashed curves). Higher values of β imply higher peak warming.

Under the present illustrative assumptions, the 1.5°C target expires after 2028, and the 2°C target vanishes after 2044. These times would be later if a period of stabilized emissions preceded the GMS. The more likely situation, however, is that a specific climate target becomes unreachable much earlier, because there are upper limits on sustained emissions reduction rates imposed by what the countries' economies can realize collectively given the present state of technology and infrastructure.

Economic models estimate that feasible maximum rates of emissions reduction may not exceed about 5% per year (*5*). Under this assumption, the 1.5°C target has become unachievable before 2012, the 2°C target will become unachievable after 2027, and the 2.5°C target will become unreachable after 2040.

These years are only illustrative of the finite time that climate targets remain available options in the presence of continued greenhouse gas emissions. Uncertainties in β, or in the rate of emissions increase, do not change the overall findings (see the second figure, panel B). But it is clear that reducing uncertainties in the quantity β, which com-

bines climate sensitivity and carbon cycle feedbacks (*2*), is most important for a more reliable estimate of which climate targets are still achievable.

As the emissions scenarios considered here illustrate, even well-intentioned and effective international efforts to limit climate change must face the hard physical reality of certain temperature targets that can no longer be achieved if too much carbon has already been emitted to the atmosphere. Both delay and insufficient mitigation efforts close the door on limiting global mean warming permanently. This constitutes more than a climate change commitment: It is the fast and irreversible shrinking, and eventual disappearance, of the mitigation options with every year of increasing greenhouse gas emissions.

References and Notes

1. M. R. Allen *et al.*, *Nature* **458**, 1163 (2009).
2. H. D. Matthews, N. P. Gillett, P. A. Stott, K. Zickfeld, *Nature* **459**, 829 (2009).
3. UNFCCC, The Copenhagen Accord, FCCC/CP/2009/11/Add.1 (United Nations Framework Convention on Climate Change, 2009).
4. UNFCCC, The Cancun Agreements, FCCC/CP/ 2010/7/Add.1 (United Nations Framework Convention on Climate Change, 2010).
5. M. den Elzen, M. Meinshausen, D. van Vuuren, *Glob. Environ. Change* **17**, 260 (2007).
6. R. J. Andres *et al.*, *Biogeosciences* **9**, 1845 (2012).
7. P. Friedlingstein *et al.*, *Nat. Geosci.* **3**, 811 (2010).
8. N. H. A. Bowerman *et al.*, *Philos. Transact. A Math. Phys. Eng. Sci.* **369**, 45 (2011).

Acknowledgments: M. Allen is acknowledged for critical and thoughtful comments.

Published online 29 November 2012

10.1126/science.1232468

PLANETARY SCIENCE

A Wet and Volatile Mercury

Observations by the MESSENGER spacecraft are revealing details of Mercury's dynamic atmosphere.

Paul G. Lucey

One of the more startling discoveries in planetary science was that the poles of Mercury feature deposits that are extremely bright at radar wavelengths (*1*), interpreted to be due to the presence of thick water ice. Because Mercury's rotation axis is almost normal to the plane of its orbit, the temperature of polar craters largely or completely shaded from the Sun should be very low. On the Moon, for example, where the rotation axis tilt is similarly small, the polar temperatures in permanently shadowed regions have been measured by infrared radiometry to be as low as 25 K (*2*). These topographic depressions might be expected to contain cold-trapped volatile material that might be introduced by comets, water-bearing asteroids, or other sources. On pages 292, 300, and 296 of this issue, Lawrence *et al.* (*3*), Paige *et al.* (*4*), and Neumann *et al.* (*5*) report on the latest results from the MESSENGER (MErcury Surface, Space ENvironment, GEochemistry, and Ranging) mission confirming the expectations that the atmosphere of Mercury is indeed a wet volatile one, as well as providing the odd surprise.

Compounds other than water ice have been suggested to account for the radar observations, with sulfur being of particular interest given the extremely high temperatures of equatorial Mercury and the abundant evidence for volcanic activity on the small planet (*6*). However, Lawrence *et al.* report depressed neutron fluxes at Mercury's north pole and show that only high concentrations of hydrogen confined to the known radar-bright locations are consistent with the neutron flux measured at both high and intermediate energies. Thermal modeling supports their conclusion. Paige *et al.* apply a thermal model of the polar Moon to polar Mercury to estimate the surface and shallow subsurface temperatures, supported by detailed topography measured by the MESSENGER laser altimeter and validated with lunar remote radiometric measurements. They find that the radar-bright areas are almost exclusively confined to places where shallow subsurface temperatures hover near 100 K or less, and owing to the exponential dependence of volatility on temperature, water is the only compound with the right volatility and cosmochemical abundance to account for the radar anomalies. On the other hand, maximum temperatures experienced by most of these radar-bright regions are too high to sustain surface ice, so that if ice is responsible for the radar features, it must be buried by a few centimeters of insulating material, such as dry Mercury soil.

These results fulfilled promises made by the MESSENGER scientists that Mercury's enigmatic polar volatile would be identified. But polar measurements contained a major surprise. The laser altimeter carried on the spacecraft, which provided the topographic measurements enabling the detailed thermal modeling, also measured the reflectance of Mercury's surface in the unilluminated polar regions. This instrument compares the strength of the outgoing laser pulse to the return power, normalized to the range to the surface. Pioneered on Mars and the Moon, this method measures the normal albedo of the surface without the influence of local topography or the need for solar illumination, which is weak or absent at the poles. Before MESSENGER's arrival at Mercury, it was anticipated that bright surface deposits of ice or sul-

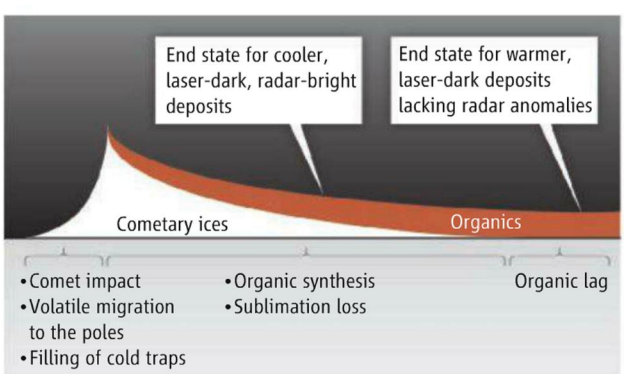

Atmosphere dynamics. Mercury's polar cold traps appear to have been filled by one or more comet impacts that introduced massive quantities of water and other volatile vapors in the tenuous atmosphere that promptly migrated to the polar cold traps. Ices began to immediately sublimate, and to acquire organic lag deposits, probably from radiation-induced chemical synthesis. The colder parts of the poles now exhibiting radar anomalies retained water ice below the lag deposit, while in warmer portions the ice entirely sublimed away, leaving the low-reflectance organic residue. Not depicted are the rare very-high-reflectance spots that are confined to the coldest portions of the pole. These may indicate a slow continuous production of water from small wet meteorites, solar wind proton interactions with oxygen in Mercury's surface, or inhibition by the very low temperatures of the organic synthesis occurring elsewhere.

Hawaii Institute of Geophysics and Planetology, University of Hawaii, 2525 Correa Road, Honolulu, HI 96822, USA. E-mail: lucey@higp.hawaii.edu

fur might be associated with the radar anomalies. Neumann *et al.* did find this association, but also found the opposite—that the surfaces of the radar anomalies are not bright, but are typically quite dark relative to average Mercury reflectance with rare exceptions.

Paige *et al.* synthesized these observations to suggest that the dark deposits are due to organics more refractory than water ice, either directly deposited with the ice as part of the same process, or formed in situ by a low-temperature organic synthesis. Production of organics by irradiated cometary ices is well established in the laboratory and has been invoked to explain planetary and astrophysical observations of comets and the interstellar medium (see the figure). Paige *et al.* suggest that as a result of exposure to solar wind and ultraviolet radiation, complex organic radiolytic products are formed from ices and accumulate as a protective lag deposit that ultimately shields ice from further sublimation. They further note that dark deposits are observed to be more extensive than radar-bright material, and also occur in locations with somewhat higher model temperatures. This is evidence that ice deposits were more widespread in the past, and that the dark deposits in areas with higher temperature and lacking radar anomalies are relic deposits of this earlier era. A few restricted portions of the polar surface are substantially brighter than typical for Mercury, and Paige *et al.* show that these surfaces are cold enough to preserve surface frost against sublimation loss.

Prior to the MESSENGER results, polar ice at Mercury (and the Moon) was generally accepted, but the new data reveal a dynamic history of these deposits. The presence of the organic lag deposits strongly indicates that comets are the source of the polar volatiles, because other proposed sources are barren with respect to the critical elements needed for organic synthesis. The results also show that the charging of the cold traps can temporarily overcome thermal instability and can be used to derive a high lower limit on the amount of water vapor that can be at least transiently retained in a transient atmosphere of Mercury in a comet impact to account for the distribution of the dark deposits.

References

1. M. A. Slade, B. J. Butler, D. O. Muhleman, *Science* **258**, 635 (1992).
2. D. A. Paige *et al.*, *Science* **330**, 479 (2010).
3. D. J. Lawrence *et al.*, *Science* **339**, 292 (2013); 10.1126/science.1229953.
4. D. A. Paige *et al.*, *Science* **339**, 300 (2013); 10.1126/science.1231106.
5. G. A. Neumann *et al.*, *Science* **339**, 296 (2013); 10.1126/science.1229764.
6. A. L. Sprague, D. M. Hunten, K. Lodders, *Icarus* **118**, 211 (1995).

10.1126/science.1232556

CHEMISTRY

Re-Engineering Nature's Catalysts

An engineered enzyme catalyzes a reaction that is fundamentally different from that catalyzed by the natural enzyme.

Alison R. H. Narayan and David H. Sherman

Natural systems have inspired many scientific and technological advances (*1*). Materials design seeks to duplicate the fiber optical features of glass sponges (*2*); inorganic chemical complexes are modeled after enzyme active sites; and synthetic chemistry strategies parallel the biosynthetic pathways that produce complex natural product molecules (*3*). Scientists have also directly manipulated nature's tools through enzyme and metabolic pathway engineering. On page 307 of this issue, Coelho *et al.* (*4*) report that a bacterial cytochrome P450—a protein that naturally catalyzes C–H bond oxidation—can be engineered to efficiently produce highly strained cyclopropanated products. This work demonstrates the biomimicry paradigm in reverse, where altering the function of one of nature's most versatile biocatalysts is directed to a transformation originally conceived and implemented by synthetic chemists.

Throughout evolutionary time, enzymes have continuously morphed to perform specific functions on defined substrates in living cells. Advances in molecular biology have enabled new strategies to maximize the synthetic utility of particular enzymes and to expand their substrate scope and catalytic activity. Directed evolution is one of the most successful approaches toward achieving these goals (*5*). This method is a laboratory-based, accelerated version of natural evolution. Mutants with beneficial properties are advanced to subsequent rounds of mutagenesis in an iterative quest for the ideal enzyme. This approach has proven fruitful for altering the substrate scope for numerous target enzymes. For example, Arnold *et al.* evolved $P450_{BM3}$ to selectively hydroxylate ethane, a much smaller molecule than the natural fatty acid substrate, to afford ethanol (*6*). Directed evolution has also been used to identify thermally stable enzyme mutants (*7*) or variants that function effectively in organic solvents (*8*).

These accomplishments have advanced the field of enzymatic catalysis. However, many continue to overlook the utility of enzymes compared to the endless modes of reactivity that can be probed and discovered by synthetic chemists. With a specific function ingrained in a protein's native design, is it possible to completely re-engineer its function through iterative mutagenesis of its corresponding gene?

To access a totally new form of catalysis requires more than just library screening of a target enzyme. This feat demands a fundamental understanding of the enzyme's structure and function combined with chemical intuition. In a pioneering study, Wilson and Whitesides used an oversized protein ligand to create a chiral environment around a metal complex. These artificial metalloenzymes, with biotin-tethered metal complexes bound to streptavidin, catalyzed asymmetric hydrogenation reactions (*9*). The power of this approach was recently expanded by Hyster *et al.*, who used biotinylated rhodium(III) complexes with streptavidin mutants for asymmetric C–H activation. The study demonstrated the influence of key second sphere residues on the reactivity and selectivity of the enzyme (*10*).

Although progress has been made to optimize the native function of enzymes, the ability to leverage an individual active site to catalyze a new type of reaction remains a greater challenge. To achieve this goal, Coelho *et al.* selected diazoester carbene precursors as their cyclopropanation reagent. These compounds form metallocarbenoids with metals such as Rh, Ru, Cu, Co, and Fe (*11*). From the metallocarbenoid intermediate, cyclopropanation occurs through the transfer of the carbene to a double bond.

Coelho *et al.* screened 92 structurally and functionally diverse $P450_{BM3}$ mutants from a larger library. They found five candidates,

Life Sciences Institute and Department of Medical Chemistry, University of Michigan, Ann Arbor, MI 48109, USA. E-mail: davidhs@umich.edu

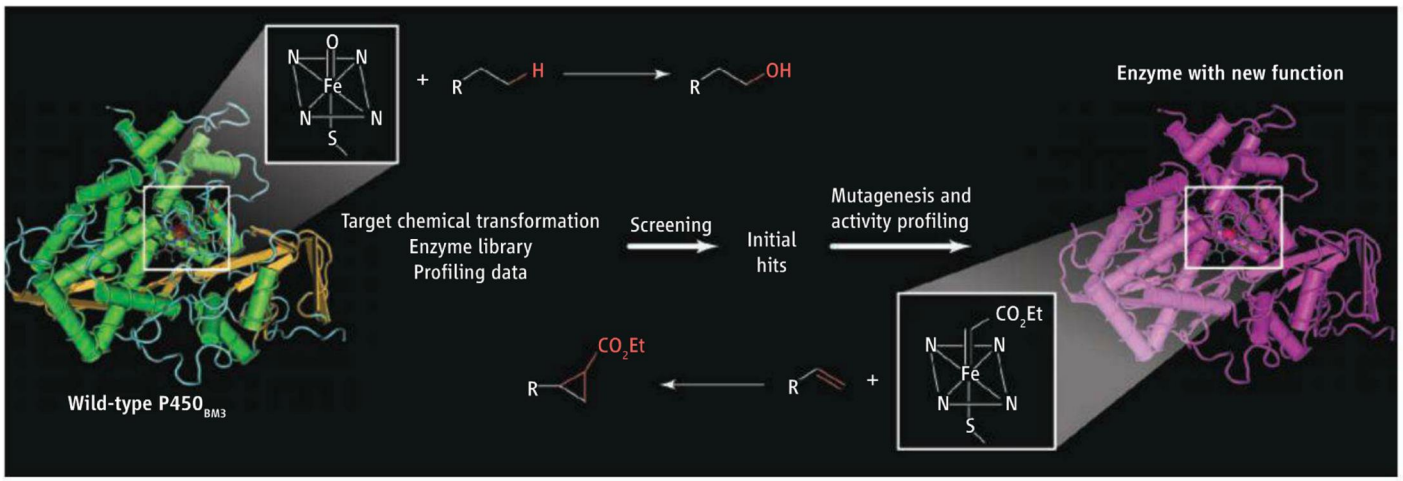

Biomimicry in reverse. The natural P450 monooxygenase enzyme catalyzes C–H bond oxidation. Through judicious choice of enzyme and substrate followed by directed evolution, Coelho *et al.* have reengineered this protein to perform a different catalytic reaction, namely cyclopropanation.

which they evolved further to a suite of diastereo- and enantioselective cyclopropanation catalysts that can favor either a *cis*- or *trans*-cyclopropane product.

An existing library of $P450_{BM3}$ variants and information on the native functionality of these proteins facilitated this impressive example of engineering new enzyme reactivity. Pairing library screening with additional information on structure and function provides an appealing model for streamlined, directed evolution efforts. For example, Fasan *et al.* recently reported the development of P450 enzymes for the regio- and stereoselective oxidation of the human antimalarial drug artemisinin. The authors performed first-sphere active-site mutagenesis, followed by high-throughput screening with a panel of model compounds; they then used the reactivity data to predict substrate scope and to drive further protein evolution efforts (*12*).

These studies show that translating classical synthetic chemical transformations into versatile chemoenzymatic reactions is ripe for expansion. However, going from a promising idea on paper to an efficient enzymatic transformation remains a formidable challenge. Drawing on multiple sources of information—such as computational modeling, x-ray structural data, reactivity profiles, and high-density library design derived from iterative mutagenesis and screening—will be essential for building a wide variety of new functions into nature's complex catalysts.

References

1. R. Breslow, *J. Biol. Chem.* **284**, 1337 (2009).
2. V. C. Sundar *et al.*, *Nature* **424**, 899 (2003).
3. P. G. Bulger *et al.*, *Nat. Prod. Rep.* **25**, 254 (2008).
4. P. S. Coelho *et al.*, *Science* **339**, 307 (2013); 10.1126/science.1231434.
5. M. T. Reetz, *Angew. Chem. Int. Ed.* **50**, 138 (2011).
6. P. Meinhold, M. W. Peters, M. M. Y. Chen, K. Takahashi, F. H. Arnold, *ChemBioChem* **6**, 1765 (2005).
7. M. T. Reetz, D. Carballeira, A. Vogel, *Angew. Chem. Int. Ed.* **45**, 7745 (2006).
8. N. Doukyu, H. Ogino, *Biochem. Eng. J.* **48**, 270 (2010).
9. M. E. Wilson, G. M. Whitesides, *J. Am. Chem. Soc.* **100**, 306 (1978).
10. T. K. Hyster *et al.*, *Science* **338**, 500 (2012).
11. H. Lebel, J.-F. Marcoux, C. Molinaro, A. B. Charette, *Chem. Rev.* **103**, 977 (2003).
12. K. Zhang, B. M. Shafer, M. D. Demars II, H. A. Stern, R. Fasan, *J. Am. Chem. Soc.* **134**, 18695 (2012).

10.1126/science.1233324

MATERIALS SCIENCE

Polymer Rigidity Improves Microporous Membranes

Microporous membranes with rigid polymer chains have high gas permeability but can separate gas molecules of slightly different sizes.

Michael D. Guiver[1,2] and Young Moo Lee[2]

Gas separation with membranes has been commercialized for more than 30 years, and includes processes such as the production of nitrogen (N_2) from air and the removal of carbon dioxide (CO_2) from natural gas. Commercial membranes have been largely derived from polymers with moderately rigid chains that pack closely to create small intermolecular spaces (or "free volume") that impart moderate to high gas selectivity. However, their relatively low gas permeability slows down the separation processes. Microporous organic polymers (MOPs) (*1*–*3*) offer higher permeability, but the polymer chains must be made sufficiently rigid to maintain good selectivity. On page 303 of this issue, Carta *et al.* (*4*) describe a soluble, highly rigid MOP, from which a highly permeable membrane with good selectivity was fabricated. For example, oxygen (O_2) and N_2 have only a 5% difference in kinetic diameters (which are related to the smallest effective dimensions of the gases), but the gas throughput of the smaller O_2 molecule is very much higher through their membrane.

Gases are separated by first pressurizing gas mixtures in contact with the membrane; each component sorbs (dissolves in it) and diffuses (passes through the free volume) through it at different rates with a character-

[1]National Research Council Canada, Ottawa, Ontario K1A 0R6, Canada. [2]WCU (World Class University) Department of Energy Engineering, Hanyang University, Seoul 133-791, Republic of Korea. E-mail: michael.guiver@nrc-cnrc.gc.ca; ymlee@hanyang.ac.kr

istic permeability P (the product of its solubility and diffusion coefficients, S and D, respectively). The selectivity $\alpha_{x/y}$ of a faster gas x exiting versus a slower gas y is the ratio P_x/P_y. Empirical performance limits have been based on the upper-bound selectivity-permeability data (*5*), and a theoretical basis for the upper bounds showed that the best way to achieve higher performance in polymeric membranes was to increase D, S, or both for a particular gas (*6*).

Gas permeability is high in MOP membranes because of their large free volume. The first MOPs studied for use as membranes were polyacetylenes, exemplified by poly(trimethylsilyl-1-propyne) (PTMSP) (*7*). Although the gas permeability of polyacetylenes is the highest among MOPs, their chain structure is not sufficiently rigid to ensure adequate size discrimination of small gas molecules. McKeown, Budd, and co-workers reported a new class of more rigid soluble microporous polymer, termed "polymers of intrinsic microporosity" (PIMs) (*8*, *9*), which have very high permeabilities (although roughly an order of magnitude lower than PTMSP), but with gas pair selectivities in a higher and more useful range (for some gas pairs, their separation performance defines or exceeds the upper bound). PIMs derive their microporosity and high free volume from rigid ladder-like polymer chains that have sites of contortion that frustrate chain packing. However, it would be wrong to assume that these structures, which are incapable of bond rotation, are entirely rigid. In the best-known example, PIM-1, the dioxane chain-forming bridges and spirobisindane (SBI) linkages (see the figure, panel A) still flex considerably (*10*). SBI has a broad bimodal profile with two dihedral angles, and the planar dioxane has a single dihedral angle with a broad distribution.

Carta *et al*. coupled higher chain rigidity with larger interchain spacing to achieve higher permeability from the gaps in the polymer chain as well as higher selectivity. In a radical departure from typical ladder-forming polymer reactions that use tetrafunctional monomers, PIMs with extremely rigid bridged bicyclic amines were formed directly in high yield from diamine monomers linked through the formation of six covalent bonds. This bond-forming reaction was discovered accidentally by Tröger in 1887; the correct bridged structure of the resulting Tröger's base (TB) was determined much later. Only now has it been exploited as a versatile polymer chain-forming reaction.

Membrane performance gains from a PIM-SBI-TB polymer were modest relative to PIM-1 because there was insufficient overall chain rigidity. By replacing both the SBI and dioxane units in PIM-1 with more rigid ethanoanthracene (EA) and TB units (see the figure, panel B), each with single narrowly distributed dihedral angles and overall unit "pincer" angles of ~107° and ~112°, respectively, the chains are much more rigid and contorted. As a result, PIM-EA-TB exhibited higher microporosity and free volume as well as dramatic separation increases in terms of permeability and selectivity, in some cases (such as O_2 and N_2) well above the previous upper bounds for some commercially relevant gas pairs.

The successful strategy of increasing chain rigidity in other microporous membrane materials having high interchain spacing to improve performance has also been demonstrated in thermally rearranged polymers (*11*) and in spirobifluorene-containing (*12*) and tetrazole-substituted PIMs (TZ-PIMs) (*13*). Increased rigidity in TZ-PIM occurs through a hydrogen-bonded network while it simultaneously incorporates CO_2-sorbing tetrazole units for enhanced CO_2/N_2 selectivity. Highly permeable and selective membrane materials may help address challenges such as large gas-stream separations containing CO_2 (*14*).

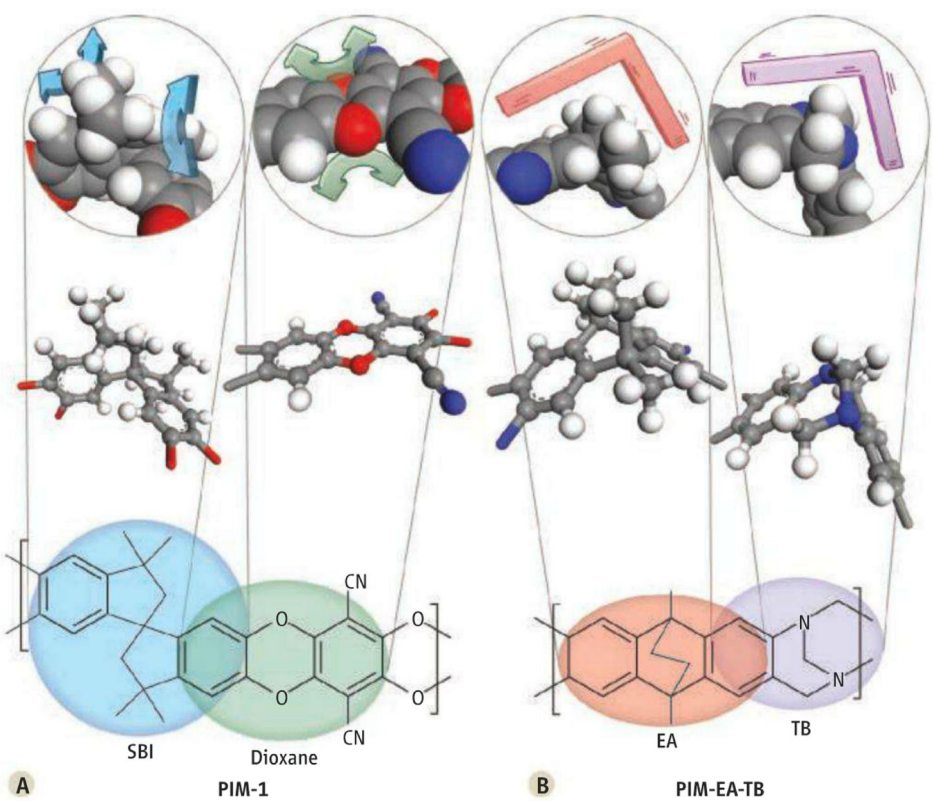

Inflexible but effective. The chains of microporous polymers that have a contorted ladder structure resist rotation, which allows them to maintain a more uniform pore structure. (**A**) The PIM-1 polymer (*9*) contains SBI and dioxane linkages, but both can bend and flex to a considerable extent. (**B**) The PIM reported by Carta *et al*., which has EA and TB units, has a more rigid architecture. This structure imparts high gas permeability in tandem with size discrimination between gases having slight differences in molecular dimensions, such as O_2 and N_2.

References and Notes

1. H. M. El-Kaderi *et al*., *Science* **316**, 268 (2007).
2. R. Dawson, A. I. Cooper, D. J. Adams, *Prog. Polym. Sci.* **37**, 530 (2012).
3. N. B. McKeown, P. M. Budd, *Macromolecules* **43**, 5163 (2010).
4. M. Carta *et al*., *Science* **339**, 303 (2013).
5. L. M. Robeson, *J. Membr. Sci.* **320**, 390 (2008).
6. B. D. Freeman, *Macromolecules* **32**, 375 (1999).
7. K. Nagai, T. Masuda, T. Nakagawa, B. D. Freeman, I. Pinnau, *Prog. Polym. Sci.* **26**, 721 (2001).
8. P. M. Budd *et al*., *Chem. Commun.* **2004**, 230 (2004).
9. P. M. Budd *et al*., *Adv. Mater.* **16**, 456 (2004).
10. M. Heuchel, D. Fritsch, P. M. Budd, N. B. McKeown, D. Hofmann, *J. Membr. Sci.* **318**, 84 (2008).
11. H. B. Park *et al*., *Science* **318**, 254 (2007).
12. C. G. Bezzu *et al*., *Adv. Mater.* **24**, 5930 (2012).
13. N. Du *et al*., *Nat. Mater.* **10**, 372 (2011).
14. N. Y. Du, H. B. Park, M. M. Dal-Cin, M. D. Guiver, *Energy Environ. Sci.* **5**, 7306 (2012).

Acknowledgement: We thank the WCU program of the government of Korea for support (grant R31-2008-000-10092-0).

10.1126/science.1232714

Neutralizing Tumor-Promoting Chronic Inflammation: A Magic Bullet?

Lisa M. Coussens,[1]* Laurence Zitvogel,[2] A. Karolina Palucka[3]

There have been substantial advances in cancer diagnostics and therapies in the past decade. Besides chemotherapeutic agents and radiation therapy, approaches now include targeting cancer cell–intrinsic mediators linked to genetic aberrations in cancer cells, in addition to cancer cell–extrinsic pathways, especially those regulating vascular programming of solid tumors. More recently, immunotherapeutics have entered the clinic largely on the basis of the recognition that several immune cell subsets, when chronically activated, foster tumor development. Here, we discuss clinical and experimental studies delineating protumorigenic roles for immune cell subsets that are players in cancer-associated inflammation. Some of these cells can be targeted to reprogram their function, leading to resolution, or at least neutralization, of cancer-promoting chronic inflammation, thereby facilitating cancer rejection.

Inflammation is a hallmark of cancer wherein diverse immune cells exert either pro- or antitumor properties (*1*, *2*) and affect therapeutic resistance (*3*). Although Virchow first hypothesized that cancer occurred at sites of chronic inflammation, postulating that immune cells release factors stimulating proliferation (of would-be tumor cells) (*4*), Coley successfully treated sarcomas with bacterial mixtures, for example, Coley's toxins, leading to tumor regression, now known to be mediated by acutely activated cytotoxic immune cells (*5*). These paradoxical properties of leukocytes owe in part to functional plasticity of myeloid- and lymphoid-lineage cells. Macrophages, for example, when exposed to type 2 cytokines like interleukin-4 (IL-4), express vascular endothelial growth factor (VEGF) and epidermal growth factor (EGF) and thereby enhance angiogenesis and mammary carcinoma metastasis, respectively (*6*). These are variably referred to as M2, alternatively activated, or type 2 macrophages. In contrast, macrophages activated through the tumor necrosis factor (TNF) receptor superfamily member CD40 become tumoricidal and deplete tumor stroma, thus enabling access by other immune cells and cytotoxic drugs and resulting in pancreatic tumor regression (*7*). Experimental and clinical data indicate that plasticity is a common property of most leukocyte subtypes and thus can be leveraged therapeutically. The immune armamentarium involved in cancer-associated inflammation encompasses a broad spectrum of immune cells and products. Critiqued below are the laboratory- and clinical-based studies providing insight into these issues and identifying potential targets for therapeutic intervention.

Tumor-Promoting Inflammation

The majority of malignant tumors (95%) have been linked to somatic (as opposed to germline) mutations in genes encoding proteins regulating critical aspects of cell cycle progression and/or death (*8*). Epidemiological studies have provided etiologic insight into many of these mutations, thus revealing that 30% of human malignancies are linked to tobacco use, 35% to diet, 14 to 20% to obesity, 18% to infectious agents, and 7% to radiation or environmental pollutants (*9*). Besides directly "initiating" the formation of cancerous cells, these factors might also act as tumor promoters by triggering acute activation of immune effector programs leading to infiltration of "initiated" tissues by immune cells (*10*, *11*). When sustained over long periods without resolution, these tissue assaults become chronic and, by various mechanisms, provide the underpinnings for tumor development (*12*, *13*). Adding fuel to the fire, age-related cellular senescence can also act as a tumor promoter by initiating several inflammatory programs (*14*), possibly explaining the higher incidence of malignancy in aged populations.

Nevertheless, several questions arise as to which subsets of immune cells directly or indirectly promote malignancy, which of these can be reprogrammed based on their functional plasticity to instead combat cancer, and to what degree these properties are generic or tissue-specific. Although most adult solid tumors (carcinomas most notably) contain infiltrates of diverse leukocyte subsets (*15*) (Fig. 1), flow cytometric analysis of solid tumors with distinct genetic anomalies (breast, lung, mesothelioma) indicates that leukocyte complexity varies depending on the tissue or organ location and stage of malignancy, suggesting that immune-based therapies will need to reflect these nuances and be more personalized.

Players and Mechanisms

Myeloid cells. Under homeostatic conditions, leukocytes are charged with maintaining tissue health. Innate immune cells, including macrophages, granulocytes, mast cells, dendritic cells (DCs), innate lymphocytes, and natural killer (NK) cells, represent the first line of defense against pathogens and foreign agents. Perturbed tissue homeostasis, such as during an infection, activates tissue-resident macrophages and mast cells to secrete matrix-remodeling proteins, cytokines and chemokines, that collectively activate local stromal cells (fibroblasts, adipocytes, vascular cells, etc.) to recruit circulating leukocytes into damaged tissue (acute inflammation), leading to elimination of pathogenic agents (tissue damage) in situ. Response to a pathogen also involves DCs, a rare cell type that is one of the key cellular sensors of microbes. DCs are bone marrow–derived cells seeded in all tissues and are thereby linked to their environment through a wealth of molecular sensors that allow them to capture invading microbes (as well as tumor antigens) and to transmit the resulting information to lymphocytes; thus, DCs provide an essential link between the innate and adaptive immune responses (*16*), a critical step because T cells cannot recognize unprocessed antigens. Upon recognition of a foreign antigen, $CD4^+$ and $CD8^+$ T lymphocytes and B lymphocytes undergo clonal expansion and mount "adaptive" responses specific to the foreign agent. When compared with other antigen-presenting cells, such as macrophages, DCs are extremely efficient; very low numbers of DCs can elicit naïve T cells to respond. Once foreign agents have been eliminated (in the context of acute tissue damage), inflammation resolves and tissue homeostasis is restored.

In tumors, these well-orchestrated series of events fail to resolve and therefore lead to chronic inflammation of the "damaged" (neoplastic) tissue. Chronically activated leukocytes supply direct and indirect mitogenic growth factors that stimulate proliferation of cancer and stromal cells (*12*). Notable examples include EGF, transforming growth factor–β (TGFβ), TNFα, and fibroblast growth factors, as well as various ILs, chemokines, histamine, and heparins (*12*). In addition, several leukocyte subsets, predominantly macrophages, granulocytes, monocytes, and mast cells, secrete diverse classes of proteolytic enzymes that modify the structure and function of extracellular matrix (ECM), leading to uncaging of ECM-sequestered mitogenic agents (*17*). Although these are typical processes of tissue repair (*15*, *18*), their chronic presence provides a survival advantage to evolving cancer cells by maintaining proliferative signaling; blunting cell death in response to matrix detachment; activation and maintenance of an-

[1]Department of Cell and Developmental Biology, Knight Cancer Institute, Oregon Health and Science University, 3181 SW Sam Jackson Park Road, Mail Code L215, Room 5508, Richard Jones Hall, Portland, OR 97239–3098, USA. [2]INSERM U1015, CICBT507, University Paris XI, Institut Gustave Roussy, 114 rue Edouard Vaillant, F-94805 Villejuif, Paris, France. [3]Baylor Institute for Immunology Research (BIIR), 3434 Live Oak Avenue, Dallas, TX 75204, USA, and Department of Oncological Sciences, Mount Sinai School of Medicine, New York, NY 10029, USA.

*To whom correspondence should be addressed. E-mail: coussenl@ohsu.edu

giogenesis; facilitating cancer cell egress from primary tumors; and impairing antitumor cytotoxic cell–mediated killing of "damaged" (cancer) cells (*2*). Thus, chronically activated myeloid cells in neoplastic tissues support many of the hallmarks of cancer (*2*).

T cells. $CD4^+$ T helper cells are key regulators of inflammatory processes in cancers. An expanding list of T helper (T_H) subsets (T_H1, 2, 9, 10, 17, and 22), specialized for promoting particular types of inflammation, function through their secretion of a restricted set of cytokines enabling immune responses (*19*), often tailored to the specific pathogen encountered. All of these distinct $CD4^+$ T cell types can contribute to tumorigenesis in various ways, depending on context. For example, regulatory T cells (T_{regs}), an immunosuppressive subset of T_H cells, inhibit cytotoxic functions of $CD8^+$ T cells, thereby preventing tumor rejection (*20*). Although in general favoring tumor rejection, T_H1 cells might contribute to tumor escape via secretion of interferon (IFN)–γ, which triggers expression of programmed cell death ligand (PDL)–1 that provides off signals to cytotoxic T cells (*21*). Furthermore, selective evolutionary pressure by IFN-γ may lead to tumor editing and selection of resistant clones, thereby facilitating tumor development (*22*). Such plasticity of outcomes is even further exemplified by the more recently identified T_H17 cells (*23*) that exert either pro- or antitumor activity depending on the tissue environment in which they reside [reviewed in (*24*)]. Their major protumor effects are linked to angiogenesis, recruitment of myeloid cells, and in particular neutrophils that secrete elastase, a protumor mediator (*24*). However, IL-17 produced by T_H17 cells can synergize with IFN-γ to induce secretion of the chemokines CXCL9 and CXCL10 by tumor cells, which in turn attract cytotoxic T cells (*24*). Such synergistic effects of IL-17 and IFN-γ could possibly be exploited for cancer therapy.

T_H2 cells are well recognized for their tumor-promoting capabilities. Breast and pancreatic cancer, for example, are heavily infiltrated by T_H2 cells (*25*) that coexpress IL-4/IL-13 and TNFα, but lack IL-10 secretion (*26*). These T_H2 cells are "driven" by OX40 ligand (L)–expressing DCs in response to cancer-derived thymic stromal lymphopoietin (TSLP) (*27*) (Fig. 2). T_H2 cells accelerate growth of breast carcinomas in humanized mouse models through production of IL-13 (*25*). In genetically engineered mouse models of mammary carcinogenesis, T_H2 cells accelerate development of pulmonary metastasis via IL-4 activation of macrophages that thereby become type 2–polarized and provide survival signals to neoplastic epithelia and chemotherapy resistance (*28*, *29*).

In addition, IL-13 produced by NK T cells induces myeloid cells to make TGFβ, which ultimately fosters T_{reg} cell development and inhibits cytotoxic T cells (*30*). Autocrine IL-13 is important in the pathophysiology of Hodgkin's disease (*31*), where it stimulates Hodgkin and Reed-Sternberg cells growth. Similar to Hodgkin's cells, breast cancer cells express phospho–signal transducer and activator of transcription 6 (STAT6) that is activated downstream of IL-13 receptor–dependent signaling (*25*), which can result in up-regulation of anti-apoptotic pathways in cancer cells that may be involved in resistance to cytotoxic $CD8^+$ T cells and cytotoxic drugs (*2*, *32*).

Clinically, the T_H2 signature in breast cancer (*33*) and the expression of the T_H2 master regulator transcription factor GATA-3 is increased in metastatic sentinel lymph nodes in breast cancer, and it is associated with rapid disease progression and diminished overall survival in pancreatic cancer (*34*). Furthermore, the pathogenic TSLP/IL-13 pathway has also been detected in the context of *Helicobacter pylori* infection that leads to chronic gastritis, the causative factor in gastric cancer (*35*). Thus, interference with this inflammatory protumor TSLP-OX40L–IL-13 axis (Fig. 2) can be considered as a novel investigational therapeutic approach for several cancer types. Nevertheless, likely owing to tissue specificity, blockade of TSLP in squamous neoplasms instead accelerates malignancy by in-

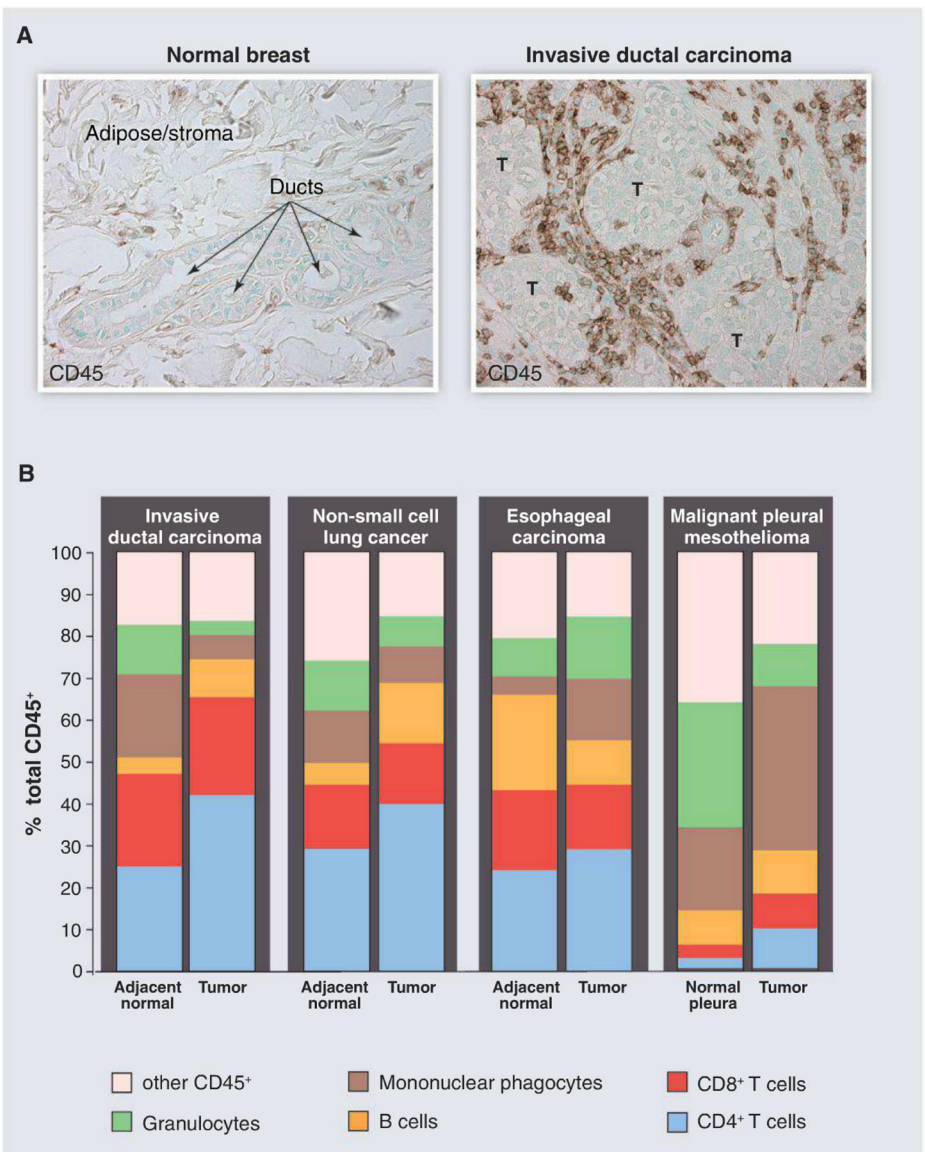

Fig. 1. Leukocyte infiltration and complexity in human cancers. (**A**) $CD45^+$ leukocytes (brown staining) in normal human breast tissue compared with invasive ductal carcinoma. These images illustrate the substantial infiltration of leukocytes into neoplastic tissue compared with "normal" tissue counterparts. T indicates tumor nests or tumor cell clusters. (**B**) Immune cell complexity of adjacent normal tissues (or normal pleura) and the indicated tumors as revealed by polychromatic flow cytometry and expressed as a percentage of $CD45^+$ cells. Colors indicate major categories of select immune cell lineages. [Images and data have not been published previously and are courtesy of the Coussens laboratory]

voking protumorigenic activities of infiltrating monocytes that in turn blunt antitumor cytotoxic $CD8^+$ T cells (*36*, *37*).

Expression of immune checkpoint molecules such as PD-1 (a T cell receptor that mediates T cell inhibition) and its ligands, PD-L1 and PD-L2, forms a major receptor/ligand inhibitory pathway regulating T cell responses. Expression of PD-L1 on surfaces of tumor cells and tumor-infiltrating myeloid cells provides an off signal to PD-1–expressing T cells and thus enables tumor cells to escape immunosurveillance. Under persistent antigen exposure (such as in chronic infections or in tumor microenvironments), both $CD4^+$ and $CD8^+$ T cells up-regulate PD-1 expression, contributing to T cell exhaustion (*38*). Blocking this pathway, for example, during chronic viral infection, reinvigorates virus-specific $CD8^+$ T cell responses and results in enhanced T cell effector responses and viral clearance (*39*). However, other studies have revealed that conventional chemotherapy paradoxically increases the number of macrophages expressing PD-L1, thereby inhibiting $CD8^+$ T cells and increasing the risk of treatment failure (*40*).

B cells. As the sole producers of immunoglobulins (Igs), B cells are critical for humoral immunity and also influence other leukocyte subtypes. For example, B cell–derived paracrine factors can be causative and/or potentiate disease by sustaining chronic inflammation during autoimmunity (*41*). The role of B cells in cancer is under intense examination. In the skin, squamous carcinogenesis is limited in the absence of B cells (*42*–*44*). Two mechanisms appear to be involved in B cell–dependent skin carcinogenesis: (i) When autoantibody IgG is deposited into neoplastic parenchyma via leaky blood vessels, ligation of immune complex/Fcγ receptors on mast cells and macrophages fosters pro-angiogenic and immunosuppressive gene expression programs (*42*, *43*); (ii) B cell secretion of IL-10 and TNFα activates protumorigenic myeloid cells that also foster cancer progression (*44*). Whether the IL-10–expressing B cells represent regulatory B cells (B_{regs}/B10) remains to be determined but is an important point to consider, because B_{regs} are resistant to αCD20 B cell–depleting therapy (*45*) and suppress the efficacy of CD20 immunotherapy (*46*). During prostate carcinogenesis, the Wnt family member wingless-type MMTV integration site family member 16B (WNT16B) is up-regulated by nuclear factor κ light polypeptide gene enhancer (NF-κB) in B cells after DNA damage and, via a paracrine mechanism, activates the canonical Wnt program in evolving tumor cells, the result of which is chemoresistance in combination with enhanced tumor cell survival and disease progression (*47*). In addition, B cell–derived lymphotoxin β promotes prostate metastasis in castration-resistant disease by stimulating inhibitor of NF-κB (IκB) kinase α (IKKα) and STAT3 activity in malignant cells, thus provoking androgen refractory regrowth and metastasis (*48*). Interestingly, B cells were found to be without functional significance during mammary carcinogenesis (*49*), further illustrating tissue specificity and perhaps oncogene specificity in the regulation of leukocyte protumorigenic activities. Taken together, immune cell functions vary by tissue and tumor type (Fig. 1), indicating that a one-size-fits-all approach will likely not be effective in immune-based therapeutic strategies.

Therapeutic Targets

Effectively counteracting or neutralizing tumor-promoting inflammation will necessitate simultaneous reprogramming or quelling of multiple immune-response programs activated in cancers. Alternatively, targeting the master regulators of adaptive immunity, DCs, and master effectors of tissue damage, macrophages, will allow a cascade of events favoring cancer rejection (Fig. 2). On the basis of available data, the pathways that present attractive targets today include (i) inhibition or sequestration of cytokines or chemokines, especially those that activate the STAT3/NF-κB pathway; (ii) depletion or reprogramming of pro-cancer tumor-associated immune cells; and (iii) harnessing cytotoxic T cells by either neutralization of T_{reg} cells, blockade of the PD-1/PD-L pathway, or inhibition of myeloid-based immunosuppressive molecules (Fig. 3). Combinations of these strategies to simultaneously favor (immunogenic) tumor cell death with conventional cytotoxic approaches may achieve a state akin to that present during acute inflammation during wound healing, thereby leading to activation of scavenging immune effectors and increased cancer cell death (Fig. 4). How these individual strategies, based on tissue, oncogene, or organ specificity and/or complexity of the immune infiltrate present, are being tailored is discussed below.

Selective inhibition or sequestration of cancer inflammation–induced cytokines and chemokines. High serum concentrations of proinflammatory

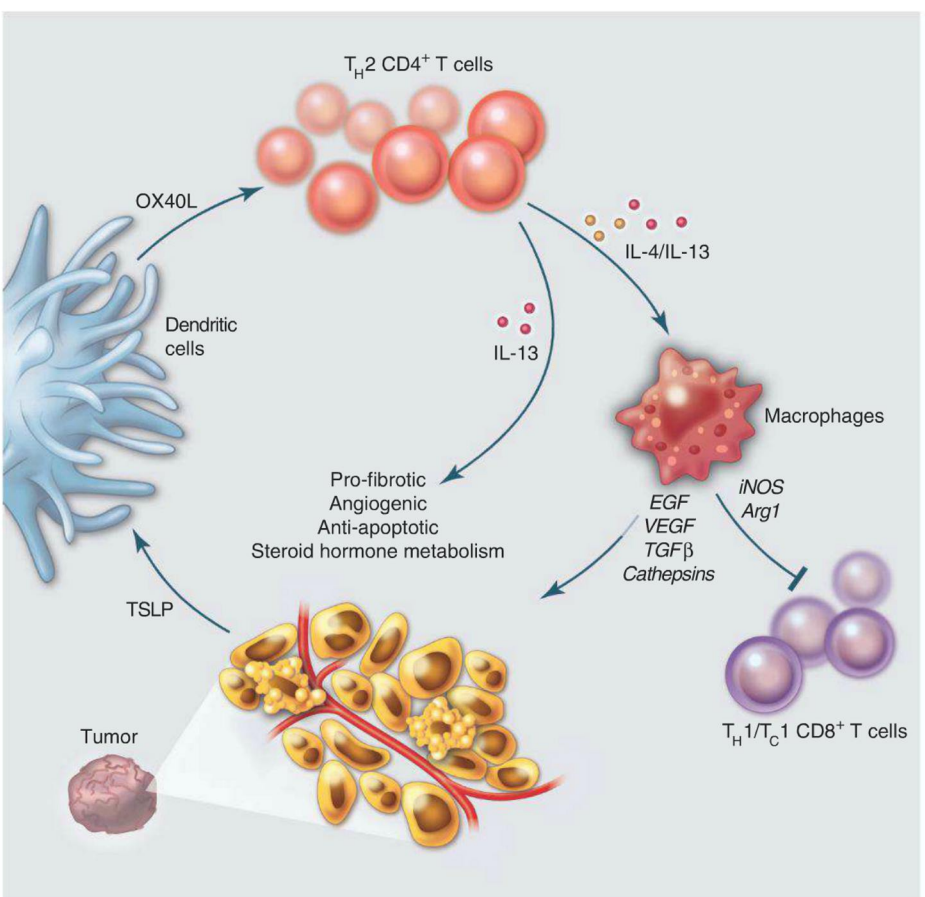

Fig. 2. Induction of T_H2-type immune responses downstream of TSLP. DCs in tumor microenvironments are exposed to cancer-derived factors—for example, TSLP—that skew their maturation toward T_H2-type inflammation, including their expression of OX40L. In this environment, responding T_H2 cells ($CD4^+$ T cells) secreting IL-4 and IL-13 promote tumor development either directly or indirectly via macrophages. Direct effects include triggering anti-apoptotic pathways and steroid metabolism in epithelial cancer cells, as well as promoting stromal fibroblast proliferation and differentiation. Indirect effects include triggering secretion of growth (EGF) and pro-angiogenic (VEGF) factors by tumor-infiltrating macrophages that also express inducible nitric oxide synthase (iNOS) and arginase (*73*) and thereby blunt $CD8^+$ T cell proliferation.

TNFα, IL-6, or inflammasome-related IL-1β/IL-18 correlate with advanced malignancies and are associated with reduced survival (*50*, *51*). Several anticytokine agents are already in use for treatment of cancer (*51*). For example, in a phase II trial of a chimeric antibody against IL-6 in ovarian cancer, those patients exhibiting a prolonged stabilization of disease showed significant declines in plasma levels of the chemokines promoting immune cell recruitment (CCL2 and CXCL12), as well as angiogenesis (VEGF) (*52*). Blockade of TNFα represents another pathway; however, chronic administration of TNF inhibitors in patients suffering from rheumatoid arthritis may increase the risk of developing lymphoma (*53*, *54*). Whether inhibiting the membrane-bound or the soluble form of TNFα makes a difference is currently under investigation.

Blockade of CCL2 may also represent a viable therapeutic strategy. In mammary cancer models, depletion of tumor cell–derived CCL2 inhibits metastatic seeding (*55*). In prostate carcinogenesis, CCL2 protects malignant cells from chemotherapy-induced cytotoxicity, and suppression of CCL2 leads to enhanced responses to taxane-based chemotherapy (*56*). Similarly, interrupting the CXCR4/CXCL12 chemokine axis can be used to sensitize resistant tumor cells to chemotherapy or radiotherapy and potentially inhibit vascularization and tumor cell spreading. This response is in part related to bone marrow–derived TIE-2–positive macrophages that are pro-angiogenic and specifically attracted to irradiated tumors in a CXCL12-dependent fashion and thereby contribute to tumor regrowth post-therapy (*57*). AMD3100 (plerixafor), approved by the Food and Drug Administration (FDA) for hematopoietic progenitor cell mobilization, reduces TIE-2–positive macrophage recruitment (*58*); the CXCL12 peptide analog was assigned an orphan drug status by the FDA for treatment of osteosarcoma.

Depletion or reprogramming of tumor-associated immune cells. We have already discussed the master regulatory role of macrophages in tumor initiation and maintenance. Consequently, blockade of macrophage colony-stimulating factor 1 or its receptor (CSF1/CSF1R) rapidly diminishes macrophage presence and promotes T_H1 responses in late-stage mammary adenocarcinomas (*59*). CSF-1–related gene signatures (*60*) and the presence of proliferating macrophages predict risk of recurrence (*61*), as well as response to chemotherapy in breast cancer (*59*). Antagonist αIL-4 therapeutic antibodies reprogram tumor-associated type 2 macrophages, monocytes, and other T_H2 cells toward T_H1 phenotypes in mammary cancer (*49*). Reprogramming macrophages can also be achieved by administration of agonistic αCD40 therapeutic antibodies as already discussed. Lastly, as another example of therapeutic interference with myeloid cells, treatment of pancreatic cancers in mice with granulocyte-macrophage colony-stimulating factor (GM-CSF) antagonists blocks monocyte recruitment and thereby favors $CD8^+$ T cell infiltrates that slow tumor development (*62*, *63*).

Rituximab, a chimeric monoclonal antibody against CD20 that is predominantly expressed on the surface of B cells, leads to B cell depletion (*64*) and thus could be considered in solid tumors. Indeed, a pilot clinical study in advanced colon cancer patients treated with rituximab reported encouraging tumor regressions [reviewed in (*65*)].

Immune cells can also be targeted and manipulated by using innate receptors involved in pathogen responses or pathogens themselves. For example, intravesical instillation of bacillus Calmette-Guérin (BCG) is effective at eliciting actute inflammation and successful tumor immunity in patients with nonmuscle invasive bladder cancer, leading to 50 to 70% clinical response (*66*), and was FDA-approved in 1990. Other TLR agonists (synthetic imidazoquinoline, imiquimod, or resiquimod) approved for treatment of genital warts and superficial basal cell carcinoma could also be envisioned to induce immune-mediated rejection of skin metastases in breast and melanoma patients (*67*, *68*).

Harnessing cytotoxic T cells. Mobilizing effector/memory antitumor-specific $CD4^+$ and $CD8^+$ T

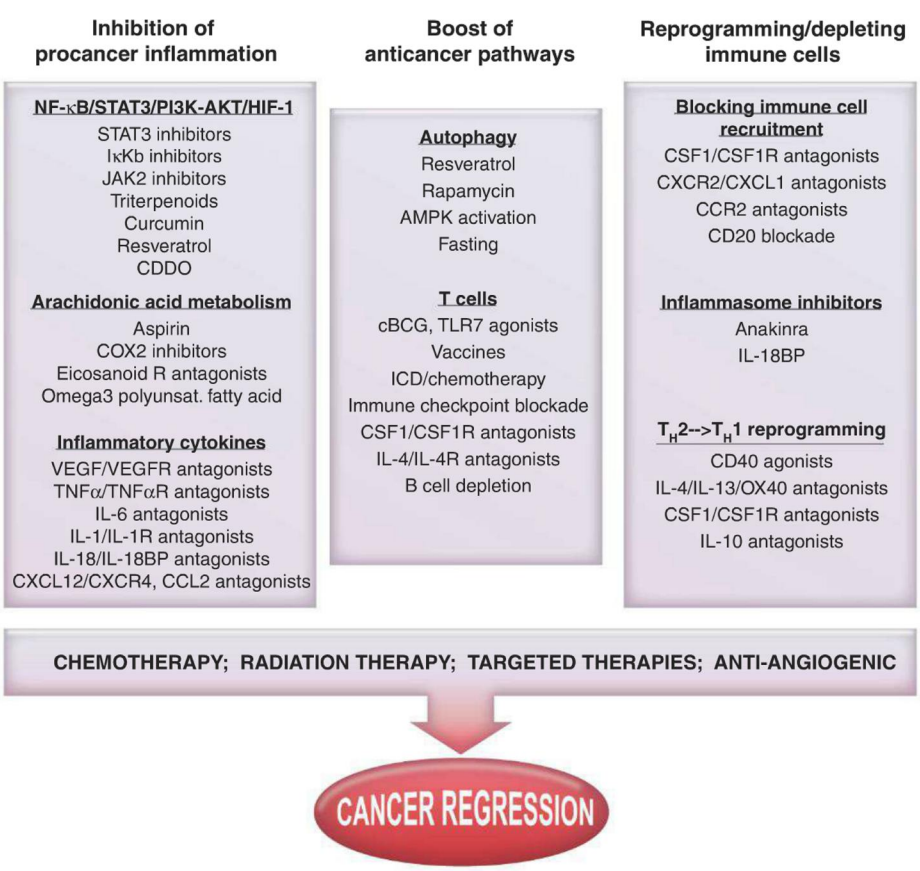

Fig. 3. Therapeutic strategies against cancer-induced chronic inflammation. Inhibiting tumor cell–intrinsic proinflammatory functions [such as blunting NF-κB/STAT3/phosphatidylinositol 3-kinase (PI3K)–Akt pathways or downstream effectors]. Moreover, turning lymphocytes into effector T_H1/T_C1 cells necessitates effective reprogramming of type 2 macrophages or immunosuppressive DCs by a concerted action of pattern recognition receptors, the inflammasome platform, or CD40 costimulation, as well as neutralization of immune checkpoint ligand/receptor interaction. In parallel, reducing the accumulation or migration of suppressive myeloid cells in primary sites or distant niches while promoting cytoreduction/debulking with irradiation, cytotoxic compounds, or antiangiogenic molecules may synergistically gear the host/tumor imbalance toward durable tumor regression. HIF-1, hypoxia-inducible factor 1; AMPK, adenosine monophosphate–activated protein kinase; JAK2, Janus kinase 2; CDDO, 2-cyano-3,12-dioxooleana-1,9(11)-dien-28-oic acid; TLR7, Toll-like receptor 7; COX2, cyclooxygenase; ICD, immunogenic cell death.

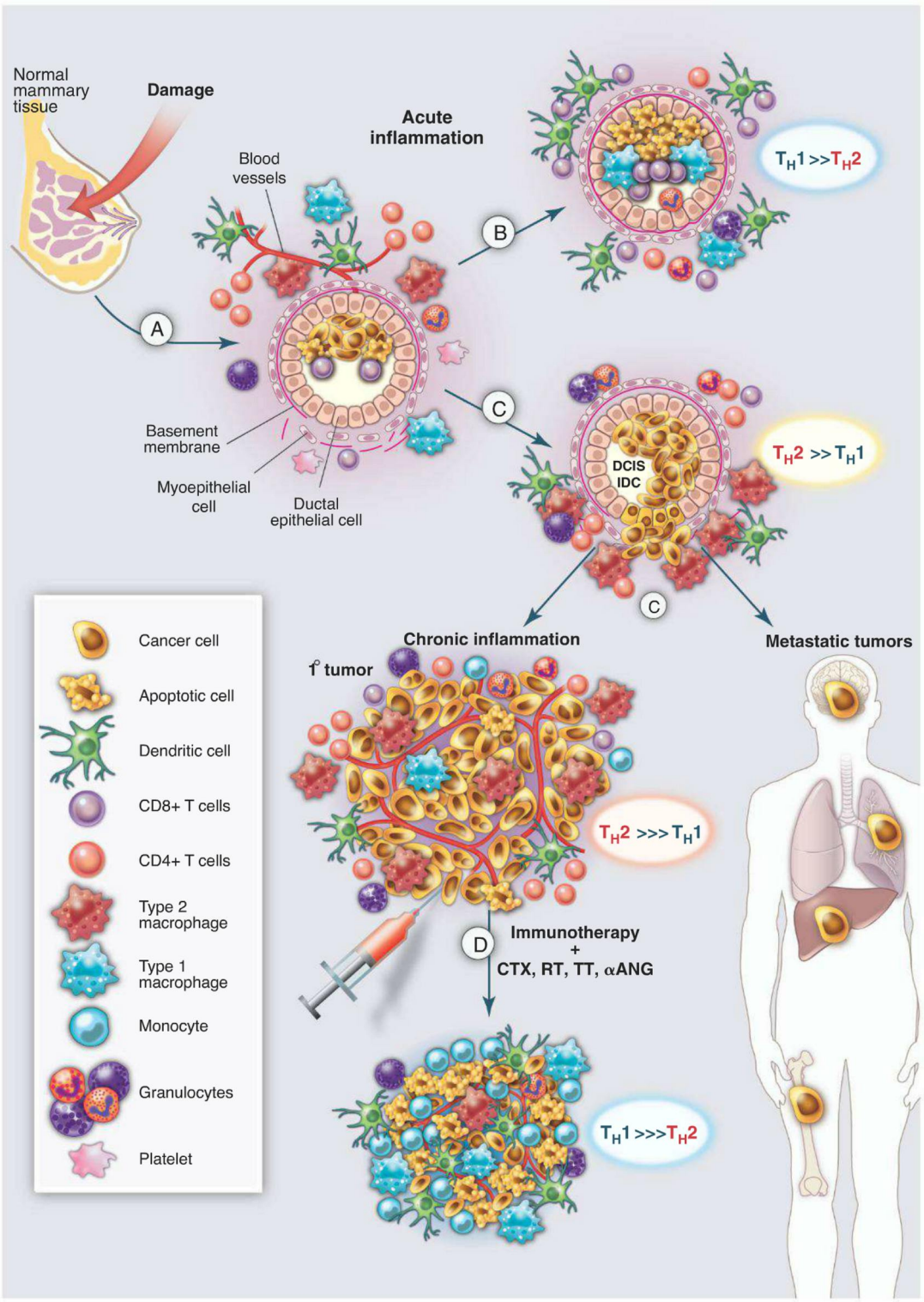

Fig. 4. Targeting tumor-promoting chronic inflammation as a therapeutic strategy. (**A**) Tissue damage results in activation of hard-wired pathways (angiogenic and immune) embedded in all tissues to facilitate healing and homeostasis. (**B**) Type 1 immune responses, aided by T_H1 cells, eradicate damaged cells to aid the healing prcess. (**C**) In tissues harboring initiated cells, neoplastic epithelial cells secrete factors such as TSLP, GM-CSF, CSF-1, and TNFα, thereby inducing recruitment of leukocytes that become T_H2-polarized and resulting in chronic activation of angiogenic and tissue remodeling programs, enhanced survival signaling to aid proliferation and blunt cell death, and generation of an immunosuppressive environment that fosters primary tumor development and aids in metastatic disseminations. (**D**) Effectively counteracting or neutralizing tumor-promoting chronic inflammation may be achieved by resetting or reprogramming the prominent T_H2-based programs activated in cancer; this may result in simultaneously favoring (immunogenic) tumor cell death, where T_H1-based immunity emerges akin to that present during acute inflammation during wound healing, thus enabling a cascade of events favoring cancer rejection, perhaps as monotherapy but more likely in combination with chemotherapy (CTX), radiotherapy (RT), targeted therapy (TT), or antiangiogenic modalities (αANG). DCIS, ductal carcinoma in situ; IDC, invasive ductal carcinoma.

cells producing high levels of IFN-γ (called T_H1 and T_C1, respectively) may, at least in part, reverse immunosuppression mediated by the tumor microenvironment. IFN-γ has pleiotropic effects on the tumor microenvironment, such as antiangiogenic activities, quelling protumorigenic properties of macrophages while also enhancing their tumoricidal properties, and enhanced processing and presentation of tumor antigens to T lymphocytes. Hence, therapeutics bolstering T_H1 programming may provide a survival advantage (Fig. 4). Vaccination—that is, the provision of an antigen together with an adjuvant to elicit therapeutic T cells in vivo—combined with modulation of the tumor microenvironment represents a very promising and powerful therapeutic strategy to boost antitumor T cell immunity as well. However achieved, the T cells elicited by a vaccine, adoptively transferred, or unleashed by modulation of the tumor microenvironment will likely require additional help provided by interference with off signals able to block their antitumor function. In particular, phase I clinical trials in patients indicate that blocking the PD-1 pathway is a promising strategy for achieving immunological control of human cancers, including lung cancer (*40*, *69*). This is somewhat

analogous to the improved survival now documented in metastatic melanoma patients treated with an antibody against the immunoregulatory molecule CTLA-4 (*70*) (e.g., ipiluminab), recently approved by the FDA. Given that PD-1 ligands are expressed in many tumor microenvironments, targeting the ligands, as opposed to their receptors, has the potential to be more effective and less toxic than current therapies targeting PD-1 and/or CTLA-4.

Concluding Remarks

Inflammation represents a link between intrinsic (oncogenes, tumor suppressors, and genome stability genes) and extrinsic (immune and stromal components) factors contributing to tumor development. This knowledge offers new and novel candidate targets for therapeutic intervention, in combination with more conventional therapeutic approaches such as chemotherapy, radiotherapy, and targeted therapy. Therapeutic manipulation of chronic inflammation in tumors is likely to enhance the clinical efficacy of therapeutic vaccination as well as adoptive T cell transfer, thus turning the chronic procancer inflammatory microenvironment into an anticancer microenvironment that is more likely to also liberate and activate existing anticancer effector T cells. Given the functional relevance of immune networking in tumors, it is imperative to incorporate immunometrics such as "the immunoscore" into traditional classification schemes to provide new prognostic and/or predictive tools to clinical practice (*71*, *72*). A better identification of tissue- and/or tumor-specific inflammatory mechanisms (obtained through next-generation sequencing, metabolomics, and epigenetics) will allow us to direct the clinical management of cancer toward a more personalized medicine. A magic bullet? Yes, but not as stand-alone monotherapy. Rather, inflammation is another piece of the puzzle constituting hallmarks of cancer, the targeting of which can bring us closer to successful therapy for this dreaded and deadly disease.

References and Notes

1. D. Hanahan, R. A. Weinberg, *Cell* **144**, 646 (2011).
2. D. Hanahan, L. M. Coussens, *Cancer Cell* **21**, 309 (2012).
3. S. I. Grivennikov, F. R. Greten, M. Karin, *Cell* **140**, 883 (2010).
4. F. Balkwill, A. Mantovani, *Lancet* **357**, 539 (2001).
5. J. Bickels, Y. Kollender, O. Merinsky, I. Meller, *Isr. Med. Assoc. J.* **4**, 471 (2002).
6. B. Ruffell, N. I. Affara, L. M. Coussens, *Trends Immunol.* **33**, 119 (2012).
7. G. L. Beatty *et al.*, *Science* **331**, 1612 (2011).
8. R. Wooster, K. E. Bachman, *Curr. Opin. Genet. Dev.* **20**, 336 (2010).
9. A. Jemal, R. Siegel, J. Xu, E. Ward, *CA Cancer J. Clin.* **60**, 277 (2010).
10. E. K. Wei, K. Y. Wolin, G. A. Colditz, *J. Clin. Oncol.* **28**, 4052 (2010).
11. M. J. Thun, S. J. Henley, T. Gansler, *Novartis Found. Symp.* **256**, 6 (2004).
12. F. Balkwill, K. A. Charles, A. Mantovani, *Cancer Cell* **7**, 211 (2005).
13. L. M. Coussens, Z. Werb, *Nature* **420**, 860 (2002).
14. A. Freund, A. V. Orjalo, P. Y. Desprez, J. Campisi, *Trends Mol. Med.* **16**, 238 (2010).
15. T. D. Tlsty, L. M. Coussens, *Annu. Rev. Pathol.* **1**, 119 (2006).
16. R. M. Steinman, J. Banchereau, *Nature* **449**, 419 (2007).
17. P. Lu, K. Takai, V. M. Weaver, Z. Werb, *Cold Spring Harb. Perspect. Biol.* **3**, a005058 (2011).
18. H. F. Dvorak, *N. Engl. J. Med.* **315**, 1650 (1986).
19. J. A. Bluestone, C. R. Mackay, J. J. O'Shea, B. Stockinger, *Nat. Rev. Immunol.* **9**, 811 (2009).
20. C. Tanchot *et al.*, *Cancer Microenviron.*, published online 27 October 2012 (10.1007/s12307-012-0122-y).
21. A. H. Sharpe, E. J. Wherry, R. Ahmed, G. J. Freeman, *Nat. Immunol.* **8**, 239 (2007).
22. H. Matsushita *et al.*, *Nature* **482**, 400 (2012).
23. C. Dong, *Nat. Rev. Immunol.* **8**, 337 (2008).
24. S. Wei, E. Zhao, I. Kryczek, W. Zou, *Oncoimmunology* **1**, 516 (2012).
25. C. Aspord *et al.*, *J. Exp. Med.* **204**, 1037 (2007).
26. Y. J. Liu *et al.*, *Annu. Rev. Immunol.* **25**, 193 (2007).
27. A. Pedroza-Gonzalez *et al.*, *J. Exp. Med.* **208**, 479 (2011).
28. V. Gocheva *et al.*, *Genes Dev.* **24**, 241 (2010).
29. T. Shree *et al.*, *Genes Dev.* **25**, 2465 (2011).
30. M. Terabe, J. M. Park, J. A. Berzofsky, *Cancer Immunol. Immunother.* **53**, 79 (2004).
31. B. F. Skinnider, T. W. Mak, *Blood* **99**, 4283 (2002).
32. W. J. Zhang *et al.*, *Cytokine* **42**, 39 (2008).
33. V. N. Kristensen *et al.*, *Proc. Natl. Acad. Sci. U.S.A.* **109**, 2802 (2012).
34. L. De Monte *et al.*, *J. Exp. Med.* **208**, 469 (2011).
35. M. Kido *et al.*, *Infect. Immun.* **78**, 108 (2010).
36. M. Di Piazza, C. S. Nowell, U. Koch, A. D. Durham, F. Radtke, *Cancer Cell* **22**, 479 (2012).
37. S. Demehri *et al.*, *Cancer Cell* **22**, 494 (2012).
38. S. Wang, L. Chen, *Curr. Top. Microbiol. Immunol.* **344**, 245 (2011).
39. P. Sakthivel, M. Gereke, D. Bruder, *Rev. Recent Clin. Trials* **7**, 10 (2012).
40. A. Hasan, H. Ghebeh, C. Lehe, R. Ahmad, S. Dermime, *Expert Opin. Ther. Targets* **15**, 1211 (2011).
41. S. Pillai, H. Mattoo, A. Cariappa, *Curr. Opin. Immunol.* **23**, 721 (2011).
42. K. E. de Visser, L. V. Korets, L. M. Coussens, *Cancer Cell* **7**, 411 (2005).
43. P. Andreu *et al.*, *Cancer Cell* **17**, 121 (2010).
44. T. Schioppa *et al.*, *Proc. Natl. Acad. Sci. U.S.A.* **108**, 10662 (2011).
45. K. M. Haas, J. C. Poe, D. A. Steeber, T. F. Tedder, *Immunity* **23**, 7 (2005).
46. M. Horikawa, V. Minard-Colin, T. Matsushita, T. F. Tedder, *J. Clin. Invest.* **121**, 4268 (2011).
47. Y. Sun *et al.*, *Nat. Med.* **18**, 1359 (2012).
48. M. Ammirante, J. L. Luo, S. Grivennikov, S. Nedospasov, M. Karin, *Nature* **464**, 302 (2010).
49. D. G. DeNardo *et al.*, *Cancer Cell* **16**, 91 (2009).
50. C. A. Dinarello, *Cancer Metastasis Rev.* **29**, 317 (2010).
51. F. R. Balkwill, A. Mantovani, *Semin. Cancer Biol.* **22**, 33 (2012).
52. M. S. Anglesio *et al.*, *Clin. Cancer Res.* **17**, 2538 (2011).
53. P. Geborek *et al.*, *Ann. Rheum. Dis.* **64**, 699 (2005).
54. T. Bongartz *et al.*, *JAMA* **295**, 2275 (2006).
55. B. Z. Qian *et al.*, *Nature* **475**, 222 (2011).
56. D. Z. Qian *et al.*, *Prostate* **70**, 433 (2010).
57. S. V. Kozin *et al.*, *Cancer Res.* **70**, 5679 (2010).
58. A. F. Welford *et al.*, *J. Clin. Invest.* **121**, 1969 (2011).
59. D. G. DeNardo *et al.*, *Cancer Discov* **1**, 54 (2011).
60. A. H. Beck *et al.*, *Clin. Cancer Res.* **15**, 778 (2009).
61. M. J. Campbell *et al.*, *Breast Cancer Res. Treat.* **128**, 703 (2011).
62. Y. Pylayeva-Gupta, K. E. Lee, C. H. Hajdu, G. Miller, D. Bar-Sagi, *Cancer Cell* **21**, 836 (2012).
63. L. J. Bayne *et al.*, *Cancer Cell* **21**, 822 (2012).
64. A. Kessel, I. Rosner, E. Toubi, *Clin. Rev. Allergy Immunol.* **34**, 74 (2008).
65. T. T. Tan, L. M. Coussens, *Curr. Opin. Immunol.* **19**, 209 (2007).
66. B. Zbar, T. Tanaka, *Science* **172**, 271 (1971).
67. S. Adams *et al.*, *Clin. Cancer Res.* **18**, 6748 (2012).
68. G. Heber *et al.*, *J. Dtsch. Dermatol. Ges.* **7**, 534 (2009).
69. J. R. Brahmer *et al.*, *J. Clin. Oncol.* **28**, 3167 (2010).
70. F. S. Hodi *et al.*, *N. Engl. J. Med.* **363**, 711 (2010).
71. J. Galon *et al.*, *J. Transl. Med.* **10**, 205 (2012).
72. J. Galon *et al.*, *J. Transl. Med.* **10**, 1 (2012).
73. A. L. Doedens *et al.*, *Cancer Res.* **70**, 7465 (2010).

Acknowledgments: The authors thank members of their laboratories for critical discussions on content and specifically A. Gunderson and B. Ruffell for critical reading of the manuscript. L.M.C. acknowledges support from the NIH/National Cancer Institute (NCI), a Department of Defense Breast Cancer Research Program Era of Hope Scholar Scholar Expansion Award, Susan B. Komen Foundation, and the Breast Cancer Research Foundation. L.Z. is supported by LIGUE Française Contre le Cancer, Fondation pour la Recherche Médicale, Institut National du Cancer (SIRIC), and Fondation Gustave Roussy. A.K.P. acknowledges the support from the BIIR and Baylor University Medical Center foundations, Susan B. Komen Foundation, Cancer Prevention Research Institute of Texas, and NIH/NCI.

10.1126/science.1232227

Evidence for Water Ice Near Mercury's North Pole from MESSENGER Neutron Spectrometer Measurements

David J. Lawrence,[1]* William C. Feldman,[2] John O. Goldsten,[1] Sylvestre Maurice,[3] Patrick N. Peplowski,[1] Brian J. Anderson,[1] David Bazell,[1] Ralph L. McNutt Jr.,[1] Larry R. Nittler,[4] Thomas H. Prettyman,[2] Douglas J. Rodgers,[1] Sean C. Solomon,[4,5] Shoshana Z. Weider[4]

Measurements by the Neutron Spectrometer on the MErcury Surface, Space ENvironment, GEochemistry, and Ranging (MESSENGER) spacecraft show decreases in the flux of epithermal and fast neutrons from Mercury's north polar region that are consistent with the presence of water ice in permanently shadowed regions. The neutron data indicate that Mercury's radar-bright polar deposits contain, on average, a hydrogen-rich layer more than tens of centimeters thick beneath a surficial layer 10 to 30 cm thick that is less rich in hydrogen. Combined neutron and radar data are best matched if the buried layer consists of nearly pure water ice. The upper layer contains less than 25 weight % water-equivalent hydrogen. The total mass of water at Mercury's poles is inferred to be 2×10^{16} to 10^{18} grams and is consistent with delivery by comets or volatile-rich asteroids.

Earth-based measurements of radar-bright regions near Mercury's north and south poles were initially reported in 1992 (*1*), and subsequent measurements showed that these unusual radar characteristics are confined to permanently shadowed regions within high-latitude impact craters (*2*). The leading explanation for the high radar reflectance is the presence of large amounts of water ice that can be thermally stable in regions of permanent shadow over geologically long periods of time (*2*). One of the primary goals of NASA's MErcury Surface, Space ENvironment, GEochemistry, and Ranging (MESSENGER) mission is to characterize Mercury's polar regions and thereby identify the principal compositional component of the radar-bright regions. Here we report the results on hydrogen concentrations near Mercury's north pole from data acquired with MESSENGER's Neutron Spectrometer (NS).

[1]The Johns Hopkins University Applied Physics Laboratory, Laurel, MD 20723, USA. [2]Planetary Science Institute, Tucson, AZ 85719, USA. [3]Institut de Recherche en Astrophysique et Planétologie, Université Paul Sabatier–CNRS–Observatoire Midi-Pyrénées, Toulouse, France. [4]Department of Terrestrial Magnetism, Carnegie Institution of Washington, Washington, DC 20015, USA. [5]Lamont-Doherty Earth Observatory, Columbia University, Palisades, NY 10964, USA.

*To whom correspondence should be addressed. E-mail: david.j.lawrence@jhuapl.edu

Planetary neutron spectroscopy is a standard technique for remotely measuring planetary hydrogen concentrations (*3*). Neutrons are created by nuclear spallation reactions when high-energy cosmic rays strike the surface of an airless or nearly airless planetary body. The energy spectra of the resulting neutrons, which are typically created at energies (E_n) exceeding ~1 to 10 MeV, are typically divided into three energy ranges: fast ($E_n > 0.5$ MeV), epithermal (0.5 eV $< E_n <$ 0.5 MeV), and thermal ($E_n < 0.5$ eV) (Fig. 1A). Hydrogen has a unique ability to moderate neutrons because hydrogen atoms and neutrons have the same mass, which allows a highly efficient momentum transfer between the two. This efficient momentum transfer causes the number of epithermal neutrons to be strongly depressed so that they are highly sensitive to the presence of hydrogen in planetary materials. Fast neutrons are also sensitive to the presence of hydrogen but vary with hydrogen concentration by a factor of 2 less than epithermal neutrons (Fig. 1B). In addition, fast neutrons are sensitive to variations of average atomic mass ($<A>$) in dry planetary materials (*4*). Finally, fast and epithermal neutrons have different sensitivities to the depth and abundance of hydrogen within a hydrogen-rich layer that is covered by tens of centimeters of a hydrogen-poor material. Consequently, combined measurements of epithermal and fast neutrons have been used to determine the burial depth of a concentrated hydrogen layer (*5*).

The NS is a scintillator-based instrument that separately measures thermal, epithermal, and fast neutrons through a combination of spacecraft Doppler and coincidence pulse processing techniques (*6*). Because of its highly eccentric orbit, the MESSENGER spacecraft is at a moderately high altitude (200 to 600 km) when it passes over or near the radar-bright regions in Mercury's north

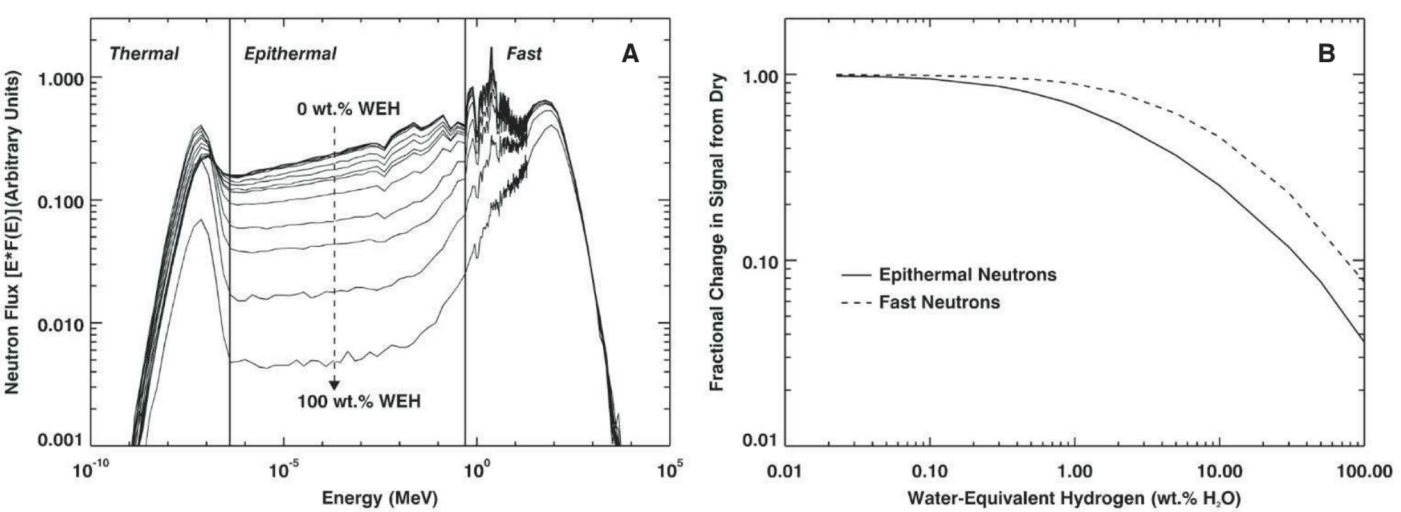

Fig. 1. (**A**) Simulated neutron flux, plotted as the product of energy and flux versus energy. Simulations were performed with the particle transport code MCNPX for a uniform sphere having Mercury's radius and appropriate soil composition (*7*, *9*) but with a variable concentration of hydrogen from 0 wt % water-equivalent hydrogen (WEH) to 100 wt % WEH. Nominal energy boundaries for thermal, epithermal, and fast neutrons are shown as vertical lines. (**B**) Simulated relative count rates on the MESSENGER NS for epithermal (solid) and fast (dashed) neutrons as a function of WEH for the same soil composition.

polar region. As a consequence, the omnidirectional neutron measurements have a large spatial footprint (300 to 900 km full-width, half maximum) compared with the size of the radar-bright regions (<40 km), so individual deposits cannot be spatially resolved (*7*). If extensive water ice is present in the locations of the radar-bright regions, fast and epithermal neutron count rates will show a count rate decrease of 4% or less poleward of latitudes 60° to 70° compared with count rates at lower latitudes (*7*).

NS data analysis has been carried out with empirically derived corrections applied in parallel with a neutron count rate simulation (*8*). The count rate simulation, which was validated with flyby data (*9*), accounts for the near-surface production of neutrons by galactic cosmic rays, their transport to the spacecraft, and their detection by the NS. The simulation was used to guide and constrain the empirical corrections and to provide a capability for bounding the surface hydrogen concentrations. The NS analysis requires corrections to account for nonisotropic solid angle variations, spacecraft obscuration effects, time variations in the incident cosmic ray flux, near-surface temperature variations, and variations from a radial velocity Doppler effect. The radial Doppler effect arises because the speed of the MESSENGER spacecraft in the direction of the spacecraft–planet-center vector has a magnitude (0 to 2 km/s) that is similar to the speed of thermal and low-energy epithermal neutrons (~2 km/s) (*10*). Doppler-induced effects are negligible for fast neutrons but have a magnitude of a few percent for low-energy epithermal neutrons and therefore need to be considered.

Fully corrected, longitudinally averaged count rates for fast neutrons are shown in Fig. 2 as a function of latitude for data collected from 26 March 2011 to 25 February 2012 (*8*). Simulated count rates were calculated for the measured count rate collection periods and include all viewing geometry effects. The simulation shows that if the radar-bright regions contain no hydrogen, fast neutrons would display no latitude dependence. In contrast, when a thick surface layer (i.e., having a thickness greater than the depth of sensitivity of the NS) consisting of 100 weight % (wt %) water-equivalent hydrogen (WEH) is included within all mapped radar-bright regions, the simulation shows a poleward decrease of 1.8% in fast neutrons relative to count rates closer to the equator. The NS measurements, in comparison, show a poleward decrease of 1.1% (Fig. 2) (*8*). When the latitude-dependent signal is averaged over two latitude zones (northward of 75°N and southward of 45°N), the fast neutron count rate at the north pole has a value of 0.9898 ± 0.0020 (two standard deviations, or 2σ) relative to unity at the equator with a statistical significance of 11σ (*8*). In comparison, simulated count rates with comparable Poisson uncertainties show that if the radar-bright regions were to contain a thick surface layer of 100 wt % water ice, then there would be a 0.978 ± 0.001 (2σ) signal with an 18σ statistical significance (*8*).

To interpret the fast neutron data, variations in the fast neutron flux unrelated to hydrogen must first be understood. From surface elemental abundances on Mercury (*11*–*15*) and assumptions on probable mineralogical assemblages (*8*), the value of $\langle A \rangle$ for Mercury's northern volcanic plains (*16*) may be lower by as much as 0.06 to 0.18 atomic mass unit (amu) than for the surrounding intercrater plains and heavily cratered terrain (*8*). With the longitudinally averaged data, an $\langle A \rangle$ decrease in the northern plains is likely to be indistinguishable from a hydrogen signal from radar-bright areas given the broad spatial footprint and limited statistics of the fast neutron data. A 0.06 to 0.18 amu change in $\langle A \rangle$ corresponds to a 0.6 to 1.8% decrease in relative fast neutron count rate (*4*). In principle, $\langle A \rangle$ variations could account for some or all of the fast neutron signal, so that signal is 0.9898 (−0.0020,+0.0102) (*8*) when all uncertainties are combined.

Two conclusions follow from the polar measurements of fast neutrons. First, the measured polar decrease is a factor of 2 smaller than expected if all radar-bright regions contained pure or nearly pure (80 to 100 wt %) water ice at the surface, so these data do not support the presence of thick surficial deposits of water ice in all radar-bright regions. Second, the regional dynamic range of ~1% for fast neutrons on Mercury is substantially smaller than that measured for Vesta (~10%) (*17*), the Moon (~38%) (*18*), or Mars (~300%) (*19*), where variations in $\langle A \rangle$ and/or hydrogen dominate. A 1% fast neutron dynamic range therefore places strong constraints on the major-element variability across Mercury's surface on the spatial scale (few hundreds to 1000 km) of the NS footprints.

Fully corrected, longitudinally averaged count rates for epithermal neutrons are shown as a function of latitude in Fig. 3 (*8*). Data collection times and selections for epithermal neutrons are the same as those for fast neutrons. The monotonic equator-to-pole variation is due mostly to the radial Doppler effect, which is treated in the latitudinally binned count rates by normalizing both the 100 wt % WEH simulation results and the measurements to the no-water simulation rates (Fig. 3B).

The dominant, remaining signal in the measured epithermal neutron data is a decrease at high latitudes, relative to the no-water simulation, that starts near latitude 70°N. The magnitude and latitude profile of this variation closely matches that of the simulated count rate for a thick, surficial layer of 100 wt % water ice at all the radar-bright regions identified from radar observations (*2*). The good agreement between the data and simulation provides strong evidence that large amounts of hydrogen in the form of water ice are present in Mercury's radar-bright regions. Using the highest-latitude value as the maximum polar signal, the epithermal neutron data show a measured polar signal of 0.976 ± 0.0025 (2σ), relative to an equatorial neutron signal of 1. Despite this strong polar signal, relating the magnitude of the polar decrease of epithermal neutrons to a hydrogen concentration within the radar-bright regions requires careful consideration of other sources of variability within the epithermal neutron data.

Differences between data and simulations that are unrelated to the high-latitude signal have magnitudes of ~0.2 to 0.5% (Fig. 3A), which are at least a factor of 5 smaller than the measured

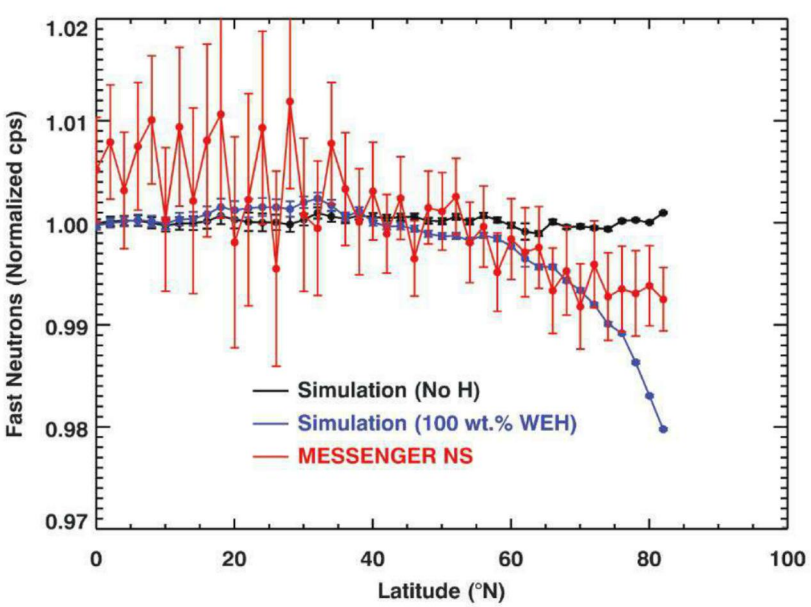

Fig. 2. Measured (red) and simulated (black, blue) fast neutron count rates in units of normalized counts per second (cps) averaged over 2°-wide latitude bins and plotted as a function of latitude. All corrections (*8*) have been applied. Counts are normalized to the mean count rate (~10 cps) at an altitude of 400 km. Simulated count rates are shown for the cases of no hydrogen (black) and for a thick layer of 100 wt % water ice (blue) located at the surface in all radar-bright regions. The error bars denote twice the measured standard deviation of the mean in each latitude bin.

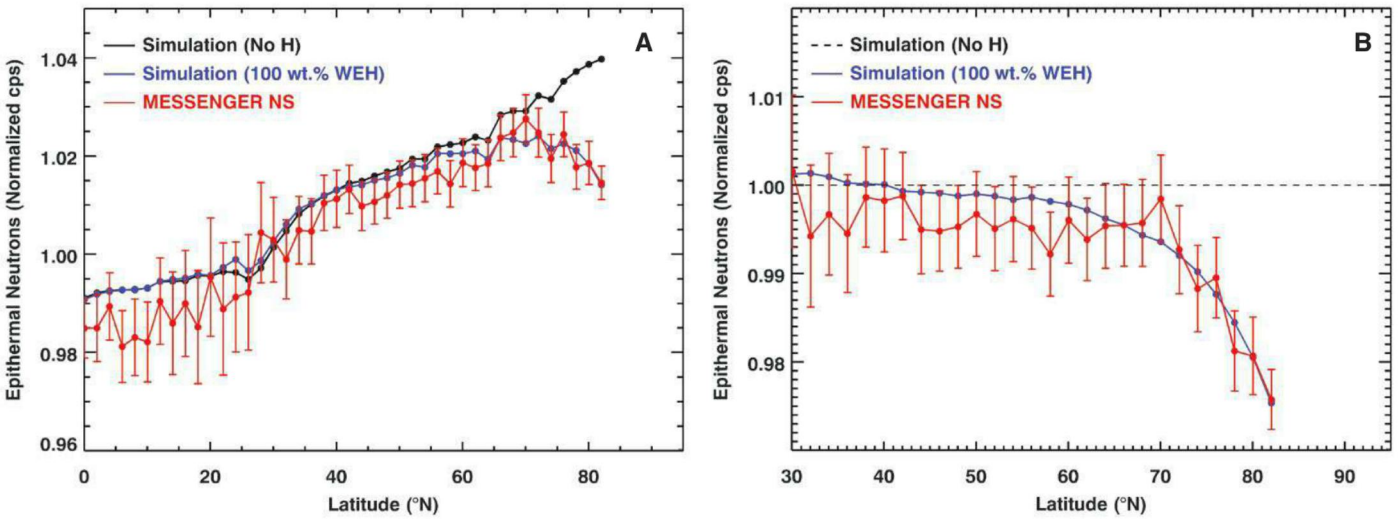

Fig. 3. (**A**) Measured (red) and simulated (black, blue) epithermal neutron count rates averaged over 2°-wide latitude bins and plotted as a function of latitude. All corrections except for a radial Doppler effect have been applied to the data (*8*). Counts are normalized to the mean count rate (~60 cps) at an altitude of 400 km. Simulated count rates are shown for the cases of no hydrogen (black) and a thick surficial layer of 100% water ice (blue) in all radar-bright regions. The error bars denote twice the measured standard deviation of the mean in each latitude bin. (**B**) Simulated and measured epithermal neutron count rates after correcting for the radial Doppler effect, which is accomplished by normalizing to the simulation with no hydrogen.

latitudinal signal of 2.4%. These differences are most notable at latitudes of 0° to 20°N and 40° to 60°N. These are latitude ranges over which the spacecraft is known to interact with populations of energetic electrons (EEs) on nearly every orbit (*20*). The presence of small EE events results in a systematic underestimate of the net neutron counts (*8*). An empirical correction was applied to reduce the magnitude of this effect to give the 0.2 to 0.5% level seen in Fig. 3A. Nonpolar latitude ranges (30° to 40°N and >60°N) over which EE events are largely absent display the best agreement between data and simulations (<0.2%). These combined results provide us with confidence that the simulation accurately represents the data and differences other than the polar effect result from an as yet imperfect correction for EE events that do not strongly affect the polar measurement.

Subsurface temperature variations are a second potential source of variation in the epithermal neutron count rate unrelated to polar hydrogen (*21*, *22*). From subsurface temperature models (*23*) and the neutron simulations (*8*), and given that epithermal neutrons are sensitive to temperatures at a product of depth and density equal to ~30 g/cm^2 (*21*), we estimate that the variations with temperature account for no more than a 0.16% variation between 70°N and 85°N. Thus, although temperature variations might widen the uncertainty limits, the effect is expected to be more than an order of magnitude smaller than the measured polar signal.

The epithermal neutron data alone provide strong evidence that Mercury's north polar radar-bright regions contain high concentrations of hydrogen, consistent with the presence of water ice. If it is assumed that the water ice is located within the radar-bright regions as a single thick layer, then the epithermal neutron data are consistent with the presence of up to 100 wt % WEH within these regions. That the 2σ uncertainty of the measurements extends to a slightly larger signal than is given for the hydrogen-rich simulation indicates that the epithermal neutron data are consistent with (but do not require) a larger total area than is specified by the known radar-bright regions. In either case, however, the inferred hydrogen concentration with a single-layer assumption is not consistent with the fast neutron data, which exhibit a smaller signal than expected for a single thick layer of water ice. The combined fast and epithermal neutron data indicate that a hydrogen-rich layer is, on average, buried beneath a layer of material noticeably less abundant in hydrogen.

To estimate hydrogen concentrations and burial depth within the radar-bright regions, the neutron signals measured from orbit must be converted to inferred neutron signals at the surface of the radar-bright regions. We used the neutron simulation as a forward model calibration of the measured signals under the assumption that the entire decrease in neutron flux originates from the radar-bright regions. This type of forward modeling technique has been applied and validated with other nuclear spectroscopy measurements involving large spatial footprints (*24*–*26*). With the forward model calibration (*8*), the inferred neutron signals at the surface of the radar-bright regions are 0.39 (−0.13,+0.61) (fast neutrons) and 0.10 ± 0.059 (epithermal neutrons) relative to equatorward values.

The independent fast and epithermal neutron measurements allow us to use a two-layer model with two free parameters constrained by the measurements (average thickness of the upper layer and hydrogen concentration in one of the layers). We considered two end-member models. For model 1, we assumed that the upper layer contains no hydrogen (w_{upper} = 0 wt % WEH), so that the effective thickness (t) of the upper layer, expressed as the product of density and thickness, and the hydrogen content of the lower layer (w_{lower}) are constrained by the data. For model 2, we assumed that the lower layer has w_{lower} = 100 wt % WEH, so that the effective thickness and hydrogen concentration of the upper layer are constrained by the data. These layering models represent an average layering structure, and actual layering need not correspond to a uniform two-layer stratigraphy across the NS field of view for all radar-bright regions. A distribution of different layer configurations among or within radar-bright regions can also satisfy the current data.

From modeled neutron fluxes convolved with the respective NS efficiencies, we calculated the relative count rates for fast and epithermal neutrons for a range of hydrogen concentrations and upper-layer thicknesses in the two-layer models. For model 1 (Fig. 4A), t = 12 to 47 g/cm^2 and w_{lower} = 12 to 100 wt % WEH. For model 2 (Fig. 4B), t = 12 to 47 g/cm^2 and w_{upper} = 0 to 25 wt % WEH. These results are consistent with an average two-layer stratigraphy in which the hydrogen concentration in the upper layer is 0 to 25 wt % WEH, the hydrogen concentration in the lower layer is 12 to 100 wt % WEH, and the effective thickness of the upper layer is 12 to 47 g/cm^2. If a typical planetary regolith density of 1.5 g/cm^3 is assumed (*27*), this effective thickness corresponds to a physical thickness of 8 to 31 cm.

Although we have analyzed the NS data in the context of large hydrogen concentrations within Mercury's permanently shadowed regions, other physical distributions of hydrogen can be considered. One possible distribution is a broad area of hydrogen enrichment poleward of ~70°N in which the hydrogen is emplaced in a single

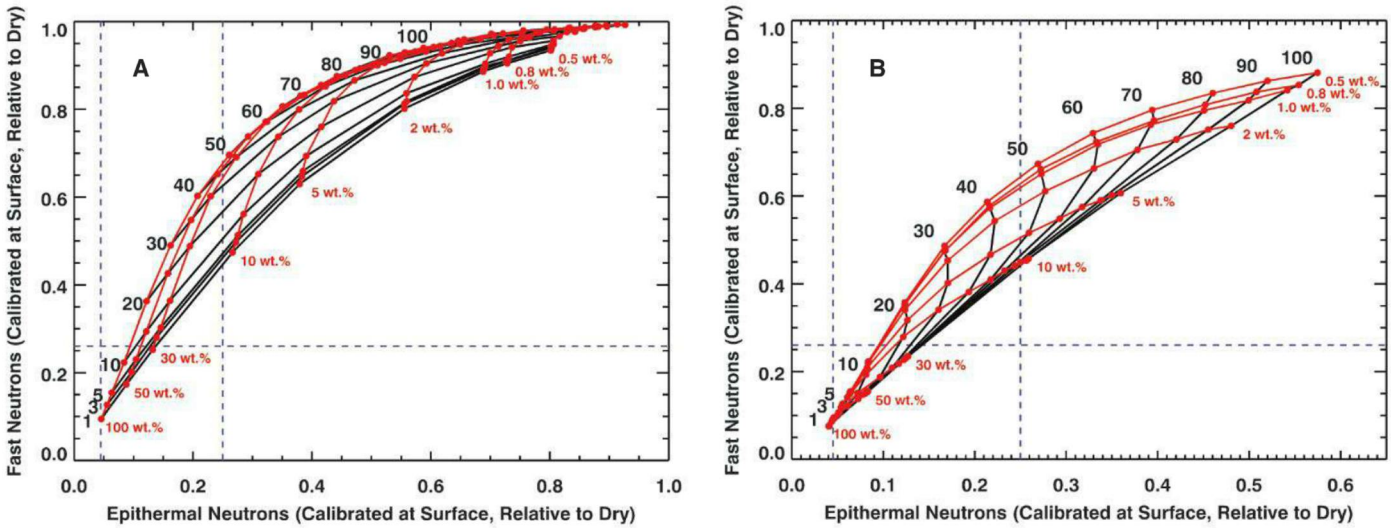

Fig. 4. (**A**) Simulated epithermal versus fast neutron relative count rates at the surface of the radar-bright regions for a two-layer model stratigraphy (model 1) with a range of values for the thickness of the upper layers and the hydrogen concentration of the lower layer. Black lines and numbers indicate upper-layer thickness contours in units of g/cm^2. Red lines and numbers indicate contours of lower-layer hydrogen concentrations in units of WEH wt %. Vertical dashed blue lines show the 2σ limits of the calibrated epithermal neutron measurements; the horizontal dashed blue line shows the lower 2σ limit of the fast neutron measurement. The lower and upper thickness values are constrained by the fast and epithermal neutrons, respectively. (**B**) Simulated and measured fast and epithermal neutron count rates for model 2; hydrogen concentration values are shown for an upper layer over a thick layer of 100 wt % water ice.

layer by solar wind. For this scenario, the measured epithermal neutron signal of 2.4% fills the NS field of view, and an average hydrogen concentration can be determined (*28*) to be 50 parts per million (ppm). The fast neutrons provide few constraints, as the measurement uncertainties allow a hydrogen concentration of 0 to 100 ppm (*28*). Nevertheless, given the excellent agreement of the epithermal neutron data with the simulation (Fig. 3) along with the strong consistency of the neutron data with other data sets, we consider that the NS observations are better understood as the result of enhanced concentrations of water ice within the radar-bright regions.

The NS results are consistent with observations made by the MESSENGER Mercury Laser Altimeter (MLA) and the Mercury Dual Imaging System (MDIS). Topographic data from MLA, together with thermal models derived from the topography, have shown that for the majority of the north polar radar-bright regions sampled by MLA, water ice is not stable at the surface (*23*, *29*). These studies suggest that any thick water ice layer in these areas is located beneath an insulating layer ~10 cm thick, and MLA reflectance measurements indicate that this surficial layer is darker than surrounding terrain at 1064-nm wavelength and may be enriched in hydrocarbon materials (*30*). The NS results, which indicate that the upper of the two layers in the north polar deposits has no more than 25 wt % WEH, are consistent with the interpretation that the radar-bright regions contain complex hydrocarbons, possibly mixed with silicate regolith. Images of the north and south polar regions by MDIS (*31*, *32*) have revealed a nearly one-to-one correspondence between radar-bright regions and areas of permanent or at least persistent shadow. Because the neutron simulations used the same locations of radar-bright features as the illumination studies, the combined results provide a self-consistent basis for interpreting the locations of hydrogen, permanent shade, and radar-bright deposits.

With the identification from neutron spectrometry of large concentrations of hydrogen within the radar-bright regions, it may now be concluded that the high radar backscatter of the polar deposits is the result of nearly pure water ice (*2*). This consideration favors our model 2, with an assumed hydrogen concentration in the lower layer of w_{lower} = 100 wt % WEH. Multi-wavelength radar data also support the interpretation that the water-rich layer, on average, is buried beneath an insulating layer of ~10-cm thickness (*2*). This thickness falls within the range of 8 to 31 cm inferred from the neutron data. The identification of large hydrogen concentrations within the radar-bright regions makes unnecessary such alternative explanations for the high radar backscatter as enhanced concentrations of sulfur (*33*) or unusual radar properties of silicate materials at low temperatures (*34*).

Given that the water ice in the polar deposits must be nearly pure, models of surface modification processes (burial and excavation by impacts, loss from ion sputtering and other surface processes, and addition of material from the atmosphere and micrometeoroids) in Mercury's polar region have shown that the bottom layer of deposits must be at least tens of centimeters thick (*35*). If we use a maximum lower-layer thickness of tens of meters as estimated from models of radar scattering (*36*) and an estimate of the area of permanent shadow in the north polar region of (1.25 to 1.46) × 10^{14} cm^2 (*2*), then an estimate of the total mass of water in the north polar region may be calculated. For a lower-layer thickness in the range 0.5 to 20 m, the total mass of water ranges from 6.2 × 10^{15} g to 2.9 × 10^{17} g. If we assume that the radar-reflective regions in the south polar region are also dominantly water ice, then from the area of permanently shadowed regions at high southern latitudes of (4.3 ± 1.4) × 10^{14} cm^2 (*32*), the total mass of ice in the south polar area ranges from 1.5 × 10^{16} to 1.1 × 10^{18} g, and the total mass of ice in both polar regions is 2.1 × 10^{16} to 1.4 × 10^{18} g. The total mass could be larger if the lower-layer thickness is greater than 20 m. The mass inferred here is consistent with values estimated earlier (*37*), and the delivery of this amount of water is possible from the impact of some combination of comets and volatile-rich asteroids onto Mercury (*37*) followed by migration to the poles with a polar cold-trapping rate of 5 to 15% (*38*). Models of surface modification that account for vertical and lateral mixing averaged over large areas indicate that a pure water ice deposit will be buried by drier material at a rate of 0.43 cm per million years (My) (*35*, *39*). The average thickness of the upper layer inferred from neutron spectrometry therefore suggests that Mercury's polar water ice was emplaced sometime in the last 18 to 70 My.

Note added in proof: Text has been modified from the version published in *Science* Express (*8*).

References and Notes

1. M. A. Slade, B. J. Butler, D. O. Muhleman, *Science* **258**, 635 (1992).
2. J. K. Harmon, M. A. Slade, M. S. Rice, *Icarus* **211**, 37 (2011).
3. T. H. Prettyman, Remote chemical sensing using nuclear spectroscopy, in *Encyclopedia of the Solar System*, L. A. McFadden, P. R. Weissman, T. V. Johnson, Eds. (Academic Press, San Diego, CA, ed. 2, 2007), pp. 765–786.

4. O. Gasnault *et al.*, *Geophys. Res. Lett.* **28**, 3797 (2001).
5. W. C. Feldman *et al.*, *Geophys. Res. Lett.* **34**, L05201 (2007).
6. J. O. Goldsten *et al.*, *Space Sci. Rev.* **131**, 339 (2007).
7. D. J. Lawrence *et al.*, *Planet. Space Sci.* **59**, 1665 (2011).
8. Supplementary online material describes the full NS data reduction and analysis.
9. D. J. Lawrence *et al.*, *Icarus* **209**, 195 (2010).
10. W. C. Feldman *et al.*, *Nucl. Instrum. Methods* **A245**, 182 (1986).
11. L. R. Nittler *et al.*, *Science* **333**, 1847 (2011).
12. P. N. Peplowski *et al.*, *Science* **333**, 1850 (2011).
13. S. Z. Weider *et al.*, *J. Geophys. Res.* **117**, E00L05 (2012).
14. P. N. Peplowski *et al.*, *J. Geophys. Res.* **117**, E00L04 (2012).
15. L. G. Evans *et al.*, *J. Geophys. Res.* **117**, E00L07 (2012).
16. J. W. Head *et al.*, *Science* **333**, 1853 (2011).
17. T. H. Prettyman *et al.*, *Science* **338**, 242 (2012).
18. S. Maurice *et al.*, *J. Geophys. Res.* **105**, 20365 (2000).
19. S. Maurice *et al.*, *J. Geophys. Res.* **116**, E11008 (2011).
20. G. C. Ho *et al.*, *Science* **333**, 1865 (2011).
21. R. C. Little *et al.*, *J. Geophys. Res.* **108**, 5046 (2003).
22. D. J. Lawrence *et al.*, *J. Geophys. Res.* **111**, E08001 (2006).
23. D. A. Paige *et al.*, *Science* **339**, 300 (2013); 10.1126/science.1231106.
24. D. J. Lawrence *et al.*, *Geophys. Res. Lett.* **32**, L07201 (2005).
25. J. J. Hagerty *et al.*, *J. Geophys. Res.* **111**, E06002 (2006).
26. T. D. Glotch *et al.*, *Geophys. Res. Lett.* **38**, L21204 (2011).
27. W. D. Carrier III, G. R. Olhoeft, W. Mendell, in *Lunar Sourcebook: A User's Guide to the Moon*, G. Heiken, D. Vaniman, B. M. French, Eds. (Cambridge Univ. Press, 1991), pp. 475–594.
28. W. C. Feldman *et al.*, *Science* **281**, 1496 (1998).
29. There is observational and thermal modeling evidence that a limited fraction of the area of permanent shadow and radar-bright regions contain surficial water ice (*23*, *30*). The neutron data, however, do not have the spatial resolution to distinguish regions of surface ice from the larger areas of shallowly buried ice. Furthermore, multiwavelength radar studies (*2*) suggest that polar deposits in the three largest north polar craters [Chesterton, Tolkien, and Tryggvadóttir (*2*)] that make a large contribution to the overall neutron signal are, on average, buried beneath a thin cover of dry soil or other comparatively ice-poor material.
30. G. A. Neumann *et al.*, *Science* **339**, 296 (2013); 10.1126/science.1229764.
31. N. L. Chabot *et al.*, *J. Geophys. Res.* 10.1029/2012JE004172 (2012).
32. N. L. Chabot *et al.*, *Geophys. Res. Lett.* **39**, L09204 (2012).
33. A. L. Sprague, D. M. Hunten, K. Lodders, *Icarus* **118**, 211 (1995).
34. L. Starukhina, L. V. Starukhina, Y. G. Shkuratov, *Icarus* **147**, 585 (2000).
35. D. Crider, R. M. Killen, *Geophys. Res. Lett.* **32**, L12201 (2005).
36. B. J. Butler, D. O. Muhleman, M. A. Slade, *J. Geophys. Res.* **98**, 15003 (1993).
37. J. I. Moses, K. Rawlins, K. Zahnle, L. Dones, *Icarus* **137**, 197 (1999).
38. B. J. Butler, *J. Geophys. Res.* **102**, 19283 (1997).
39. The surface modification models do not account for thermal effects (*23*) that can operate on time scales much shorter than impact gardening processes (*35*). Thus, the emplacement times implied by the neutron data represent an upper limit.

Acknowledgments: We thank the MESSENGER team for their contributions to the development and operation of the spacecraft, P. G. Lucey and two anonymous reviewers for comments that improved the manuscript, D. Delapp and D. Seagraves of Los Alamos National Laboratory for early help in the data reduction and calibration, respectively, and D. Hurley for discussions regarding surface modification models. This work was supported by the NASA Discovery Program, with funding for MESSENGER provided under contract NAS5-97271 to The Johns Hopkins University Applied Physics Laboratory and NASW-00002 to the Carnegie Institution of Washington. Several authors are supported by NASA's MESSENGER Participating Scientist Program. All original data reported in this paper are archived by the NASA Planetary Data System.

Supplementary Materials

www.sciencemag.org/cgi/content/full/science.1229953/DC1
Supplementary Text
Figs. S1 to S23
Tables S1 to S4
References (*40*–*51*)

10 September 2012; accepted 13 November 2012
Published online 29 November 2012;
10.1126/science.1229953

Bright and Dark Polar Deposits on Mercury: Evidence for Surface Volatiles

Gregory A. Neumann,[1]* John F. Cavanaugh,[1] Xiaoli Sun,[1] Erwan M. Mazarico,[2] David E. Smith,[2] Maria T. Zuber,[2] Dandan Mao,[3] David A. Paige,[4] Sean C. Solomon,[5,6] Carolyn M. Ernst,[7] Olivier S. Barnouin[7]

Measurements of surface reflectance of permanently shadowed areas near Mercury's north pole reveal regions of anomalously dark and bright deposits at 1064-nanometer wavelength. These reflectance anomalies are concentrated on poleward-facing slopes and are spatially collocated with areas of high radar backscatter postulated to be the result of near-surface water ice. Correlation of observed reflectance with modeled temperatures indicates that the optically bright regions are consistent with surface water ice, whereas dark regions are consistent with a surface layer of complex organic material that likely overlies buried ice and provides thermal insulation. Impacts of comets or volatile-rich asteroids could have provided both dark and bright deposits.

Mercury's near-zero obliquity and impact-roughened topography (*1*) prevent direct sunlight from reaching substantial portions of its polar regions. Lacking major convective or conductive sources of heat, the permanently shadowed, near-surface regolith experiences temperatures similar to those of the icy Galilean satellites (*2*). It has long been believed on theoretical grounds that such conditions are favorable to the accumulation of volatiles (*3*, *4*). Even with Mercury's close proximity to the Sun, extremes of daytime temperature are not expected to penetrate regolith to substantial depth, allowing near-surface water ice, if present, to remain stable against sublimation for billions of years (*2*). Such hypotheses were renewed when Earth-based radar observations of Mercury, at wavelengths from 3.6 to 70 cm (*5*–*9*), revealed regions of high backscatter and depolarization at both poles. Radar observations suggested that deposits of nearly pure water ice up to several meters thick lie at or near the surface. Analysis of altimetry and roughness measurements from the Mercury Laser Altimeter (MLA) (*10*, *11*) on the MErcury Surface, Space ENvironment, GEochemistry, and Ranging (MESSENGER) spacecraft (*12*) indicates that craters hosting radar-bright deposits at high northern latitudes are not anomalously shallow, nor do they display distinctive roughness properties in comparison with craters that lack such deposits (*13*). Consequently, the radar-bright material does not form a thick layer overlying regolith (*13*). A thinner surficial layer containing substantial concentrations of ice would, however, be optically brighter than the surrounding terrain (*14*) and should be detectable by active remote sensing.

We report here measurements with MLA of surface reflectance in permanently shadowed north polar regions of Mercury. The MLA instrument illuminates surface spots 20 to 80 m in diameter at 350- to 450-m intervals (*10*). The receiver system measures threshold-crossing times of the received pulse waveforms at two voltages (*15*). A single low-threshold crossing provides surface elevation, and the timing of the rising and falling signal levels for strong returns at both low and high thresholds enables MLA to estimate the received pulse energy and make active measurements of surface reflectance, r_s, via the lidar link equation (*16*, *17*) and preflight sensor calibrations (*10*).

During its primary mapping mission, MESSENGER orbited Mercury in an eccentric orbit with a 12-hour period and a ~200- to 400-km periapsis altitude at 60° to 70°N. In this orbit, the MLA ranged to Mercury from 29 March 2011

[1]NASA Goddard Space Flight Center, Code 698, Greenbelt, MD 20771, USA. [2]Department of Earth, Atmospheric, and Planetary Sciences, Massachusetts Institute of Technology, Cambridge, MA 02139, USA. [3]Sigma Space Corporation, Lanham, MD 20706, USA. [4]Department of Earth and Space Sciences, University of California, Los Angeles, CA 90095, USA. [5]Department of Terrestrial Magnetism, Carnegie Institution of Washington, Washington, DC 20015, USA. [6]Lamont-Doherty Earth Observatory, Columbia University, Palisades, NY 10964, USA. [7]The Johns Hopkins Applied Physics Laboratory, Laurel, MD 20723, USA.

*To whom correspondence should be addressed. E-mail: gregory.a.neumann@nasa.gov

to 16 April 2012, densely sampling the north polar region in nadir mode northward to 83.5°N and sparsely in off-nadir mode at more northerly latitudes (Fig. 1A) (*1*). More than 4 million topographic and 2 million reflectance measurements were collected at latitudes greater than 65°N in the first year of mapping. Of 700 orbital profiles, 60 targeted latitudes higher than 84°N with off-nadir ranges, some yielding energy measurements and some not (fig. S1). Orbital geometry and power and thermal constraints precluded observations of many polar craters, and measurements of those that were accessible at oblique incidence returned noisier measurements than at nadir orientation.

A map of radar cross section in the north polar region at S-band (12.6-cm wavelength) (*9*) (Fig. 1B) shows many regions of high backscatter cross section; other such regions extend beyond the limits of the map to latitudes as low as 67°N. The polarization characteristics of these regions are suggestive of cold-trapped volatiles (*5*, *6*, *18*). These radar-bright (RB) features generally coincide with high-latitude, steep-walled craters of which the southern floors are permanently shadowed from direct sunlight because of Mercury's near-zero obliquity. The largest RB features lie north of 85°N, whereas the 108-km-diameter Prokofiev crater [previously given the informal name "K" (*18*)] has a crescent-shaped RB region behind its steep (17° slope) north-facing wall, just south of 85°N (Fig. 1B). With a depth-to-diameter ratio of 0.025, typical for a complex crater of this size, only a portion of its floor can lie in permanent shadow, consistent with the shape of the RB region. An unnamed 1.5-km-deep, 18-km-diameter crater "Z" lies on the central floor of Prokofiev and is RB. The 62-km-diameter crater Kandinsky (formerly "J") to the north has a nearly circular RB region (Fig. 1B). These and similar regions may now be subjected to illumination models that use detailed polar topography (*19*).

A plot of the maximum illumination flux over 10 solar days is shown in Fig. 1C. We modeled the primary shadowing of the finite disk of the Sun with the orbital and rotational geometry of Mercury following an earlier methodology (*20*). Zero flux corresponds to areas of near-permanent shadow that receive only scattered light. Mercury's orbital eccentricity and 3:2 spin–orbit resonance result in lower average solar flux near longitudes of 90° and 270°E. Shallow, degraded craters and craters lying near the 0° and 180°E longitudes of Mercury's equatorial "hot poles" have higher average illumination. Except for relatively fresh craters on the northern smooth plains (*1*), there are few RB features along these azimuths south of 85°N.

The reflectance measurements binned at 1 km by 1 km resolution are shown in Fig. 1D. The log-normally distributed quantity r_s has a mean of 0.17 ± 0.05 (SD), and 98% of returns have $r_s < 0.3$ (fig. S1). For comparison, the broadband geometric albedo of Mercury from space is 0.142 (*21*). About 7% of returns comprise a secondary "MLA-dark" (MD) mode distinguished by $r_s < 0.1$. This mode is seen in regions that are markedly darker than their surroundings. These regions coincide with areas where many received pulses do not trigger at the high threshold (fig. S2), although weak laser output, oblique incidence, steep terrain, and/or extreme range, as well as low reflectivity, can lead to poor signal recovery. The deficit of energy measurements in many MD regions indicates that the measured r_s values are upper bounds for surface albedoes that are lower by factors of 2 to 3 than their surroundings.

Many of the MD regions are associated with polar craters containing RB material (Fig. 2). The larger MD regions generally enclose the RB features. MD returns lie mainly within regions of very low peak illumination, although not necessarily permanent shadow. The reflectance is low

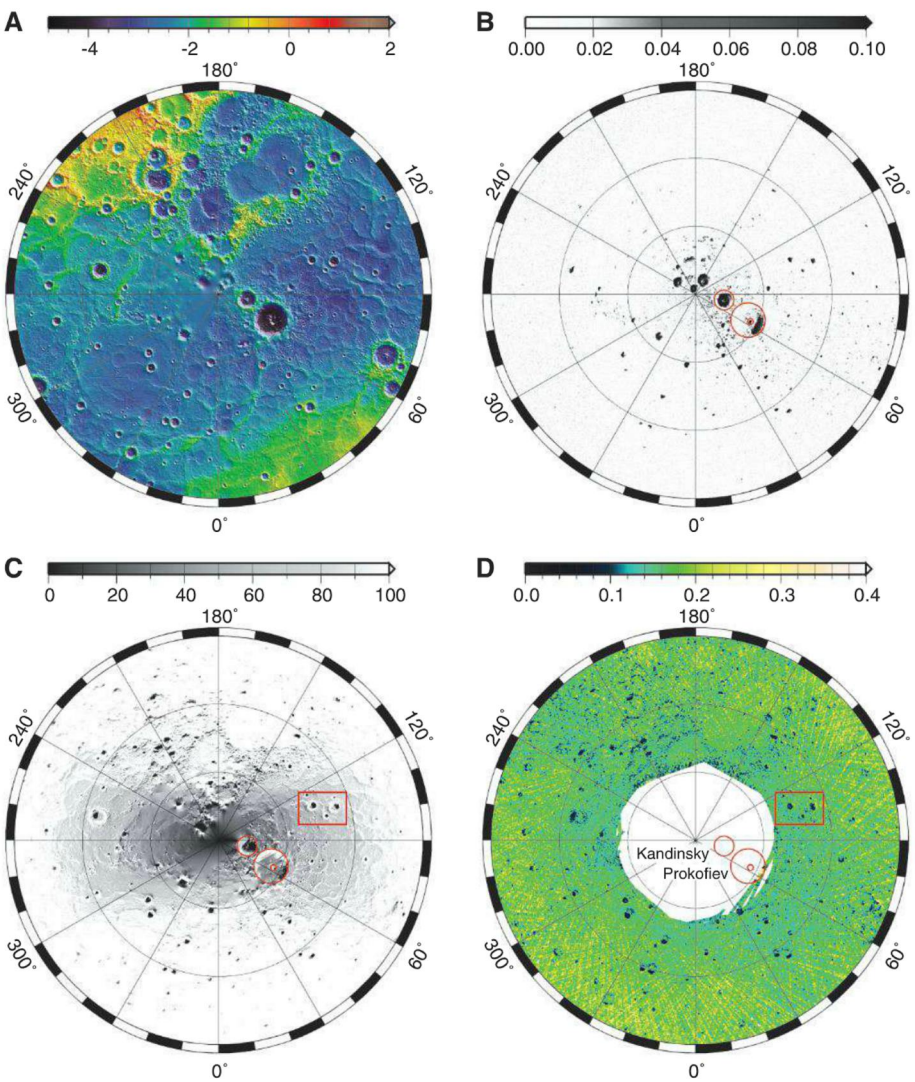

Fig. 1. Maps of topography, radar cross section, solar illumination, and reflectance in polar stereographic projection southward to 75°N. Kandinsky and Prokofiev craters are outlined in three of the four panels. (**A**) Topography (color scale in km) and shaded relief; the datum is a sphere of radius 2440 km. (**B**) Earth-based radar image (*9*) displayed as a dimensionless radar cross section per unit area. (**C**) Maximum incident solar flux over a 10-year period as a percentage of the solar constant at 1 astronomical unit (AU) from an illumination model. The red box outlines the region shown in Fig. 2. (**D**) The 1064-nm bidirectional reflectance from MLA low- and high-threshold measurements in near-nadir directions, median-averaged in 1 km–by–1 km bins. At latitudes poleward of 84°N, MLA obtained only a limited number of off-nadir profiles, and the projected reflectance data in this region are interpolated by a nearest-neighbor weighted average only within 2 km of data whose incidence angles were less than 10°.

Table 1. Classification of 175 craters according to radar and optical characteristics of associated deposits.

Radar	MLA dark	MLA bright/mixed	MLA normal	MLA undetermined
Bright	96	9	0	24
Dark	28	0	15	3

over the southern floors and the northward-facing walls of virtually all craters at latitudes between 75° and 84°N. Darkening also occurs on some poleward-facing exterior rim slopes of craters in the otherwise smooth plains within the 320-km-diameter Goethe basin. Such darkening extends into regions that are partially illuminated.

The asymmetric distribution of MD regions with respect to terrain slope direction does not simply result from observing geometry, surface roughness, or the magnitude of the surface slope. The pulses returning from the MD portions are not noticeably wider or narrower than those from the illuminated portions, nor do equator-facing portions of the floor show lower reflectance. If surface slope or roughness were causing reduced energy return, the darker regions would have a circular outline. The correspondence of dark material with pole-facing slopes and the lack of such darkening in most craters southward of 70°N appears to rule out instrumental effects or observational geometry as a cause of the surficial darkening.

To assess the relations between MLA-dark features, RB deposits, and illumination, we examined (*22*) 175 regions of low illumination identified as lying within craters varying in size from ~7 to 108 km in diameter (*23*) and from 65°N poleward (Table 1). All craters with RB deposits and sufficient MLA sampling show at least some MD features in their poleward-facing portions. Of 128 RB craters with RB deposits, 96 contain collocated MD portions, whereas there are 28 additional craters with MD material that lack a corresponding RB signature. Two such craters (b5 and f5) (Fig. 2 and fig. S3) are relatively pristine (>1 km deep), so their interiors may not be visible to Earth-based radar. Twelve such craters are <14 km in diameter. Those craters with MD material that lack a RB signature and are 14 km or larger in diameter are at latitudes south of 80°N. As with the RB regions, MLA-dark deposits are more prevalent near 90° and 270°E, longitudes that receive less average illumination as a result of Mercury's spin-orbit resonance and eccentric orbit, and in fresh craters on the smooth plains. At latitudes north of 75°N, 15 similar shadowed regions (putatively small craters) with neither a RB signature nor MD material are located mainly on an elevated area surrounding Purcell crater between longitudes 170° and 230°E. Radar coverage may be partial-

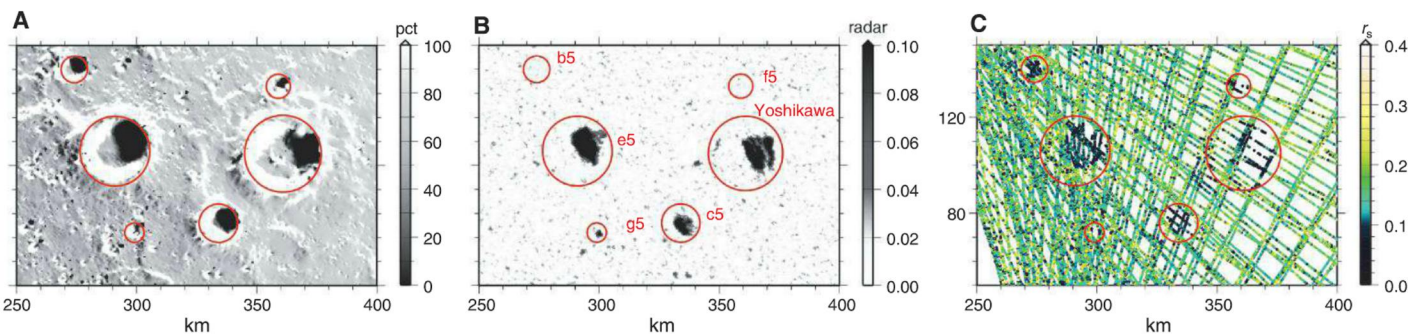

Fig. 2. Regional view of the area outlined in Fig. 1, in polar stereographic projection. Red circles show the outlines of six craters. (**A**) Maximum incident solar flux, as a percentage of the solar constant at 1 AU. (**B**) Radar cross-section per unit area. The projected radar map (*9*) has been shifted by 4 km to account for differences in projection and to achieve optimal registration with the MLA-based maps. Regions of interest (*22*) are labeled. (**C**) MLA reflectance (colored dots).

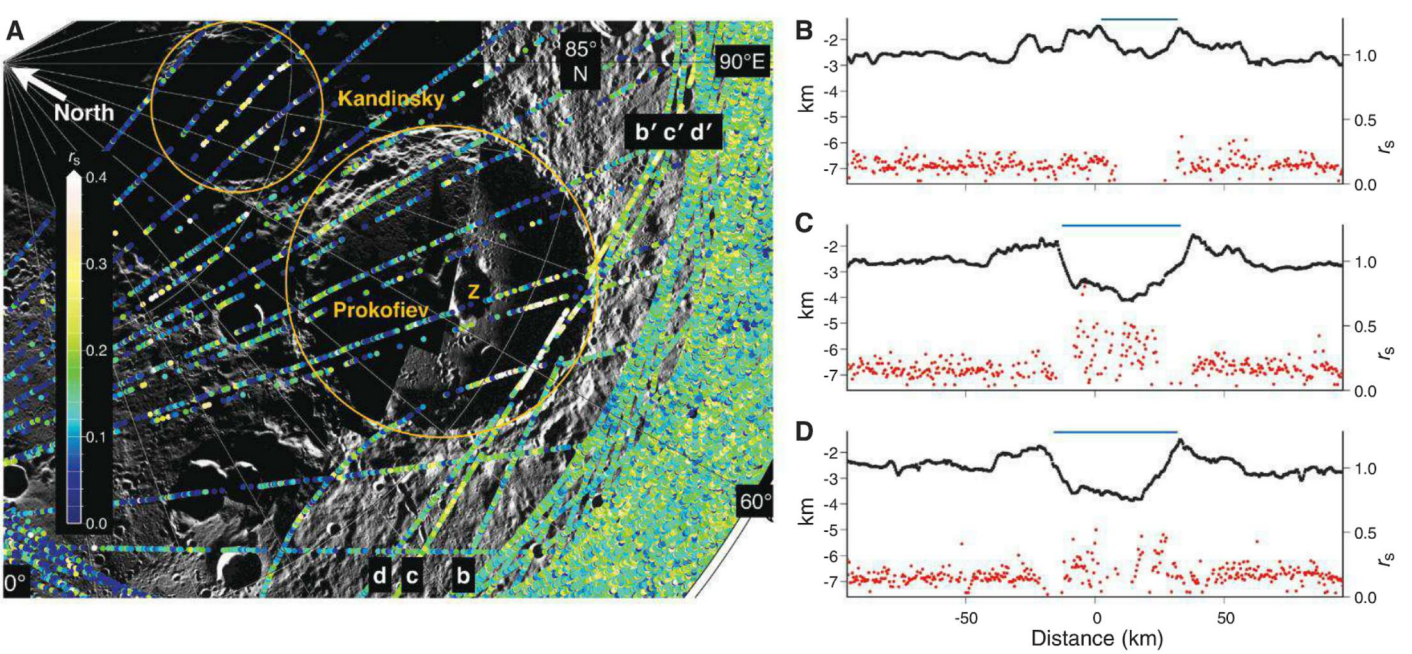

Fig. 3. (**A**) MLA reflectance measurements (colored dots) of the north polar region from longitude 0° to 90°E and latitude 82.5° to 90°N. Background is a mosaic of MDIS (*34*) frames at different illumination geometries and has a nonlinear contrast stretch for visibility. Three profiles through Prokofiev (b-b′, c-c′, and d-d′) were acquired at near-nadir orientation. Profiles through Kandinsky were acquired at ~30° off-nadir orientation. (**B** to **D**) Profiles of height (black lines) and reflectance (red dots) through Prokofiev acquired on 22 through 24 March 2012 starting at 0308 UTC on each day, at a 5° to 7° nadir angle. Vertical exaggeration is 10:1. The profiles are centered at longitude 60°E and traverse the poleward-facing wall of Prokofiev crater in an approximate west-to-east direction. The blue lines show the modeled extent of low average solar flux (<50 W m^{-2} or <0.04 of terrestrial).

ly obscured by rough terrain in this sector, but the lack of RB features more likely has a thermal origin at these "hot pole" longitudes in locations where partial illumination might preclude stability of near-surface water ice (fig. S4).

Although the MLA-dark regions are more abundant and extensive than RB regions, there are at least nine areas within the largest RB regions at very high latitudes in which the MLA reflectances are optically bright. The nine craters hosting RB material, at latitudes between 82.5° and 88.5°N, have portions with $r_s > 0.3$ as well as areas that are anomalously dark or that return no reflectance measurements. The two most prominent such craters are north of 84.9°N latitude.

Craters Kandinsky and Prokofiev, for which high radar cross sections suggest thick, near-surface ice deposits (*18*), are shown in Fig. 3. Their regions of permanent shadow (Fig. 1C) have many reflectance values in excess of 0.3 (pink or white symbols), especially along the southern portion of Prokofiev. Three profiles crossing the RB region are plotted along track in Fig. 3, B to D. Profile 3B grazed the uppermost kilometer of the crater wall and recorded no high-threshold detections in regions of shadow. Profile 3C passed 2 km into the interior along the north-facing wall and shows many strongly reflective returns (red symbols) up to the edges of the crater, where such returns dropped out for several seconds. Profile 3D reached portions of the crater floor that are in permanent shadow and recorded variable reflectance. These profiles are the only ones to date obtained over the shadowed interior of Prokofiev at the relatively small incidence angles (6° to 7°) for which reflectance measurements are most reliable. Two profiles nearest to crater Z (Fig. 3A) also include returns with $r_s > 0.3$, as do several traversing crater Kandinsky to the north, but the measurements are noisier owing to incidence angles greater than 25°.

The observations of 1064-nm reflectance from laser altimetry thus fall into three categories: Most are typical of Mercury reflectivity as a whole; a subset is much darker; and a smaller subset is substantially brighter. The association of MD regions with RB regions in near-permanent shadow suggests that a thin, radar-transparent layer of optically dark material overlies and surrounds the postulated polar ice deposits. If water ice were present in the ground as a matrix between mineral grains, it could lower the reflectance relative to dry ground but would sublimate rapidly and lose optical contrast if exposed to high temperatures. The presence of MD regions in many smaller craters without RB deposits, areas where scattered light raises average temperatures (*2*, *24*), indicates the presence of volatiles that are both darker than water ice and stable to higher temperatures.

The identification of optically bright regions associated with large RB features at the highest (>84.9°N) latitudes is consistent with the hypothesis that water ice is exposed at the surface in areas where surface temperatures are never sufficiently high for substantial loss by sublimation. The surface measurements are averages over footprints that are dozens of meters in extent and could represent a thin or unevenly distributed layer of optically bright material that has not been covered by dust or regolith. However, to the extent that MLA-bright and RB characteristics are sampling the same material, the associated deposits must have a thickness of at least several meters. The reflectance measurements presented here strongly suggest that one of the largest and deepest regions of permanent shadow in crater Prokofiev is a host for water ice deposits exposed at the surface.

The existence of these dark and bright surfaces and their association with topography indicates that their formation processes operated during geologically recent times and may be active on Mercury today. The rates of darkening and brightening must be higher than those for processes that act to homogenize surface reflectance, such as impact gardening. Were vertical mixing by impact gardening dominant at the meter scale, we would expect that the polar deposits would have reflectance values (and radar backscatter characteristics) more similar to those of surrounding terrain.

Detailed thermal models (*25*) suggest that surface temperatures in the majority of the high-latitude craters with RB deposits that MLA has observed to date are too warm to support persistent water ice at the surface, but the temperatures in their shadowed areas are compatible with the presence of surficial dark organic material. Modeled subsurface temperatures in these dark regions are permissive of stable water ice beneath a ~10-cm-thick layer of thermally insulating material. In contrast, thermal modeling of the bright areas is supportive of surface water ice. This interpretation of the surface reflectance at 1064 nm is fully consistent with the radar results as well as with neutron spectroscopic measurements of Mercury's polar regions (*26*). The bright and dark areas can be ascribed collectively to the deposition of water and organic volatiles derived from the impacts of comets or volatile-rich asteroids on Mercury's surface and migrated to polar cold traps via thermally stimulated random walk (*27*–*29*).

References and Notes

1. M. T. Zuber *et al.*, *Science* **336**, 217 (2012).
2. A. R. Vasavada, D. A. Paige, S. E. Wood, *Icarus* **141**, 179 (1999).
3. K. Watson, B. C. Murray, H. Brown, *J. Geophys. Res.* **66**, 3033 (1961).
4. J. R. Arnold, *J. Geophys. Res.* **84**, 5659 (1979).
5. M. A. Slade, B. J. Butler, D. O. Muhleman, *Science* **258**, 635 (1992).
6. J. K. Harmon, M. A. Slade, *Science* **258**, 640 (1992).
7. B. J. Butler, D. O. Muhleman, M. A. Slade, *J. Geophys. Res.* **98**, 15,003 (1993).
8. G. J. Black, D. B. Campbell, J. K. Harmon, *Icarus* **209**, 224 (2010).
9. J. K. Harmon, M. A. Slade, M. S. Rice, *Icarus* **211**, 37 (2011).
10. J. F. Cavanaugh *et al.*, *Space Sci. Rev.* **131**, 451 (2007).
11. The MLA is a time-of-flight laser range finder that uses direct detection and pulse-edge timing to determine precisely the range from the MESSENGER spacecraft to Mercury's surface. MLA's laser transmitter emits 6-ns-long pulses at an 8-Hz rate with 20 mJ of energy at a wavelength of 1064 nm. Return echoes are collected by an array of four refractive telescopes and are detected with a single silicon avalanche photodiode detector. The timing of laser pulses is measured with a set of time-to-digital converters linked to a crystal oscillator for which the frequency is monitored from Earth.
12. S. C. Solomon, R. L. McNutt Jr., R. E. Gold, D. L. Domingue, *Space Sci. Rev.* **131**, 3 (2007).
13. M. J. Talpe *et al.*, *J. Geophys. Res.* **117**, E00L13 (2012).
14. G. B. Hansen, T. B. McCord, *J. Geophys. Res.* **109**, E01012 (2004).
15. The MLA measures the threshold crossing times of the received pulses at two discriminator voltages simultaneously, a low threshold for maximum sensitivity and a threshold about twice as high to give four sample points of the received pulse waveform. A laser pulse may result in triggers at one or both thresholds or not at all. Ranging with low-threshold detections is possible at ranges up to 1500 km, but steady returns that cross both low and high thresholds are obtained mostly at altitudes less than ~600 km and with near-nadir (<20°) incidence. When a pulse is detected by a pair of discriminators, its energy and duration may be inferred from a model waveform that accounts for the dispersion in time of return pulses as a result of surface slope and/or roughness. To estimate the pulse energy, we adopted a simple triangular model that fits the rising and falling edges of the trigger at each threshold. This model generates values nearly equal to a Gaussian model for well-constrained pulses. Energy is a nonlinear function of pulse timing measurements and tends to have a long-tailed or approximate log-normal distribution, as illustrated in the supplementary materials.
16. C. S. Gardner, *IEEE Trans. Geosci. Rem. Sens.* **30**, 1061 (1992).
17. The lidar link equation is $E_{rx} = E_{tx}\eta_r(A_r/R^2)(r_s/\pi)$, where E_{rx} is the received signal pulse energy, E_{tx} is the transmitted laser pulse energy, η_r is the receiver optics transmission, A_r is the receiver telescope aperture area, R is range, and r_s is the target surface reflectivity (relative to Lambertian). The ratio r_s of reflected energy to incoming energy (i.e., irradiance/solar flux, often simply written *I/F*) would be unity for a perfect diffusive reflector for which the transmitter and receiver orientation are perpendicular to the surface. Mercury's reflectivity at optical wavelengths normally lies in a range from 0.08 to 0.12 (*30*–*32*), but because of the opposition effect (*33*) the average 1064-nm reflectance is about 50% higher, or about 0.17.
18. J. K. Harmon, P. J. Perillat, M. A. Slade, *Icarus* **149**, 1 (2001).
19. The topography derived from 700 MLA profiles (29 March 2011 to 1 May 2012) provides a near-complete topographic map of the northern hemisphere northward to 84°N at a resolution of 0.5 km. Craters Prokofiev and Kandinsky were sampled by several off-nadir profiles, from which radial averages of topography were constructed and used to fill in the unsampled interior after adding pseudo-random noise, with a root variance of 70 m, and decimating and interpolating with the blockmedian and surface programs of the Generic Mapping Tools (http://gmt.soest.hawaii.edu). We modeled the average and maximum illumination conditions over a Mercury day by using an approach (*20*) developed to assess illumination conditions of polar regions of the Moon.
20. E. Mazarico, G. A. Neumann, D. E. Smith, M. T. Zuber, M. H. Torrence, *Icarus* **211**, 1066 (2011).
21. A. Mallama, D. Wang, R. A. Howard, *Icarus* **155**, 253 (2002).
22. We selected 175 representative regions of interest from maps of permanent shadow derived from MLA topography, radar cross section, and MLA-dark regions, as shown in the supplementary materials. Because

many craters are not resolved by MLA, we also selected craters with diameters ≥7 km from MESSENGER images. Smaller RB deposits were not considered because most appear from images to lie in small secondary craters, at the foot of poleward-facing scarps, or in rough terrain and are inadequately sampled by MLA. The radar-bright deposits were mapped with a threshold of 0.075 in the MATLAB image processing toolbox and correlated with craters identified in MLA topography and MESSENGER images. Labels assigned in uppercase are consistent with previous nomenclature (*15*); lowercase letters and numerals were assigned to provisional features. Regions with MLA energy measurements were classified as dark, normal, or bright/mixed according to their contrast in brightness with those of surround areas; gaps in high-threshold returns were also taken to indicate darker material. Bright regions are surrounding those for which more than half of the returns have $r_s > 0.3$.

23. Diameters of large craters were fit to the maximum MLA topographic contours of the rims, whereas the diameters of smaller craters were estimated from Mercury Dual Imaging System (*34*) image mosaics. Locations are less certain for smaller features inadequately sampled by MLA. Diameters of craters sampled ranged from 7 to 108 km, not including the 320-km-diameter Goethe basin. Not included are several degraded and partially flooded craters, such as a 133-km-diameter degraded crater that encloses Purcell but for which the relief does not create an area of permanent shadow.
24. D. A. Paige, S. E. Wood, A. R. Vasavada, *Science* **258**, 643 (1992).
25. D. A. Paige *et al.*, *Science* **339**, 300 (2013); 10.1126/science.1231106.
26. D. J. Lawrence *et al.*, *Science* **339**, 292 (2013); 10.1126/science.1229953.
27. B. J. Butler, *J. Geophys. Res.* **102**, 19,283 (1997).
28. J. A. Zhang, D. A. Paige, *Geophys. Res. Lett.* **36**, L16203 (2009).
29. J. A. Zhang, D. A. Paige, *Geophys. Res. Lett.* **37**, L03203 (2010).
30. T. B. McCord, J. B. Adams, *Science* **178**, 745 (1972).
31. F. Vilas, *Icarus* **64**, 133 (1985).
32. W. E. McClintock *et al.*, *Science* **321**, 62 (2008).
33. T. Gehrels, *Astrophys. J.* **123**, 331 (1956).
34. S. E. Hawkins III *et al.*, *Space Sci. Rev.* **131**, 247 (2007).

Acknowledgments: The MESSENGER project is supported by the NASA Discovery Program under contracts NAS5-97271 to the Johns Hopkins University Applied Physics Laboratory and NASW-00002 to the Carnegie Institution of Washington. We are grateful for the myriad of contributions from the MLA instrument and MESSENGER spacecraft teams and for comments by P. Lucey and two anonymous referees that improved the manuscript.

Supplementary Materials

www.sciencemag.org/cgi/content/full/science.1229764/DC1
Supplementary Text
Figs. S1 to S5
Reference (*35*)

5 September 2012; accepted 14 November 2012
Published online 29 November 2012;
10.1126/science.1229764

Thermal Stability of Volatiles in the North Polar Region of Mercury

David A. Paige,[1]* Matthew A. Siegler,[1,2] John K. Harmon,[3] Gregory A. Neumann,[4] Erwan M. Mazarico,[4] David E. Smith,[5] Maria T. Zuber,[5] Ellen Harju,[1] Mona L. Delitsky,[6] Sean C. Solomon[7,8]

Thermal models for the north polar region of Mercury, calculated from topographic measurements made by the MErcury Surface, Space ENvironment, GEochemistry, and Ranging (MESSENGER) spacecraft, show that the spatial distribution of regions of high radar backscatter is well matched by the predicted distribution of thermally stable water ice. MESSENGER measurements of near-infrared surface reflectance indicate bright surfaces in the coldest areas where water ice is predicted to be stable at the surface, and dark surfaces within and surrounding warmer areas where water ice is predicted to be stable only in the near subsurface. We propose that the dark surface layer is a sublimation lag deposit that may be rich in impact-derived organic material.

Earth-based radar observations have yielded maps of anomalously bright, depolarizing features on Mercury that appear to be localized in permanently shadowed regions near the planet's poles (*1*, *2*). Observations of similar radar signatures over a range of radar wavelengths imply that the radar-bright features correspond to deposits that are highly transparent at radar wavelengths and extend to depths of several meters below the surface (*3*). Cold-trapped water ice has been proposed as the most likely material to be responsible for these features (*2*, *4*, *5*), but other volatile species that are abundant on Mercury, such as sulfur, have also been suggested (*6*).

[1]Department of Earth and Space Sciences, University of California, Los Angeles, CA 90095, USA. [2]Jet Propulsion Laboratory, Pasadena, CA 91109, USA. [3]National Astronomy and Ionosphere Center, Arecibo, PR 00612, USA. [4]NASA Goddard Space Flight Center, Greenbelt, MD 20771, USA. [5]Department of Earth, Atmospheric and Planetary Sciences, Massachusetts Institute of Technology, Cambridge, MA 02139, USA. [6]California Specialty Engineering, Flintridge, CA 91012, USA. [7]Department of Terrestrial Magnetism, Carnegie Institution of Washington, Washington, DC 20015, USA. [8]Lamont-Doherty Earth Observatory, Columbia University, Palisades, NY 10964, USA.

*To whom correspondence should be addressed. E-mail: dap@moon.ucla.edu

Measurements of surface reflectance at a wavelength of 1064 nm, made with the Mercury Laser Altimeter (MLA) onboard the MESSENGER (MErcury Surface, Space ENvironment, GEochemistry, and Ranging) spacecraft, have revealed the presence of surface material that collocates approximately with radar-bright areas within north polar craters and that has approximately half the average reflectance of the planet, as well as bright material within Kandinsky and Prokofiev craters that has approximately twice the average planetary reflectance (*7*). MLA measurements have also provided detailed maps of the topography of Mercury's north polar region (*8*). Here, we apply this information in conjunction with a ray-tracing thermal model, previously used to predict temperatures in the polar regions of Earth's Moon (*9*), to calculate the thermal stability of volatile species in the north polar region of Mercury.

Maximum and average modeled temperatures (*10*) over one complete 2-year illumination cycle for the north polar region of Mercury are shown in Fig. 1, A and B. The topography model north of 84°N latitude has been extrapolated from only a few off-nadir data tracks, so model temperatures within this circle should be taken only as estimates. On Mercury, biannual average temperatures can be interpreted as close approximations to the nearly constant subsurface temperatures that exist below the penetration depths of the diurnal temperature wave [about 0.3 to 0.5 m for ice-free regolith, and several meters for ice-rich areas (*5*, *9*)]. The latitudinal and longitudinal symmetries in surface and near-surface temperatures result from Mercury's near-zero obliquity, eccentric orbit, and 3:2 spin-orbit resonance (*11*, *12*).

Comparison between the areal coverage of model-calculated biannual maximum and average temperatures and the thermal stability of a range of candidate volatile species (Fig. 2) provides strong evidence that Mercury's anomalous radar features are due dominantly to the presence of thermally stable water ice, rather than some other candidate frozen volatile species. Within the region sampled, the vast majority of locations within which biannual average temperatures are less than ~100 K are radar-bright, whereas for areas with biannual average temperatures of greater than 100 K there are almost no radar-bright deposits (Fig. 2C). This distribution suggests that the radar-bright features are due to the presence of a volatile species that is not thermally stable at temperatures higher than ~100 K. Because of the exponential dependence of vacuum sublimation loss rates with temperature, the thermal stabilities of the candidate volatile species shown in Fig. 2A over time scales of millions to billions of years are well separated in temperature. As shown in Fig. 2A and fig. S8, 1 mm of exposed water ice—or 1 mm of water ice buried beneath a 10-cm-thick lag deposit—would sublimate to a vacuum in 1 billion years at temperatures of 100 to 115 K, which we interpret as strong evidence that Mercury's anomalous radar features are due dominantly to the presence of thermally stable water ice. If the radar-bright deposits were composed primarily of a material with a higher or lower volatility than water ice, we would expect them to be thermally stable in areas with lower or higher annual average temperatures than we observe. As illustrated in Fig. 2, B and C, the fractional areal coverage of radar-bright regions that are also just sufficiently

cold to trap subsurface water is nearly unity, whereas for elemental sulfur, the fractional area is less than 1 in 500. Although the temperatures of Mercury's radar-bright regions are not a good match to thermal stability temperatures of sulfur, the existence of cold traps at lower latitudes dominated by sulfur and other less volatile cold-trapped species cannot be excluded, nor can the possibility that Mercury's water-ice cold traps themselves also contain minor quantities of less volatile cold-trapped species.

The calculated depths at which near-surface water ice would be lost to sublimation at a rate of less than 1 mm per billion years, under the assumption that the ice deposits are covered by material that has the same thermophysical properties as average surface material on Mercury (*5*, *10*), are shown in Fig. 1C. The thermal model results predict that most of Mercury's water ice deposits equatorward of 83°N would be thermally stable only if buried beneath a ~10-cm-thick layer of low-conductivity, ice-free, soil-like material—a result consistent with interpretations of available radar data (*3*). At higher latitudes, the thermal model results predict that temperatures in larger impact craters are sufficiently cold to permit the stability of surface ice deposits. The observation of anomalously high MLA surface reflectance values in Kandinsky and Prokofiev craters (*7*) is consistent with the interpretation that the polar deposits in those craters contain water ice exposed at the surface.

Comparisons of the areal coverage of model-calculated biannual maximum and average temperatures for MLA-dark areas to all areas measured by MLA in the circumpolar region 75° to 83°N are shown in Fig. 2, D and E. The MLA-dark regions display a wider range of temperatures and are spatially more extensive than the radar-bright regions, even after accounting for Earth visibility. Area ratios for biannual maximum temperatures in MLA-dark regions peak near 0.8 at ~160 K and decrease rapidly at progressively lower temperatures. We interpret this trend as indicating an increasing tendency for the thermal stability of bright surface water ice deposits as biannual maximum temperatures approach 100 K, which we document in an unusually cold impact crater at 82.0°N, 215°E (fig. S3).

In total, the results of the thermal model calculations combined with radar and MLA reflectance measurements present a quantitatively consistent case that Mercury's polar deposits are composed dominantly of water ice. This conclusion is independently reinforced by measurements of the flux of fast and epithermal neutrons made with MESSENGER's Neutron Spectrometer (*13*). In the region studied, radar-bright deposits are observed to be in essentially every surface and subsurface location where water ice is thermally

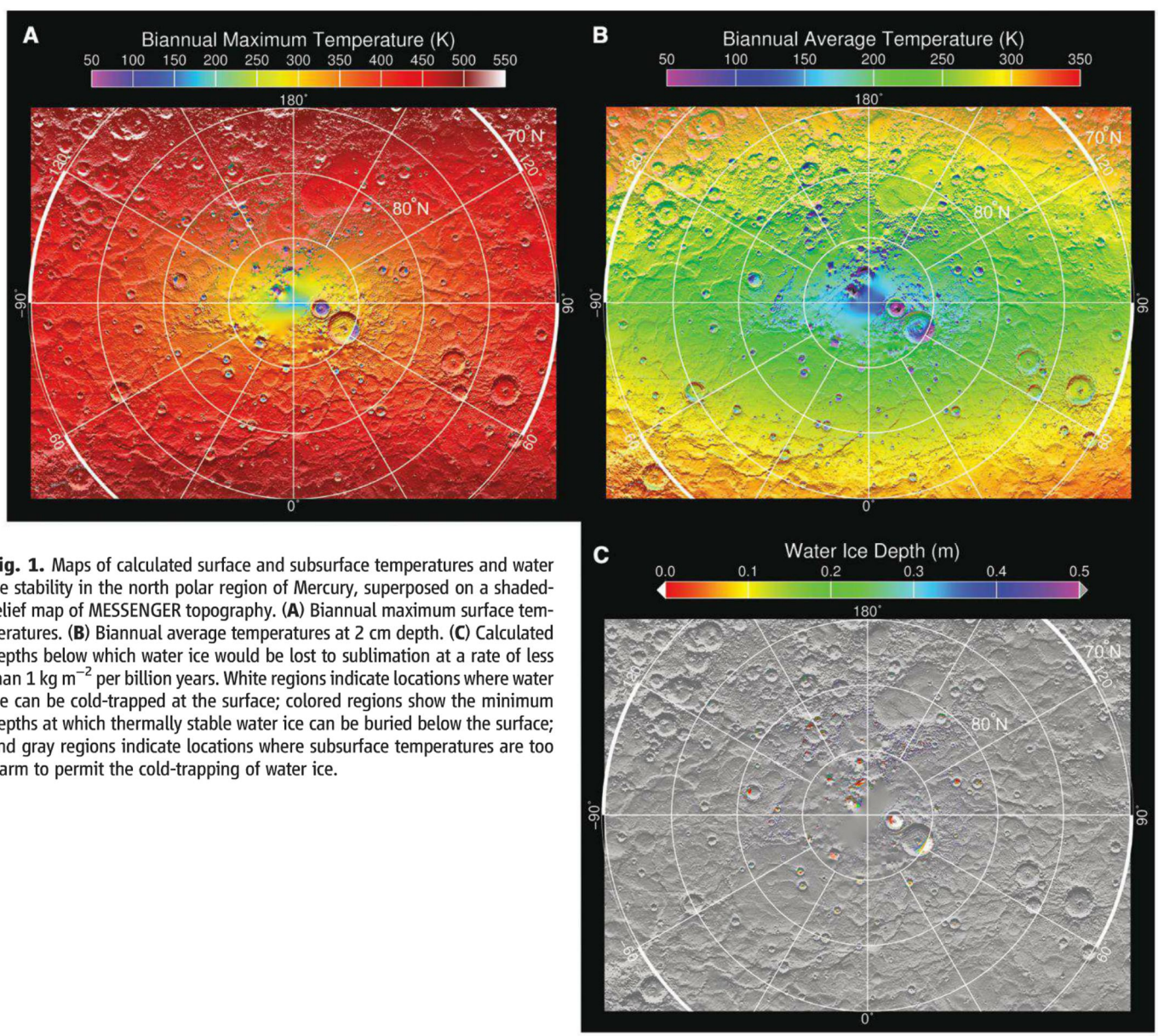

Fig. 1. Maps of calculated surface and subsurface temperatures and water ice stability in the north polar region of Mercury, superposed on a shaded-relief map of MESSENGER topography. (**A**) Biannual maximum surface temperatures. (**B**) Biannual average temperatures at 2 cm depth. (**C**) Calculated depths below which water ice would be lost to sublimation at a rate of less than 1 kg m^{-2} per billion years. White regions indicate locations where water ice can be cold-trapped at the surface; colored regions show the minimum depths at which thermally stable water ice can be buried below the surface; and gray regions indicate locations where subsurface temperatures are too warm to permit the cold-trapping of water ice.

stable, despite the activity of such ice destruction processes as Lyman α photodissociation (*14*) and burial by meteoroid gardening (*15*). Calculated temperatures in the coldest locations on Mercury are sufficiently low that water molecules in these cold traps have very little diffusive mobility (*16*). The fact that bright surface ice deposits are observed in these locations requires a geologically recent or ongoing supply of water. In regions of currently stable ground ice, temperatures are sufficiently warm to allow for diffusive vertical and lateral mobility of water (*17*), which has enabled water to actively migrate to sites of present thermal stability.

The thermal model results provide insights into the nature and origin of MLA-dark surface deposits. Figure 2D shows that equatorward of 84°N dark material is found almost universally in regions with biannual average temperatures of 100 K and biannual maximum temperatures of 160 K, but dark material is entirely absent in regions with biannual average temperatures greater than 210 K and biannual maximum temperatures greater than 300 K. This systematic temperature dependence would not be apparent if the dark material were being redistributed about this region by impact processes alone. The distribution of dark material must be controlled by the presence of volatile substances that are not thermally stable above these temperatures. Given the clear association between the dark material and water ice that exists on Mercury today, we suggest that one of these volatile substances is water. As shown in Fig. 2A and fig. S7, the temperature at which a water ice deposit can be considered thermally stable depends on the time scale under consideration. At a temperature of 102 K, for instance, a meter-thick layer of pure water ice would sublimate to space in 1 billion years, whereas at a temperature of 210 K, a meter-thick layer of pure water ice would sublimate in 35 days.

We suggest that the MLA-dark deposits are largely sublimation lags formed on the surfaces of metastable water ice—that is, that Mercury's polar deposits were more extensive at some point in the past, and then retreated rapidly to their present long-term thermally stable state. Because Mercury's low obliquity [2.04 ± 0.08 arc min (*18*)] is likely to have persisted since its capture into a Cassini state >3.5 billion years ago (*19*), thermal conditions at Mercury's poles have been relatively stable. The formation of the MLA-dark deposits by sublimation lag requires episodic, but temporally coincident, sources of both water and nonwater contaminants. Because metastable ice deposits must accumulate on time scales that are shorter than those at which they sublimate, the formation of the MLA-dark deposits by sublimation lag is compatible with episodic deposition of water and other volatiles by asteroids and comets.

The composition of the MLA-dark deposits is not known. However, materials with similarly low albedos are routinely observed on the surfaces of comets (*20*, *21*), asteroids (*22*–*24*), and outer solar system objects (*25*, *26*) and are generally attributed to the presence of macromolecular carbonaceous material, rather than to the effects of radiation damage of pure ice (*22*, *24*–*26*). As shown in Fig. 2, the thermal stability temperatures of a selection of simple organic compounds are such that if they were present in the Mercury polar environment, they would be readily incorporated into accumulating water ice deposits and cold-trapped directly onto surrounding warmer regions. The processing of simple organic material into dark macromolecular carbonaceous material is facilitated by high-energy photons and particles (*10*, *27*–*31*), which are abundant in Mercury's polar environment because of the configuration of magnetic field lines and the pattern of ion precipitation at Mercury's high latitudes (*10*, *32*, *33*). Under this scenario, asteroidal and cometary impacts episodically release water and simple organic compounds into the Mercury environment, where they migrate to the polar regions, become cold-trapped, and accumulate. The mixture of water ice and organic material sublimates and is reprocessed to form a dark sublimation lag deposit that is analogous to that observed on the surfaces of comet nuclei today. The radar absorption properties of low-density macromolecular carbonaceous material have been measured and are found to be less lossy than low-density soil (*34*). Therefore, the presence of a layer of organic-rich material overlying ground ice deposits, or the presence of minor concentrations of organic-rich material within ice deposits, is not inconsistent with available radar observations. The possibility for synthesis of organic compounds in the permanently shadowed regions of Earth's Moon has been suggested (*35*), and the spectroscopic detection of simple organic compounds during the impact of the Lunar Crater

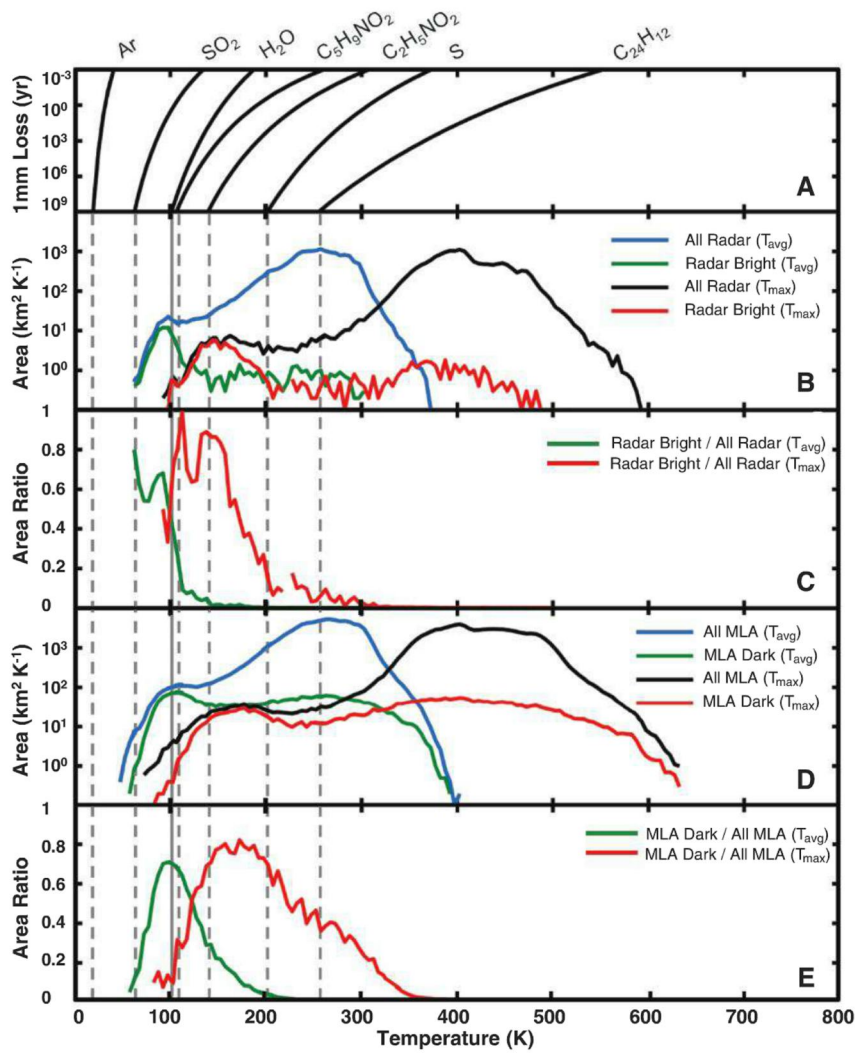

Fig. 2. Histograms of calculated biannual maximum (T_{max}) and biannual average (T_{avg}) temperatures for radar-bright and MLA-dark areas in the north polar region of Mercury compared with the stability temperatures of a range of candidate volatile species. (**A**) Vacuum sublimation loss times for 1-mm-thick pure layers of selected cold-trapped volatile species as a function of temperature (*37*, *38*). (**B** and **C**) Temperature histograms and areal coverage for radar-bright areas within Earth-visible areas at the times of the radar measurements in the region 75° to 83°N, 30° to 90°E (*39*). (**D** and **E**) Temperature histograms and areal coverage for MLA-dark areas for the region 75° to 83°N.

Observation and Sensing Satellite (*36*) provides further evidence that organic material and organic precursors coexist within the polar cold traps of solar system airless bodies.

Forming Mercury's ground ice deposits via the sublimation of a mixture of water ice and organic contaminants solves a long-standing problem regarding their origin. Today, thick deposits of ground ice are found near 75°N in areas with biannual maximum surface temperatures in excess of 150 K. At these temperatures, pure exposed water ice deposited by a cometary impact would sublimate at a rate of 1 m per 1000 years. The ice deposit would disappear on time scales of tens of thousands of years if not thermally protected by a ~10-cm-thick layer of overlying ice-free material, but this geometry is problematic because the time scales for burial to these depths by impact-gardened soil from adjacent regions is estimated to be on the order of tens of millions of years (*3*, *15*). If Mercury's ground ice deposits contain sufficient less-volatile cold-trapped contaminants to create a surface lag deposit as they sublimate, then it would not be necessary to invoke a recent cometary impact to explain their present vertical and horizontal distribution. The fact that all of Mercury's surface and subsurface water ice deposits appear to be in a thermally stable configuration means that the sources of water and the mobility of water in Mercury's environment are sufficiently robust to overcome the combined effects of all other processes that would tend to destroy and disrupt them.

References and Notes

1. M. A. Slade, B. J. Butler, D. O. Muhleman, *Science* **258**, 635 (1992).
2. J. K. Harmon, M. A. Slade, M. S. Rice, *Icarus* **211**, 37 (2011).
3. J. K. Harmon, *Space Sci. Rev.* **132**, 307 (2007).
4. D. A. Paige, S. E. Wood, A. R. Vasavada, *Science* **258**, 643 (1992).
5. A. R. Vasavada, D. A. Paige, S. E. Wood, *Icarus* **141**, 179 (1999).
6. A. L. Sprague, D. M. Hunten, K. Lodders, *Icarus* **118**, 211 (1995).
7. G. A. Neumann *et al.*, *Science* **339**, 296 (2013); 10.1126/science.1229764.
8. M. T. Zuber *et al.*, *Science* **336**, 217 (2012).
9. D. A. Paige *et al.*, *Science* **330**, 479 (2010).
10. See supplementary materials on *Science* Online.
11. S. Soter, J. Ulrichs, *Nature* **214**, 1315 (1967).
12. Despite the extreme range of surface temperatures on Mercury, Fig. 1B indicates that there exists a ~4°-wide circumpolar zone with annual average temperatures between 273 and 373 K, a potential near-surface environment for liquid water that is the most extensive in the solar system outside Earth.
13. D. J. Lawrence *et al.*, *Science* **339**, 292 (2013); 10.1126/science.1229953.
14. T. H. Morgan, D. E. Shemansky, *J. Geophys. Res.* **96**, 1351 (1991).
15. D. Crider, R. M. Killen, *Geophys. Res. Lett.* **32**, L12201 (2005).
16. N. Schorghofer, G. J. Taylor, *J. Geophys. Res.* **112**, E02010 (2007).
17. M. A. Siegler, B. G. Bills, D. A. Paige, *J. Geophys. Res.* **116**, E03010 (2011).
18. J. L. Margot *et al.*, *J. Geophys. Res.* **117**, E00L09 (2012).
19. S. J. Peale, *Astrophys. J.* **79**, 722 (1974).
20. R. Z. Sagdeev *et al.*, *Nature* **321**, 262 (1986).
21. H. U. Keller, L. Jorda, in *The Century of Space Science*, J. A. M. Bleeker, J. Geiss, M. Huber, Eds. (Kluwer Academic, Dordrecht, Netherlands, 2001), vol. 2, pp. 1235–1276.
22. J. Gradie, J. Veverka, *Nature* **283**, 840 (1980).
23. E. F. Tedesco *et al.*, *Astron. J.* **97**, 580 (1989).
24. J. F. Bell, D. R. Davis, W. K. Hartmann, M. J. Gaffey, in *Asteroids II*, R. P. Binzel, T. Gehrels, M. S. Matthews, Eds. (Univ. of Arizona Press, Tucson, AZ, 1989), pp. 921–945.
25. D. P. Cruikshank, C. M. Dalle Ore, *Earth Moon Planets* **92**, 315 (2003).
26. D. P. Cruikshank, T. L. Roush, M. J. Bartholomew, T. R. Geballe, Y. J. Pendleton, *Icarus* **135**, 389 (1998).
27. D. L. Mitchell *et al.*, *Icarus* **98**, 125 (1992).
28. R. E. Johnson, J. F. Cooper, L. J. Lanzerotti, G. Strazzulla, *Astron. Astrophys.* **187**, 889 (1987).
29. L. J. Lanzerotti *et al.*, *J. Geophys. Res.* **92**, 14949 (1987).
30. R. E. Johnson, *J. Geophys. Res.* **96**, 17553 (1991).
31. R. E. Johnson, in *Solid-State Astrophysics, Enrico Fermi Series*, G. Strazzula, E. Bussoletti, Eds. (North Holland, Amsterdam, 1991), pp. 129–168.
32. J. A. Slavin *et al.*, *Science* **324**, 606 (2009).
33. N. Mouawad *et al.*, *Icarus* **211**, 21 (2011).
34. P. Paillou *et al.*, *Geophys. Res. Lett.* **35**, L18202 (2008).
35. P. G. Lucey, *Proc. SPIE* **4137**, 84 (2000).
36. A. Colaprete *et al.*, *Science* **330**, 463 (2010).
37. J. A. Zhang, D. A. Paige, *Geophys. Res. Lett.* **36**, L16203 (2009).
38. J. A. Zhang, D. A. Paige, *Geophys. Res. Lett.* **37**, L03203 (2010).
39. This region was selected because it has the highest density of Earth-based radar measurements at the most favorable viewing geometries.

Acknowledgments: Supported by NASA grant NNX07AR64G. We thank L. Carter, A. McEwen, D. Schriver, and M. Slade for assistance with this research. The MESSENGER project is supported by the NASA Discovery Program under contract NAS5-97271 to The Johns Hopkins University Applied Physics Laboratory and NASW-00002 to the Carnegie Institution of Washington. MESSENGER data used in this study are available through the NASA Planetary Data System Geosciences Node. Arecibo radar data used in this study are available at www.naic.edu/~radarusr/Mercpole.

Supplementary Materials

www.sciencemag.org/cgi/content/full/science.1231106/DC1
Materials and Methods
Figs. S1 to S8
References (*40*–*56*)

4 October 2012; accepted 14 November 2012
Published online 29 November 2012;
10.1126/science.1231106

An Efficient Polymer Molecular Sieve for Membrane Gas Separations

Mariolino Carta,[1] Richard Malpass-Evans,[1] Matthew Croad,[1] Yulia Rogan,[1] Johannes C. Jansen,[2] Paola Bernardo,[2] Fabio Bazzarelli,[2] Neil B. McKeown[1]*

Microporous polymers of extreme rigidity are required for gas-separation membranes that combine high permeability with selectivity. We report a shape-persistent ladder polymer consisting of benzene rings fused together by inflexible bridged bicyclic units. The polymer's contorted shape ensures both microporosity—with an internal surface area greater than 1000 square meters per gram—and solubility so that it is readily cast from solution into robust films. These films demonstrate exceptional performance as molecular sieves with high gas permeabilities and good selectivities for smaller gas molecules, such as hydrogen and oxygen, over larger molecules, such as nitrogen and methane. Hence, this polymer has excellent potential for making membranes suitable for large-scale gas separations of commercial and environmental relevance.

Commercially important membrane-based gas separations include O_2 and N_2 enrichment of air, hydrogen recovery from ammonia production or hydrocarbon processing, and the upgrading of natural gas (*1*). They also have potential for both post-combustion and pre-combustion CO_2 capture during electricity generation from fossil fuels (*2*, *3*). Polymer membranes provide an energy-efficient method for gas separations because they do not require thermal regeneration, a phase change, or active moving parts in their operation and as such are predicted to play a growing role in an energy-constrained and low-carbon future (*4*). However, polymers suffer from a well-defined trade-off between the desirable properties of permeability and selectivity for the required gas component. Presently, most commercial gas-separation membranes are based on a few polymers with low permeability and high selectivity; therefore, large membrane areas are required to compensate for lack of permeance, which increases costs and space requirements for large-scale applications. Unfortunately, highly permeable microporous polymers demonstrate insufficient selectivity for practical applications because, unlike classical molecular sieves such as zeolites, they possess ill-defined voids that because of chain flexibility fluctuate in size and so have limited size-selectivity (*5*). However, microporous polymers have the great advantage over classical inorganic molecular sieve materials of being easily processed into membranes (such as thin coatings or hollow fibers). Therefore, it is an important challenge to develop microporous polymers that behave as efficient

[1]School of Chemistry, Cardiff University, Cardiff CF10 3AT, UK. [2]Institute on Membrane Technology, Consiglio Nazionale delle Ricerche, ITM-CNR, c/o University of Calabria, Via P. Bucci 17/C, 87030 Rende (CS), Italy.

*To whom correspondence should be addressed. E-mail: mckeownnb@cardiff.ac.uk.

molecular sieves so that they can provide both the permeability and selectivity to support large-scale gas separations.

Robeson used data from a very large number of polymers to quantify the trade-off between single gas permeability (P_x) and ideal selectivity ($\alpha_{xy} = P_x/P_y$) for a number of gas pairs (*6*, *7*). Empirical upper bounds in plots of $log\ \alpha_{xy}$ versus $log\ P_x$ were established, and the position of data points of new polymers relative to these upper bounds is used routinely as an indicator of their potential performance for gas separations. In effect, the positions of the upper bounds represent the state of the art for approaching true molecular sieve behavior in polymers. Hence, rigid glassy polymers that facilitate size-selective gas diffusivity through reduced chain mobility, especially those composed of fused-ring ladder-like structures such as polymers of intrinsic microporosity (PIMs; PIM-1, for example) (Fig. 1C), help to define the present upper bounds (*6*, *8*). Freeman's theoretical analysis of the position of the upper bounds suggests that further enhancement in gas selectivities could be achieved by designing polymers with even greater shape persistence (*9*). Recently, we tested this prediction by making a PIM in which the relatively flexible spirobisindane (SBI) component of PIM-1 was replaced with the more rigid spirobifluorene unit (PIM-SBF). The enhanced gas selectivities demonstrated by PIM-SBF resulted in data with modest advances above the current Robeson upper bounds for most gas pairs of interest (*10*). However, because of the inherent flexibility of the spiro-centers and dioxan linking groups used to assemble these PIMs (*11*), a fundamental structural redesign is required to provide microporous polymers that offer substantial further increases in rigidity and performance.

Molecular modeling of potential structural components for assembling polymers with greater shape-persistence suggests that bridged bicyclic ring systems, such as ethanoanthracene (EA), are highly inflexible when compared with the spiro-centers and dioxan rings used commonly within PIMs (Fig. 1D). However, devising an efficient polymerization reaction on the basis of forming bridged bicyclic linking groups is a difficult synthetic challenge because of the need for the simultaneous formation of multiple covalent bonds. With this challenge in mind, we noted that the bridged bicyclic amine 2,8-dimethyl-6H,12H-5,11-methanodibenzo[b,f][1,5]diazocine, commonly called Tröger's base (TB), can be prepared in excellent yield, despite requiring the participation of five precursor molecules and the net formation of six covalent bonds for its construction (*12*). TB was originally reported in 1887 after its serendipitous isolation from the reaction between *p*-toluidine and dimethoxymethane (*13*) and has since been the subject of numerous studies because of its interesting stereochemistry (*14*), supramolecular chemistry (*15*, *16*), and strongly basic nature for organocatalysis (*17*). However, TB has rarely been used as a component for polymer construction (*18*, *19*), and these previous studies involved preformed TB monomers rather than in situ formation of the TB unit during the polymerization reaction. The rigidity conferred on TB by its bridged bicyclic structure was confirmed through modeling (Fig. 1D); therefore, it was anticipated that polymers prepared by using TB polymerization from suitably rigid aromatic diamine monomers would be highly shape-persistent. Hence, we designed two monomers, 2,6(7)-diamino-9,10-dimethylethanoanthracene and 5,5′,(6),(6′)-diamino-3,3,3′,3′-tetramethyl-1,1′-spirobisindane, to assess the efficiency of the proposed TB polymerization reaction and, if successful, to provide PIM-like fused-ring macromolecular structures.

Once synthesized, each monomer was subsequently reacted with five equivalents of dimethoxymethane in trifluoroacetic acid (TFA) at

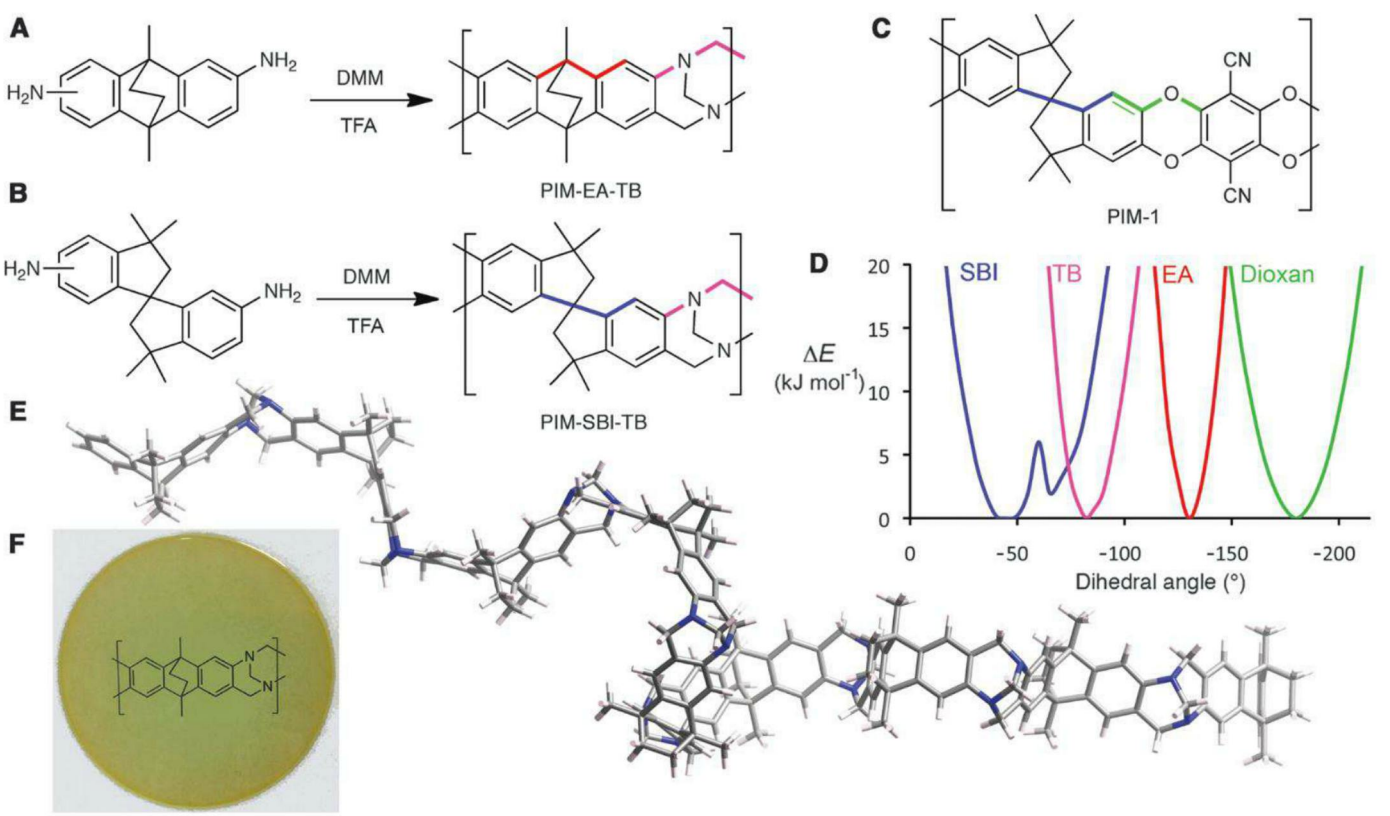

Fig. 1. The synthesis and molecular structures of (**A**) PIM-EA-TB and (**B**) PIM-SBI-TB (DMM, dimethoxymethane; TFA, trifluoroacetic acid). (**C**) The structure of PIM-1, the archetypal PIM. (**D**) A plot showing the increase in energy associated with the deviation in the marked dihedral angle within the bridged bicyclic units of EA (red) and TB (purple) as compared with typical components of PIMs, such as the spiro-center of SBI (blue) and the dioxan linking unit (green). The narrower energy wells of the bridged bicyclic units TB and EA demonstrate their greater rigidity. (**E**) A molecular model of PIM-EA-TB showing its contorted shape, which combined with its rigidity generates intrinsic microporosity due to an inability to pack efficiently in the solid state. (**F**) A solvent-cast film (10 cm in diameter) of PIM-EA-TB, through which is visible its molecular structure printed on a piece of paper.

ambient temperature (Fig. 1, A and B) until the solutions became too viscous to stir (*20*, *21*). Each of the resulting colorless polymers proved highly soluble in chloroform, which can be attributed to their highly contorted macromolecular structures (Fig. 1E). This allowed for analysis by means of gel permeation chromatography (GPC), which indicated that the TB polymerization reaction yields polymers of high average molecular mass—typically, number-average molecular weight (M_n) > 40,000 and weight-average molecular weight (M_w) > 100,000—relative to polystyrene standards (fig. S1). The polymers as reprecipitated powders demonstrate intrinsic microporosity by nitrogen adsorption at low pressure, at 77 K (fig. S2). Apparent BET (Brunauer, Emmett, Teller) surface areas of 1028 $m^2\ g^{-1}$ for the ethanoanthracene-based TB polymer (PIM-EA-TB) and 745 $m^2\ g^{-1}$ for the spirobisindane-based TB polymer (PIM-SBI-TB) were calculated from the isotherms. The apparent surface area for PIM-EA-TB is greater than for previously reported PIMs (*22*) or other solution-processable, amorphous microporous materials, such as those derived from molecular cages (*23*, *24*). Thermal gravimetric analysis (TGA) indicated that neither PIM-EA-TB nor PIM-SBI-TB lose mass below 260°C except for the loss of adsorbates below 100°C. They are also stable toward hydrolysis in mild aqueous acids and bases. Casting of chloroform solutions gave optically transparent films (Fig. 1F), of good mechanical strength (fig. S3), that proved suitable for gas permeability measurements.

The single gas permeabilities and ideal selectivities of PIM-EA-TB films of different thickness (91 and 180 μm), which had first been soaked in methanol and then dried in air at room temperature, are given in Table 1. Methanol (or ethanol) treatment has been shown previously to reverse the effects of physical aging for highly permeable glassy polymers and also to remove the last residues of casting solvent (*8*, *25*). Therefore, this treatment allows a direct comparison between the gas permeabilities of different polymers. The equivalent data for films of PIM-SBI-TB (128 and 157 μm), which had been treated under identical conditions to those of PIM-EA-TB, are also provided in Table 1 for comparison. The gas permeabilities of PIM-EA-TB are particularly high, which is consistent with its enhanced microporosity. As is generally the case for thicker films of glassy polymers (*26*, *27*), the gas permeabilities are higher, and selectivities are lower, and this is attributed to the smaller relative contribution of a more densely packed surface region of the film relative to thinner films. Unusually for a PIM, the order of gas permeabilities of PIM-EA-TB is $H_2 > CO_2 > He > O_2 > CH_4 > N_2$, whereas normally CO_2 permeates more than H_2, and O_2 permeates more than He (*5*), suggesting a greater preference for the transport of smaller gas molecules. PIM-SBI-TB has a much lower permeability and shows the usual trend for PIMs.

Table 1. Single gas permeability P_x, diffusivity D_x, solubility coefficient S_x, and their corresponding selectivities with respect to N_2 for methanol-treated films of PIM-EA-TB (181 μm) and PIM-SBI-TB (157 μm). Values for a thinner film (95 and 128 μm, respectively) are given between parentheses. Values for the 181-μm PIM-EA-TB film aged for 24 hours are given in square brackets. Each value is an average of two separate measurements on the same film. O_2/N_2 mixed gas permeability data through a 3-day-old 129-μm PIM-EA-TB film are given in curly brackets; these are an average of eight measurements over the pressure range up to 7 bar (fig. S4). Dashes indicate no units or not applicable.

Sample	Transport parameters	N_2	O_2	CO_2	CH_4	H_2	He
PIM-EA-TB	P_x [Barrer]	525	2150	7140	699	7760	2570
		(380)	(1630)	(5100)	(572)	(7310)	(2720)
		[370]	[1590]	[4780]	[502]	[6155]	[2070]
		{176}	{971}				
	α (P_x/PN_2) [—]	—	4.1	13.6	1.3	14.8	4.9
			(4.3)	(13.4)	(1.5)	(19.2)	(7.2)
			[4.3]	[12.9]	[1.4]	[16.6]	[5.6]
			{5.5}				
	D_x [10^{-12} m^2/s]	99.5	318	87	36	>7000*	>10000*
		(40.5)	(177)	(41)	(12)	(>5000)	(>6000)
		[49.1]	[210]	[60.7]	[14.9]	[>5000]	[>6000]
	D_x/DN_2 [—]	—	3.7	1.0	0.32	90	116
	S_x [$cm^3\ cm^{-3}\ bar^{-1}$]	4.7	6.0	57.0	14.8	<0.8*	<0.2*
		(7.0)	(6.9)	(92)	(35.5)	(<1.1)	(<0.3)
		[5.7]	[6.0]	[58.5]	[25.2]	(<1.1)	(<0.3)
	S_x/SN_2 [—]	—	1.1	12.0	4.3	<0.06	<0.02
PIM-SBI-TB	P_x [Barrer]	232	720	2900	450	2200	878
		(215)	(657)	(2720)	(406)	(2110)	(858)
	α (P_x/PN_2) [—]	—	3.1	12.5	1.9	9.4	3.8
			(3.1)	(12.7)	(1.9)	(9.8)	(4.0)
	D_x [10^{-12} m^2/s]	75.2	201	74	31.5	3500	>5000*
		(70.1)	(187)	(66)	(19.1)	(>3000)*	(>5000)*
	D_x/DN_2 [—]	—	2.7	1.0	0.35	45	69
	S_x [$cm^3\ cm^{-3}\ bar^{-1}$]	2.3	2.7	29.4	10.7	0.47	<0.12*
		(2.3)	(2.6)	(30.7)	(10.5)	(<0.5)	(<0.12)
	S_x/SN_2[—]	—	1.35	13	4.6	<0.20	<0.05

*For He and H_2, the very short time lag (<1 s) allows only an estimation of the minimum limit of D and maximum limit of S but are accurate for N_2, O_2, CO_2, and CH_4 (table S1).

The gas selectivities of PIM-EA-TB are remarkably high for such a permeable polymer, so that its data lie well above the 2008 Robeson upper bounds (*6*) for O_2/N_2, H_2/N_2, H_2/CH_4, and H_2/CO_2, each of which is of technological relevance (Fig. 2, A to D). This performance can be directly ascribed to the molecular sieving characteristics of PIM-EA-TB facilitating enhanced diffusivity selectivity (D_x/D_y) (Table 1) for molecules with smaller kinetic diameters (He = 2.69, H_2 = 2.89, and O_2 = 3.46 Å) over those of larger diameter (CO_2 = 3.3, N_2 = 3.64, and CH_4 = 3.87 Å). The improved performance relative to the upper bound is particularly evident for gas pairs that include H_2 (Fig. 1, B, C, and D). In addition, for H_2/N_2 and H_2/CH_4 the H_2 permeation is faster (7760 Barrer), and selectivities are higher ($\alpha H_2/N_2$ = 15 and $\alpha H_2/CH_4$ = 11) than for PIM-SBF (PH_2 = 6320 Barrer, $\alpha H_2/N_2$ = 8, and $\alpha H_2/CH_4$ = 6), which is the only other solution-processable polymer that provides data above the 2008 upper bounds for these gas pairs (*10*). Therefore, PIM-EA-TB has unrivalled potential for making highly permeable membranes for separations involving H_2, such as its recovery from ammonia production, hydrocarbon processing, or precombustion carbon capture. For the latter, it is likely that the modest H_2/CO_2 selectivity demonstrated at 25°C will be enhanced at the required elevated temperatures (150 to 200°C) because of a large reduction in CO_2 solubility that facilitates CO_2 transport at lower temperatures (*28*).

PIM-EA-TB also shows promise for the separation of O_2 from N_2 as permeability data surpass the 2008 upper bound (Fig. 2A). Hence, the performance of PIM-EA-TB for the O_2 enrichment of air was assessed over a range of feed pressures up to 7 bar by using a slightly aged (3-day-old) methanol-treated film of 181 μm thickness (fig. S4). The observed permeabilities of O_2 (900 to 1100 Barrer) and N_2 (160 to 205 Barrer) were almost independent of pressure and gave excellent O_2/N_2 selectivity (4.5 to 6.1). The rapid aging of PIM-EA-TB is a general feature of ultra-permeable polymers, but in this case, it is accompanied by a commensurate increase in selectivity so that a data point derived from the average of the O_2 and N_2 permeabilities also lies well above the upper bound (Fig. 2A, data point 4). This result suggests that PIM-EA-TB has excellent potential for the important industrial applications of nitrogen and oxygen enrichment from air because further

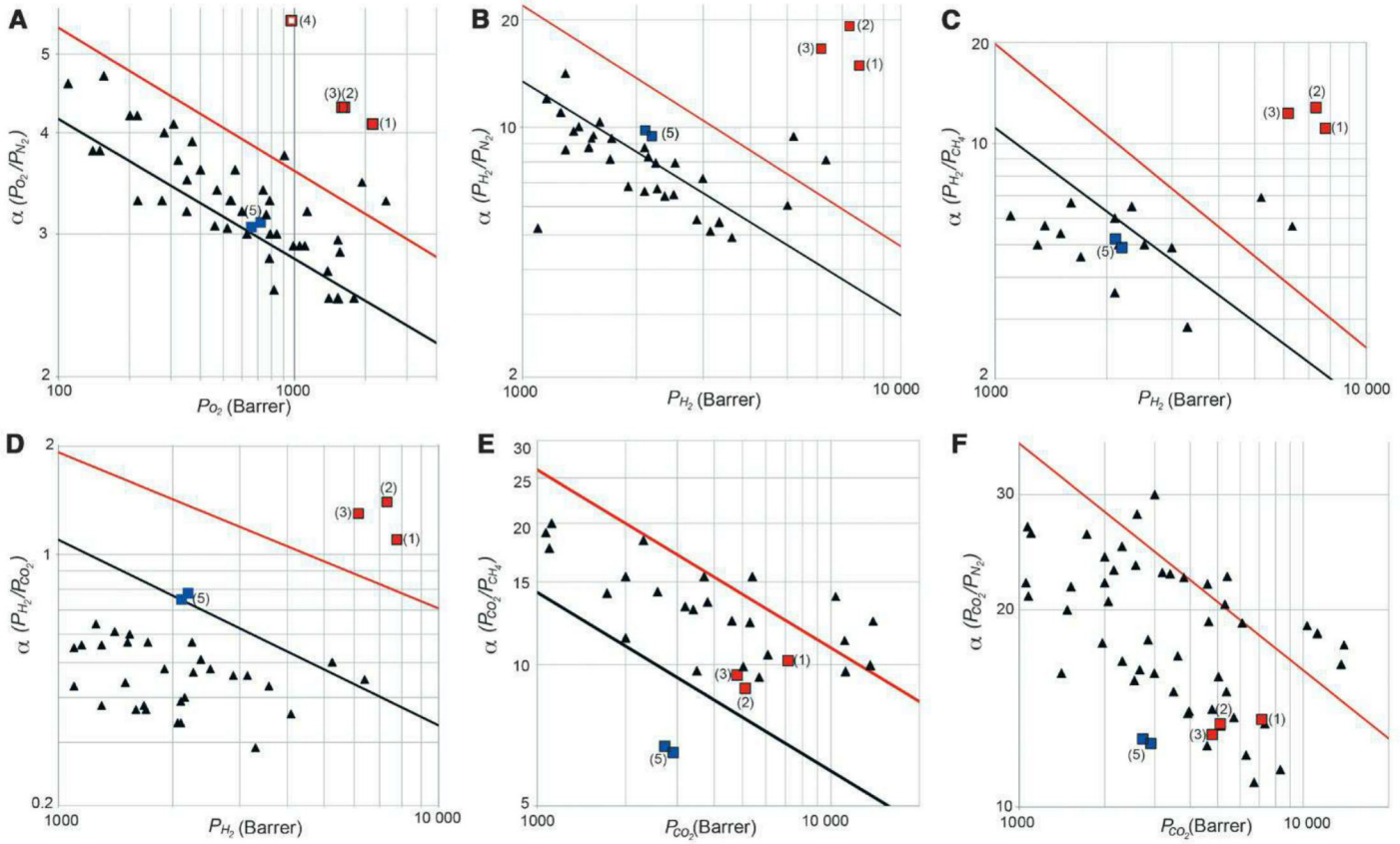

Fig. 2. Portions of the Robeson plots (log α_{xy} versus log P_x) relevant to highly permeable polymers for (**A**) O_2/N_2; (**B**) H_2/N_2; (**C**) H_2/CH_4; (**D**) H_2/CO_2; (**E**) CO_2/CH_4, and (**F**) CO_2/N_2 gas pairs showing the data for methanol-treated PIM-EA-TB, with data points 1 (solid red square) for a 181-μm film, 2 (solid red square) for a 95-μm film, and 3 (solid red square) for the same 181-μm film after aging for 24 hours. Data point 4 (open red square) represents an average value for O_2 permeabilities and O_2/N_2 selectivities obtained for air at variable feed pressures on a 129-μm sample (fig. S4). The black and red lines represent the 1991 (*7*) and 2008 (*6*) upper bounds, respectively. Data points 5 (solid blue squares) are from 157- and 128-μm films of PIM-SBI-TB. Other data points (solid black triangles) represent PIMs (*10*, *30*–*38*) and other highly permeable polymers (*39*–*42*) that have been reported since the upper bounds were updated in 2008. For PIM data points above the 2008 upper bounds, see (*10*, *30*, *34*, *37*).

physical aging and the use of thinner films are likely to produce a membrane with commercially desirable O_2/N_2 selectivity while maintaining high permeability relative to polymers presently used for these processes.

The performance of PIM-EA-TB for the gas pairs CO_2/N_2 and CO_2/CH_4 falls below the 2008 upper bounds (Fig. 2, E and F). However, for these gas pairs the selectivity is primarily due to the much higher solubility of CO_2 [solubility selectivity (S_x/S_y)] (Table 1) rather than selectivity based on diffusivity. Very high CO_2 solubility is a characteristic feature of all PIMs. PIM-EA-TB has complementary behavior to the promising thermally rearranged (TR) polymers and tetrazole-substituted PIMs (TZ-PIMs) that lie above the 2008 upper bound for CO_2/N_2 and CO_2/CH_4 (*29*, *30*).

The single gas permeabilities and selectivities of PIM-SBI-TB films (from 128- and 157-μm films) are within the range that is typical for PIMs for all gas pairs (Fig. 2 and Table 1). Most PIMs contain the SBI component, and molecular modeling shows that it is relatively flexible as compared with the EA component of PIM-EA-TB (Fig. 2D) (*11*). Therefore, it can be deduced that the enhanced molecular sieve behavior of PIM-EA-TB (fig. S5) is attributable to the combined rigidity of the bridged bicyclic TB and EA units rather than originating from the TB unit alone. In addition to providing an inflexible structural unit, TB also offers in-built amines suitable for quaternization via reaction with alkyl dihalides, which may be useful for simple cross-linking reactions to aid membrane stability and reduce physical aging. Furthermore, given the range of available aromatic diamine monomers, the TB polymerization reaction could be used to prepare polymers with diverse applications beyond gas separation membranes, which take advantage of the functionality of TB.

References and Notes

1. P. Bernardo, E. Drioli, G. Golemme, *Ind. Eng. Chem. Res.* **48**, 4638 (2009).
2. N. Y. Du, H. B. Park, M. M. Dal-Cin, M. D. Guiver, *Environ. Sci.* **5**, 7306 (2012).
3. T. C. Merkel, M. J. Zhou, R. W. Baker, *J. Membr. Sci.* **389**, 441 (2012).
4. Y. Yampolskii, *Macromolecules* **45**, 3298 (2012).
5. P. M. Budd, N. B. McKeown, *Polym. Chem.* **1**, 63 (2010).
6. L. M. Robeson, *J. Membr. Sci.* **320**, 390 (2008).
7. L. M. Robeson, *J. Membr. Sci.* **62**, 165 (1991).
8. P. M. Budd *et al.*, *J. Membr. Sci.* **325**, 851 (2008).
9. B. D. Freeman, *Macromolecules* **32**, 375 (1999).
10. C. G. Bezzu *et al.*, *Adv. Mater.* **24**, 5930 (2012).
11. M. Heuchel, D. Fritsch, P. M. Budd, N. B. McKeown, D. Hofmann, *J. Membr. Sci.* **318**, 84 (2008).
12. D. Didier *et al.*, *Tetrahedron* **64**, 6252 (2008).
13. J. Tröger, *J. Prakt. Chem.* **36**, 227 (1887).
14. V. Prelog, P. Wieland, *Helv. Chim. Acta* **27**, 1127 (1944).
15. S. Sergeyev, *Helv. Chim. Acta* **92**, 415 (2009).
16. B. Dolenský, M. Havlík, V. Král, *Chem. Soc. Rev.* **41**, 3839 (2012).
17. E. Poli, E. Merino, U. Diaz, D. Brunel, A. Corma, *J. Phys. Chem. C* **115**, 7573 (2011).
18. X. Du *et al.*, *Chem. Commun. (Camb.)* **46**, 970 (2010).
19. A. Abdolmaleki, S. Heshmat-Azad, M. Kheradmand-fard, *J. Appl. Polym. Sci.* **122**, 282 (2011).
20. Materials and methods are available as supplementary materials on *Science* Online.
21. N. B. McKeown, M. Carta, M. Croad, UK Patent Appl. PCT/GB2011/051703; WO 2012/035327 (2010).
22. M. Carta, K. J. Msayib, P. M. Budd, N. B. McKeown, *Org. Lett.* **10**, 2641 (2008).
23. S. Jiang *et al.*, *Nature Commun.* **2**, 207 (2011).
24. M. W. Schneider *et al.*, *Chemistry* **18**, 836 (2012).
25. K. Nagai, A. Higuchi, T. Nakagawa, *J. Polym. Sci., B, Polym. Phys.* **33**, 289 (1995).
26. M. S. McCaig, D. R. Paul, *Polymer (Guildf.)* **41**, 629 (2000).

27. K. D. Dorkenoo, P. H. Pfromm, *Macromolecules* **33**, 3747 (2000).
28. B. W. Rowe, L. M. Robeson, B. D. Freeman, D. R. Paul, *J. Membr. Sci.* **360**, 58 (2010).
29. H. B. Park *et al.*, *Science* **318**, 254 (2007).
30. N. Du *et al.*, *Nat. Mater.* **10**, 372 (2011).
31. N. Y. Du, G. P. Robertson, I. Pinnau, M. D. Guiver, *Macromolecules* **43**, 8580 (2010).
32. N. Y. Du, G. P. Robertson, J. S. Song, I. Pinnau, M. D. Guiver, *Macromolecules* **42**, 6038 (2009).
33. N. Y. Du, G. P. Robertson, I. Pinnau, M. D. Guiver, *Macromolecules* **42**, 6023 (2009).
34. N. Du, G. P. Robertson, I. Pinnau, S. Thomas, M. D. Guiver, *Macromol. Rapid Commun.* **30**, 584 (2009).
35. N. Y. Du *et al.*, *Macromolecules* **41**, 9656 (2008).
36. R. Short *et al.*, *Chem. Commun. (Camb.)* **47**, 6822 (2011).
37. D. Fritsch, G. Bengtson, M. Carta, N. B. McKeown, *Macromol. Chem. Phys.* **212**, 1137 (2011).
38. B. S. Ghanem, N. B. McKeown, P. M. Budd, D. Fritsch, *Macromolecules* **41**, 1640 (2008).
39. B. S. Ghanem *et al.*, *Macromolecules* **42**, 7881 (2009).
40. M. Gringolts *et al.*, *Macromolecules* **43**, 7165 (2010).
41. M. Calle, A. E. Lozano, J. G. de La Campa, J. de Abajo, *Macromolecules* **43**, 2268 (2010).
42. Y. Hu, M. Shiotsuki, F. Sanda, B. D. Freeman, T. Masuda, *Macromolecules* **41**, 8525 (2008).

Acknowledgments: Part of the work leading to these results has received funding from the European Community's Seventh Framework Programme (FP7/2007-2013) under grant agreement NMP3-SL-2009-228631, project DoubleNanoMem. We also thank the Engineering and Physical Sciences Research Council for funding (grants EP/G01244X and EP/G062129/1). K. Pilnácek and G. Clarizia are gratefully acknowledged for their help in the data elaboration and the performance of mixed-gas permeation measurements. We thank G. Hutchings (Cardiff University) for reading the manuscript and making helpful suggestions. A patent has been filed through Cardiff University on the polymer synthesis presented in this report (UK patent application PCT/GB2011/051703; WO 2012/035327 (2010).

Supplementary Materials

www.sciencemag.org/cgi/content/full/339/6117/303/DC1
Materials and Methods
Figs. S1 to S5
Table S1
References (*43*–*51*)

27 July 2012; accepted 6 November 2012
10.1126/science.1228032

Olefin Cyclopropanation via Carbene Transfer Catalyzed by Engineered Cytochrome P450 Enzymes

Pedro S. Coelho,[1]* Eric M. Brustad,[2]* Arvind Kannan,[1] Frances H. Arnold[1]†

Transition metal–catalyzed transfers of carbenes, nitrenes, and oxenes are powerful methods for functionalizing C=C and C–H bonds. Nature has evolved a diverse toolbox for oxene transfers, as exemplified by the myriad monooxygenation reactions catalyzed by cytochrome P450 enzymes. The isoelectronic carbene transfer to olefins, a widely used C–C bond–forming reaction in organic synthesis, has no biological counterpart. Here we report engineered variants of cytochrome $P450_{BM3}$ that catalyze highly diastereo- and enantioselective cyclopropanation of styrenes from diazoester reagents via putative carbene transfer. This work highlights the capacity to adapt existing enzymes for the catalysis of synthetically important reactions not previously observed in nature.

The many strategies for functionalizing C=C and C–H bonds that have evolved in nature have captivated the imaginations of chemists and form the foundation of biomimetic chemistry (*1*, *2*). The reverse of this, using inspiration from synthetic chemistry to discover and develop new biocatalysts, is a nascent frontier in molecular engineering, whose recent highlights include C–H activation by artificial rhodium enzymes (*3*) and the de novo design of Diels-Alderases (*4*). Synthetic chemists have developed powerful methods for direct C=C and C–H functionalization based on transition metal–catalyzed carbenoid and nitrenoid transfers, reactions that are widely used to synthesize natural product intermediates and pharmaceuticals (*5*). The asymmetric cyclopropanation of olefins with high-energy carbene precursors (e.g., acceptor-substituted diazo reagents) is a hallmark reaction that generates up to three stereogenic centers in a single step to make the important cyclopropane motif, featured in many natural products and therapeutic agents (*6*). Limited to using physiologically accessible reagents, nature catalyzes intermolecular cyclopropane formation through wholly different strategies, typically involving olefin addition to the methyl cation of *S*-adenosyl methionine or through cyclization of dimethylallyl pyrophosphate–derived allylic carbenium ions (*7*). As a result, the diverse cyclopropanation products that can be formed by metallocarbene chemistry cannot be readily accessed by engineering natural cyclopropanation enzymes. We hypothesized that a natural metalloenzyme, the iron-heme–containing cytochrome P450, could be engineered to catalyze formal carbenoid transfers, thereby combining the high levels of regio- and stereoselectivity of enzymes with the synthetic versatility of carbene-based strategies.

Members of the cytochrome P450 enzyme family catalyze myriad oxidative transformations, including hydroxylation, epoxidation, oxidative ring coupling, heteroatom release, and heteroatom oxygenation (*8*). Most transformations encompassed by this broad catalytic scope manifest the reactivity of the same high-valent iron-oxene intermediate, compound I (Fig. 1). Inspired by the impressive chemo-, regio-, and stereoselectivities with which cytochrome P450s can insert O atoms into C–H and C=C bonds, we investigated whether these enzymes could be engineered to mimic this chemistry for isoelectronic carbene transfer reactions via a high-valent iron-carbenoid species (Fig. 1). Here we report that variants of the cytochrome P450 from *Bacillus megaterium* (CYP102A1, or $P450_{BM3}$) are efficient catalysts for the asymmetric metallocarbene-mediated cyclopropanation of styrenes.

Because iron porphyrins catalyze carbene-based cyclopropanations (*9*, *10*), we first probed whether some common heme proteins display measurable levels of cyclopropanation activity in aqueous media (phosphate buffer, with 5% methanol cosolvent). We chose the reaction between styrene and ethyl diazoacetate (EDA) (Fig. 2), a well-recognized model system for validating new cyclopropanation catalysts. Initial experiments showed that optimal formation of the desired cyclopropanation products occurred in the presence of a reducing agent (e.g., sodium dithionite, $Na_2S_2O_4$) under anaerobic conditions (tables S1 to S4). Horseradish peroxidase (HRP), cytochrome c (cyt c), myoglobin (Mb), and $P450_{BM3}$ all displayed multiple turnovers toward the cyclopropane products, with HRP, cyt c, and Mb showing negligible enantioinduction, and formed the trans cyclopropane with over 90% diastereoselectivity, which is comparable to the diastereoselectivity induced by free hemin (table S1). $P450_{BM3}$, despite forming the cyclopropane products in low yield, catalyzed the reaction with different diasteroselectivity (cis:trans 37:63) and slight enantioinduction (Table 1), showing that carbene transfer and selectivity are dictated by the heme cofactor bound in the enzyme active site.

We then explored whether the activity and selectivity of heme-catalyzed cyclopropanation could be enhanced by engineering the protein sequence. $P450_{BM3}$ is a well-studied, soluble, self-sufficient (heme and diflavin reductase domains are fused in a single polypeptide, ~120 kD), long-chain, fatty acid monooxygenase. More than a decade of protein engineering attests to the functional plasticity of this biocatalyst (*11*). From our work using directed evolution to engineer cytochrome $P450_{BM3}$ for synthetic applications, we have accumulated thousands of variants that exhibit monooxygenase activity on a wide range of substrates (*12*). We tested some of these variants

[1]Division of Chemistry and Chemical Engineering, California Institute of Technology, Pasadena, CA 91125, USA. [2]Department of Chemistry and Carolina Center for Genome Sciences, University of North Carolina at Chapel Hill, Chapel Hill, NC 27599, USA.

*These authors contributed equally to this work.
†To whom correspondence should be addressed. E-mail: frances@cheme.caltech.edu

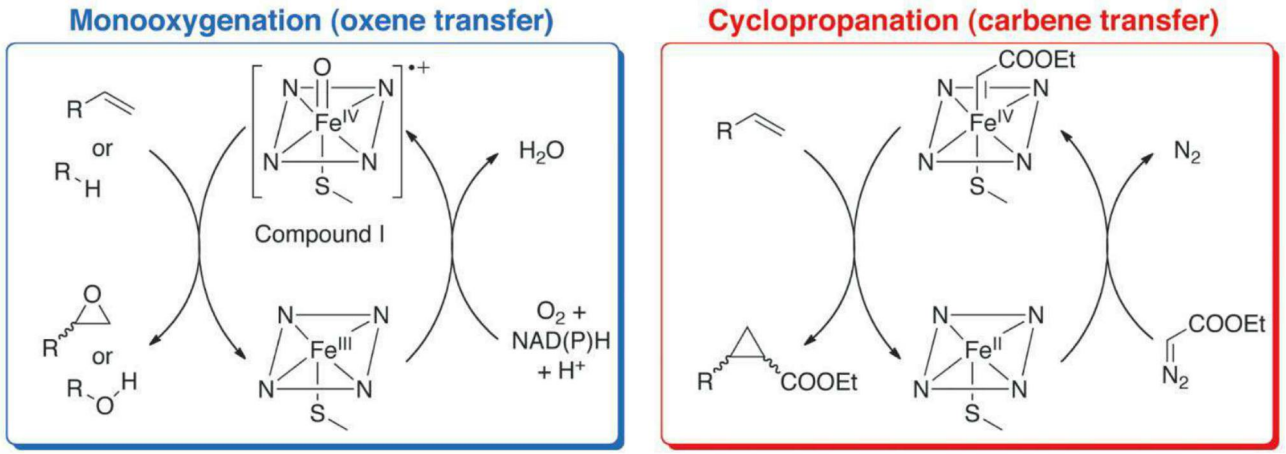

Fig. 1. (**Left**) Canonical mode of reactivity of cytochrome P450s. Monooxygenation of olefins and C-H bonds to epoxides and alcohols catalyzed by the ferryl porphyrin radical intermediate (compound I). (**Right**) Artificial mode of formal carbene transfer activity of cytochrome P450s, using diazoester reagents as carbene precursors.

for altered cyclopropanation diastereo- and enantioselectivity by analysis of product distributions using gas chromatography (GC) with a chiral stationary phase. A panel of 92 $P450_{BM3}$ variants, chosen for diversity of activity and protein sequence, was screened in *Escherichia coli* lysate for the reaction of styrene and EDA under aerobic conditions in the presence of $Na_2S_2O_4$ (tables S5 and S6). The 10 most promising hits were selected for purification and characterization under standardized anaerobic reaction conditions (Table 1 and table S7).

Five of the 10 selected P450s showed improvements in activity as compared to the wild type [total turnover numbers (TTNs) > 100], a comprehensive range of diastereoselectivities, with cis:trans ratios varying from 9:91 to 60:40, and up to 95% enantioselectivities (table S7). For example, variant H2-5-F10, which contains 16 amino acid substitutions, catalyzes 294 total turnovers, equivalent to ~58% yield under these conditions (0.2% enzyme loading with respect to EDA). This represents a 50-fold improvement over wild-type $P450_{BM3}$. Furthermore, mutations affect both the diastereo- and enantioselectivity of cyclopropanation: H2-5-F10 favors the trans cyclopropanation product (cis:trans 16:84) with 63% enantiomeric excess (ee_{trans}), whereas H2A10, with a TTN of 167, shows reversed diastereoselectivity (cis:trans 60:40) with high enantioselectivity (95% ee_{cis}).

We used H2A10 to verify the role of the enzyme in catalysis and identify optimal conditions (table S8 and figs. S1 and S2). Heat inactivation produced diastereo- and enantioselectivities similar to those obtained with free hemin, consistent with protein denaturation and release of the cofactor. Complete inhibition was achieved by preincubating the reaction mixture with carbon monoxide, which irreversibly binds the reduced P450 heme, confirming that catalysis occurs at the active site. Air inhibited the cyclopropanation reaction by about 50%, showing that dioxygen and EDA compete for reduced Fe^{II}. Cyclopropanation was also achieved with NADPH (reduced nicotinamide adenine dinucleotide phosphate) as the reductant, confirming that the activity can also be driven by the endogenous electron transport machinery of the diflavin-containing reductase domain. The presence of a reducing agent in substoichiometric amounts proved essential for cyclopropanation (table S9), implying that the active species is Fe^{II} rather than the resting-state Fe^{III}.

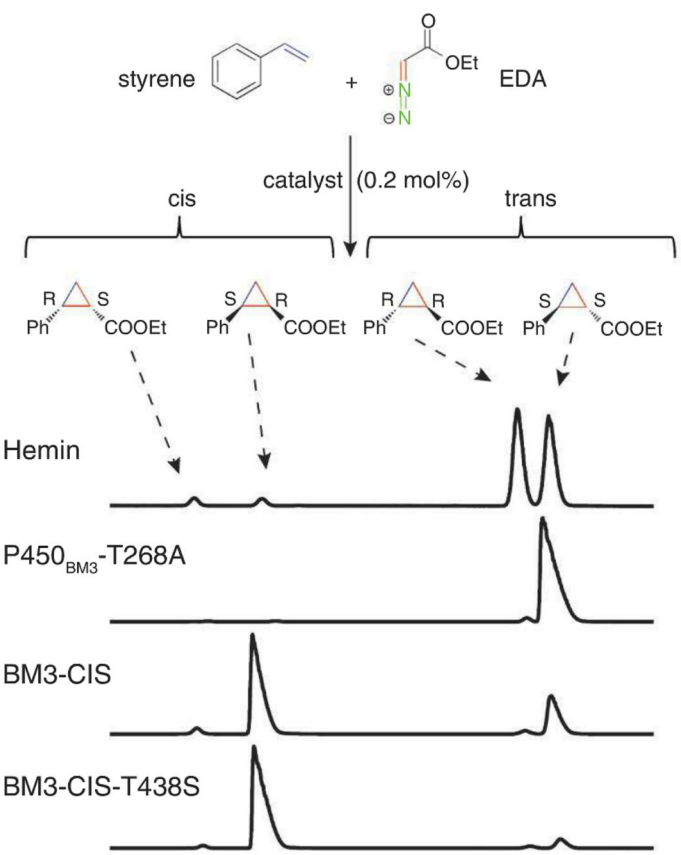

Fig. 2. Absolute stereoselectivity of select $P450_{BM3}$ cyclopropanation catalysts. Reaction conditions were as follows: 20 μM catalyst, 30 mM styrene, 10 mM EDA, 10 mM $Na_2S_2O_4$, under argon in aqueous potassium phosphate buffer (pH 8.0) and 5% MeOH cosolvent for 2 hours at 298 K. Enzyme loading was 0.2 mol % with respect to EDA. The structures of each product stereoisomer are shown above the reaction gas chromatograms.

Highly active $P450_{BM3}$ variants H2A10, H2-5-F10, and H2-4-D4 have three to five active-site alanine substitutions with respect to 9-10A-TS-F87V (12 mutations from $P450_{BM3}$, supplementary materials text), which itself shows negligible cyclopropanation activity. These variants exhibit a range of TTNs, diastereoselectivity, and enantioselectivity (Table 1). To better understand how protein sequence controls P450-mediated cyclopropanation, we constructed 12 variants to

Table 1. Stereoselective $P450_{BM3}$ cyclopropanation catalysts. Reactions were run in aqueous phosphate buffer (pH 8.0) and 5% MeOH cosolvent at room temperature under argon with 30 mM styrene, 10 mM EDA, 0.2 mol % catalyst (with respect to EDA), and 10 mM $Na_2S_2O_4$. Yields, diastereomeric ratios, and enantiomeric excess were determined by GC analysis. Yields are based on EDA. See the supplementary text for protein sequences indicating mutations from wild-type $P450_{BM3}$.

Catalyst	% yield	TTN	cis:trans	% ee_{cis}*	% ee_{trans}†
Hemin	15	73	6:94	–1	0
$P450_{BM3}$	1	5	37:63	–27	–2
$P450_{BM3}$-T268A	65	323	1:99	–15	–96
9-10A-TS-F87V	1	7	35:65	–41	–8
H2-5-F10	59	294	16:84	–41	–63
H2A10	33	167	60:40	–95	–78
H2-4-D4	41	206	53:47	–79	–33
BM3-CIS	40	199	71:29	–94	–91
BM3-CIS-I263A	38	190	19:81	–62	–91
BM3-CIS-A328G	37	186	83:17	52	–45
BM3-CIS-T438S	59	293	92:8	–97	–66

*(*R*,*S*) – (*S*,*R*). †(*R*,*R*) – (*S*,*S*).

Table 2. Scope of P450-catalyzed cyclopropanation of styrenyl substrates. Ar = *p*-X-C_6H_4. Reaction conditions were as follows: 20 μM catalyst, 30 mM olefin, 10 mM diazoester, 10 mM $Na_2S_2O_4$, under argon in aqueous potassium phosphate buffer (pH 8.0) and 5% MeOH cosolvent for 2 hours at 298 K. Enzyme loading was 0.2 mol % with respect to diazoester. N/A, not available when enantiomers did not separate to baseline resolution.

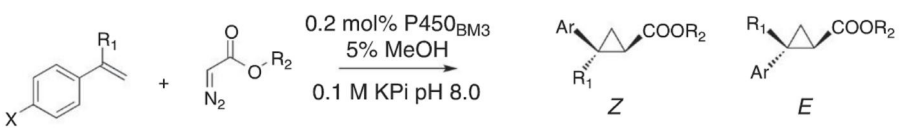

Reagents	P450 catalyst	TTN	*Z* : *E*	%ee_Z	%ee_E
R_1 = H, X= Me, R_2 = Et	BM3-CIS	228	78 : 22	-81	N/A
R_1 = H, X= OMe, R_2 = Et	H2-5-F10	364	11 : 89	38	N/A
R_1 = H, X= CF_3, R_2 = Et	7-11D	120	76 : 24	31	59
R_1 = Me, X= H, R_2 = Et	7-11D	157	41 : 49	42	N/A
R_1 = H, X= H, R_2 = *t*-Bu	H2A10	120	3 : 97	N/A	N/A

assess the contributions of individual alanines to catalysis and stability [table S10 (*13*)]. T268A is key for achieving high cyclopropanation activity, and this mutation alone converts inactive 9-10A-TS-F87V into an active cyclopropanation catalyst. Variant 9-10A-TS-F87V-T268A (here called BM3-CIS) is a competent cyclopropanation catalyst (199 TTNs), displays strong preference for the cis product (cis:trans 71:29), forms both diastereomers with over 90% *ee,* and is as stable as wild-type $P450_{BM3}$. Other active site alanine mutations tune the product distribution. The addition of I263A to BM3-CIS reverses diastereoselectivity (cis:trans 19:81). We also investigated the effects of similar mutations introduced in the poorly active wild-type $P450_{BM3}$ (table S11). $P450_{BM3}$-T268A, with a single mutation, is an active cyclopropanation catalyst (323 TTNs, Table 1) with exquisite trans-selectivity (cis:trans 1:99) and high enantioselectivity for the major diastereomer (–96% ee_{trans}, Fig. 1). Whereas BM3-CIS is a cis-selective cyclopropanation catalyst, identical active-site mutations in wild-type $P450_{BM3}$ result in a trans-selective enzyme (table S11), demonstrating that mutations outside of the active site also influence the stereochemical outcome.

Because the design of cis-selective small-molecule catalysts for diazocarbonyl-mediated cyclopropanations has proven more challenging than that of their trans counterparts (*14*), we investigated whether active-site engineering of $P450_{BM3}$ could provide robust cis-selective water-compatible catalysts to complement existing organometallic systems (*15*). We chose five active site residues (L181, I263, A328, L437, and T438) for individual site-saturation mutagenesis (*13*). The A328G, T438A, T438S, and T438P variants exhibited enhanced cis-selectivity (table S12). A328G also reversed the enantioselectivity for the cis-diastereomer (Table 1). BM3-CIS-T438S displayed the highest diastereo- and enantioselectivities (cis:trans 92:8 and –97% ee_{cis}) and maintained TTNs comparable to those of BM3-CIS (Table 1).

BM3-CIS exhibits Michaelis-Menten kinetics (fig. S3 and table S13) with relatively high Michaelis constant values for the olefin (~1.5 mM) and the diazoester (~5 mM), reflecting the lack of evolutionary pressure for this enzyme to bind these substrates. BM3-CIS exhibits a notable catalytic rate constant (k_{cat}) for cyclopropanation of 100 min^{-1}, comparable to the k_{cat} of many native P450s for hydroxylation, but about 50 times less than $P450_{BM3}$-catalyzed fatty acid hydroxylation (table S14). Free hemin does not exhibit saturation kinetics and displays slower initial rates than BM3-CIS (only 30 min^{-1} at 10 mM styrene and 15 mM EDA), indicating that the protein scaffold enhances k_{cat} as compared to the free cofactor in solution. When used at 0.2 mole % (mol %) equivalent, BM3-CIS–catalyzed cyclopropanations reached completion after 30 min. Adding more EDA enhanced turnovers for cyclopropanes and preserved BM3-CIS stereoselectivity (table S15), confirming catalyst integrity and implying that the reaction stops because of EDA depletion rather than inactivation.

To assess the substrate scope of $P450_{BM3}$-catalyzed cyclopropanation, we investigated the activities of six variants against a panel of olefins and diazo compounds (Table 2 and tables S16 to S20). P450 cyclopropanation is robust to both electron-donating (*p*-vinylanisole and *p*-vinyltoluene) and electron-withdrawing (*p*-trifluoromethylstyrene) substitutions on styrene, and variant 7-11D showed consistent cis-selectivity for these substrates. The P450s were also active on 1,1-disubstituted olefins (i.e., α-methyl styrene), with chimeric P450 C2G9R1 forming cyclopropanes in 77% yield (with respect to EDA). The P450s were only moderately active with *t*-butyl diazoacetate as substrate (<30% yield), forming the trans product with >87% selectivity and offering no advantage over free hemin (table S20). For reactions involving EDA and aryl-substituted olefins, however, the P450s consistently outperformed the free cofactor in both activity and stereoselectivity.

Screening natural enzymes against synthetic reagents chosen based on chemical intuition offers a simple strategy for identifying enzymes with basal levels of non-native activity. As we have shown, a single mutation can be enough to promote such activity and achieve synthetically useful stereoselectivities. The accumulation of beneficial mutations by directed evolution or other protein engineering strategies can generate a spectrum of highly active catalysts for desired substrate and product specificities. The established reaction promiscuity of natural enzymes (*16*, *17*) and the

surprising ease with which cyclopropanation activity could be installed into $P450_{BM3}$ suggest that this approach will be useful for other synthetically important transformations for which biological counterparts do not yet exist.

References and Notes

1. J. T. Groves, *Proc. Natl. Acad. Sci. U.S.A.* **100**, 3569 (2003).
2. R. Breslow, *J. Biol. Chem.* **284**, 1337 (2009).
3. T. K. Hyster, L. Knörr, T. R. Ward, T. Rovis, *Science* **338**, 500 (2012).
4. J. B. Siegel *et al.*, *Science* **329**, 309 (2010).
5. H. M. L. Davies, J. R. Manning, *Nature* **451**, 417 (2008).
6. H. Lebel, J.-F. Marcoux, C. Molinaro, A. B. Charette, *Chem. Rev.* **103**, 977 (2003).
7. L. A. Wessjohann, W. Brandt, T. Thiemann, *Chem. Rev.* **103**, 1625 (2003).
8. E. M. Isin, F. P. Guengerich, *Biochim. Biophys. Acta Gen. Subj.* **1770**, 314 (2007).
9. J. R. Wolf, C. G. Hamaker, J.-P. Djukic, T. Kodadek, L. K. Woo, *J. Am. Chem. Soc.* **117**, 9194 (1995).
10. B. Morandi, E. M. Carreira, *Science* **335**, 1471 (2012).
11. C. J. C. Whitehouse, S. G. Bell, L.-L. Wong, *Chem. Soc. Rev.* **41**, 1218 (2012).
12. J. C. Lewis, F. H. Arnold, *Chimia (Aarau)* **63**, 309 (2009).
13. Materials and methods are available as supplementary materials on *Science* Online.
14. A. Caballero, A. Prieto, M. M. Diaz-Requejo, P. J. Perez, *Eur. J. Inorg. Chem.* **2009**, 1137 (2009).
15. I. Nicolas, P. Le Maux, G. Simonneaux, *Coord. Chem. Rev.* **252**, 727 (2008).
16. U. T. Bornscheuer, R. J. Kazlauskas, *Angew. Chem. Int. Ed.* **43**, 6032 (2004).
17. O. Khersonsky, C. Roodveldt, D. S. Tawfik, *Curr. Opin. Chem. Biol.* **10**, 498 (2006).

Acknowledgments: This work was funded by the Division of Chemical Sciences, Geosciences, and Biosciences, Office of Basic Energy Sciences of the U.S. Department of Energy through grant DE-FG02-06ER15762. E.M.B. was supported by a Ruth M. Kirschstein National Institutes of Health (NIH) postdoctoral fellowship, award number F32GM087102, from the National Institute of General Medical Sciences and a generous startup fund from the University of North Carolina Chapel Hill. P.S.C., E.M.B., and F.H.A. have filed through the California Institute of Technology a provisional patent application that is based on the results presented here. The authors thank Z. J. Wang for helpful discussions during the preparation of the manuscript.

Supplementary Materials

www.sciencemag.org/cgi/content/full/science.1231434/DC1
Materials and Methods
Supplementary Text
Figs. S1 to S3
Tables S1 to S20
References (*18*–*35*)

12 October 2012; accepted 30 November 2012
Published online 20 December 2012;
10.1126/science.1231434

Metamaterial Apertures for Computational Imaging

John Hunt,[1,4]* Tom Driscoll,[1,2,4] Alex Mrozack,[3] Guy Lipworth,[1,4] Matthew Reynolds,[4] David Brady,[4] David R. Smith[1,4]

By leveraging metamaterials and compressive imaging, a low-profile aperture capable of microwave imaging without lenses, moving parts, or phase shifters is demonstrated. This designer aperture allows image compression to be performed on the physical hardware layer rather than in the postprocessing stage, thus averting the detector, storage, and transmission costs associated with full diffraction-limited sampling of a scene. A guided-wave metamaterial aperture is used to perform compressive image reconstruction at 10 frames per second of two-dimensional (range and angle) sparse still and video scenes at K-band (18 to 26 gigahertz) frequencies, using frequency diversity to avoid mechanical scanning. Image acquisition is accomplished with a 40:1 compression ratio.

Imaging systems can be characterized by object dimension [for instance, two-dimensional (2D) for photographs] and information dimension (for example, the number of pixels in an image). Conventional imaging systems are built around the assumption that the object dimension must be conserved in the information dimension, regardless of the inherent information content of the scene. Compressive measurement leverages the realization that measurements need not conserve form of dimension in this sense (*1*–*3*). Indeed, the concept of dimension indicates that measurements are well ordered in some space, implying that adjacent measurements sample similar object data. Information-transfer efficiency, however, is maximized if object data measured by successive measurements are as distinct as possible.

At the diffraction limit, the finite size of the aperture used to form an image imposes a maximum pixel dimension N equal to the space-bandwidth product (SBP), which represents the number of measurement modes needed to exactly reproduce an arbitrary scene (*4*, *5*). In a conventional imaging system, the measurement modes might be thought of as diffraction-limited spots, each of which samples a small portion of the scene (Fig. 1A). Because these modes have little or no spatial overlap in the detector plane, they can be acquired nearly independently and simultaneously with N detectors, such as a charge-coupled device array. However, for natural scenes, many of the modes provide little to no useful data; therefore, they can be substantially compressed without excessive loss of image fidelity (*6*).

The concept of a measurement mode can be generalized, such that the imaging process can be expressed mathematically by the relation $\mathbf{g} = \mathbf{Hf}$, where $\mathbf{g}$ is a collection of measurements, $\mathbf{H}$ is the measurement matrix (a row-wise array of all measurement modes), and $\mathbf{f}$ is the sampled scene. To form a completely determined data set of measurements (thus enabling a unique linear solution for $\mathbf{f}$), the rank of $\mathbf{H}$ must equal the scene's data dimension (*7*). Compressive sampling allows reconstruction of underdetermined scenes, finding $\mathbf{f}$ by solving the minimization problem $\arg\min_{\mathbf{f}} \|\mathbf{g} - \mathbf{Hf}\|_2^2 + \lambda R(\mathbf{f})$, where $\arg\min_{\mathbf{f}}$ denotes the value of $\mathbf{f}$ that minimizes the expression, λ is a scalar weighting factor, and $R(\mathbf{f})$ expresses some prior knowledge about the likely composition of the scene. Typically in compressive sampling, R is the l_1-norm of the scene, represented in an appropriate basis, which reflects the inherent sparsity that exists in natural scenes. This nonlinear minimization problem is rigorously solvable, even with highly underdetermined measurement data sets (*8*–*10*).

Imaging systems for radio frequency and millimeter-wave electromagnetics have generally been of two types: scanned single-pixel systems and multielement phased-arrays (or synthetic phased arrays). The measurement modes used by classical single-pixel systems are typically inefficient at collecting imaging data. For instance, a rasterizing scanned beam collects information about only one point in space at a time. Multielement phased array systems have much more flexibility in the measurement modes they can access, but these systems sacrifice the size, weight, power, and price advantages of single-pixel systems.

New approaches to imaging at these frequencies have made use of lenses and spatially modulated masks combined with single-pixel detectors to make compressed measurements. One of the pioneering implementations of this form of compressive imaging, depicted in Fig. 1B, was carried out at optical (*11*) and terahertz frequencies with the use of random static (*12*) and dynamic (*13*) masks. Other groups have presented additional ways to introduce mode diversity (*14*). We show that metamaterial apertures have distinct advantages for compressive imaging because they can be engineered to support custom-designed complex measurement modes that vary with frequency. Leveraging the same electromagnetic

[1]Center for Metamaterials and Integrated Plasmonics, Duke University, Box 90291, Durham, NC 27708, USA. [2]Department of Physics, University of California San Diego, La Jolla, CA 92093, USA. [3]Fitzpatrick Institute for Photonics and Electrical and Computer Engineering, Duke University, Durham, NC 27708, USA. [4]Department of Electrical and Computer Engineering, Duke University, Durham, NC 27708, USA.

*To whom correspondence should be addressed. E-mail: john.hunt@duke.edu

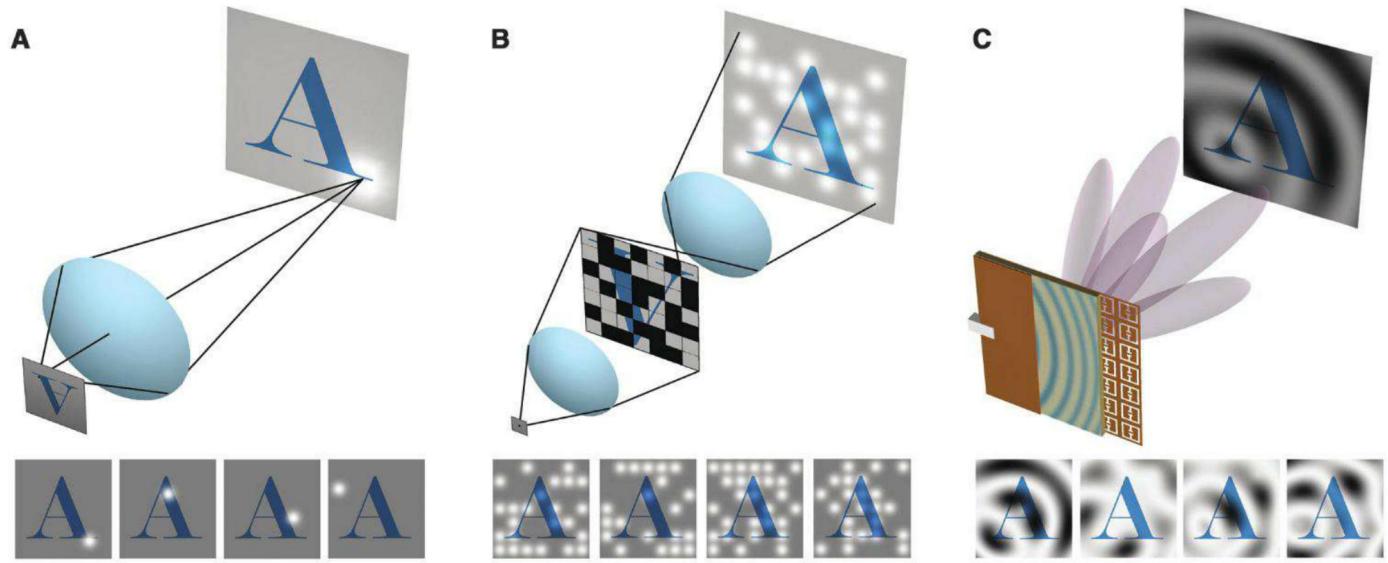

Fig. 1. Comparison of (**A**) conventional and (**B** and **C**) compressive imaging schemes. A conventional imager uses a lens to form measurement modes that effectively map all parts of an object to a detector/image plane. Each mode contributes highly specific and localized information, and all modes can be captured simultaneously with a pixel array or other detector. Within single-pixel schemes, many types of modes can be used to form the image, with measurements being captured sequentially. In the example shown in (B), a random mask and two lenses are used to project incoherent modes that sample the entire scene. The microwave metamaterial imager reported here (C) makes use of a planar waveguide that feeds a holographic array of ELCs, removing the need for lenses. The waveguide acts as a coherent single-pixel device, with the array of ELCs serving to produce the illuminating complex spatial modes.

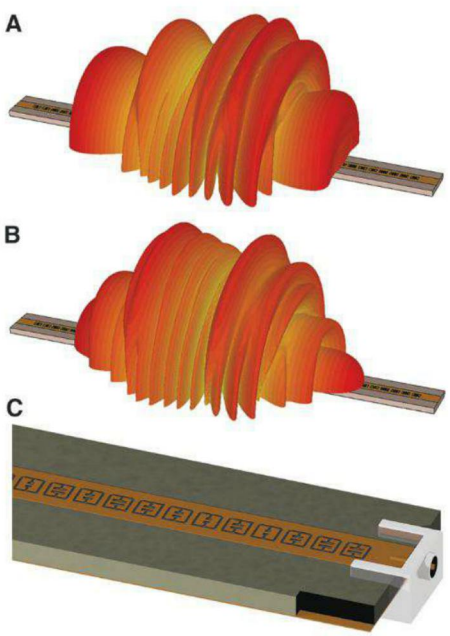

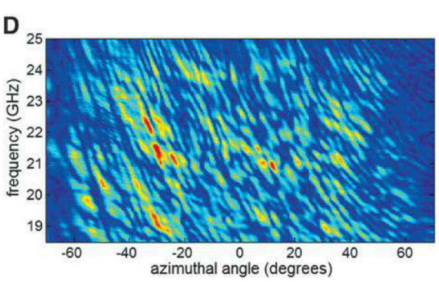

Fig. 2. Simulated far-field profiles for the metamaterial aperture at two frequencies: 18.5 GHz (**A**) and 21.8 GHz (**B**). Resonant metamaterial apertures (**C**) can create mode distributions that vary with frequency. (**D**) Measured magnitude of the measurement matrix, **H**, as a function of angle and frequency.

flexibility that metamaterials have shown in many other contexts (*15*–*20*), we can construct an imaging aperture suitable for single-pixel operation that can project nearly arbitrary measurement modes into the far-field, constrained only by the size of the aperture and resonant elements.

We use a 1D metamaterial aperture to perform compressed imaging of various 2D (one angle plus range) canonically sparse scenes. Our imaging device consists of a leaky waveguide, formed by patterning the top conductor of a standard microstrip line with complementary electric-inductor-capacitors (cELCs) (*21*, *22*) metamaterial elements (Fig. 2C). This configuration is equivalent to the schematic of the compressive imager in Fig. 1C, except that the aperture becomes one-dimensional. Each cELC acts as a resonant element that couples energy from the waveguide mode to free space. The resonance frequency and spectral shape of each cELC controls the amplitude and phase of the transmitted wave, such that the far-field modes can be designed by modifying the geometry of the cELCs along the microstrip. By controlling the design and distribution of the individual elements, which affect both the scattered-field characteristics as well as the guided-wave characteristics, nearly any desired aperture mode can be created.

For canonically sparse scenes, an efficient set of measurement modes are those that distribute energy randomly across both the amplitude and phase space of the scene. The dispersion present in resonant metamaterial elements makes frequency a natural choice for indexing the modes, creating a mapping between the measurement modes and frequency. Thus, by sweeping the frequency of the illuminating signal across the available bandwidth, we access the aperture modes sequentially, without having to move or reconfigure the aperture. For image reconstruction schemes that use an arbitrary set of measurement modes, it is essential that the modes be as orthogonal as possible to each other, which places demands on the sharpness and separation of the resonances, with sharper resonances yielding less correlated modes.

We have fabricated a random-mode metamaterial aperture, 40 cm in length, designed to operate in the K band from 18.5 to 25 GHz. Two samples of the measurement modes for this design are plotted in Fig. 2, A and B, and the complete measurement matrix is plotted in Fig. 2C. In our demonstration, scenes are illuminated by far-field radiation from a single source: a low-directivity horn antenna. Backscattered radiation from objects in the scene floods the metamaterial

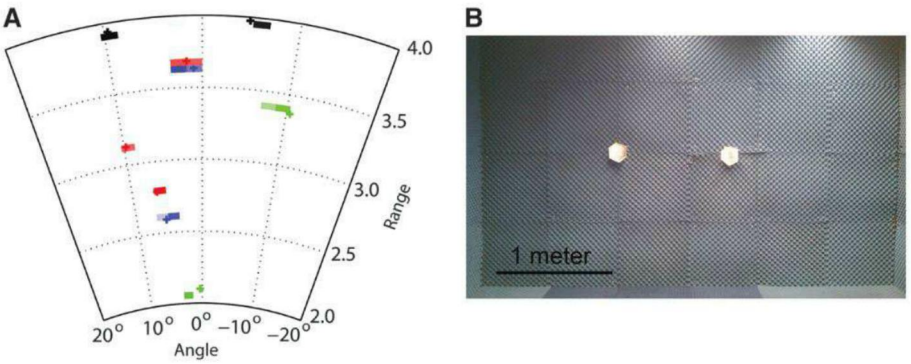

Fig. 3. (**A**) Reconstructions of four different static scenes (differentiated by color), consisting of two (black, green, and blue) or three (red) 10-cm scattering objects. The solid "+" symbols show the actual location of objects, and the pixels show the reconstructed image. Pixel size reflects the maximum instrument resolution. The image has been cropped from the full field of view of ±70°. (**B**) Photograph of a single scene corresponding to the black markers in (A).

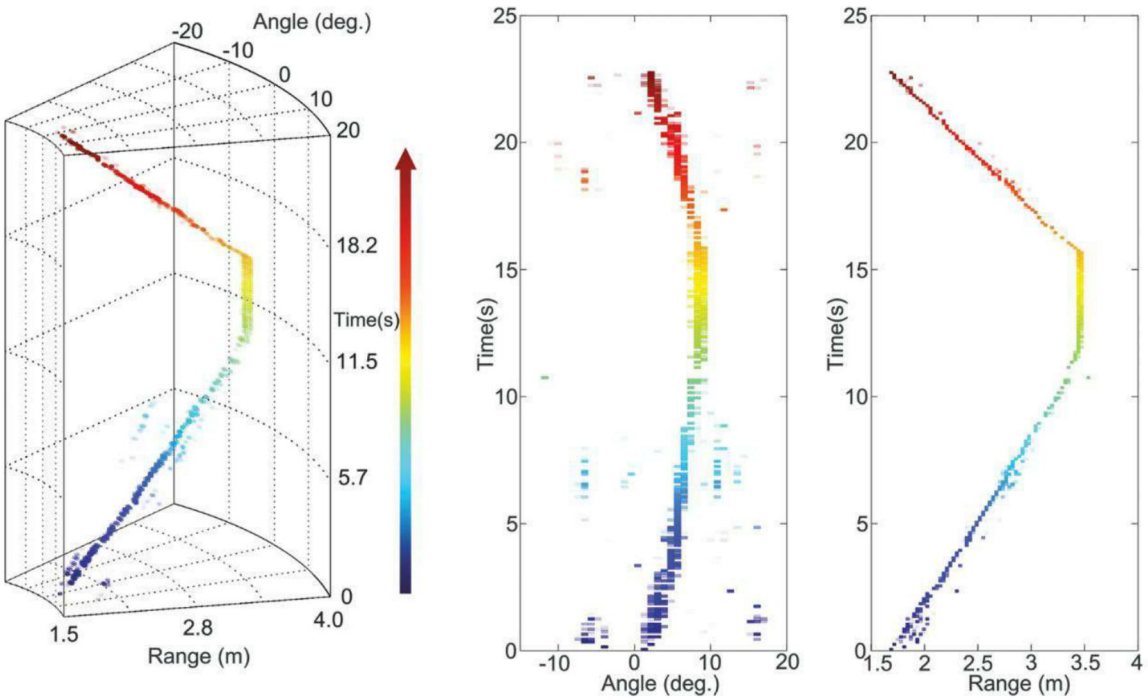

Fig. 4. (**Left**) Image of a single moving object at 10-Hz frequency. Each voxel is sized to match the spatio-temporal resolution of the metamaterial aperture, and the amplitude of the reconstructed scattering density is mapped to the transparency of each voxel. Voxels are also color-coded in time, from blue to red. (**Right**) Data projections in two dimensions.

aperture, which selectively admits only one specific mode at each measured frequency. The resulting (complex) signal is measured by a vector network analyzer.

We formed several simple sparse scenes inside an anechoic chamber with dimensions of 4 m by 4 m by 3 m. Each scene contained two or three scattering objects (retroreflectors), 10 cm in diameter, located at arbitrary positions in the chamber. Figure 3B shows one such scene. All scenes were reconstructed using the TwIST code (*23*).

For an aperture of this size and bandwidth, the diffraction-limited angular resolution is 1.7°, and the bandwidth-limited range resolution is 4.6 cm. Across a field of view of ±70° in angle and 1.5 to 4 m in range, the equivalent SBP = 4475. Our measurement, however, contains only 101 values, representing a compression ratio of more than 40:1. We note that the acquisition of a complete data set for the scenes in Fig. 3 requires only 100 ms, which makes the imaging of moving scenes a tantalizing possibility.

To demonstrate the imaging of moving scenes, we performed repeated 100-ms sweeps while moving an object through the scene. The acquisition speed in this experiment was limited by the signal-to-noise-ratio—primarily due to the network analyzer, which is designed for operational flexibility rather than high dynamic range or sweep speed. We imaged a single scattering object moving through the scene on a linear path at ~0.2 m/s. Figure 4 depicts the reconstructed scene. The object position in angle and range, mapped as a function of time, is observed in the retrieved scene. These data are presented in video format along with a camera recording of the object motion in movie S1.

A major advantage of metamaterial radiators in this application is the ability to incorporate tuning (*24*–*27*). Dynamically varying the resonance of the metamaterial elements would enable reconfigurable measurement modes. Dynamic tuning also frees the frequency bandwidth, effectively enabling hyperspectral imaging (*28*).

The imaging system we present here combines a computational imaging approach with custom aperture hardware that allows compression to be performed on the physical layer that is used to do the illumination and/or recording. The use of metamaterials is a convenient tool for the creation of such apertures, as metamaterial techniques offer a well-understood design path. Leveraging the resonant nature of metamaterial elements also creates frequency diversity of the measurement modes, giving an all-electrical method of quickly sweeping through a mode set. This metamaterial approach scales linearly with frequency through terahertz frequencies with correspondingly higher resolutions. Due to their small form factor and lack of moving parts, similar systems may extend microwave and millimeter-wave imaging capabilities.

References and Notes

1. E. J. Candès, *Proc. Int. Congress Math.* **3**, 1433 (2006).
2. D. L. Donoho, *IEEE Trans. Inf. Theory* **52**, 1289 (2006).

3. C. F. Cull, D. A. Wikner, J. N. Mait, M. Mattheiss, D. J. Brady, *Appl. Opt.* **49**, E67 (2010).
4. E. Abbe, *J. R. Microsc. Soc.* **3**, 790 (1883).
5. A. W. Lohmann, in "The space–bandwidth product, applied to spatial filtering and holography," *Research Paper RJ-438* (IBM San Jose Research Laboratory, San Jose, CA, 1967), pp. 1–23.
6. R. M. Willett, R. F. Marcia, J. M. Nichols, *Opt. Eng.* **50**, 072601 (2011).
7. D. J. Brady, *Optical Imaging and Spectroscopy* (Wiley, Hoboken, NJ, 2008).
8. E. J. Candès, *C. R. Math.* **346**, 589 (2008).
9. D. J. Brady, K. Choi, D. L. Marks, R. Horisaki, S. Lim, *Opt. Express* **17**, 13040 (2009).
10. L. Potter, E. Ertin, J. Parker, M. Cetin, *Proc. IEEE* **98**, 1006 (2010).
11. D. Takhar *et al.*, *Proc. SPIE Comput. Imaging IV* **6065**, 606509 (2006).
12. W. L. Chan *et al.*, *Appl. Phys. Lett.* **93**, 121105 (2008).
13. W. L. Chan *et al.*, *Appl. Phys. Lett.* **94**, 213511 (2009).
14. A. Mahalanobis, M. Neifeld, V. K. Bhagavatula, T. Haberfelde, D. Brady, *Appl. Opt.* **48**, 5212 (2009).
15. J. B. Pendry, D. Schurig, D. R. Smith, *Science* **312**, 1780 (2006).
16. T. Driscoll *et al.*, *Appl. Phys. Lett.* **88**, 081101 (2006).
17. N. B. Kundtz, D. R. Smith, *Nat. Mater.* **9**, 129 (2010).
18. Y. Urzhumov, D. R. Smith, *Phys. Rev. B* **83**, 205114 (2011).
19. E. Narimanov, *Nat. Mater.* **7**, 273 (2008).
20. Z. Jacob, L. V. Alekseyev, E. Narimanov, *Opt. Express* **14**, 8247 (2006).
21. R. Liu *et al.*, *Appl. Phys. Lett.* **94**, 073506 (2009).
22. J. D. Baena *et al.*, *IEEE Trans. Microw. Theory Tech.* **53**, 1451 (2005).
23. J. M. Bioucas-Dias, M. A. Figueiredo, *IEEE Trans. Image Process.* **16**, 2992 (2007).
24. W. J. Padilla, A. J. Taylor, C. Highstrete, M. Lee, R. D. Averitt, *Phys. Rev. Lett.* **96**, 107401 (2006).
25. T. Driscoll *et al.*, *Science* **325**, 1518 (2009).
26. H. T. Chen *et al.*, *Nature* **444**, 597 (2006).
27. D. Shrekenhamer *et al.*, *Opt. Express* **19**, 9968 (2011).
28. Z. Xu, E. Y. Lam, *J. Opt. Soc. Am. A Opt. Image Sci. Vis.* **27**, 1638 (2010).

Acknowledgments: This work was supported by a grant from the Air Force Office of Scientific Research (no. FA9550-09-1-0539). Data and code are available at http://people.duke.edu/~jdh51/Data_Metamaterial_Apertures_for_Computational_Imaging.zip.

Supplementary Materials

www.sciencemag.org/cgi/content/full/339/6117/310/DC1
Supplementary Text
Figs. S1 to S3
Movie S1

11 September 2012; accepted 22 November 2012
10.1126/science.1230054

Climate Events Synchronize the Dynamics of a Resident Vertebrate Community in the High Arctic

Brage B. Hansen,[1]†‡ Vidar Grøtan,[1]† Ronny Aanes,[1,2]* Bernt-Erik Sæther,[1] Audun Stien,[3] Eva Fuglei,[2] Rolf A. Ims,[4] Nigel G. Yoccoz,[4] Åshild Ø. Pedersen[2]

Recently accumulated evidence has documented a climate impact on the demography and dynamics of single species, yet the impact at the community level is poorly understood. Here, we show that in Svalbard in the high Arctic, extreme weather events synchronize population fluctuations across an entire community of resident vertebrate herbivores and cause lagged correlations with the secondary consumer, the arctic fox. This synchronization is mainly driven by heavy rain on snow that encapsulates the vegetation in ice and blocks winter forage availability for herbivores. Thus, indirect and bottom-up climate forcing drives the population dynamics across all overwintering vertebrates. Icing is predicted to become more frequent in the circumpolar Arctic and may therefore strongly affect terrestrial ecosystem characteristics.

In the Arctic, climate is now changing rapidly (*1*), affecting the population dynamics of many species, as well as trophic interactions among them (*2*). It is well recognized (*3*) that spatial correlations in climate can enforce synchronous fluctuations among populations within the same species [the "Moran effect" (*4*)]—increasing the likelihood of species extinctions (*5*, *6*). More far-reaching consequences may be expected if such climate-enforced synchronization acts on the level of ecological communities (*7*, *8*). However, linking cross-species synchrony to common environmental drivers has proven difficult as variation among species in the form of density regulation and response to other environmental drivers often has a desynchronizing effect (*9*). Thus, observed synchrony usually results from trophic interactions, such as the cofluctuations among predators because of shared prey (*3*). Nonetheless, one rare example of vertebrates that fluctuate synchronously but are not linked by trophic interactions comes from the Arctic, where populations of caribou (*Rangifer tarandus*) and musk oxen (*Ovibos moschatus*) on opposite coasts of Greenland seem synchronized by large-scale weather oscillations (*7*), but see (*10*).

Here, we ask how climate and weather events influence population dynamics across the entire overwintering vertebrate community on the high-arctic island of Spitsbergen, Svalbard (Fig. 1 and fig. S1). In winter, this trophic system at 78°N includes only three herbivores, the wild Svalbard reindeer (*R. t. platyrhynchus*), Svalbard rock ptarmigan (*Lagopus muta hyperborea*), and sibling vole (*Microtus levis*), as well as their shared consumer, the arctic fox (*Vulpes lagopus*). The species are sympatric and widely distributed across the archipelago, except for the vole, which is only found in a small bird cliff area (*11*). In the short summer season, migratory birds including seabirds, geese, and waders also breed in Svalbard, and polar bears (*Ursus maritimus*) occasionally go on shore throughout the year. However, the few resident terrestrial vertebrates and the lack of widespread endemic arctic rodents with multiannual population cycles, such as arctic lemmings (*Lemmus* spp. and *Dicrostonyx* spp.), makes the Svalbard terrestrial food web and its trophic dynamics simpler than many other high-arctic ecosystems (*12*).

We found correlated population fluctuations across all four overwintering members of the community (Fig. 1), specifically the presence of positive interspecific correlations in the annual changes in population sizes or population indexes (*13*) when the arctic fox data were advanced by 1 year (Figs. 2B and 3). One plausible hypothesis explaining this synchrony is that climate influences the herbivores in a broadly similar way because of common effects on plant availability, operating through variation in snowpack properties or vegetation growth. This generates bottom-up effects on their shared consumer. To test this, we fitted linear regressions (*13*) that modeled population growth rate as a function of log population size (or index) and weather covariates obtained from a local weather station that were expected to influence the herbivore food supply.

Model selection (table S1) suggested that, after accounting for density dependence, the number of rainy days in winter (hereafter, "winter rain") (Fig. 2A) was the best predictor of annual population growth rates across species. Winter rain had a significantly negative effect on all species (tables S2 to S5). Model selection also revealed an additional positive effect of summer temperature on the species'

[1]Centre for Conservation Biology, Department of Biology, Norwegian University of Science and Technology, NO-7491 Trondheim, Norway. [2]Norwegian Polar Institute, Fram Centre, NO-9296 Tromsø, Norway. [3]Norwegian Institute for Nature Research, Fram Centre, NO-9296 Tromsø, Norway. [4]Department of Arctic and Marine Biology, University of Tromsø, NO-9037 Tromsø, Norway.

*Present address: Norwegian Directorate for Nature Management, Tungasletta 2, NO-7047 Trondheim, Norway.
†These authors contributed equally to this work.
‡To whom correspondence should be addressed. E-mail: brage.b.hansen@ntnu.no

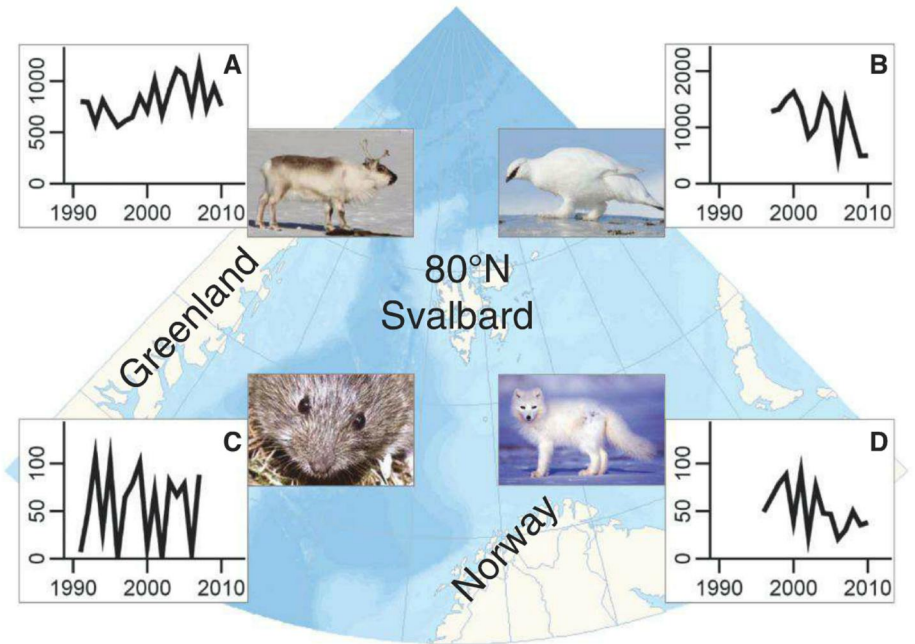

Fig. 1. The study system in high-arctic Svalbard. Annual population abundances (or indexes) are shown for the overwintering vertebrates: (**A**) wild reindeer, (**B**) rock ptarmigan, (**C**) sibling vole, and (**D**) arctic fox (advanced by 1 year).

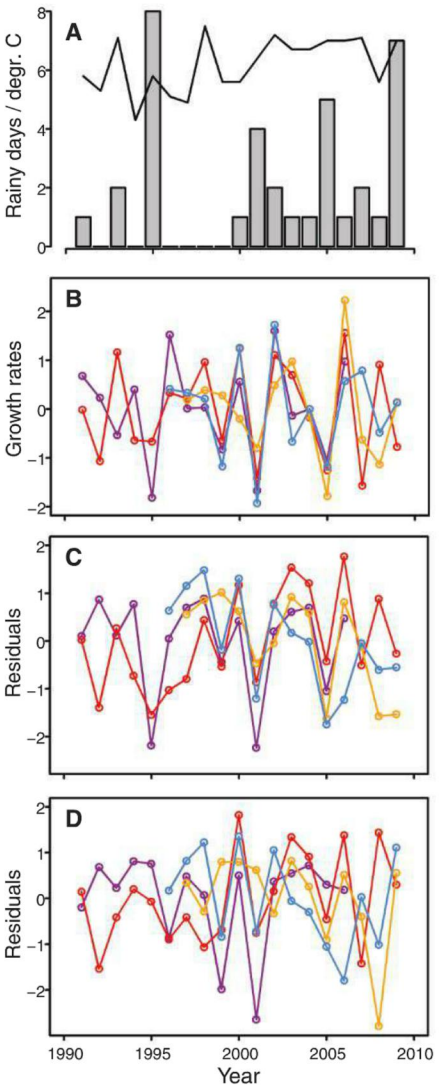

Fig. 2. Annual fluctuations in weather and population parameters for the vertebrates overwintering in Svalbard. (**A**) Weather variables acting as synchronizing agents across species, i.e., total number of rainy days during the core winter season [December year (*t*) through March year (*t* + 1), bars] and mean temperature in summer [July–August year (*t*), solid line]. (**B**) Standardized population growth rates ($\log[N_{t+1}] - \log[N_t]$) of sibling vole (purple), wild reindeer (red), rock ptarmigan (orange), and arctic fox (blue; advanced by 1 year). (**C** and **D**) Residuals from linear models of population growth rates when including (C) only density and (D) density and weather variables as covariates.

growth rates. We evaluated the synchronizing effect of climate by testing whether estimates of the among-species correlation in model residuals were reduced when compared with estimates from a model including only effects of density dependence (*14*). The correlation in model residuals was lower for all species pairs (Fig. 3) and, on average, was significantly reduced (mean $r = 0.10$ versus $r = 0.43$; Fig. 4) when we included winter rain and summer temperature as predictor variables (Fig. 2, C and D). As hypothesized, this suggests that climate enforces the synchrony among the herbivores and induces lagged fox-herbivore correlations through changes in abundance of prey and reindeer carrion.

Fluctuations in summer and winter climate can influence the herbivores' food supply directly and indirectly, respectively. First, at these latitudes, even a slight increase in summer temperature increases the green biomass available for herbivores (*15*). Second, there is emerging evidence that warmer and rainier winters can generate a similar negative response in many northern populations of small (*16*–*18*) and large herbivores (*19*–*21*) owing to changes in snowpack characteristics. Warm spells and rain generate crust-ice layers through thaw-freezing cycles, and heavy rain may percolate through the entire snowpack and cause ground icing (*19*, *22*). A thick ice layer can build up on the deeply frozen ground and encapsulate most of the short-growing vegetation on the high-arctic tundra (*19*). Previous studies of other populations of Svalbard reindeer have shown that extreme winter rain (many rainy days) and associated icing dramatically suppress food accessibility (*19*) and contribute significantly to the population dynamics (*19*, *21*) by simultaneously reducing survival (causing mass mortality in calves and old animals) (*21*) and fecundity (*21*, *23*). Rain-on-snow and icing events also have a negative effect on the sibling voles (*11*), and their fluctuations in abundance therefore follow changes in local reindeer fecundity (*23*). Our analyses demonstrate that particularly rainy (≥4 rainy days) (Fig. 2A) and, hence, icy winters generate simultaneous population crashes in all overwintering herbivores. This drives them into 2 years or more of synchronous fluctuations, as the decline is followed by an increase because of reduced food competition and, in the case of vole and ptarmigan, possibly reduced predation pressure. The dynamics of the herbivores may subsequently diverge because of contrasting density regulation and other environmental drivers (*9*) and then be forced back into synchronous decline with the next icing event. None of the herbivores seem able to recover during the summer following icing. This is due to low fecundity in reindeer (*23*) and, most likely, few breeding voles (*11*) and ptarmigans (for which springtime body condition also affects fecundity) (*24*). The vole and ptarmigan may also be subject to a top-down effect of fox predation. Accordingly, climate drives the herbivore synchrony, but the mechanisms can differ among species.

A lagged correlation is not uncommon for fox-prey population abundance dynamics (*12*). In the lemming-free Svalbard ecosystem, foxes are not functional predators of reindeer, and the fox population abundance is most likely related to the availability of reindeer carrion (*25*, *26*)—the most important terrestrial food at the onset of fox breeding. More important, a rainy and icy winter with excess of carrion is likely to be followed by a winter with distinct scarcity of carrion (table S6). This occurs because high mortality of calves and old individuals in the icy winter and low subsequent calf production result in a low-density population with reduced

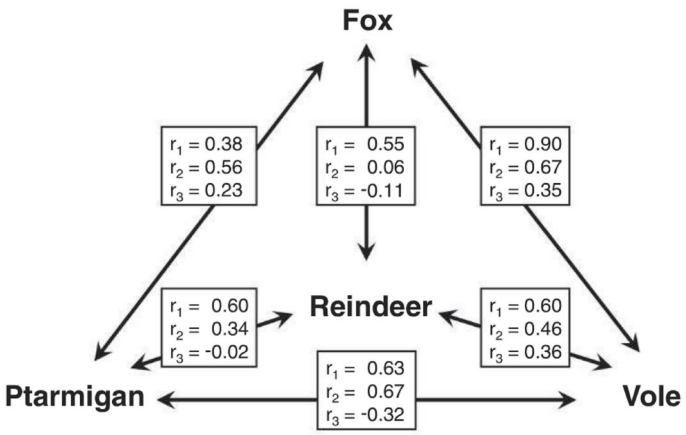

Fig. 3. Pairwise correlations in population parameters between the vertebrates overwintering in Svalbard. Correlation coefficients are given for population growth rates (r_1) and residuals from linear models of population growth rates when including density (r_2) and including density and climate (r_3), i.e., winter rain and summer temperature, as covariates. Note that the fox data were advanced by 1 year.

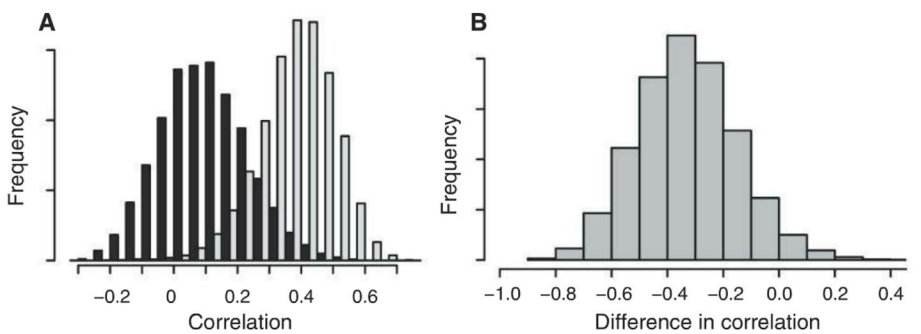

Fig. 4. Effect of climate (winter rain and summer temperature) on population synchrony. **(A)** Simulated mean between-species correlations in residuals from linear models of population growth rates including only density (light gray bars) versus including density and weather (dark gray bars). **(B)** Difference in between-species correlations in model residuals when excluding versus including weather (median difference = −0.334, 5th percentile = −0.614, 95th percentile = −0.025). Note that the fox data were advanced by 1 year.

food competition and predominantly high-quality individuals entering the next winter (*21*, *23*). The combination of these highs and subsequent lows in carrion availability influences the fox growth rate (table S7 and fig. S2) and is most likely the mechanism that forces the observed dynamics of reindeer and foxes into lagged correlations. The icy conditions that cause these correlated population fluctuations have been frequent in Svalbard since the mid 1990s, i.e., during most of our study period, because of high temperatures and frequent rain on snow (*19*). If, however, icing occurs even more frequently, a different pattern of cofluctuations may emerge because consecutive severe winters would cause less distinct ups and downs in carrion.

This study has demonstrated cross-species synchronization of population dynamics by climate that operates among unrelated species with different patterns of density regulation and a large variation in life-history strategies, ranging from the slow (reindeer) to the very fast (vole) (*11*) end of the life-history continuum (*27*). The Svalbard tundra is characterized by few species, with a lack of specialist predators, and multiannual predator-prey cycles. This eliminates the potential for trophic interactions to cause synchrony (*3*, *28*, *29*) and obscure synchronizing effects of climate. Although not shown previously, in such a simple ecosystem it may not be surprising that climate-induced vegetation "blocking" generates a trophic effect on all primary consumers that wells up to the secondary consumer. It also appears that rapid responses to environmental change are particularly pronounced in arctic herbivores. Svalbard is characterized by large weather fluctuations and has been considered an "early warning" system (*30*) for the projected increase in extreme events and rainfall during winter across the Arctic (*1*). As demonstrated here, such extreme events may have broad ecological implications (*2*). Warmer and rainier winters may already have contributed to dampened fluctuations in many rodent populations (*16*, *18*) and the decline in many caribou and reindeer populations in the northern hemisphere (*31*). Such changes are, in turn, expected to influence other ecosystem components (*17*, *32*), as shown here. The present study therefore represents a bellwether of how future changes in climate and extreme events during winter may contribute to shape ecosystem functioning and stability in the terrestrial Arctic.

References and Notes

1. Arctic Monitoring and Assessment Programme, *Snow, Water, Ice and Permafrost in the Arctic (SWIPA): Climate Change and the Cryosphere* (AMAP, Oslo, 2011).
2. E. Post *et al.*, *Science* **325**, 1355 (2009).
3. A. Liebhold, W. D. Koenig, O. N. Bjornstad, *Annu. Rev. Ecol. Evol. Syst.* **35**, 467 (2004).
4. P. A. P. Moran, *Aust. J. Zool.* **1**, 291 (1953).
5. E. Post, M. C. Forchhammer, *Proc. Natl. Acad. Sci. U.S.A.* **101**, 9286 (2004).
6. M. Heino, V. Kaitala, E. Ranta, J. Lindstrom, *Proc. R. Soc. London B Biol. Sci.* **264**, 481 (1997).
7. E. Post, M. C. Forchhammer, *Nature* **420**, 168 (2002).
8. J. H. Myers, *Ecology* **79**, 1111 (1998).
9. B.-E. Sæther *et al.*, *J. Anim. Ecol.* **76**, 315 (2007).
10. J. O. Vik, N. C. Stenseth, G. Tavecchia, A. Mysterud, O. C. Lingjærde, *Nature* **427**, 697 (2004).
11. N. G. Yoccoz, R. A. Ims, *Ecol. Bull.* **47**, 137 (1999).
12. R. A. Ims, E. Fuglei, *Bioscience* **55**, 311 (2005).
13. Materials and methods are available as supplementary materials on *Science* Online.
14. S. Engen, R. Lande, B.-E. Sæther, T. Bregnballe, *J. Anim. Ecol.* **74**, 601 (2005).
15. R. van der Wal, D. O. Hessen, *Perspect. Plant Ecol. Evol. Syst.* **11**, 231 (2009).
16. K. L. Kausrud *et al.*, *Nature* **456**, 93 (2008).
17. O. Gilg, B. Sittler, I. Hanski, *Glob. Change Biol.* **15**, 2634 (2009).
18. R. A. Ims, J.-A. Henden, S. T. Killengreen, *Trends Ecol. Evol.* **23**, 79 (2008).
19. B. B. Hansen, R. Aanes, I. Herfindal, J. Kohler, B.-E. Saether, *Ecology* **92**, 1917 (2011).
20. M. Forchhammer, D. Boertmann, *Ecography* **16**, 299 (1993).
21. E. J. Solberg *et al.*, *Ecography* **24**, 441 (2001).
22. J. Putkonen, G. Roe, *Geophys. Res. Lett.* **30**, 1188 (2003).
23. A. Stien *et al.*, *Biol. Lett.* **8**, 1002 (2012).
24. J. B. Steen, S. Unander, *Ornis Scand.* **16**, 191 (1985).
25. N. E. Eide, A. Stien, P. Prestrud, N. G. Yoccoz, E. Fuglei, *J. Anim. Ecol.* **81**, 640 (2012).
26. E. Fuglei, N. A. Øritsland, P. Prestrud, *Polar Biol.* **26**, 93 (2003).
27. B.-E. Sæther, Ø. Bakke, *Ecology* **81**, 642 (2000).
28. O. N. Bjørnstad, R. A. Ims, X. Lambin, *Trends Ecol. Evol.* **14**, 427 (1999).
29. R. A. Ims, H. P. Andreassen, *Nature* **408**, 194 (2000).
30. K. J. Rennert, G. Roe, J. Putkonen, C. M. Bitz, *J. Clim.* **22**, 2302 (2009).
31. L. S. Vors, M. S. Boyce, *Glob. Change Biol.* **15**, 2626 (2009).
32. N. M. Schmidt *et al.*, *Proc. R. Soc. London Ser. B Biol. Sci.* **279**, 4417 (2012).

Acknowledgments: Data collection was financed by the Norwegian Polar Institute, University of Tromsø, Norwegian Institute for Nature Research, Norwegian Research Council (ALV and NORKLIMA grants), Governor of Svalbard, and French Polar Institute. This study was financed by NORKLIMA (grants 178561/S30 and 216051), the European Research Council (ERC-2010-AdG 268562), and Centre for Conservation Biology (Norwegian University of Science and Technology). We thank the Norwegian Meteorological Institute (weather data), Governor of Svalbard (ptarmigan data), and Erik Ropstad (ptarmigan photo). Data are presented (table S8) in supplementary materials.
Author contributions: A.S., R.A.I., N.G.Y., and E.F. collected vole data. R.A. collected reindeer data. E.F. collected fox data. E.F. and Å.Ø.P. controlled ptarmigan data. R.A., B.B.H., and B.E.S. initiated the study. V.G. analyzed data and wrote Materials and Methods. B.B.H. wrote the manuscript. All authors contributed on later manuscript versions.

Supplementary Materials

www.sciencemag.org/cgi/content/full/339/6117/313/DC1
Materials and Methods
Figs. S1 and S2
Tables S1 to S8
References (*33*, *34*)

2 July 2012; accepted 29 November 2012
10.1126/science.1226766

Invasive Plants Have Scale-Dependent Effects on Diversity by Altering Species-Area Relationships

Kristin I. Powell,[1]* Jonathan M. Chase,[2] Tiffany M. Knight[1]

Although invasive plant species often reduce diversity, they rarely cause plant extinctions. We surveyed paired invaded and uninvaded plant communities from three biomes. We reconcile the discrepancy in diversity loss from invaders by showing that invaded communities have lower local richness but steeper species accumulation with area than that of uninvaded communities, leading to proportionately fewer species loss at broader spatial scales. We show that invaders drive scale-dependent biodiversity loss through strong neutral sampling effects on the number of individuals in a community. We also show that nonneutral species extirpations are due to a proportionately larger effect of invaders on common species, suggesting that rare species are buffered against extinction. Our study provides a synthetic perspective on the threat of invasions to biodiversity loss across spatial scales.

Many empirical studies show dramatic reductions of native biodiversity in the presence of invasive species (*1*–*3*). However, evidence that invasive species cause native species extinctions is rare, although it might be expected given the overwhelming evidence of their negative effects (*4*–*7*). Although invasive predators and parasites are known to have caused extinctions of many species (*8*), competition with invasive plants is rarely implicated in extinction (*5*, *9*). In fact, in some cases the presence of invasive plants can actually increase species richness, leading to questions about whether most invasive species are really a leading threat to the conservation of native biodiversity (*9*, *10*).

A difference in the spatial scales of investigation might explain the controversy between studies that find reductions in biodiversity and those that find no effects or positive effects on biodiversity. Studies that find invasive-plant–mediated reductions in biodiversity typically investigate small spatial scales (<25 m^2), whereas studies that find little evidence for negative effects of plant invaders on extinctions take place at much broader spatial scales (*2*). We hypothesized that this discrepancy can be resolved by understanding whether and how invasive species alter the scaling of species richness with area [the species-area relationship (SAR), $S = cA^z$, where S is species number, A is area, and c and z are constants). Specifically, the effect of invasive species will become increasingly tempered with sampling scale if the invader decreases the intercept (c) and/or increases the slope (z) of the log-log SAR [$\log(S) = z\log(A) + \log(c)$].

We examined the scale-dependent influence of invasive plant species, which we define as the subset of nonnative plant species that have high rates of population growth and become dominant members of the community to which they are introduced (*11*–*13*). The influence of non-native plant species that do not achieve such dominance is not as controversial and has little negative influence on species richness at any scale. We haphazardly chose three disparate, forested biomes from across the United States that are experiencing established but ongoing invasions. We chose species with disparate growth forms and physiology across biomes in order to explore possible generality of their effects on diversity. Our study systems were as follows: hardwood hammock forests in central Florida that are being invaded by *Dianella ensifolia* (cerulean flax lily), a dense mat-forming understory herb introduced from Asia and Africa (*14*); oak-hickory forests in eastern Missouri that are being invaded by *Lonicera maackii* (Amur honeysuckle), a mid-story shrub introduced from East Asia that creates low light levels and soil allelopathy (*15*, *16*); and tropical mesic forests on the Big Island of Hawai'i that are being invaded by *Morella faya* (fire tree), a nitrogen-fixing canopy tree introduced from Macaronesia (*17*).

We identified multiple pairs of sites on opposite sides of each ongoing invasion front. Invaded communities were dominated (>90% cover) by the focal invader, which was present for at least 30 years (based on population structure and conversations with local managers). To minimize variation among site conditions other than the presence of the invader, paired 500-m^2 communities were identified according to the following three criteria: they were spatially proximate and occurred on similar soil and topographic conditions; they had very low densities of the invasive species but had a population structure indicative of future growth (for example, many individuals of each stage class); they had the same dominant and subdominant native overstory species, suggesting similarity in the underlying environmental conditions (fig. S1) (*18*).

We found a universally lower intercept (c) and steeper slope (z) of the SAR in invaded communities relative to uninvaded communities across biomes (Fig. 1 and fig. S2). Each plant invader caused large species richness reductions at small scales but a much smaller proportional reduction in species richness at broad scales (Fig. 1 and fig. S3). These patterns support our hypothesis that the discrepancy between studies that find larger or smaller influences of invasive species on native biodiversity can be reconciled by considering spatial scale.

The influence of invasive species on the slope of the SAR (z) results from the tension between four non–mutually exclusive mechanisms: a neutral sampling effect, nonneutral shifts in the relative abundance of species, local species extirpations, and/or shifts in the aggregation among individuals (*19*–*21*). First, by reducing the absolute number of individuals in invaded habitats (*3*, *22*, *23*), invasive species can decrease c and increase z through a neutral sampling effect, so long as the

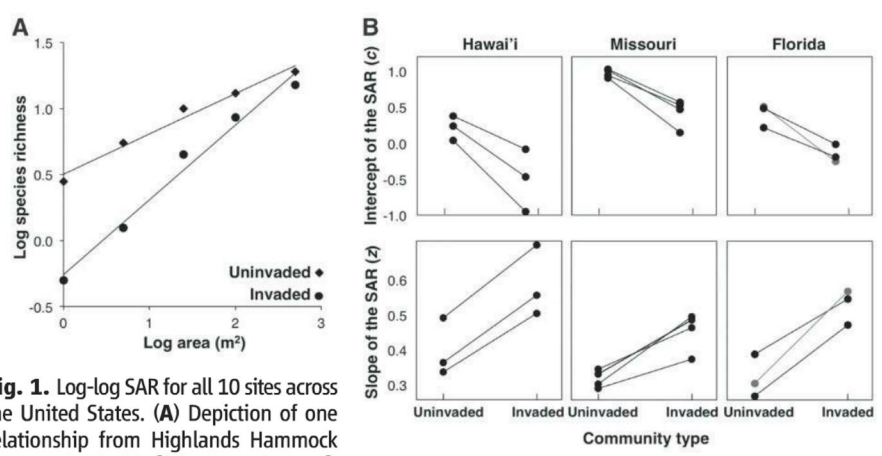

Fig. 1. Log-log SAR for all 10 sites across the United States. (**A**) Depiction of one relationship from Highlands Hammock State Park, Florida [(B), shown in gray], highlighting how increases in the SAR slopes (z) in invaded communities lead to smaller species richness declines with increasing spatial scale. (**B**) Decreases in the intercepts (c) and increases in the slopes (z) of the invaded SAR for Hawai'i (invasive plant *M. faya*: c, $t = 4.702$, $P = 0.042$; z, $t = 15.541$, $P = 0.004$), Missouri (invasive plant *L. maackii*; c, $t = 7.219$, $P = 0.005$; z, $t = 6.151$, $P = 0.009$), and Florida (invasive plant *D. ensifolia*; c, $t = 5.194$, $P = 0.035$; z, $t = 6.783$, $P = 0.021$).

[1]Department of Biology, Washington University in St. Louis, St. Louis, MO 63130, USA. [2]St. Louis, MO, USA.

*To whom correspondence should be addressed. E-mail: kipowell@wustl.edu.

SAR has a maximum species richness (*2*, *19*, *24*). Second, invasive species can alter the shape of the relative species abundance distribution (SAD) through nonneutral effects on species' abundances (*2*, *21*, *25*). If native communities become more even in the presence of invaders, z will increase, whereas if native communities become less even, z will decrease. Third, both sampling effects and shifts in the shape of the SAD due to an invader can increase deterministic and stochastic local extirpations, which will decrease z. Fourth, the degree of intra- and interspecific aggregation of individuals within a community will influence z; less aggregated communities have a steeper z than that of more aggregated communities (*18*, *21*, *25*).

To dissect the relative influence of the four main mechanisms on z, we used null model analyses on spatially explicit abundance data collected in 50 1-m^2 plots evenly distributed within each 500-m^2 SAR plot (*18*). Because dissecting the effects of aggregation versus local extirpations requires a different type of null model, it was not possible to dissect all of the possible mechanisms in a single analysis. Thus, we first determined whether there were differences in aggregation between invaded and uninvaded communities by measuring the bias—or difference in area under curves—between the species rarefaction (nonspatially explicit null expectation) and accumulation (spatially explicit) curves [modified from (*26*)]. We found no significant difference in bias between invaded compared with uninvaded communities within or across sites (paired t tests for each plant invader, $-1.015 < t < 1.924$, $0.194 < P < 0.994$) (fig. S4) (*18*), indicating that differences in aggregation are unlikely to be a cause of observed shifts in z.

We next devised a null model approach to dissect the effects of invasive species due to neutral sampling effects, local species extirpations, and shifts in the shape of the SAD (table S1) (*18*). In all cases, there was a large reduction in the number of individuals in the invaded community (ranging from 65 to 91% loss of individuals), which led to large increases in z due to the sampling effect (Fig. 2 and Table 1). However, predicted changes in z solely due to the sampling effect were universally higher than the observed changes in z (Fig. 2) (*18*). We found that species extirpations moderated the influence of neutral sampling effects on z. In all invaded communities, there were fewer species in our largest sample area than expected from neutral sampling, suggesting that these species were subject to a deterministic or stochastic negative influence of small populations on extirpation. Although one site did show a more even SAD in the invaded community, species extirpations outweighed the influence of invaders on the shape of the SAD (Fig. 2).

Although the observed shifts in the slope of the SAR (z) were largely due to neutral sampling effects moderated by local extirpations, we asked whether the local extirpations might have resulted because rarer species were inherently more susceptible to invaders or, instead, simply victims of low population numbers. We examined abundance changes in each species' response to invaders and determined the deviation of their abundance in the invaded community relative to that expected from neutral sampling effects (*18*, *27*). Species that were common in uninvaded communities tended to deviate negatively from abundances expected from sampling effects (they were more strongly influenced by the invader), whereas species that were rarer in uninvaded communities tended to deviate positively from expected abundances (they were less strongly influenced) (Table 1 and fig. S5). This result could have emerged from at least two nonexclusive mechanisms, including common species having greater niche overlap with invaders (*28*) and/or rare species possessing life history traits—such as shade tolerance or growth under low-resource conditions (*29*)—that allow them to proportionately maintain their abundance in the presence of invaders (*30*).

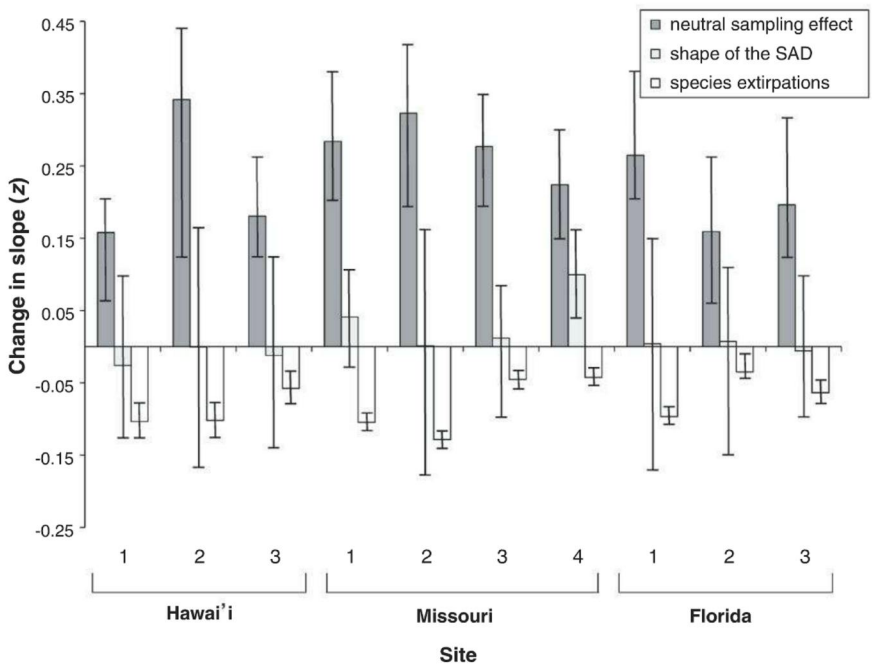

Fig. 2. Contribution of neutral sampling effects (dark gray bars), nonneutral changes in the relative species abundance distribution (light gray bars), and species extirpations beyond those expected from sampling (white bars) to the observed difference in the slope (z) of the SAR between invaded and uninvaded communities. The sum of the bars for each site is equivalent to the observed change in slope between invaded and uninvaded communities across 50 1-m^2 plots. Positive bars contribute to a higher slope observed in the invaded relative to the uninvaded community, whereas negative bars moderate the observed difference in slopes. Error bars are 95 percentile confidence intervals (table S1) (*18*).

Table 1. The loss of individuals (excluding the focal invader) and Kendall's rank correlation explaining shifts in species' abundances for all sites. Kendall's rank correlations show the relationship between a species' abundance in the uninvaded community and its deviation from its expected abundance in the invaded community. Significant P values reflect larger negative effects of plant invaders on common as compared with rare species.

Site	Sampled site	Individuals in uninvaded community	Individuals in invaded community	Kendall's rank correlation coefficient (τ)	Kendall's rank correlation P value
Hawai'i	1	223	77	−0.231	0.109
	2	163	17	−0.405	0.014
	3	241	59	−0.369	0.010
Missouri	1	4378	374	−0.381	<0.001
	2	1460	228	−0.378	<0.001
	3	840	98	−0.442	<0.001
	4	4348	486	−0.407	<0.001
Florida	1*	569*	120*	−0.482*	<0.001*
	2	362	127	−0.230	0.072
	3	369	129	−0.308	0.040

*Corresponds to the Highlands Hammock State Park example shown in Fig. 1A.

Thus, rarer species may be more buffered from extinction than expected from neutral sampling effects. However, time-lagged extinctions due to extinction debt may lead to additional species loss (*31*).

Although an examination of how hundreds of common and rare species were disproportionately influenced by invaders is beyond the scope of this study, we can glean insights by examining the traits of common and rare species at the study sites. For example, in Hawai'i the native sedge *Carex wahuensis* was rare in the absence of the invader but became proportionately more common in the presence of the invader, likely because it could tolerate lower light and/or take advantage of higher nitrogen imposed by the invasive *M. faya* (*32*). Likewise, in Missouri several native species known to be shade tolerant (such as *Desmodium glutinosum* and *Trillium recurvatum*) (*33*) were proportionately less influenced by the invasive *L. maacki* than were shade-intolerant species.

Overall, by explicitly focusing on scale-dependent processes, the results from our study reconcile the differences observed among local- and broad-scale effects of invasive plant species on biodiversity. Decreased intercepts (c) and increased slopes (z) of the SAR were primarily caused by neutral sampling effects. In addition, disproportionately smaller effects on rare species' abundances moderated species loss at the broadest spatial scale. Understanding the mechanisms by which invasive species shift species abundance distributions could improve our ability to forecast future invasion-induced extinctions. Although particularly harmful to native biodiversity at small spatial scales, invasive species' effects may be reversed through targeted control to increase native species abundances, at least until future extinction debt is paid.

References and Notes

1. M. Gaertner, A. D. Breeyen, C. Hui, D. M. Richardson, *Prog. Phys. Geogr.* **33**, 319 (2009).
2. K. I. Powell, J. M. Chase, T. M. Knight, *Am. J. Bot.* **98**, 539 (2011).
3. M. Vilà *et al.*, *Ecol. Lett.* **14**, 702 (2011).
4. D. F. Sax, S. D. Gaines, J. H. Brown, *Am. Nat.* **160**, 766 (2002).
5. J. Gurevitch, D. K. Padilla, *Trends Ecol. Evol.* **19**, 470 (2004).
6. L. C. Maskell, G. Firbank, K. Thompson, J. M. Bullock, S. M. Smart, *J. Ecol.* **94**, 1052 (2006).
7. T. J. Stohlgren, D. T. Barnett, C. S. Jarnevich, C. Flather, J. Kartesz, *Ecol. Lett.* **11**, 313, discussion 322 (2008).
8. M. A. Davis, *Bioscience* **53**, 481 (2003).
9. D. F. Sax, S. D. Gaines, *Proc. Natl. Acad. Sci. U.S.A.* **105** (suppl. 1), 11490 (2008).
10. M. A. Davis *et al.*, *Nature* **474**, 153 (2011).
11. C. S. Kolar, D. M. Lodge, *Trends Ecol. Evol.* **16**, 199 (2001).
12. L. Valéry, H. Fritz, J.-C. Lefeuvre, D. Simberloff, *Biol. Inv.* **10**, 1345 (2008).
13. J. Gurevitch, G. A. Fox, G. M. Wardle, D. Inderjit, D. Taub, *Ecol. Lett.* **14**, 407 (2011).
14. J. T. Hutchinson, E. A. Gandy, K. A. Langeland, *Inv. Plant Sci. Manage.* **4**, 349 (2011).
15. M. H. Collier, J. L. Vankat, M. R. Hughes, *Am. Midl. Nat.* **147**, 60 (2002).
16. M. Dorning, D. Cipollini, *Plant Ecol.* **184**, 287 (2006).
17. P. M. Vitousek, L. R. Walker, *Ecol. Monogr.* **59**, 247 (1989).
18. Materials and methods are available as supplementary materials on *Science* online.
19. F. W. Preston, *Ecology* **43**, 185 (1962).
20. R. M. May, in *Ecology and Evolution of Communities*, M. L. Cody, J. M. Diamond, Eds. (Harvard Univ. Press, Cambridge, MA, 1975), pp. 81–120.
21. F. He, P. Legendre, *Ecology* **83**, 1185 (2002).
22. S. J. Meiners, S. T. A. Pickett, M. L. Cadenasso, *Ecography* **25**, 215 (2002).
23. T. P. Rooney, S. M. Wiegmann, D. A. Rogers, D. M. Waller, *Conserv. Biol.* **18**, 787 (2004).
24. T. D. Olszewski, *Oikos* **104**, 377 (2004).
25. J. L. Green, A. Ostling, *Ecology* **84**, 3090 (2003).
26. M. D. Collins, D. Simberloff, *Environ. Ecol. Stat.* **16**, 89 (2009).
27. J. M. Chase, N. J. B. Kraft, K. G. Smith, M. Vellend, B. D. Inouye, *Ecosphere* **2**, art24 (2011).
28. A. S. MacDougall, B. Gilbert, J. M. Levine, *J. Ecol.* **97**, 609 (2009).
29. C. C. Daehler, *Annu. Rev. Ecol. Evol. Syst.* **34**, 183 (2003).
30. O. Chabrerie, J. Loinard, S. Perrin, R. Saguez, G. Decocq, *Biol. Invasions* **12**, 1891 (2010).
31. D. Tilman, R. M. May, C. L. Lehman, M. A. Nowak, *Nature* **371**, 65 (1994).
32. P. B. Adler, C. M. D'Antonio, J. T. Tunison, *Pac. Sci.* **52**, 69 (1998).
33. P. Bierzychudek, *New Phytol.* **90**, 757 (1982).

Acknowledgments: We are grateful to H. Bailey, J. Hidalgo, J. Powell, and M. Schutzenhofer for field assistance. We thank B. Allan, E. Gandy, T. Hingtgen, R. Loh, T. Mohrman, and J. Shaw for support with permits and logistics at each field site. The members of the Chase and Knight labs and three anonymous reviewers provided invaluable feedback and greatly improved the analysis and presentation of the manuscript. J.M.C. is an independent researcher. Funding was provided by NSF DGE 1143954 (to K.I.P.), DEB 1110629, and the Tyson Research Center at Washington University in St. Louis. Original data for species richness and area available on Dryad (doi: 10.5061/dryad.qq08m).

Supplementary Materials

www.sciencemag.org/cgi/content/full/339/6117/316/DC1
Materials and Methods
Figs. S1 to S5
Table S1
Reference (*34*)

2 July 2012; accepted 20 November 2012
10.1126/science.1226817

Structure of Histone mRNA Stem-Loop, Human Stem-Loop Binding Protein, and 3′hExo Ternary Complex

Dazhi Tan,[1] William F. Marzluff,[2,3] Zbigniew Dominski,[2,3] Liang Tong[1]*

Metazoan replication-dependent histone messenger RNAs (mRNAs) have a conserved stem-loop (SL) at their 3′-end. The stem-loop binding protein (SLBP) specifically recognizes the SL to regulate histone mRNA metabolism, and the 3′-5′ exonuclease 3′hExo trims its 3′-end after processing. We report the crystal structure of a ternary complex of human SLBP RNA binding domain, human 3′hExo, and a 26-nucleotide SL RNA. Only one base of the SL is recognized specifically by SLBP, and the two proteins primarily recognize the shape of the RNA. SLBP and 3′hExo have no direct contact with each other, and induced structural changes in the loop of the SL mediate their cooperative binding. The 3′ flanking sequence is positioned in the 3′hExo active site, but the ternary complex limits the extent of trimming.

Metazoan replication-dependent histone mRNAs have a conserved stem-loop (SL) structure at their 3′-end (*1*, *2*), distinct from the polyadenylate tail found on all other known eukaryotic mRNAs (*3*, *4*). The stem-loop binding protein (SLBP) (*5*), also known as hairpin binding protein (*6*), is a central regulator of histone mRNA metabolism. SLBP and the U7 small nuclear ribonucleoprotein (snRNP) (*7*) are required for the 3′-end processing of histone pre-mRNAs (fig. S1). SLBP is also required for the export, stability, and translation of mature mRNAs. The 3′-5′ exonuclease 3′hExo (also known as Eri-1) forms a tight ternary complex with SL and SLBP. 3′hExo can trim three nucleotides in vitro from the processed histone mRNA 3′-end, and SLBP protects against further trimming (*8*–*11*). 3′hExo is required for replication-dependent histone mRNA degradation (*12*). It is also involved in microRNA homeostasis (*13*) and 5.8*S* rRNA 3′-end maturation (*14*, *15*). The stem-loop RNA consists of a six–base pair stem and a four-base loop, as well as flanking sequences at both ends (fig. S1). SLBP (31 kD) has high affinity for the SL (dissociation constant K_d = 1 to 10 nM) (*16*–*20*). It contains a ~70-residue RNA binding domain (RBD) (Fig. 1A and fig. S2). 3′hExo (40 kD) consists of an N-terminal SAP domain (~60 residues) followed by a nuclease domain (~220 residues) that belongs to the DEDDh superfamily (Fig. 1A and fig. S3) (*9*–*11*, *21*).

We report here the crystal structure at 2.6 Å resolution of the ternary complex of human SLBP RBD, human 3′hExo (SAP and nuclease domains), and a 26-nucleotide SL with consensus sequence (Fig. 1, A and B, and table S1) (*22*). Clear electron density was observed for all 26 nucleotides of the SL (Fig. 1C). The stem (nucleotides 6 to 11 and 16 to 21) has a slightly flattened

[1]Department of Biological Sciences, Columbia University, New York, NY 10027, USA. [2]Department of Biochemistry and Biophysics, University of North Carolina, Chapel Hill, NC 27599, USA. [3]Program in Molecular Biology and Biotechnology, University of North Carolina, Chapel Hill, NC 27599, USA.

*To whom correspondence should be addressed. E-mail: ltong@columbia.edu

classical A-form structure (fig. S4 and table S2). Of the four nucleotides in the loop, the first (U12), second (U13), and fourth (C15) bases are flipped out (Fig. 1D). In the 3′ flanking sequence, nucleotides 22 to 25 continue the helical structure of the stem, but the base of the last nucleotide (A26) is flipped by ~180° relative to C25 (Fig. 1C). The riboses of all four nucleotides in the loop (nucleotides 12 to 15) and C25 are in the 2′ endo configuration, and the RNA backbone adopts sharp turns at these nucleotides.

The structure of SLBP RBD contains three helices (αA, αB, and αC). Helices αA and αC interact with the 5′ flanking sequence, the 5′ arm of the stem, and the loop of the RNA (Fig. 1B), consistent with earlier data (*9*, *16*, *18*). In particular, helix αC is positioned closest to the SL and may function as a ruler that can measure the length of the stem, with residues near its N terminus (conserved Lys^{177}-Tyr^{178}-Ser^{179}-Arg^{180}-Arg^{181} motif, fig. S2) contacting the 5′-end of the stem and the 5′ flanking sequence and its C-terminal region contacting the loop.

The only direct recognition between SL and SLBP is through the guanine base of the second nucleotide of the stem (G7), via two hydrogen bonds with the side-chain guanidinium group of Arg^{181} (Fig. 2A). The side chain of Tyr^{144} (αA) is π-stacked with the first and the third base, and the side chain of His^{195} (αC) with the fourth base of the loop (Fig. 2B). Other interactions are primarily between the RNA backbone and the SLBP RBD (Fig. 2C and fig. S5).

Nucleotides 3 to 5 in the 5′ flanking sequence, also implicated in binding to SLBP (*9*, *16*, *18*), have interactions with the RBD (fig. S6). Besides residues Tyr^{178} and Ser^{179}, the connection between αA and αC is not in direct contact with the RNA (Fig. 1B). This segment contains the conserved Thr^{171}-Pro^{172}-Asn^{173}-Lys^{174} sequence, and Thr^{171} phosphorylation produces a factor of 7 enhancement in the affinity for SL (*19*). This residue is located near the side chains of Lys^{146} (αA), Tyr^{151} (αA), and Trp^{190} (αC), and its phosphorylation may affect the positioning of the αA and αC helices (fig. S6). Tyr^{151} is part of the conserved Tyr-Asp-Arg-Tyr motif (fig. S2), and the affinity of the Tyr^{151} → Phe mutant for SL is lower by a factor of ~10 relative to wild-type SLBP (*23*).

3′hExo contacts the loop, the 3′ arm of the stem, and the 3′ flanking sequence of the SL (Fig. 1B), as suggested by earlier studies (*9*–*11*). The SAP domain contains three helices (α1 to α3) and interacts primarily with the loop of the SL through α1 (Figs. 1B and 2B). The U13 base interacts with the side chains of Tyr^{66} (α1) and Lys^{111} (α3), and the C15 base has a hydrogen bond to the side chain of Arg^{78} (α1). Additional interactions are with the backbone of the RNA (Fig. 2C and fig. S7).

Nucleotides 24 to 26 at the 3′-end of the SL are located in the active site of the nuclease domain of 3′hExo (Fig. 1B). The C25 base is π-stacked with that of C24 on one face and the side chain of Trp^{233} on the other (Fig. 3A), thereby breaking the helical pattern of the RNA. The side chain of Arg^{261} is located close to the base and ribose of both C24 and C25 (Fig. 3A). In comparison, the first two nucleotides of the 3′ flanking sequence (A22 and C23) do not make direct contacts with 3′hExo (Fig. 3B). The binding mode of the last nucleotide (A26) is similar to that of AMP in the nuclease domain reported earlier (Fig. 3A) (*21*). The phosphate group of A26 is located near the cluster of acidic side chains that coordinate two metal ions for catalysis.

The crystal also contained a 3′hExo-SL binary complex (Fig. 3C and fig. S8). SLBP RBD has low solubility, and some of it precipitated during the preparation of the complex. The nuclease domains of 3′hExo in the two complexes have essentially the same conformation (root-mean-square distance 0.4 Å). The SAP domain shows a small movement (~5° rotation), together with a movement of the RNA (Fig. 3C). However, the first eight nucleotides of the SL, including three at the base of the stem, are disordered in this binary complex (Fig. 3C). The structure of this binary complex is similar to that of 3′hExo in complex with a stem-loop RNA without any flanking sequences reported earlier (PDB entry 1ZBH), although the SAP domain in that crystal comes from another 3′hExo molecule of a domain-swapped dimer (fig. S9).

Transversion of the second base pair of the stem led to a factor of >200 reduction in affinity for SLBP, whereas transversion of the first, third, fourth, or fifth base pair led to a factor of <5 reduction (*18*), consistent with the structural observations (Fig. 2A and fig. S5). Mutation of Arg^{181} in SLBP also inhibited SL binding in yeast three-hybrid assays (*24*, *25*). In comparison, transversion of the second base pair had little effect on 3′hExo binding (*9*), also consistent with the structure (table S3). To further validate the structural observations, we introduced mutations in the SL-SLBP RBD and SL-3′hExo interfaces and determined their effects on the formation of the binary and ternary complexes. Overall, the mutagenesis results are in good agreement with the structure (fig. S10 and table S4).

The modes of SL recognition by the RBD of SLBP and the SAP domain of 3′hExo appear to be distinct from other RNA binding proteins. The SLBP RBD does not have a close structural homolog in the PDB. Although the SAP domain has structural similarity to a domain in the recombination endonuclease VII (*26*), it does not share a common mode of nucleic acid interaction with that domain.

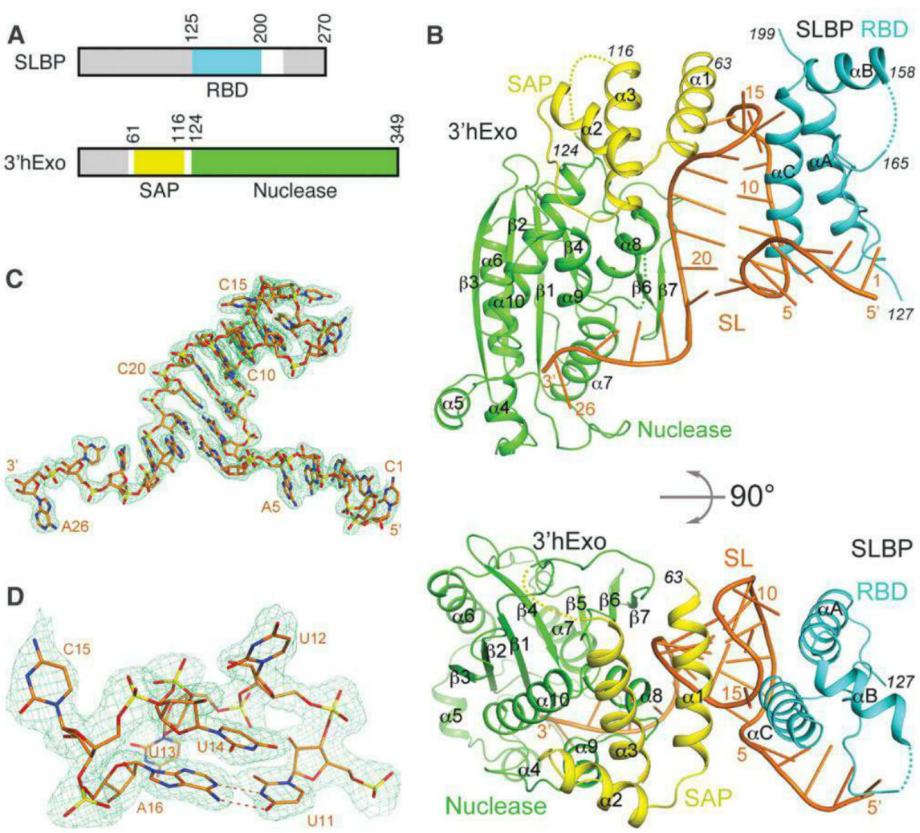

Fig. 1. Structure of human SLBP RBD, human 3′hExo, and SL RNA ternary complex. (**A**) Domain organizations of human SLBP and human 3′hExo. Residues not included in the expression constructs are shown in gray. (**B**) Schematic drawings of the structure of the ternary complex of human SLBP RBD (cyan), human 3′hExo (SAP domain in yellow and nuclease domain in green), and 26-nucleotide SL RNA (orange). (**C**) Simulated annealing omit $F_{obs} - F_{calc}$ electron density (light green) for the SL RNA at 2.6 Å resolution, contoured at 3σ. Phosphorus atoms are in yellow, oxygens in red, and nitrogens in blue. (**D**) Close-up of the loop region of the SL RNA. All the structure figures were produced with PyMOL (www.pymol.org).

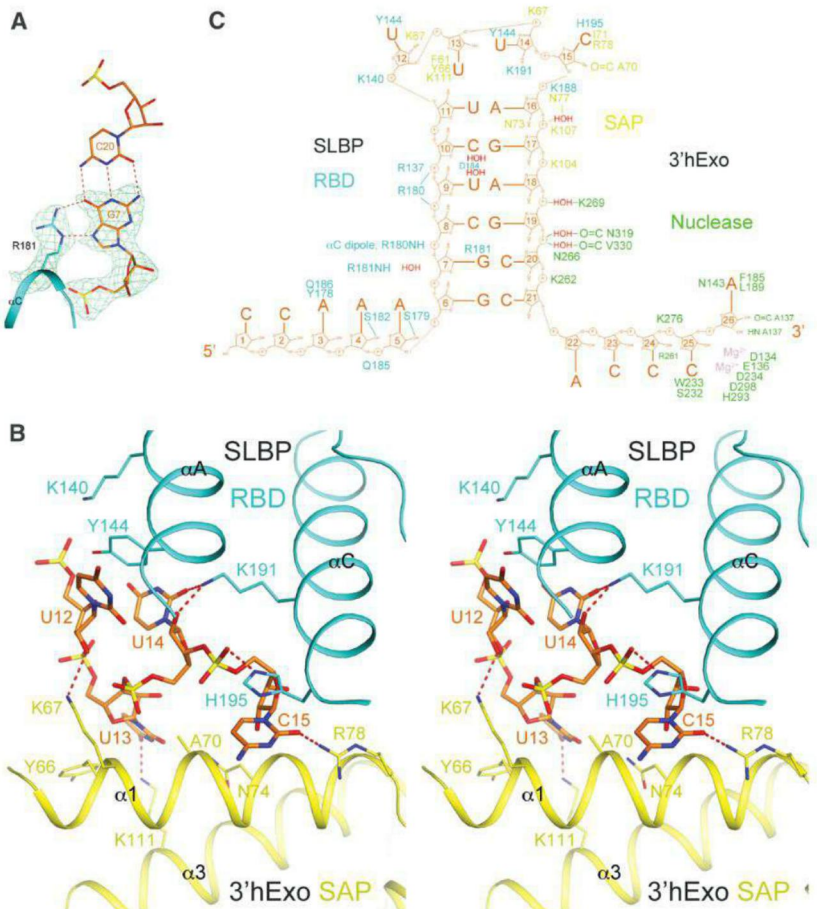

Fig. 2. Interactions between the SL RNA and SLBP RBD and 3′hExo. (**A**) Specific recognition of G7 in the second base pair of the stem (orange) by hydrogen bonding (dashed lines in red) with the side chain of Arg^{181} (cyan) of SLBP. Simulated annealing omit $F_{obs} - F_{calc}$ electron density for G7 and Arg^{181} is also shown, contoured at 5σ. (**B**) Stereopair showing interactions of the loop of the SL RNA (orange) with the SLBP RBD (cyan) and the 3′hExo SAP domain (yellow). (**C**) Schematic drawing summarizing the interactions between SL and SLBP RBD (cyan) and 3′hExo.

Our studies suggest that SLBP RBD and 3′hExo recognize the overall shape of the SL (especially its loop) rather than the sequence; this idea is also supported by observations from the single-transversion studies (*9*, *18*). At the same time, the sequence of the SL plays a role in determining its shape. The first (U12) and third (U14) nucleotides of the loop are highly conserved (fig. S11) and contribute to the specificity of recognition (*9*, *18*). *Caenorhabditis elegans* SLBP is more selective for a C at the first position of the loop, whereas human SLBP binds RNAs with C or U at the first position with comparable affinity (*17*). Tyr^{144} of human SLBP is replaced by an Arg residue in *C. elegans* SLBP, and this may result in a distinct mechanism of recognizing the C in the first nucleotide of the loop (Fig. 2B).

There are no direct contacts between SLBP RBD and 3′hExo in the ternary complex (Fig. 1B and fig. S12). The RBD and SAP domain are arranged on opposite sides of the loop, and they approach each other most closely there. Cooperative binding between the two proteins (*9*–*11*) is likely attributable to induced structural changes in the loop, such that binding of one protein induces a conformation of the loop that promotes the binding of the other protein. In structures of the SL alone in solution (*27*, *28*), the conformation of the loop region is different from that in the complex observed here (fig. S13).

3′hExo has primarily bipartite interactions with the SL. The SAP domain recognizes the loop while the nuclease domain binds the 3′ flanking sequence (Fig. 1B). Disruption of interactions at either of these two sites leads to reduced binding (*9*, *10*). Nucleotide A26 would be the leaving group for the 3′-5′ exonuclease activity (Fig. 3A), which does not show sequence preference (*9*),

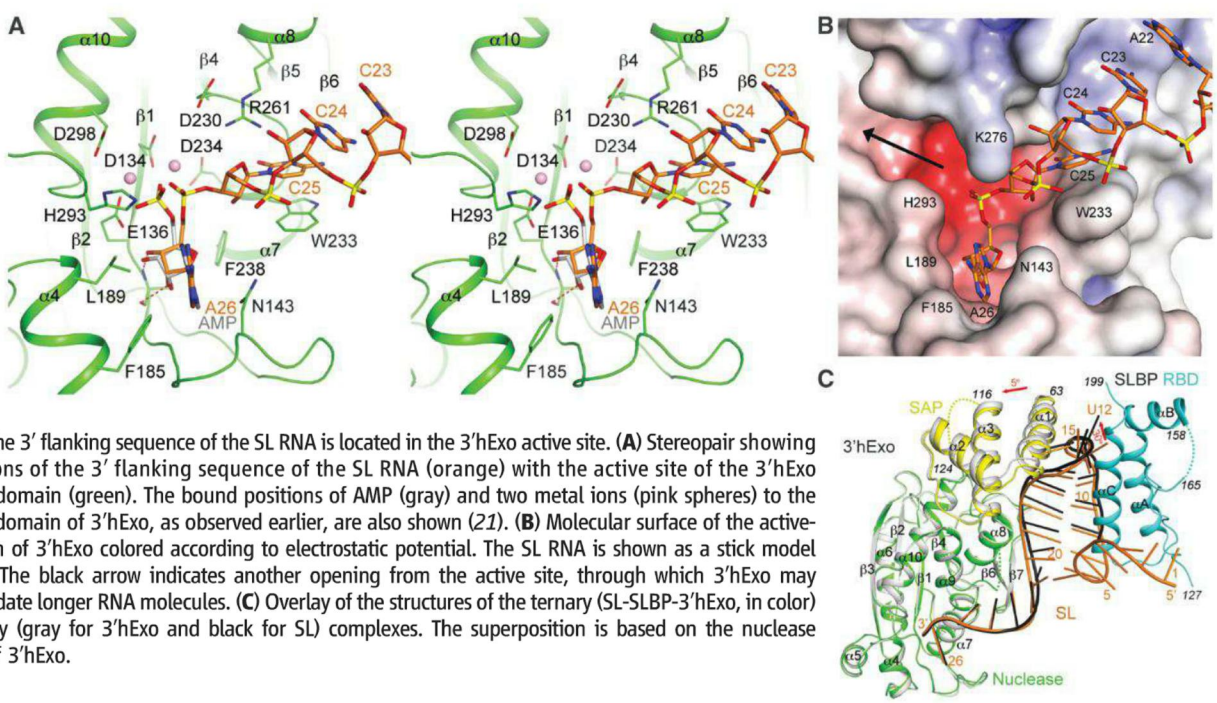

Fig. 3. The 3′ flanking sequence of the SL RNA is located in the 3′hExo active site. (**A**) Stereopair showing interactions of the 3′ flanking sequence of the SL RNA (orange) with the active site of the 3′hExo nuclease domain (green). The bound positions of AMP (gray) and two metal ions (pink spheres) to the nuclease domain of 3′hExo, as observed earlier, are also shown (*21*). (**B**) Molecular surface of the active-site region of 3′hExo colored according to electrostatic potential. The SL RNA is shown as a stick model (orange). The black arrow indicates another opening from the active site, through which 3′hExo may accommodate longer RNA molecules. (**C**) Overlay of the structures of the ternary (SL-SLBP-3′hExo, in color) and binary (gray for 3′hExo and black for SL) complexes. The superposition is based on the nuclease domain of 3′hExo.

as neither C25 nor A26 is recognized specifically. Although 3′hExo can remove the last three nucleotides of the SL (*9*), further degradation is not possible because the 3′-end of the shortened SL can no longer reach the active site of 3′hExo in the ternary complex (Fig. 3B), thereby explaining how SLBP protects histone mRNAs from excessive trimming by 3′hExo.

Besides recognizing the SL RNA, another function of SLBP is the recruitment of U7 snRNP and stabilization of its interaction with the histone pre-mRNA for 3′-end processing (fig. S1) (*23*, *29*). The 20 residues immediately C-terminal to the RBD of SLBP are required for this processing (*29*). These residues are present in the recombinant SLBP used in the current structural studies, but they are disordered. A second region required for processing is located in helix αB of the RBD, especially the Tyr-Asp-Arg-Tyr motif (Fig. 1B and fig. S6), where mutation of the Asp and Arg residues to Gln and Cys, respectively, did not affect binding but abolished processing (*23*). Our structure shows that these two regions are likely located close to each other (fig. S6) and therefore also identifies a surface feature of SLBP that is involved in histone pre-mRNA 3′-end processing (fig. S14).

References and Notes

1. Z. Dominski, W. F. Marzluff, *Gene* **396**, 373 (2007).
2. W. F. Marzluff, E. J. Wagner, R. J. Duronio, *Nat. Rev. Genet.* **9**, 843 (2008).
3. J. Zhao, L. Hyman, C. L. Moore, *Microbiol. Mol. Biol. Rev.* **63**, 405 (1999).
4. C. R. Mandel, Y. Bai, L. Tong, *Cell. Mol. Life Sci.* **65**, 1099 (2008).
5. Z. F. Wang, M. L. Whitfield, T. C. Ingledue 3rd, Z. Dominski, W. F. Marzluff, *Genes Dev.* **10**, 3028 (1996).
6. F. Martin, A. Schaller, S. Eglite, D. Schümperli, B. Müller, *EMBO J.* **16**, 769 (1997).
7. K. L. Mowry, J. A. Steitz, *Science* **238**, 1682 (1987).
8. T. E. Mullen, W. F. Marzluff, *Genes Dev.* **22**, 50 (2008).
9. Z. Dominski, X.-C. Yang, H. Kaygun, M. Dadlez, W. F. Marzluff, *Mol. Cell* **12**, 295 (2003).
10. X.-C. Yang, M. Purdy, W. F. Marzluff, Z. Dominski, *J. Biol. Chem.* **281**, 30447 (2006).
11. X.-C. Yang, M. P. Torres, W. F. Marzluff, Z. Dominski, *Mol. Cell. Biol.* **29**, 4045 (2009).
12. K. P. Hoefig *et al.*, *Nat. Struct. Mol. Biol.* 10.1038/nsmb.2450 (2012).
13. M. F. Thomas *et al.*, *Blood* **120**, 130 (2012).
14. K. M. Ansel *et al.*, *Nat. Struct. Mol. Biol.* **15**, 523 (2008).
15. H. W. Gabel, G. Ruvkun, *Nat. Struct. Mol. Biol.* **15**, 531 (2008).
16. A. S. Williams, W. F. Marzluff, *Nucleic Acids Res.* **23**, 654 (1995).
17. F. Michel, D. Schümperli, B. Müller, *RNA* **6**, 1539 (2000).
18. D. J. Battle, J. A. Doudna, *RNA* **7**, 123 (2001).
19. C. H. Borchers *et al.*, *Proc. Natl. Acad. Sci. U.S.A.* **103**, 3094 (2006).
20. M. Zhang, T. T. Lam, M. Tonelli, W. F. Marzluff, R. Thapar, *Biochemistry* **51**, 3215 (2012).
21. Y. Cheng, D. J. Patel, *J. Mol. Biol.* **343**, 305 (2004).
22. See supplementary materials on *Science* Online.
23. Z. Dominski, J. A. Erkmann, J. A. Greenland, W. F. Marzluff, *Mol. Cell. Biol.* **21**, 2008 (2001).
24. F. Martin, F. Michel, D. Zenklusen, B. Müller, D. Schümperli, *Nucleic Acids Res.* **28**, 1594 (2000).
25. S. Jaeger, G. Eriani, F. Martin, *FEBS Lett.* **556**, 265 (2004).
26. C. Biertümpfel, W. Yang, D. Suck, *Nature* **449**, 616 (2007).
27. E. S. DeJong, W. F. Marzluff, E. P. Nikonowicz, *RNA* **8**, 83 (2002).
28. K. Zanier *et al.*, *RNA* **8**, 29 (2002).
29. Z. Dominski, L. X. Zheng, R. Sanchez, W. F. Marzluff, *Mol. Cell. Biol.* **19**, 3561 (1999).

Acknowledgments: We thank N. Whalen, S. Myers, R. Jackimowicz, and H. Robinson for access to the X29A beamline at the National Synchrotron Light Source. Supported by NIH grants GM077175 (L.T.) and GM029832 (W.F.M. and Z.D.). The structure has been deposited at the Protein Data Bank (accession code 4HXH).

Supplementary Materials

www.sciencemag.org/cgi/content/full/339/6117/318/DC1
Materials and Methods
Figs. S1 to S14
Tables S1 to S4
References (*30*–*40*)

10 August 2012; accepted 14 November 2012
10.1126/science.1228705

Identifying Personal Genomes by Surname Inference

Melissa Gymrek,[1,2,3,4] Amy L. McGuire,[5] David Golan,[6] Eran Halperin,[7,8,9] Yaniv Erlich[1]*

Sharing sequencing data sets without identifiers has become a common practice in genomics. Here, we report that surnames can be recovered from personal genomes by profiling short tandem repeats on the Y chromosome (Y-STRs) and querying recreational genetic genealogy databases. We show that a combination of a surname with other types of metadata, such as age and state, can be used to triangulate the identity of the target. A key feature of this technique is that it entirely relies on free, publicly accessible Internet resources. We quantitatively analyze the probability of identification for U.S. males. We further demonstrate the feasibility of this technique by tracing back with high probability the identities of multiple participants in public sequencing projects.

Surnames are paternally inherited in most human societies, resulting in their co-segregation with Y-chromosome haplotypes (*1*–*5*). Based on this observation, multiple genetic genealogy companies offer services to reunite distant patrilineal relatives by genotyping a few dozen highly polymorphic short tandem repeats across the Y chromosome (Y-STRs). The association between surnames and haplotypes can be confounded by nonpaternity events, mutations, and adoption of the same surname by multiple founders (*5*). The genetic genealogy community addresses these barriers with massive databases that list the test results of Y-STR haplotypes along with their corresponding surnames. Currently, there are at least eight databases and numerous surname project Web sites that collectively contain hundreds of thousands of surname-haplotype records (table S1).

The ability of genetic genealogy databases to breach anonymity has been demonstrated in the past. In a number of public cases, male adoptees and descendants of anonymous sperm donors used recreational genetic genealogy services to genotype their Y-chromosome haplotypes and to search the companies' databases (*6*–*9*). The genetic matches identified distant patrilineal relatives and pointed to the potential surnames of their biological fathers. By combining other pieces of demographic information, such as date and place of birth, they fully exposed the identity of their biological fathers. Lunshof *et al.* (*10*) were the first to speculate that this technique could expose the full identity of participants in sequencing projects. Gitschier (*11*) empirically approached this hypothesis by testing 30 Y-STR haplotypes of CEU participants in these databases and reported that potential surnames can be detected. [CEU participants are multigenerational families of northern and western European ancestry in Utah who had originally had their samples collected by CEPH (Centre d'Etude du Polymorphisme Humain) and were later reconsented to participate in the HapMap project.] However, these surnames could match thousands of individuals, and the study did not pursue full re-identification at a single-person resolution.

Our goal was to quantitatively approach the question of how readily surname inference might be possible in a more general population, apply this approach to personal genome data sets, and demonstrate end-to-end identification of individuals with only public information. We show that full identities of personal genomes can be exposed via surname inference from recreational genetic genealogy databases followed by Internet searches. In all cases in which individuals were studied who had donated DNA samples, the informed consent statements they had signed stated privacy breach as a potential risk and the data usage terms did not prevent re-identification. Representatives of relevant organizations that funded the original studies were notified and confirmed the compliance of this study with their guidelines (*12*).

As a primary resource for surname inference, we focused on Ysearch (www.ysearch.org) and

[1]Whitehead Institute for Biomedical Research, 9 Cambridge Center, Cambridge, MA 02142, USA. [2]Harvard–Massachusetts Institute of Technology (MIT) Division of Health Sciences and Technology, MIT, Cambridge, MA 02139, USA. [3]Program in Medical and Population Genetics, Broad Institute of MIT and Harvard, Cambridge, MA 02142, USA. [4]Department of Molecular Biology and Diabetes Unit, Massachusetts General Hospital, Boston, MA 02114, USA. [5]Center for Medical Ethics and Health Policy, Baylor College of Medicine, Houston, TX 77030, USA. [6]Department of Statistics and Operations Research, Tel Aviv University, Tel Aviv 69978, Israel. [7]School of Computer Science, Tel Aviv University, Tel Aviv 69978, Israel. [8]Department of Molecular Microbiology and Biotechnology, Tel-Aviv University, Tel Aviv 69978, Israel. [9]The International Computer Science Institute, Berkeley, CA 94704, USA.

*To whom correspondence should be addressed. E-mail: yaniv@wi.mit.edu

SMGF (www.smgf.org), the two largest public genetic genealogy databases with free-of-charge, built-in search engines. The interfaces of these engines are quite similar and allow users to insert a combination of Y-STR alleles and search for matching records on the basis of genetic similarity. The retrieved records contain surnames typically with information about the patrilineal line, such as geographical locations, potential spelling variants, and pedigrees. In total, these databases contain ~39,000 unique surname entries from ~135,000 records. The distribution of records per surname is significantly correlated ($R^2 = 0.78$, $P < 1.20 \times 10^{-6}$) with surname frequencies in the United States, suggesting an overall good representation of this population (Fig. 1A).

To test the probability of surname inference, we challenged the two databases with an orthogonal cohort of Y-STR haplotypes consisting of 34 markers (table S2) from 911 individuals, primarily with Caucasian ancestry, whose surnames are known (table S3). This cohort was compiled from YBase, a distinct genetic genealogy database, and contains individuals with 521 surnames that segregate in the U.S. population. In each haplotype query, our surname recovery algorithm began by retrieving the database record with the shortest time to most recent common ancestor (TMRCA) with the input haplotype (fig. S1 and table S4). Then, it calculated a confidence score that the surname match of the retrieved record is significantly better than other matches. If the score passed a user-defined threshold, the algorithm assigned the record's surname to the input haplotype; otherwise, it categorized it as "unknown." We tested the algorithm with a range of confidence thresholds to explore the trade-off between successful versus wrong recovery of surnames. Finally, we weighted the results using a stratified sampling approach to reflect the frequency of surnames in the U.S. population (*13*).

Our analysis projects a success rate of ~12% (SD = 2%) in recovering surnames of U.S. Caucasian males (Fig. 1B and fig. S2). This rate can be accomplished with a conservative threshold that would return a wrong surname in 5% of cases and label 83% of cases as unknown. Higher success rates of up to 18% can be achieved at the price of increased probability to recover an incorrect surname. Because our input cohort is based on individuals who were tested with genetic genealogy services, our results are presumably mostly relevant to socio-economic groups with high participation in these services—namely, upper- and middle-class U.S. Caucasians.

Combining the recovered surname with additional demographic data can narrow down the identity of the sample originator to just a few individuals. The analysis above indicated that most recovered surnames are quite rare, with frequencies of less than 1:4000 in the U.S. population, corresponding to <40,000 males (Fig. 1C and fig. S3) (*13*). We considered a scenario in which the genomic data are available with the target's year of birth and state of residency, two identifiers that are not protected by the United States Health Insurance Portability and Accountability Act (HIPAA) (*14*). Searching individuals by year of birth, state, and surname combinations is supported by various online public record search engines, such as PeopleFinders.com or USA-people-search.com. On the basis of extensive simulations with the U.S. Census data, our results predict that year of birth and state alone are weak identifiers and searches based on their combination would match at least 60,000 U.S. males in 50% of cases (Fig. 1D). However, when surname information is added to the search, the median list size shrinks to only 12 males, which are few enough matches to investigate individually.

Next, we established the feasibility of Illumina sequencing to produce accurate Y-STR haplotypes. Using lobSTR, an algorithm for STR

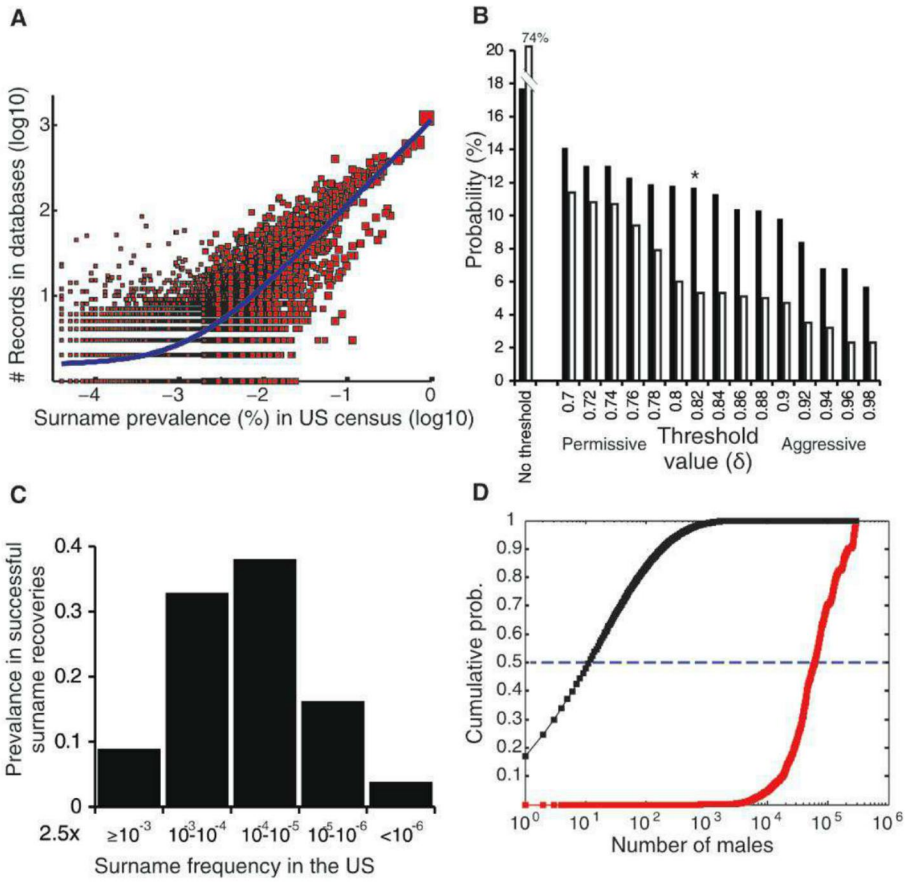

Fig. 1. Quantitative assessment of identification via surname inference. (**A**) The number of Ysearch and SMGF records as a function of surname prevalence in the U.S. population. The best-fit line is shown in blue. (**B**) Expected performance of surname recovery. The probability of successful recovery (closed bars) and wrong recovery (open bars) is shown at different surname confidence thresholds. The star indicates the middle-range performance threshold that was described in the main text. (**C**) The expected distribution of recovered surnames as a function of their prevalence. Most recovered surnames are expected to have a frequency of 1:4000 individuals or less. (**D**) The cumulative distribution function of U.S. males with a profile that matches a specific age, state, and surname combination (black) compared to the distribution when only age and state are known (red). The median is labeled with a dashed line.

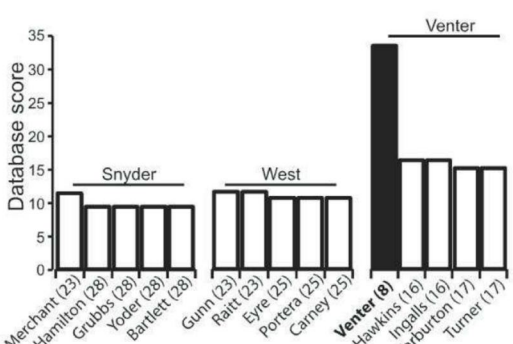

Fig. 2. The top five records retrieved after searching Ysearch with the Y-STR haplotypes of Michael Snyder, John West, and Craig Venter. The expected number of generations to the MRCA is given in parentheses for each record. Searching with Craig Venter returned a "Venter" record (closed bar) as the top match.

Table 1. Comparison of CEU identification cases.

Feature	Pedigree 1		Pedigree 2		Pedigree 3
Genome for surname recovery	Paternal grandfather	Maternal grandfather	Paternal grandfather	Maternal grandfather	Father
Surname freq. in U.S.*	Rare	Rare	Common	Rare	Rare
Meioses between target and source	3	5	5	7	2
Relationship between target and source	Nephew	First cousin once removed	Great-great nephew	Second cousin once removed	Grandchild
Supporting evidence	State of residency, pedigree structure, age, and maiden name are the same		State of residency, pedigree structure, age, and maiden name are the same		State of residency, pedigree structure are the same (ages are not given)
P (random match)†	$<5 \times 10^{-9}$		$<5 \times 10^{-6}$		$<10^{-5}$

*Common: surnames with a prevalence of $>10^{-4}$; Rare: surnames with a prevalence of $\leq 10^{-4}$. †The estimated probability of finding at least one family with the same characteristics after scanning all Utah households.

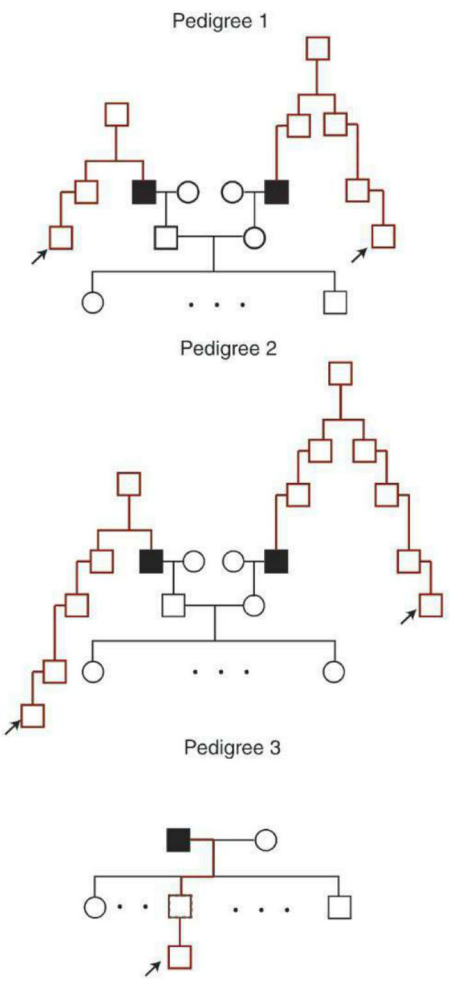

Fig. 3. Illustrations of the three CEU pedigrees (black) showing how genetic information from distant patrilineal relatives (arrow; red, patrilineal lines) can identify individuals. Filled squares represent sequenced individuals. To respect the privacy of these families, only abbreviated versions are presented. The sex of the CEU grandchildren was randomized. The numbers of grandchildren are not given.

profiling from raw sequencing reads (*15*), we processed 10 high-coverage male genomes from the Human Genome Diversity Panel (HGDP). lobSTR produced Y-STR haplotypes with an average number of 53 out of the possible 79 genealogical markers (table S5). Comparing these haplotypes to capillary electrophoresis results revealed 99% accuracy. We further found that even at lower sequencing coverage of 10×, informative haplotypes can be obtained by lobSTR (fig. S4). To test the ability to retrieve genetic genealogy records with the Illumina haplotypes, we profiled STRs from the genome of a U.S. Caucasian male from our lab collection that was sequenced with Illumina 100–base pair (bp) reads to a coverage of 13×. In parallel, we submitted this sample to the genealogy service of Sorenson Genomics and created a Ysearch record based on their results. A search with the Illumina haplotype returned his Ysearch entry as a top record (fig. S5).

The National Center for Biotechnology Information archives host a small number of genomes from identified individuals, providing good test cases for identification via surname inference. We used lobSTR to extract Y-STR haplotypes from the genomes of John West (*16*), Michael Snyder (*17*), and Craig Venter (*18*) (table S6). Searching Ysearch and SMGF with the Y-STR haplotypes of West and Snyder did not return their surnames and resulted in low matches to records with relatively ancient MRCAs 23 to 28 generations ago (*13*). A search with Craig Venter's haplotype returned a clear match to a "Venter" record that was concordant at all 33 comparable markers and with an estimated TMRCA of less than eight generations (Fig. 2 and table S7). We further tested whether it would be feasible to trace back Craig Venter by combining the inferred surname with demographic profiling. A query for "Surname: Venter; Year of Birth: 1946; State: California" in online public record search engines retrieved two matching records of males, one of whom was Craig Venter himself.

Surname inference from personal genomes puts the privacy of current de-identified public data sets at risk (*19*). We focused on the male genomes in the collection of Utah Residents with Northern and Western European Ancestry (CEU). The informed consent of these individuals did not definitively guarantee their privacy and stated that future techniques might be able to identify them (*20*). To test the ability to trace back the identities of these samples from personal genomes, we processed with lobSTR 32 Illumina genomes of CEU male founders that reside in public repositories of the 1000 Genomes Project (*21*) and the European Nucleotide Archive that were sequenced with read lengths of at least 76 bp. Most of these genomes were sequenced to a shallow depth of less than 5× and produced sparse Y-STR haplotypes. We selected the 10 genomes that had the most complete Y-STR haplotypes with a range of 34 to 68 markers to attempt surname recovery. Searching the genetic genealogy databases returned top-matching records with Mormon ancestry in 8 of the 10 individuals for whom the top hit had at least 12 comparable markers. Moreover, for four individuals, the top match consisted of multiple records with the same surname, increasing the confidence that the correct surname was retrieved. This potentially high surname recovery rate stems from a combination of the deep interest in genetic genealogy among this population and the large family sizes, which exponentially increases the number of targeted individuals for every person who is tested.

In five surname recovery cases, we fully identified the CEU individuals and their entire families with very high probabilities (Table 1). These five cases belonged to three pedigrees, in two of which the surnames of both the paternal and maternal grandfathers were recovered. Our strategy for tracing back individuals relied on the recovered surnames as well as publicly available Internet resources such as record search engines, obituaries, and genealogical Web sites, and demographic metadata available in the Coriell Cell Repository Web site. The year of birth was inferred by subtracting the ages in Coriell from the year of collecting samples. Each complete pedigree re-identification took 3 to 7 hours by a single person. The identified families matched exactly to the corresponding pedigree descriptions in the Coriell database: The number of children, the birth order of daughters and sons, and the state of residence were identical. All grandparents were alive in 1984, the year that the CEU cell line collection was established (*22*). In the two cases of a dual surname recovery from both grandfathers, the surname of the father

and the maiden name of the mother matched exactly to the grandfathers' surnames, substantially increasing the confidence of the recovery. Coriell also lists the ages (*23*) during sample collection for these two pedigrees, which agreed with the age differences of all tested cases with the identified family members. Using genealogical Web sites, we traced the patrilineal lineage that connects each identified genome through the MRCA to the record originator in the genetic genealogy database (Fig. 3). This analysis revealed that two to seven meiosis events link the CEU genome to the record source. Finally, we calculated that the probability of finding random families in the Utah population with these exact demographic characteristics is less than 1 in 10^5 to 5×10^9 (*13*). In total, surname inference breached the privacy of nearly 50 individuals from these three pedigrees.

This study shows that data release, even of a few markers, from one person can spread through deep genealogical ties and lead to the identification of another person who might have no acquaintance with the person who released his genetic data. The propagation of information through shared male lines amplifies the range of identification, allowing ~135,000 records to potentially target several million U.S. males. Another feature of this identification technique is that it entirely relies on free, publicly available resources. It can be completed end-to-end with only computational tools and an Internet connection. The compatibility of our technique with public record search engines makes it much easier to continue identifying other data sets in the same pedigree, including female genomes, once one male target is identified. We envision that the risk of surname inference will grow in the future. Genetic genealogy enthusiasts add thousands of records to these databases every month. In addition, the advent of third-generation sequencing platforms with longer reads will enable even higher coverage of Y-STR markers, further strengthening the ability to link haplotypes and surnames.

Similar to other genetic privacy issues (*24*–*30*), preventing surname inference from public whole-genome data sets might be quite challenging. Masking Y-STR markers could limit the effectiveness of the method presented in this study, but this approach is not sustainable (*13*). Our analysis suggests that Y-STR haplotypes can be imputed back from single-nucleotide polymorphisms (SNPs) on the Y chromosome (Y-SNPs) when a large reference set of male genomes will be available (fig. S6). In addition, community efforts, such as the Y Chromosome Genome Comparison, have already started exploring the association between Y-SNPs and surnames (table S1) and might allow bypassing Y-STR masking. We also posit that restricting genetic genealogy information is not practical, as some of the data are already scattered in multiple end-user Web sites and genealogy mailing lists.

Existing policy tools, such as controlled-access databases with data use agreements, may mediate the exposure of genomic information to surname inference. However, in our view, the appropriate response to genetic privacy challenges is not for the public to stop donating samples or for data sharing to stop. These would be devastating reactions that could substantially hamper scientific progress. Rather, we believe that establishing clear policies for data sharing, educating participants about the benefits and risks of genetic studies (*31*), and the legislation of proper usage of genetic information (*32*) are pivotal ingredients to support the genomic endeavor.

References and Notes

1. B. Sykes, C. Irven, *Am. J. Hum. Genet.* **66**, 1417 (2000).
2. T. E. King, S. J. Ballereau, K. E. Schürer, M. A. Jobling, *Curr. Biol.* **16**, 384 (2006).
3. B. McEvoy, D. G. Bradley, *Hum. Genet.* **119**, 212 (2006).
4. T. E. King, M. A. Jobling, *Mol. Biol. Evol.* **26**, 1093 (2009).
5. T. E. King, M. A. Jobling, *Trends Genet.* **25**, 351 (2009).
6. R. Lehmann-Haupt, "Are sperm donors really anonymous anymore?" *Slate*, 1 March 2010.
7. G. Naik, "Family secrets: An adopted man's 26-year quest for his father," *Wall Street Journal*, 2 May 2009.
8. R. Stein, "Found on the Web, with DNA: A boy's father," *Washington Post*, 13 November 2005.
9. A. Motluk, *New Sci.* **188**, 6 (3 November 2005).
10. J. E. Lunshof, R. Chadwick, D. B. Vorhaus, G. M. Church, *Nat. Rev. Genet.* **9**, 406 (2008).
11. J. Gitschier, *Am. J. Hum. Genet.* **84**, 251 (2009).
12. L. L. Rodriguez, L. D. Brooks, J. H. Greenberg, E. D. Green, *Science* **339**, 275 (2013).
13. See supplementary materials on *Science* Online.
14. *Federal Register: 45 CFR 164.514(b-c)* (2002).
15. M. Gymrek, D. Golan, S. Rosset, Y. Erlich, *Genome Res.* **22**, 1154 (2012).
16. N. Leat, L. Ehrenreich, M. Benjeddou, K. Cloete, S. Davison, *Forensic Sci. Int.* **168**, 154 (2007).
17. S. K. Lim, Y. Xue, E. J. Parkin, C. Tyler-Smith, *Int. J. Legal Med.* **121**, 124 (2007).
18. S. Levy *et al.*, *PLoS Biol.* **5**, e254 (2007).
19. Full details of this analysis were provided to the reviewers. However, they are not presented here to respect the privacy of these families. Further inquiries can be made to the corresponding author.
20. http://hapmap.ncbi.nlm.nih.gov/downloads/elsi/CEPH_Reconsent_Form.pdf.
21. The 1000 Genomes Project Consortium, *Nature* **467**, 1061 (2010).
22. S. M. Prescott, J. M. Lalouel, M. Leppert, *Annu. Rev. Genomics Hum. Genet.* **9**, 347 (2008).
23. Based on the results of this study, the NIH removed the ages from Coriell to a secure location (*12*).
24. Z. Lin, A. B. Owen, R. B. Altman, *Science* **305**, 183 (2004).
25. F. R. Bieber, C. H. Brenner, D. Lazer, *Science* **312**, 1315 (2006).
26. N. Homer *et al.*, *PLoS Genet.* **4**, e1000167 (2008).
27. K. B. Jacobs *et al.*, *Nat. Genet.* **41**, 1253 (2009).
28. H. K. Im, E. R. Gamazon, D. L. Nicolae, N. J. Cox, *Am. J. Hum. Genet.* **90**, 591 (2012).
29. D. W. Craig *et al.*, *Nat. Rev. Genet.* **12**, 730 (2011).
30. E. E. Schadt, S. Woo, K. Hao, *Nat. Genet.* **44**, 603 (2012).
31. A. L. McGuire, R. A. Gibbs, *Science* **312**, 370 (2006).
32. Presidential Commission for the Study of Bioethical Issues, Privacy and Progress in Whole Genome Sequencing. Privacy and Progress in Whole Genome Sequencing (2012).

Acknowledgments: We thank FamilyTreeDNA and SMGF for technical assistance. We also thank D. Esposito, A. Goren, G. Fink, D. Page, W. Kramer, and R. Ronen for useful discussions. Y.E. is an Andria and Paul Heafy Family Fellow. This publication was supported by a gift from Jim and Cathy Stone (Y.E.), the National Defense Science and Engineering Graduate Fellowship (M.G.), and the Edmond J. Safra Center for Bioinformatics at Tel-Aviv University (D.G. and E.H.).

Supplementary Materials

www.sciencemag.org/cgi/content/full/339/6117/321/DC1
Supplementary Text
Figs. S1 to S6
Tables S1 to S7
References

31 August 2012; accepted 3 December 2012
10.1126/science.1229566

GDE2 Promotes Neurogenesis by Glycosylphosphatidylinositol-Anchor Cleavage of RECK

Sungjin Park,[1]* Changhee Lee,[1]* Priyanka Sabharwal,[1] Mei Zhang,[1] Caren L. Freel Meyers,[2] Shanthini Sockanathan[1]†

The six-transmembrane protein glycerophosphodiester phosphodiesterase 2 (GDE2) induces spinal motor neuron differentiation by inhibiting Notch signaling in adjacent motor neuron progenitors. GDE2 function requires activity of its extracellular domain that shares homology with glycerophosphodiester phosphodiesterases (GDPDs). GDPDs metabolize glycerophosphodiesters into glycerol-3-phosphate and corresponding alcohols, but whether GDE2 inhibits Notch signaling by this mechanism is unclear. Here, we show that GDE2, unlike classical GDPDs, cleaves glycosylphosphatidylinositol (GPI) anchors. GDE2 GDPD activity inactivates the Notch activator RECK (reversion-inducing cysteine-rich protein with kazal motifs) by releasing it from the membrane through GPI-anchor cleavage. RECK release disinhibits ADAM (a disintegrin and metalloproteinase) protease-dependent shedding of the Notch ligand Delta-like 1 (Dll1), leading to Notch inactivation. This study identifies a previously unrecognized mechanism to initiate neurogenesis that involves GDE2-mediated surface cleavage of GPI-anchored targets to inhibit Dll1-Notch signaling.

The transition from cellular proliferation to differentiation is tightly controlled so as to ensure appropriate numbers of distinct cell types are formed and to prevent the depletion or uncontrolled proliferation of progenitor cells. Glycerophosphodiester phosphodiesterase 2

(GDE2) is necessary and sufficient to induce differentiation of spinal motor neuron (MN) subtypes. GDE2 acts non–cell-autonomously by inhibiting Notch signaling in neighboring Oligodendrocyte transcription factor 2 ($Olig2^+$) MN progenitors using extracellular glycerophosphodiester phosphodiesterase (GDPD) domain activity (*1*–*4*). Because Notch is activated by ligands Delta-like (Dll) and Jagged (Jag) expressed in adjacent cells, we tested whether GDE2 might target Dll1 and Jag1 function (*3*, *5*). Jag1 and Dll1 are expressed in nonoverlapping domains within the ventral spinal cord, and genetic ablation of either ligand causes domain-specific precocious neuronal differentiation (fig. S1A) (*5*–*7*). Spinal cords of mice lacking GDE2 ($Gde2^{-/-}$) showed a specific loss of MNs and V0 interneurons, no changes in the total number of V1 interneurons or V2 interneurons, but an increase in the ratio of V2a:V2b interneurons (Fig. 1, A to I) (*3*). These domain-specific deficits correspond to regions of Dll1 expression and function, suggesting that GDE2 specifically targets Dll1 but not Jag1 activity (fig. S1A).

Dll1 is inactivated through cleavage and release of its extracellular domain (ECD) by the ADAM (a disintegrin and metalloproteinase) metalloprotease family (*5*). To determine whether GDE2 GDPD activity promotes Dll1 shedding, we coelectroporated plasmids expressing GDE2 and C-terminal Flag-tagged Dll1 (Dll1-Flag) into chick spinal cords and analyzed Dll1 processing by means of protein immunoblotting. Overexpression of Dll1-Flag generated full-length Dll1 and a processed 30-kD C-terminal fragment (CTF) (Fig. 1J). Overexpression of GDE2 and Dll1-Flag induced accumulation of a C-terminal 42-kD Dll1 product (Dll1-42) that was not generated by coexpression of the two-pass transmembrane GDPD protein GDE1 (*4*, *8*) or by catalytically inactive GDE2 GDPD mutants (GDE2.APML) (Fig. 1J) (*3*). A corresponding N-terminal Dll1 ECD fragment was detected after overexpressing a double-tagged version of Dll1 (Myc-Dll1-Flag) (fig. S2). Fluorescence-activated cell sorting (FACS) analysis of Dll1 expression showed decreased Dll1 surface expression in MNs when GDE2 was overexpressed in chick spinal cords and a corresponding increase of endogenous Dll1 surface expression in GFP^+ MNs purified from *HB9:GFP;*$Gde2^{-/-}$ animals (fig. S3) (*9*). Consistent with the Dll1-specific function of GDE2, no changes in Jag1 expression (Jag1FL) or processing (Jag1CTF) were detected in spinal cords overexpressing GDE2 or in spinal cords of $Gde2^{-/-}$ animals (Fig. 1, J and K). These data indicate that GDE2 GDPD activity stimulates Dll1 processing and decreases the availability of cell-surface Dll1 in vivo. In addition to removing surface Dll1 for Notch receptor activation, the released Dll1 ECD is reported to inhibit Notch signaling by a dominant-negative activity (*5*); thus, Dll1 should function cooperatively with GDE2 to induce MN differentiation. Indeed, overexpression of GDE2 with Dll1 in chick spinal cords enhanced the ability of GDE2 to induce premature differentiation of ventricular zone (VZ) progenitors into $Isl2^+$ MNs (Fig. 1, L to N).

GDE2 did not induce Dll1-42 accumulation when coexpressed with Dll1-Flag in heterologous human embryonic kidney (HEK) 293T cells; thus, GDE2-dependent processing of Dll1 is likely indirect (fig. S1B). Overexpression of ADAM10 and Dll1-Flag in chick spinal cords induced formation of Dll1-42 and decreased surface Dll1, suggesting that Dll1-42 may be generated through ADAM metalloprotease activity (figs. S3B and S4). Further, ADAM10 that was overexpressed in chick spinal cords effectively cleaved Dll1Δclv, which lacks a reported ADAM10 cleavage site mapped in vitro (*10*), suggesting that Dll1-42 may be generated by ADAM proteolytic activity through a separate cleavage site that is preferentially used in vivo (fig. S4). Thus, GDE2 GDPD activity appears to stimulate ADAM-dependent processing of Dll1 to Dll1-42, inducing MN differentiation.

The GPI-anchored protein, reversion-inducing cysteine-rich protein with kazal motifs (RECK), activates Notch signaling in cortical progenitors by directly inhibiting ADAM10-dependent Dll1 processing (*11*, *12*). *RECK* mRNA is enriched in VZ cells and overlaps with GDE2 expression in newly differentiating MNs during neurogenesis (fig. S5, A and B). Depletion of *RECK* in spinal cords by two different short hairpin RNAs (shRNAs) (fig. S5, C and D) lowered Notch signaling as assayed by reduced expression of downstream Notch target genes *Hes5* and *Blbp* (*5*) and the induction of premature MN differentiation in the VZ (Fig. 2, A to L). Moreover, loss of RECK specifically induced accumulation of Dll1-42 in spinal cords but did not alter Jag1 expression and processing to Jag1CTF (Fig. 2M). These phenotypes are similar to those caused by GDE2 overexpression and indicate that GDE2 GDPD activity may promote Dll1 shedding by inactivating RECK (*1*–*3*).

To determine how GDE2 GDPD activity might inactivate RECK, we tested whether GDE2 exhibits classical GDPD phospholipase-D (PLD) catalysis in a coupled spectrophotometric assay of GDPD function (Fig. 3, A and B) (*13*). Membrane fractions of HEK293T cells transfected with control GDE1 showed GDPD activity when incubated with glycerophosphoserine (GPSerine), or a cyclic glycerol-1,2-phosphate intermediate (cyG[1,2]P) that is not substrate-specific and formed by GDPD enzymes during their predicted two-step catalytic mechanism (Fig. 3, A and B) (*14*). However, GDE2 showed no GDPD activity in either case (Fig. 3B). The GDPD domains of the six-transmembrane GDEs (GDE2, GDE3, and GDE6) are homologous to the catalytic X domain of phosphatidyl-inositol phospholipase C (PI-PLC). GDE3, unlike GDE1, hydrolyzes GPinositol through a PLC-type cleavage mechanism (*15*, *16*). Because exogenous bacterial PI-PLCs cleave and release GPI-linked proteins from membranes, we tested whether GDE2 GDPD activity inactivates RECK through GPI-anchor cleavage. We overexpressed GDE2 and RECK in HEK293T cells and assayed the culture medium for cleaved RECK ECD by means of protein immunoblotting. GDE2 and RECK coexpression released RECK into the medium, as does treatment with PI-PLC, whereas medium prepared from cells that were transfected with vector alone, GDE1, or catalytically inactive GDE2.APML contained little RECK (Fig. 3, C and E). Repeated Triton X-114 extraction of medium from cells overexpressing GDE2 and RECK yielded RECK in hydrophilic fractions, ruling out potential medium contamination by membrane-bound RECK (Fig. 3D) (*17*). Further, sequential expression of RECK and GDE2 released RECK into the medium (fig. S6), suggesting that GDE2 acts on surface GPI-anchored RECK and does not promote aberrant RECK discharge through disruption of RECK synthesis, modification, or transport. Consistent with inactivation of RECK by GDE2 through cleavage of its GPI-anchor, endogenous RECK processing examined by Triton X-114 partitioning of cortical extracts showed reduced RECK release in $Gde2^{-/-}$ animals compared with that of wild-type (WT) littermates (fig. S7).

To date, two vertebrate GPI-anchor cleaving enzymes have been identified that use phospholipase-type cleavage mechanisms, GPI-PLD, and the vertebrate homolog of *Drosophila* Notum (*18*, *19*). Notum failed to release RECK into the medium of transfected HEK293T cells, whereas GPI-PLD led to effective RECK cleavage (fig. S8A). Analysis of surface biotinylated RECK in transfected HEK293T cells showed that GDE2 activity releases biotinylated RECK from the surface membrane into the medium; in contrast, GPI-PLD did not, suggesting that GPI-PLD cleavage of RECK is intracellular and occurs within the endoplasmic reticulum or Golgi (Fig. 3F). Taken together, these observations indicate that GDE2-mediated release of RECK occurs on the cell surface and is independent from the function of known vertebrate GPI-anchor–cleaving enzymes.

To define the mechanism of RECK release by GDE2, we radiolabeled transfected HEK293T cells and confirmed that the RECK ECD released into the medium by GDE2 expression contained components of the GPI-anchor such as [^{3}H] inositol or [^{3}H] ethanolamine, whereas a secreted version of RECK ECD (sRECK) that lacked the GPI-anchor was poorly labeled under identical conditions (Fig. 3G and fig. S8B) (*20*). Moreover, cells overexpressing RECK in which the GPI-anchor was replaced with the transmembrane domain from the non–GPI-anchored CD2 protein failed to produce RECK in the medium in the presence of GDE2 (fig. S9, A and B) (*21*, *22*). These observations indicate that RECK release by

[1]Solomon Snyder Department of Neuroscience, School of Medicine, Johns Hopkins University, PCTB1004, 725 N Wolfe Street, Baltimore, MD 21205, USA. [2]Department of Pharmacology and Molecular Sciences, School of Medicine, Johns Hopkins University, WBSB 301A, 725 N Wolfe Street, Baltimore, MD 21205, USA.

*These authors contributed equally to this work.
†To whom correspondence should be addressed. E-mail: ssockan1@jhmi.edu

GDE2 involves specific cleavage within the GPI-anchor—a concept supported by the ability of GDE2 to cleave other unrelated GPI-anchored proteins, such as the glypicans GPC2 and GPC4 (fig. S10). PLD cleavage of the GPI-anchor would result in loss of a phosphate group from the phosphatidylinositol domain of released RECK when compared with PLC cleavage mechanisms (Fig. 3G). Comparison of radiolabeled [^{32}P] incorporation between RECK ECD generated by GDE2 or GPI-PLD expression normalized to [^{3}H] inositol levels showed that RECK released by GDE2

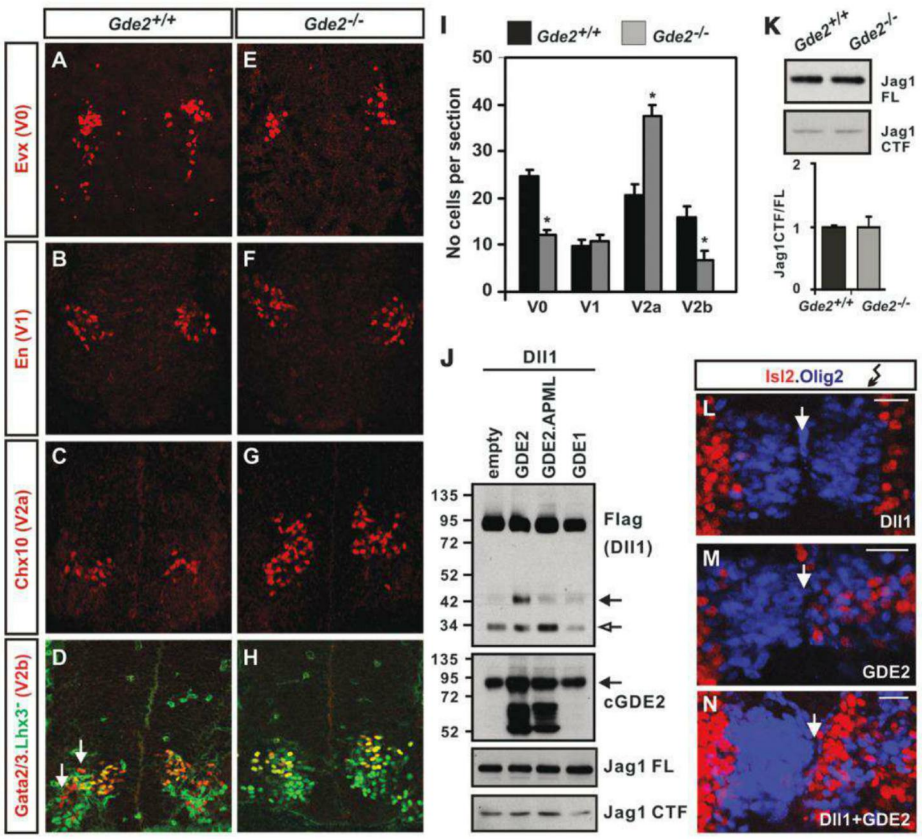

Fig. 1. Stimulation of Dll1 shedding by GDE2. (**A** to **H**) Coronal sections of embryonic day 13 (E13.5) mouse spinal cords. Arrows mark V2b interneurons (red). (**I**) Graph quantifying interneuron numbers in WT and *Gde2*$^{-/-}$ mutants; mean ± SEM, $n = 4$ embryos, two-tailed t test: V0, $^{*}P = 0.0016$; V1, $P = 0.4778$; V2a, $^{*}P = 0.0028$; V2b, $^{*}P = 0.0088$. (**J**) Western blots of extracts of chick spinal cords electroporated with Dll1-Flag plasmid; in the top blot, the open arrow indicates 30-kD Dll1 C-terminal fragment, and the solid arrow indicates C-terminal 42-kD Dll1 product (Dll1-42). In the top middle blot, the solid arrow (GDE2) indicates endogenous glycosylated GDE2, and the bottom bands are hypoglycosylated GDE2. (**K**) Western blot of Jag1 processing (FL, full length; CTF, C-terminal fragment) and quantification of Jag1 CTF/FL ratios from E12.5 embryonic spinal cord extracts. (**L** to **N**) Close-up of electroporated chick spinal cords (right) shows increased Isl2^{+} MNs (red) when Dll1 is coelectroporated with GDE2. Arrows indicate midline. Scale bar, 20 μm.

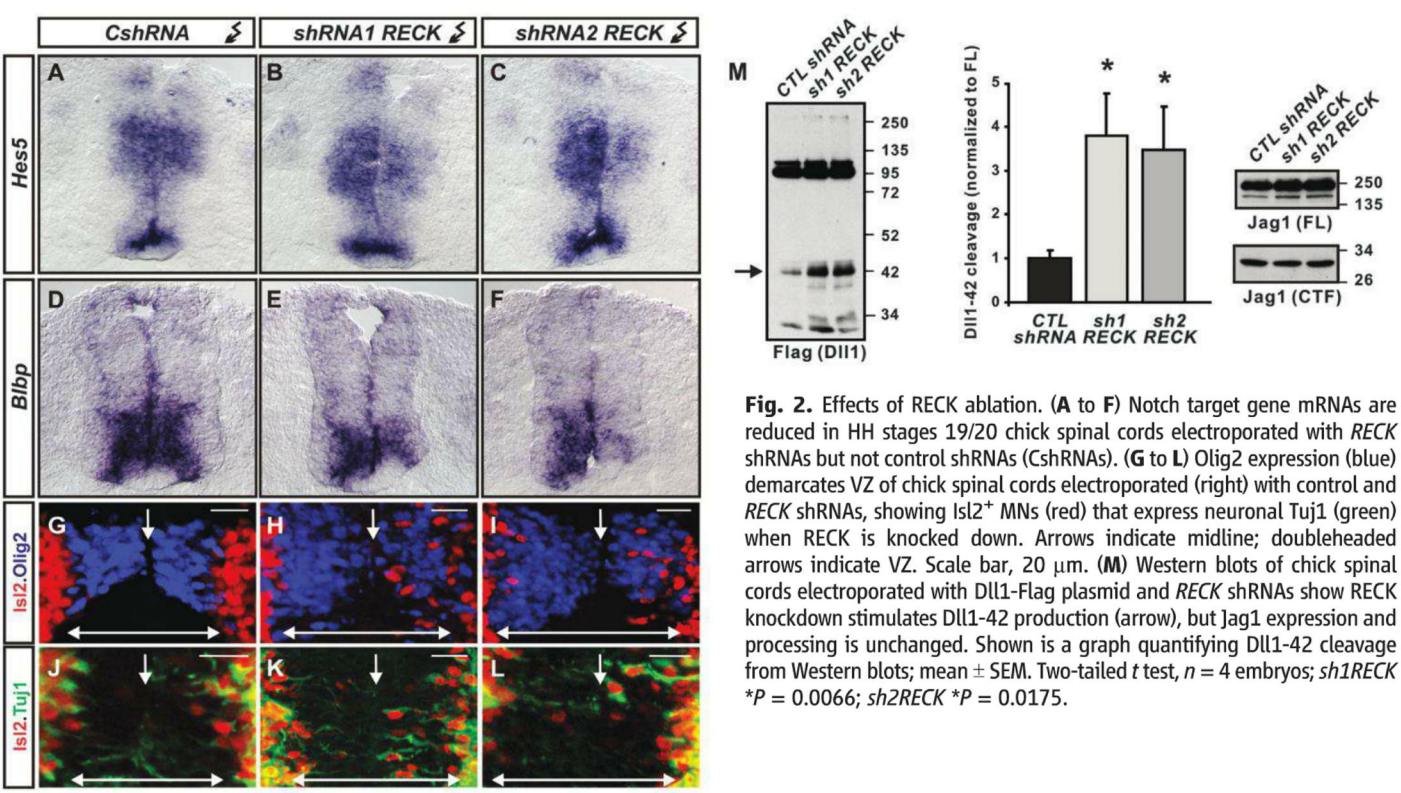

Fig. 2. Effects of RECK ablation. (**A** to **F**) Notch target gene mRNAs are reduced in HH stages 19/20 chick spinal cords electroporated with *RECK* shRNAs but not control shRNAs (CshRNAs). (**G** to **L**) Olig2 expression (blue) demarcates VZ of chick spinal cords electroporated (right) with control and *RECK* shRNAs, showing Isl2^{+} MNs (red) that express neuronal Tuj1 (green) when RECK is knocked down. Arrows indicate midline; doubleheaded arrows indicate VZ. Scale bar, 20 μm. (**M**) Western blots of chick spinal cords electroporated with Dll1-Flag plasmid and *RECK* shRNAs show RECK knockdown stimulates Dll1-42 production (arrow), but Jag1 expression and processing is unchanged. Shown is a graph quantifying Dll1-42 cleavage from Western blots; mean ± SEM. Two-tailed t test, $n = 4$ embryos; *sh1RECK* $^{*}P = 0.0066$; *sh2RECK* $^{*}P = 0.0175$.

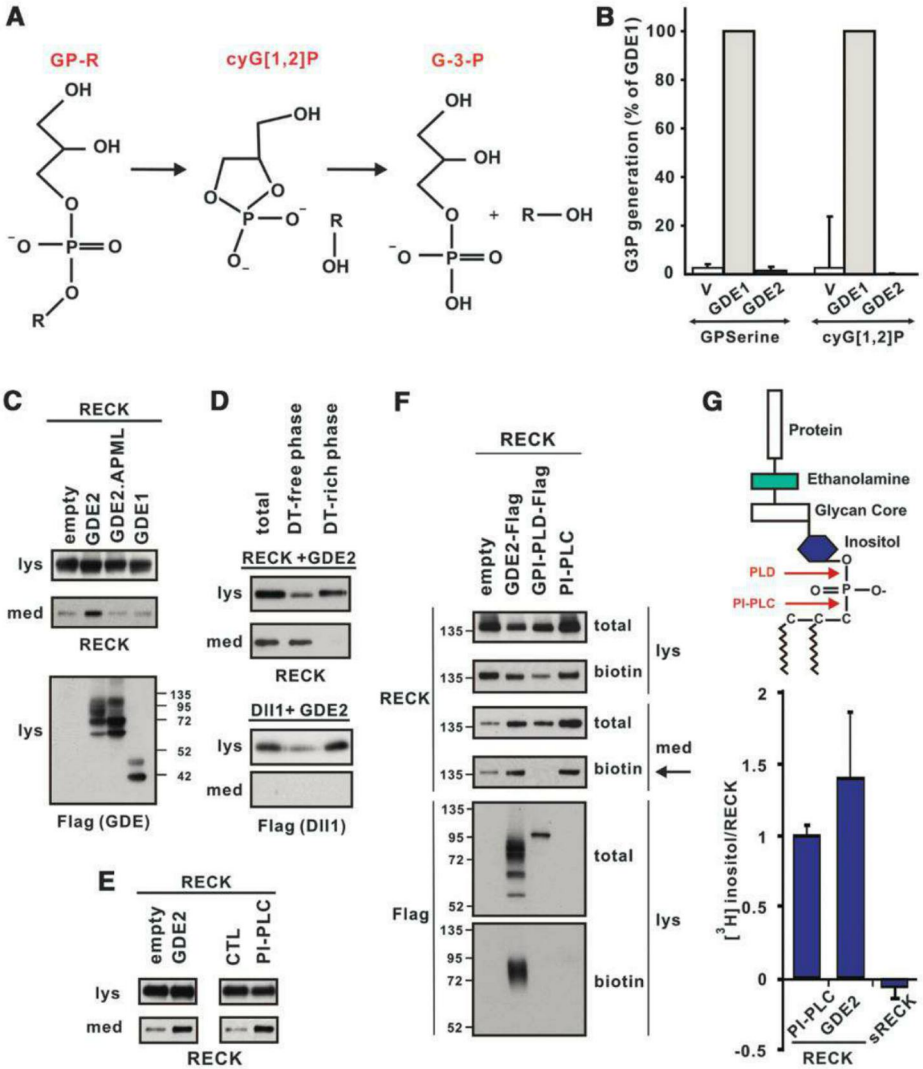

Fig. 3. GDE2 cleaves RECK within the GPI-anchor. (**A**) Schematic of two-step GDPD catalysis. (**B**) Graph quantifying in vitro GDPD assay in transfected HEK293T cells using glycerophosphoserine (GPSerine) and synthetic cyclic glycerol[1,2] phosphate intermediate. v, empty vector. (**C** to **E**) Western blots of transfected HEK293T cell lysates (lys) and medium (med). (C) RECK is detected in the medium when catalytically active GDE2 is present. (D) After sequential Triton X-114 extraction cleaved, RECK is observed in the Detergent (DT)–free hydrophilic phase, whereas Dll1, which is not cleaved by GDE2, is retained in the DT-rich hydrophobic phase of the lysate. (E) RECK ECD is generated by GDE2 or PI-PLC activities. (**F**) Western blot of lysates (lys) and medium (med) of HEK293T cells transfected with RECK and C-terminal Flag-tagged GDE2 or GPI-PLD. Surface RECK is labeled by biotin. GDE2 but not GPI-PLD releases surface-biotinylated RECK into the medium (arrow). Both GDE2 and GPI-PLD are visualized by antibodies to Flag, but only GDE2 is labeled by biotin, indicating that GDE2 is localized to the cell surface. PI-PLC was added to intact cells and serves as a positive control. (**G**) Schematic of GPI-anchor (top) and graph quantifying amount of radiolabel incorporated into RECK or sRECK when GDE2 or PI-PLC is present (bottom). Mean ± SEM; n = 4 to 12 samples.

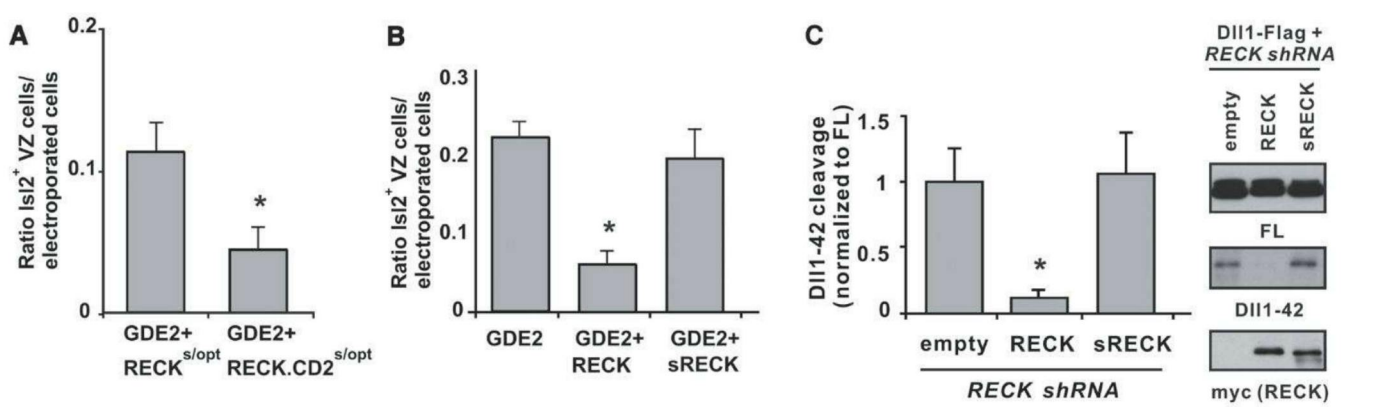

Fig. 4. GDE2 inactivates RECK through GPI-anchor cleavage. (**A** and **B**) Graphs quantifying ratio of ectopic Isl2$^+$ VZ MNs normalized to the number of transfected GDE2 cells. Mean ± SEM, two-tailed t test. (A) Suboptimal levels of plasmids expressing RECK$^{s/opt}$ or RECK-CD2$^{s/opt}$ were coelectroporated with GDE2. RECK-CD2 was more effective than was RECK in suppressing GDE2-dependent MN generation. *P = 0.0306; n = 5 embryos. (B) Plasmids expressing RECK or sRECK were coelectroporated with GDE2; RECK effectively suppressed GDE2 function, but sRECK did not (*$P = 5.59 \times 10^{-5}$; n = 8 to 10 embryos) as compared with GDE2. (**C**) Western blot of extracts of chick spinal cords electroporated with Dll1-Flag and *RECK* shRNA targeting 3′ untranslated region to detect full-length (FL) and processed Dll1-42. The phenotype is rescued by exogenous plasmids expressing WT RECK open reading frame but not sRECK. Densitometric quantification of Dll1-42, mean ± SEM, n = 4 embryos. Two-tailed t test, *P = 0.013 compared with empty.

contained higher ratios of [^{32}P]:[^{3}H] inositol than when cleaved by GPI-PLD (table S1). This observation suggests that GDE2 release of RECK does not use a similar mechanism to GPI-PLD. Bacterial PI-PLC cleavage of GPI linkages creates a distinct stable 1,2 cyclic inositol phosphate ring (cyIno[1,2]P), which is recognized by antibodies to cross-reacting determinant (CRD) (*23*, *24*). RECK ECD generated from GDE2 overexpression did not cross-react with antibodies to CRD (fig. S8C), suggesting that GDE2 cleavage of GPI-anchors is different to that of bacterial PI-PLC; however, this observation is consistent with reports that mammalian PLC enzymes have different kinetics to bacterial PI-PLCs and fail to generate stable cyclic intermediates (*25*).

If GDE2 inactivates RECK to induce MN differentiation, then overexpression of RECK might overcome GDE2 inhibition and suppress GDE2-dependent induction of premature MN generation in the VZ. We used Cre-lox techniques to generate mosaic expression of GDE2 in Olig2^{+} MN progenitors. This caused neighboring cells to differentiate into Isl2^{+} MNs (*3*, *26*). WT GPI-anchored RECK overexpressed with GDE2 effectively suppressed GDE2-dependent premature MN differentiation (Fig. 4B and fig. S9, E and F). Overexpressed RECK-CD2 more effectively suppressed GDE2 induction of MN differentiation than did equivalent amounts of GPI-anchored RECK (Fig. 4A and fig. S9, C and D), further indicating that GDE2 inactivates RECK to induce MN differentiation through cleavage of the GPI-anchor.

RECK ECD generated after GPI-anchor cleavage should be inactive and fail to maintain Olig2^{+} MN progenitors through Notch activation. However, soluble versions of RECK that lack the GPI-anchor are active in other systems, suggesting that the activity of cleaved RECK is context-dependent (*11*). Using similar Cre-lox approaches, we compared the effects of WT RECK and sRECK to inhibit GDE2-dependent MN generation in electroporated chick spinal cords. Overexpression of WT RECK with GDE2 suppressed GDE2-dependent premature differentiation of MNs (Fig. 4B and fig. S9F); in contrast, sRECK failed to suppress GDE2 activity (Fig. 4B and fig. S9G). WT RECK was sufficient to prevent increased Dll1 shedding resulting from ablation of endogenous RECK by shRNAs, whereas sRECK had no effect (Fig. 4C). These observations suggest that RECK ECD fails to inhibit Dll1 shedding and imply that GDE2 GDPD-dependent cleavage of RECK clears active RECK from the membrane.

Our data suggest a model in which GDE2 promotes MN differentiation by inactivating surface-bound RECK through GPI-anchor cleavage, thus allowing ADAM protein function (fig. S11). GDE2 cleaves GPI-anchored proteins at the cell surface in multiple in vitro and in vivo contexts that are independent of known GPI-anchor–cleaving enzymes. These observations support direct modes of cleavage, an activity shared by its family members GDE3 and GDE6 (fig. S10) (*4*); nevertheless, it remains possible that their function could involve stimulation of unidentified cleaving enzymes. GPI-anchored proteins are key regulators of signaling pathways that control diverse biological processes in the developing and adult organism (*27*, *28*). Understanding how these pathways are regulated through GPI-anchor cleavage in normal and diseased states might be gained by further analysis of six-transmembrane GDE GDPD protein expression, transport, and activity.

References and Notes

1. M. Rao, S. Sockanathan, *Science* **309**, 2212 (2005).
2. Y. Yan, P. Sabharwal, M. Rao, S. Sockanathan, *Cell* **138**, 1209 (2009).
3. P. Sabharwal, C. Lee, S. Park, M. Rao, S. Sockanathan, *Neuron* **71**, 1058 (2011).
4. N. Yanaka, *Biosci. Biotechnol. Biochem.* **71**, 1811 (2007).
5. B. D'Souza, L. Meloty-Kapella, G. Weinmaster, *Curr. Top. Dev. Biol.* **92**, 73 (2010).
6. C. E. Lindsell, J. Boulter, G. diSibio, A. Gossler, G. Weinmaster, *Mol. Cell. Neurosci.* **8**, 14 (1996).
7. U. Marklund *et al.*, *Development* **137**, 437 (2010).
8. B. Zheng, C. P. Berrie, D. Corda, M. G. Farquhar, *Proc. Natl. Acad. Sci. U.S.A.* **100**, 1745 (2003).
9. H. Wichterle, I. Lieberam, J. A. Porter, T. M. Jessell, *Cell* **110**, 385 (2002).
10. E. Six *et al.*, *Proc. Natl. Acad. Sci. U.S.A.* **100**, 7638 (2003).
11. T. Muraguchi *et al.*, *Nat. Neurosci.* **10**, 838 (2007).
12. J. S. Rhee, L. M. Coussens, *Trends Cell Biol.* **12**, 209 (2002).
13. N. Ohshima *et al.*, *J. Bacteriol.* **190**, 1219 (2008).
14. L. Shi, J. F. Liu, X. M. An, D. C. Liang, *Proteins* **72**, 280 (2008).
15. D. Corda *et al.*, *J. Biol. Chem.* **284**, 24848 (2009).
16. M. J. Rebecchi, S. N. Pentyala, *Physiol. Rev.* **80**, 1291 (2000).
17. T. L. Doering, P. T. Englund, G. W. Hart, *Curr. Protoc. Protein Sci.* Chap. 12, Unit 12.5 (2001).
18. H. Tsujioka, Y. Misumi, N. Takami, Y. Ikehara, *Biochem. Biophys. Res. Commun.* **251**, 737 (1998).
19. A. Traister, W. Shi, J. Filmus, *Biochem. J.* **410**, 503 (2008).
20. M. G. Paulick, C. R. Bertozzi, *Biochemistry* **47**, 6991 (2008).
21. A. Gallet, L. Staccini-Lavenant, P. P. Thérond, *Dev. Cell* **14**, 712 (2008).
22. D. Yan, Y. Wu, Y. Feng, S. C. Lin, X. Lin, *Dev. Cell* **17**, 470 (2009).
23. J. D. Bangs, D. Hereld, J. L. Krakow, G. W. Hart, P. T. Englund, *Proc. Natl. Acad. Sci. U.S.A.* **82**, 3207 (1985).
24. S. E. Zamze, M. A. Ferguson, R. Collins, R. A. Dwek, T. W. Rademacher, *Eur. J. Biochem.* **176**, 527 (1988).
25. D. W. Heinz, L. O. Essen, R. L. Williams, *J. Mol. Biol.* **275**, 635 (1998).
26. B. Zhuang, Y. S. Su, S. Sockanathan, *Neuron* **61**, 359 (2009).
27. D. Yan, X. Lin, *Cold Spring Harb. Perspect. Biol.* **1**, a002493 (2009).
28. A. Fico, F. Maina, R. Dono, *Cell. Mol. Life Sci.* **68**, 923 (2011).

Acknowledgements: We thank P. Englund, M. Goulding, T. M. Jessell, and B. Novitch for antibodies; J. Filmus for Notum plasmids; the Flow Cytometry and Cell Sorting Core Facility, Johns Hopkins Bloomberg School of Public Health; C. Cave III, A. L. Kolodkin, P. F. Worley, and Y. Yan for comments on the manuscript; and lab members for discussions. This work was funded by National Institute of Neurological Disorders and Stroke RO1NS046336.

Supplementary Materials

www.sciencemag.org/cgi/content/full/339/6117/324/DC1
Materials and Methods
Figs. S1 to S11
Table S1
References (*29*–*34*)

23 October 2012; accepted 19 November 2012
10.1126/science.1231921

Interstitial Dendritic Cell Guidance by Haptotactic Chemokine Gradients

Michele Weber,[1] Robert Hauschild,[1] Jan Schwarz,[1] Christine Moussion,[1] Ingrid de Vries,[1] Daniel F. Legler,[2] Sanjiv A. Luther,[3] Tobias Bollenbach,[1] Michael Sixt[1]*

Directional guidance of cells via gradients of chemokines is considered crucial for embryonic development, cancer dissemination, and immune responses. Nevertheless, the concept still lacks direct experimental confirmation in vivo. Here, we identify endogenous gradients of the chemokine CCL21 within mouse skin and show that they guide dendritic cells toward lymphatic vessels. Quantitative imaging reveals depots of CCL21 within lymphatic endothelial cells and steeply decaying gradients within the perilymphatic interstitium. These gradients match the migratory patterns of the dendritic cells, which directionally approach vessels from a distance of up to 90-micrometers. Interstitial CCL21 is immobilized to heparan sulfates, and its experimental delocalization or swamping the endogenous gradients abolishes directed migration. These findings functionally establish the concept of haptotaxis, directed migration along immobilized gradients, in tissues.

Several guidance cues operate in vertebrates, with the most prominent group being chemokines. In vitro, many chemokines induce directional cell migration when offered as gradients. However, the best established in vivo example of chemokine function does not rely on gradients: During extravasation from the blood stream, chemokines immobilized on the luminal surface of blood vessels (*1*–*3*) trigger the local arrest of leukocytes, which precedes their exit into the tissue (*4*). Less is known about how chemokines act beyond the endothelium (*5*), and, especially within lymphatic organs, chemokines seem to rather cause random motility than directional responses (*5*). The sparse body of existing evidence for directional guidance is largely inferred from the migratory trajectories of cells without information on actual chemokine distribution (*6*–*8*). Only two studies visualized chemokine gradients in parenchymal organs (*9*, *10*),

and the concept that gradients trigger directional migration has not been addressed with manipulative approaches.

We used mature dendritic cells (DCs) that migrate from the dermal interstitium into afferent lymphatic vessels (LVs) (*11*) as a model system to study chemokine function in situ. To track DCs en route to LVs, we used tissue explants of split mouse ears (*12*). Within minutes after addition of exogenous DCs onto exposed dermal tissue, the cells entered the interstitium and approached nearby LVs in a directed manner (Fig. 1, A to D, and movie S1). Single-cell tracking within the almost-planar anatomy of the mouse ear (fig. S1) revealed that cells switched from nondirectional to increasingly directional persistent movement toward the vessel at a distance of about 90 μm from the vessel wall (Fig. 1, B to D, and fig. S2). When located between two LVs, DCs occasionally extended protrusions toward both vessels, indicating the simultaneous presence of two conflicting signals. There the cells often spanned distances of more than 50 μm before they retracted one protrusion and finally entered one of the vessels (Fig. 1E and movie S2). In line with previous studies (*13*), DCs deficient for the chemokine receptor CCR7 did not approach LVs. CCR7 dependency was cell-autonomous, because the presence of comigrating wild-type DCs could not rescue CCR7-deficient cells (Fig. 1F). Hence, the involvement of secondarily induced paracrine guidance cues that might relay the directional information was excluded. CCR7 has two ligands, CCL19 and CCL21. By using tissues and DCs from CCL19-deficient animals (*14*), we found, in agreement with an earlier report (*15*), that CCL19 was not required for intravasation into afferent LVs (fig. S3).

We therefore measured the localization of the other CCR7 ligand, CCL21, within the dermis. Whole-mount immunostainings of ear sheets that were previously fixed and permeabilized revealed a punctuate CCL21 staining that was exclusively associated with LVs as revealed by lymphatic vessel endothelial hyaluronan receptor 1 (LYVE-1) and basement membrane stainings (Fig. 2, A and B). Disrupting the trans-Golgi network by tissue treatment with brefeldin A led to loss of the punctuate pattern and to scattering of CCL21 within individual LYVE-1–bordered (*16*) lymphatic endothelial cells (Fig. 2B). This suggests that the main source of CCL21 production is lymphatic endothelium, which harbors intracellular depots of this chemokine. Because intracellular CCL21 is not available for cells, especially when located at a distance from the vessel, we used unfixed, nonpermeabilized tissues to exclusively detect extracellular chemokine. The punctuate pattern was not detected. Although the signals were considerably lower than in the permeabilized tissue, the interstitial distribution of CCL21 became apparent: CCL21 peaked on the vessel wall and appeared to gradually fade with increasing distance from the vessel (Fig. 2C).

To quantitatively analyze these interstitial gradients, we first ensured that our detection method amplified the chemokine signal linearly (fig. S4) and then measured the averaged intensity of interstitial CCL21 staining as a function of distance from the LV margin. Integration of data from multiple ear sheets revealed that the mean CCL21 signal steeply decayed around the vessel and flattened in the intervessel area (Fig. 2D and fig. S5, A and B). Stainings for CCL19 with identical secondary reagents revealed a uniform pattern of background signal in both CCL19-deficient and control tissues. This background signal invariably approached the leveled-out CCL21 signal remote from the vessel (Fig. 2D and fig. S5, C to G). The slopes of CCL21 gradients appeared smooth upon signal integration over large areas or multiple samples. However, migrating single cells have only access to local information, which exhibited considerably more noise, with local concentration peaks that could potentially trap the cells on their path to the vessel. The widely accepted spatial paradigm of eukaryotic (as opposed to prokaryotic) gradient sensing assumes that cells quantitatively detect concentration differences over their entire surface and polarize toward higher concentrations (*17*). Hence, we calculated vector maps of the local gradients as they would be

[1]IST Austria (Institute of Science and Technology Austria), Am Campus 1, A-3400 Klosterneuburg, Austria. [2]Biotechnology Institute Thurgau (BITg) at the University of Konstanz, Unterseestrasse 47, CH-8280 Kreuzlingen, Switzerland. [3]Department of Biochemistry, University of Lausanne, Chemin des Boveresses 155, CH-1066 Epalinges, Switzerland.

*To whom correspondence should be addressed. E-mail: Sixt@ist.ac.at

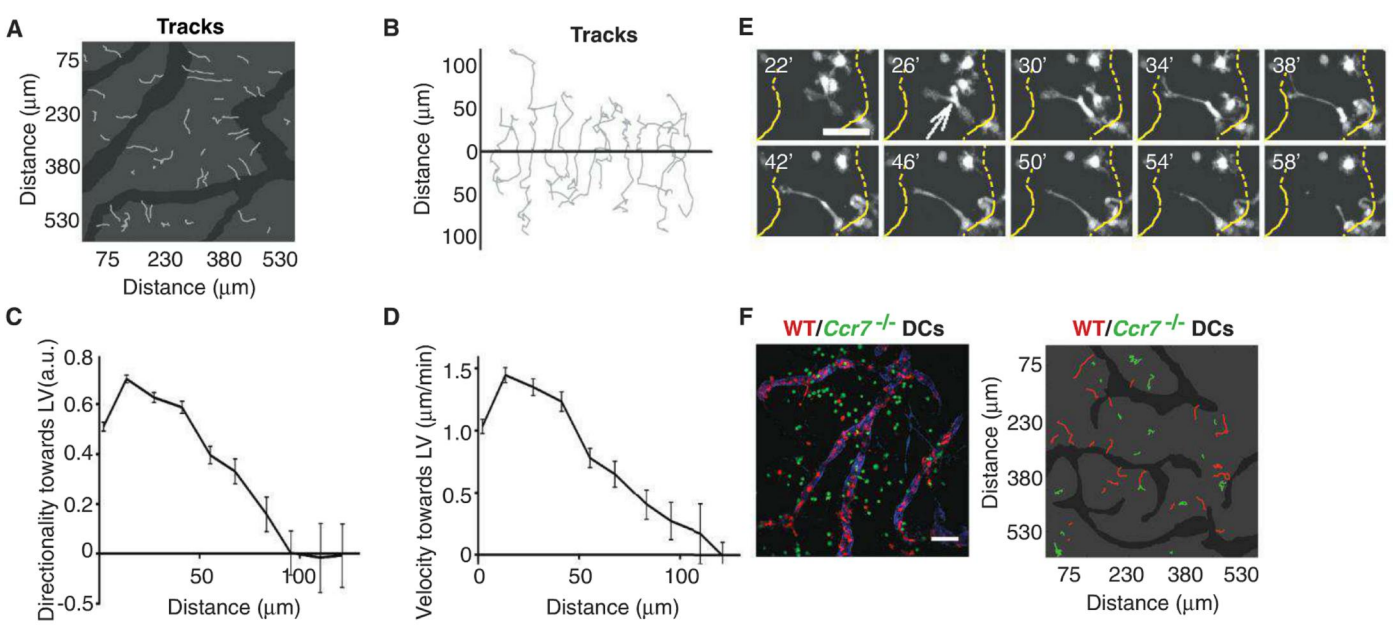

Fig. 1. DCs move directionally toward CCL21-expressing LVs in the dermal interstitium. (**A** to **D**) Tracks of DCs migrating in ear explants. (A) Migratory paths (lines in gray) tracked from a representative 60-min movie, overlaid onto the LV mask (dark gray). (B) Selected tracks (gray) from five movies (n = 200, three independent experiments) reorientated to nearest LV (LV margin at distance = 0 indicated by the black horizontal line). (C and D) Directionality and velocity toward LV as a function of distance to the nearest LV. Mean ± SEM is shown. n = 200, three independent experiments. a.u., arbitrary units. (**E**) Wild-type DC (highlighted by the white arrow) migrating between two adjacent vessels (indicated by yellow dotted lines). Scale bar indicates 50 μm. (**F**) (Left) Z-stack projection showing wild-type (red) and *Ccr7*$^{-/-}$ DCs (green) after 120-min incubation with ear sheets stained for LYVE-1 (blue). Scale bar, 100 μm. (Right) DC migration paths tracked from a representative 60-min movie, overlaid onto the LV mask (dark gray).

sensed by a cell of a given diameter. For cell diameters below 9 μm, no coherent vector field emerged (Fig. 2E and movie S3). When assuming a cell size of 15 to 50 μm, which reflects the fluctuating span of a migrating DC (Fig. 1E), we retrieved vector fields pointing from the interstitium toward the next vessel for CCL21 but not for control stainings (Fig. 2, E and F, and movie S2). We next computed average local concentration deltas for given cell sizes as a function of distance from the vessel. For an assumed cell size of 36 μm, this "functional gradient"

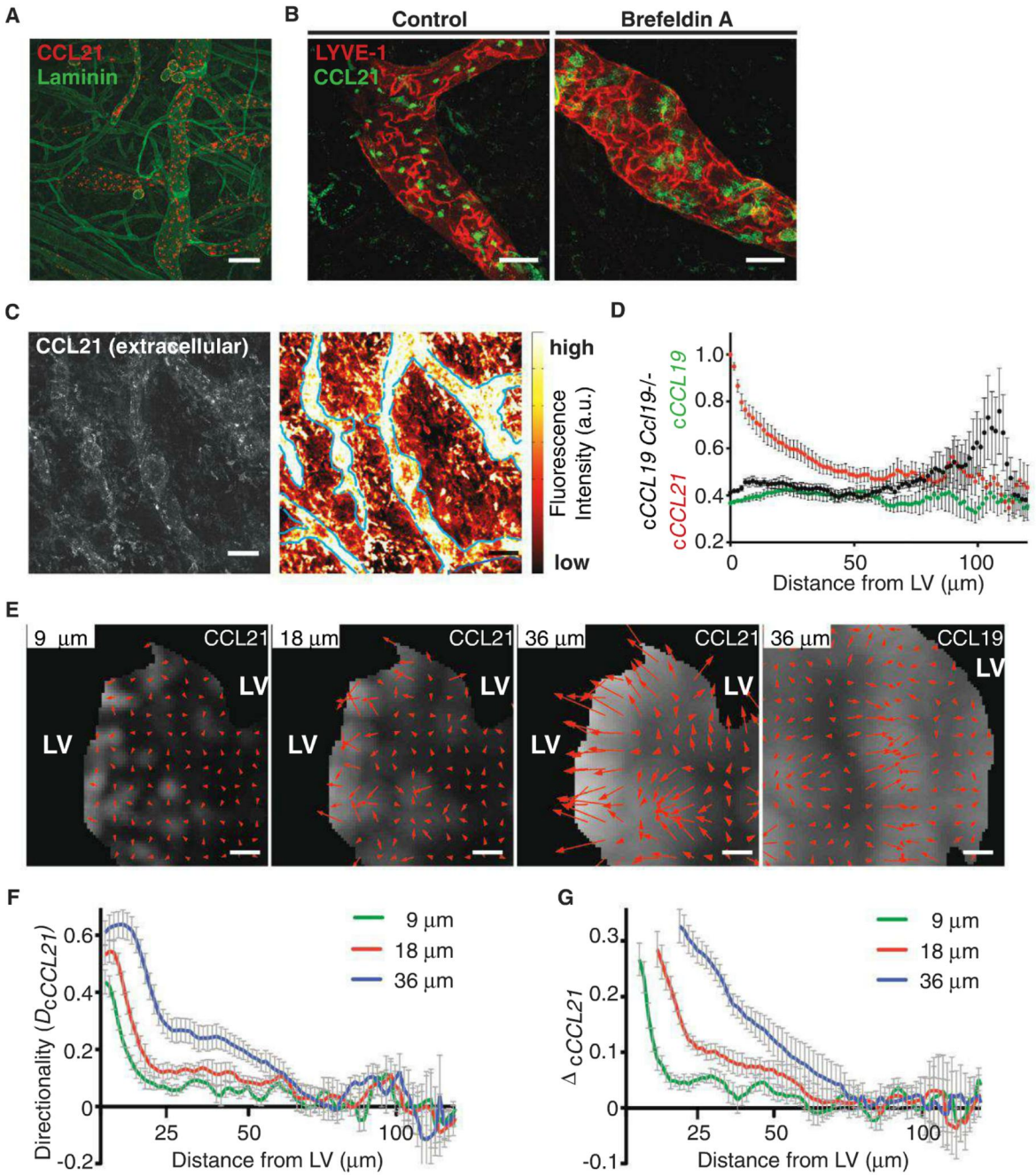

Fig. 2. Visualization and quantification of an interstitial CCL21 gradient. (**A**) Z-stack projection of permeabilized ear dermis stained for CCL21 (red) and laminin (green). Scale bar, 100 μm. (**B**) CCL21 (green) LYVE-1+ (red) co-staining of permeabilized ear dermis after treatment with 25 μg/ml brefeldin A. Scale bar, 25 μm. (**C**) Z-stack projection of nonpermeabilized ear dermis stained for CCL21. Gray scale shows maximum intensity projection (left). Right image shows same staining as color-coded average projection. LV boundaries are indicated by the blue dotted line based on LYVE-1 staining (as shown in fig. S2). Scale bars, 100 μm. A representative image from $n = 9$ out of four independent experiments is shown. (**D**) Quantification of interstitial CCL21 and CCL19 staining as function of distance from the nearest LV margin. Mean signal intensities relative to average maximum CCL21 signal ± SEM are shown (red, CCL21; green, CCL19 in *Ccl19*$^{+/+}$ ear; $n = 9$; four independent experiments; black, CCL19 in *Ccl19*$^{-/-}$ ear; $n = 5$; two experiments). (**E**) Vector maps of local chemokine gradients. Arrow length and direction indicate concentration rise in CCL21 after averaging over circular surface area with indicated diameter (virtual cell size). Gray scale indicates averaged intensities. Scale bar, 15 μm. (**F**) Directionality of CCL21 gradients (D_c) for indicated virtual cell size as cosine of angle between direction toward closest point of LV and direction of increasing chemokine concentration. Means ± SEM for $n = 6$ from three independent experiments are shown. (**G**) Average local CCL21 concentration delta (Δ) as a function of distance to nearest LV, calculated for indicated virtual cell size. Means ± SEM for $n = 7$ from four independent experiments are shown.

faded at a distance of 75 to 90 μm from the vessel wall (Fig. 2G) and thus matched the migratory behavior of the cells that increased directionality in a similar perimeter around the vessel as we have shown above (Fig. 1C). To estimate how well the detected gradients comply with the distribution of LVs within the dermis, we calculated distance maps of afferent LVs over large areas. We found that a cell that is randomly localized within the interstitium would need to travel an average distance of 47 ± 3 μm to reach the nearest LV (fig. S6, A and B) and that 92% of the interstitial space lies within a 90-μm perimeter around the LV network (fig. S6C). In accordance with this, endpoint analysis of intravasation assays only occasionally revealed few cells that were left "stranded" in the middle between vessels with large spacing (fig. S6D). These data demonstrate a relative invariability of the intervessel distance and imply that the range of the CCL21 gradient is very well adapted to the distribution of LVs in the skin.

We next challenged our correlative evidence for DC guidance by a CCL21 gradient using experimental manipulations. To test to what degree a continuous release of CCL21 is required to maintain the gradient, we extensively washed the ear explants and performed migration assays in the presence of brefeldin A to terminate possible chemokine secretion from LVs. Because we previously found that CCL21 can be proteolytically cleaved at the C terminus by a DC-associated protease (*18*), we also pharmacologically blocked this putative cleavage event, which might cause solubilization of CCL21. In both cases, we found that cells still approached LVs (fig. S7, A and B) and conclude that a continuous release of CCL21 is dispensable for directed DC migration within the approximate 2-hour time window of our assays. This suggests that the functionally active CCL21 gradient is stored within the homeostatic dermis.

In contrast to CCL19, CCL21 has a highly charged C-terminal extension that binds glycosaminoglycans (GAGs) and is thought to immobilize the chemokine to extracellular matrix or cell surfaces (*18*, *19*). Our previous findings together with the fact that we could detect CCL21 gradients by histological methods, which necessarily include washing steps where unbound proteins are removed, were consistent with the assumption that CCL21 in the dermis is not soluble. We therefore performed a series of experiments in which we perturbed the distribution of endogenous CCL21 by addition of exogenous chemokine. To this end, we pre-incubated ear explants with an excess of exogenous recombinant CCL21, washed them to remove the soluble CCL21 fraction, and quantified the impact on gradient shapes and DC migration. We found that exogenous CCL21 diffusely localized within the dermal interstitium and thereby masked and flattened the endogenous CCL21 gradients (Fig. 3A and fig. S8A). In the pretreated explants, a large fraction of DCs was misguided within the interstitium and ultimately remained scattered remote from the vessels (Fig. 3, B to D; fig. S8B; and movie S4). Additionally, pretreatment of the explants with a C-terminally truncated version of CCL21, which is incapable of binding GAGs (*19*), as well as with a GAG-binding but nonsignaling mutant did not change the migratory pattern of the cells (Fig. 3D and fig. S8C). To exclude that exogenous CCL21 affects DC migration nonspecifically, for example, by masking electrostatic interactions, we pretreated ear explants with exogenous CXCL13 and CXCL12, which also bind GAGs (*20*) yet

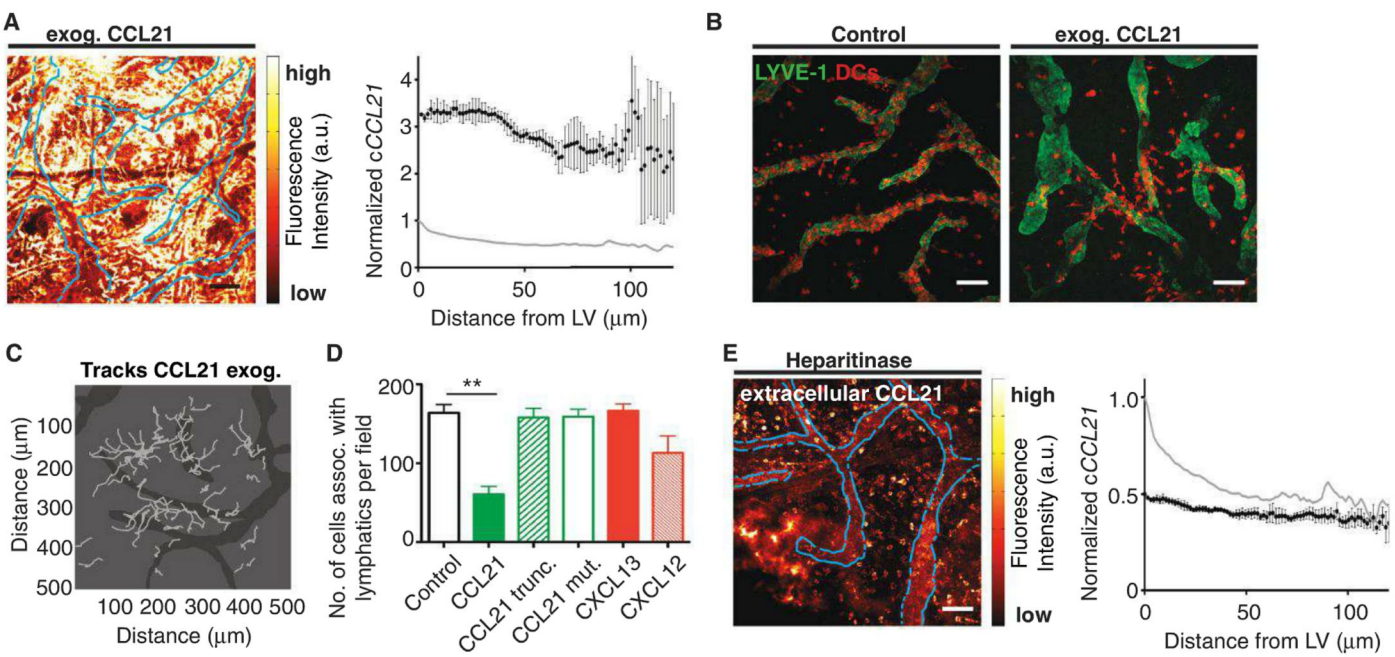

Fig. 3. The CCL21 gradient is functional and immobilized to heparan sulfates. (**A**) (Left) Z-stack projection of CCL21 immunostaining (false color-coded) of nonpermeabilized ear dermis after incubation with 0.6 μg/ml CCL21. LYVE-1–positive LVs are indicated by the blue dotted line. Scale bar, 100 μm. (Right) c*CCL21* after incubation with exogenous CCL21. Gray line indicates endogenous CCL21 as shown in Fig. 2. $n = 3$, two independent experiments. (**B**) Z-stack projections of DCs (red) and LYVE-1 immunostaining (green) after a 120-min co-incubation of DCs with ear sheets. Tissue was either vehicle-treated or incubated with CCL21 before addition of DCs. $n = 3$, two independent experiments. (**C**) DC tracks (light gray lines) from representative 60-min movie with CCL21 pre-incubation, overlaid onto LV mask (dark gray). (**D**) Number of DCs associated with LVs after 120-min crawl-in. Indicated chemokine was pre-incubated at 0.6 μg/ml before addition of DCs. Control versus CCL21, $^{**}P = 0.006$; control versus CCL21trunc, $P = 0.382$; control versus CCL21mut, $P = 0.8163$, control versus CXCL13, $P = 0.458$; control versus CXCL12, $P = 0.0642$. $n = 3$, at least two independent experiments. (**E**) Z-stack projection of nonpermeabilized ear dermis stained for CCL21 (false color-coded, left) and quantification of c*CCL21* (right) in nonpermeabilized ear dermis after treatment with 50 mIU heparitinase. Gray line in graph indicates endogenous CCL21 as in Fig. 2. (**F**) Numbers of DCs associated with LVs in ear dermis after 120 min of crawl-in. $n = 5$, three independent experiments ($^{**}P = 0.004$). All scale bars, 100 μm. Error bars indicate SEM.

do not trigger CCR7, and saw no significant effects on DC migration (Fig. 3D and fig. S8C). Together, these findings establish the functional activity of the immobilized CCL21 gradients that we identified before and show that, although DCs carry the receptor for and can respond to CXCL12, CCL21 gradients dominate. In addition, the chemokine pattern appears not to be determined by the distribution of CCL21 binding sites but most likely by the diffusion range of CCL21, which is trapped by sugar residues once it is released from the LVs (*21*).

CCL21 was shown to bind via its C-terminal domain sulfated sugars like heparin, heparan, dermatan, and chondroitin sulfates with low nanomolar affinities (*19*, *22*, *23*), potentially explaining the observed long retention times of CCL21 within the dermis and the inability of C-terminally truncated CCL21 to outcompete the endogenous gradients. To test which of the sugar moieties are involved in the immobilization of CCL21, we pretreated ear explants with sugar-degrading enzymes and found that heparitinase, which effectively removed heparan sulfates (fig. S9A), severely changed the CCL21 pattern. Quantifications revealed an almost complete flattening of the gradient and a drop to signal levels similar to control stainings, whereas tissue integrity was not affected (Fig. 3E and figs. S5G, S9B, and S10A). Consequently, DC migration in heparitinase-treated explants was severely diminished (Fig. 3F and fig. S10B). Heparan sulfate distribution patterns in untreated dermis did not match these of CCL21 (fig. S9A), corroborating the concept that not the tissue-binding sites for CCL21 but rather its distribution range determines the shape of the CCL21 gradient. These findings demonstrate that, like in the lumen of blood endothelium (*2*), interstitial CCL21 is immobilized to heparan sulfate residues, which either decorate cell surfaces or interstitial matrix components. This immobilized chemokine fraction is sufficient to guide intravasation of DCs, whereas adhesion molecules of the integrin family are dispensable for path-finding (*24*).

The term "haptotaxis" was originally introduced to describe cell migration along adhesive gradients, a phenomenon that was successfully constituted in vitro but still lacks direct in vivo support (*25*). Interstitial guidance by heparan sulfate immobilized chemokine gradients, as demonstrated here, can be viewed as a second variant of haptotaxis. The facts that (i) many chemokines bind GAGs (*26*), (ii) GAG interaction is important for the leukocyte-recruiting activity of some chemokines upon instillation into animals (*27*), and (iii) leukocytes have the ability to migrate along immobilized chemokine gradients in vitro (*28*, *29*) suggest that haptotaxis could be a widely used principle. Because immobilized gradients are insensitive to mechanical perturbations, they certainly constitute a robust and stable infrastructure for cellular guidance, whereas attraction by soluble gradients might be rather transient in nature.

References and Notes

1. J. Middleton *et al.*, *Cell* **91**, 385 (1997).
2. X. Bao *et al.*, *Immunity* **33**, 817 (2010).
3. R. Alon, *Immunity* **33**, 654 (2010).
4. E. C. Butcher, L. J. Picker, *Science* **272**, 60 (1996).
5. S. H. Wei, I. Parker, M. J. Miller, M. D. Cahalan, *Immunol. Rev.* **195**, 136 (2003).
6. F. Castellino *et al.*, *Nature* **440**, 890 (2006).
7. L. I. R. Ehrlich, D. Y. Oh, I. L. Weissman, R. S. Lewis, *Immunity* **31**, 986 (2009).
8. B. Boldajipour *et al.*, *Cell* **132**, 463 (2008).
9. T. Okada *et al.*, *PLoS Biol.* **3**, e150 (2005).
10. B. McDonald *et al.*, *Science* **330**, 362 (2010).
11. D. Alvarez, E. H. Vollmann, U. H. von Andrian, *Immunity* **29**, 325 (2008).
12. H. Pflicke, M. Sixt, *J. Exp. Med.* **206**, 2925 (2009).
13. R. Förster *et al.*, *Cell* **99**, 23 (1999).
14. A. Link *et al.*, *Nat. Immunol.* **8**, 1255 (2007).
15. M. R. Britschgi, S. Favre, S. A. Luther, *Eur. J. Immunol.* **40**, 1266 (2010).
16. P. Baluk *et al.*, *J. Exp. Med.* **204**, 2349 (2007).
17. A. Levchenko, P. A. Iglesias, *Biophys. J.* **82**, 50 (2002).
18. K. Schumann *et al.*, *Immunity* **32**, 703 (2010).
19. J. Hirose *et al.*, *Biochim. Biophys. Acta* **1571**, 219 (2002).
20. J. L. de Paz *et al.*, *ACS Chem. Biol.* **2**, 735 (2007).
21. P. Müller, A. F. Schier, *Dev. Cell* **21**, 145 (2011).
22. M. Bax, S. J. van Vliet, M. Litjens, J. J. García-Vallejo, Y. van Kooyk, *PLoS One* **4**, e6987 (2009).
23. K. Uchimura *et al.*, *BMC Biochem.* **7**, 2 (2006).
24. T. Lämmermann *et al.*, *Nature* **453**, 51 (2008).
25. R. J. Petrie, A. D. Doyle, K. M. Yamada, *Nat. Rev. Mol. Cell Biol.* **10**, 538 (2009).
26. A. Rot, U. H. von Andrian, *Annu. Rev. Immunol.* **22**, 891 (2004).
27. C. L. Salanga, T. M. Handel, *Exp. Cell Res.* **317**, 590 (2011).
28. A. Rot, *Eur. J. Immunol.* **23**, 303 (1993).
29. U. Haessler, M. Pisano, M. Wu, M. A. Swartz, *Proc. Natl. Acad. Sci. U.S.A.* **108**, 5614 (2011).

Acknowledgments: We thank M. Frank for technical assistance and S. Cremer, P. Schmalhorst, and E. Kiermaier for critical reading of the manuscript. This work was supported by a Humboldt Foundation postdoctoral fellowship (to M.W.), the German Research Foundation (Si1323-1,2 to M.S.), the Human Frontier Science Program (HFSP-RGP0058/2011 to M.S.), the European Research Council (ERC StG 281556 to M.S.), and the Swiss National Science Foundation (31003A_127474 to D.F.L., 130488 to S.A.L.). The authors declare no conflicts of interest. The data reported in the manuscript are tabulated in the main paper and in the supplementary materials.

Supplementary Materials

www.sciencemag.org/cgi/content/full/339/6117/328/DC1
Materials and Methods
Figs. S1 to S10
References (*30*)
Movies S1 to S4

6 August 2012; accepted 20 November 2012
10.1126/science.1228456

Chronic Stress Triggers Social Aversion via Glucocorticoid Receptor in Dopaminoceptive Neurons

Jacques Barik,[1,2,3,4]* Fabio Marti,[3,4,5] Carole Morel,[3,4,5] Sebastian P. Fernandez,[3,4,6] Christophe Lanteri,[2,3,7] Gérard Godeheu,[2,3,7] Jean-Pol Tassin,[2,3,7] Cédric Mombereau,[3,4,8] Philippe Faure,[3,4,5] François Tronche[1,2,3,4]*

Repeated traumatic events induce long-lasting behavioral changes that are key to organism adaptation and that affect cognitive, emotional, and social behaviors. Rodents subjected to repeated instances of aggression develop enduring social aversion and increased anxiety. Such repeated aggressions trigger a stress response, resulting in glucocorticoid release and activation of the ascending dopamine (DA) system. We bred mice with selective inactivation of the gene encoding the glucocorticoid receptor (GR) along the DA pathway, and exposed them to repeated aggressions. GR in dopaminoceptive but not DA-releasing neurons specifically promoted social aversion as well as dopaminergic neurochemical and electrophysiological neuroadaptations. Anxiety and fear memories remained unaffected. Acute inhibition of the activity of DA-releasing neurons fully restored social interaction in socially defeated wild-type mice. Our data suggest a GR-dependent neuronal dichotomy for the regulation of emotional and social behaviors, and clearly implicate GR as a link between stress resiliency and dopaminergic tone.

Traumatic experiences and social stress, such as aggression, may contribute to the onset of psychiatric disorders, including post-traumatic stress disorder and major depression (*1*, *2*). These situations trigger stress responses including the activation of the hypothalamic-pituitary-adrenal (HPA) axis and the release of its final output, the glucocorticoid hormones (GCs). This mechanism is central to the orchestration of the physiological and behavioral responses of vertebrates as they adapt to environmental stimuli (*3*). However, disproportionate or excessively long-lived stress responses expose the organism to deleterious outcomes and can precipitate the development of psychiatric disorders such as pathological anxiety, depression, and inability to socially perform (*4*–*6*). The molecular and cellular mechanisms underlying the etiology of stress-related psychiatric conditions remain unclear. Hence, understanding how individuals control emotions and cope with stressful events is a major clinical concern in the treatment of psychiatric illnesses.

GCs activate two related nuclear receptors: the glucocorticoid receptor (GR) expressed ubiquitously, and the mineralocorticoid receptor (MR), present in discrete brain regions. Both act as transcription

factors, controlling gene expression in the nucleus and participating in the rapid modulation of neuronal excitability at the membrane. During stress response, MR is involved in the appraisal of novel situations, whereas GR facilitates the consolidation of stress-related information (*7*). Molecular genetic approaches showed that GR modulates stress-related behaviors, including emotional behaviors, cognitive functions, and addictive states (*8*–*10*).

Male mice are territorial animals attacking any conspecific intruder; this behavior is modulated by HPA axis activity and dopamine (DA) (*11*–*13*). High GC levels lower the threshold for attack latency, possibly involving MR, whereas low levels trigger inappropriate attack targeting (*11*, *14*). We addressed here the role of GR in persistent behavioral changes after repeated social defeat. Social defeat repeated daily for 10 days leads to increased anxiety and social aversion (*15*). A single aggression in naïve mice led, 45 min later, to a marked increase (factor of >60) in circulating GC levels (basal, 6.2 ± 1.3 ng/ml; acute aggression, 392.6 ± 51 ng/ml; $n = 6$, $P < 0.01$, unpaired t test). Stressors that ultimately trigger a rise in glucocorticoid levels can alter the excitability of midbrain dopamine-releasing neurons (DA neurons) and consequently affect DA release (*16*). These neurons from the ventral tegmental area (VTA) project to limbic and cortical structures and participate in the modulation of motor control, reward, and emotions (*17*–*19*). They are activated in response to psychosocial stimuli (*17*) and sustain social aversion in mice exposed to repeated aggression by increasing brain-derived neurotrophic factor (BDNF) levels (*20*). Furthermore, they participate in the modulation of anxiety-like behaviors and cognitive functions (*21*).

Could GR activation in DA neurons be involved in social aversion? Mice selectively deprived of GR in DA neurons (*10*) ($Nr3c1^{loxP/loxP}$;TgBACDATiCre mice, hereafter termed GR^{DATCre}) and control littermates were subjected to daily social defeats for 10 consecutive days (see supplementary text) and compared to undefeated littermates. We measured their reactivity and habituation to a new environment by recording daily locomotor activity prior to each aggression. Undefeated GR^{DATCre} and control littermates exhibited similar expected novelty-reaction and habituation of exploratory behaviors that became apparent throughout the course of the experiment (fig. S1A). In contrast, both groups of defeated mice rapidly displayed neophobic responses marked by a pronounced hypolocomotion already seen after the first days of aggression. To assess social behavior under basal conditions or after aggression, we recorded the time spent establishing social contacts with an unfamiliar mouse, as previously described (*20*), in a low-luminosity (20 lux) environment to minimize the impact of emotional behaviors. Undefeated control and GR^{DATCre} mice spent a comparable amount of time performing social behavior. This was measured by the increase of time spent in the vicinity of a male mouse contained in a polycarbonate box placed in an open field. Repeated defeat triggered social avoidance in both genotypes, indicated by a substantial reduction in the time spent performing social contacts. This rules out the involvement of GR in DA neurons as a mediator of the outcome of chronic social defeat stress (Fig. 1A). This paradigm also engendered, regardless of genotype, strong anxiety-like behaviors as assessed by the elevated zero-maze and the dark-light box, two tests based on approach-avoidance conflicts (fig. S1, B and C), and no change in despair behavior as measured by the forced-swim test (fig. S1D). These results show that although stress provoked changes in behavior after repeated social defeat, this did not involve the activation of GR in DA cells.

Dopaminoceptive neurons of the nucleus accumbens (NAc) exert positive feedback on DA neuron activity through projection onto the VTA, relayed locally by interneurons (*22*, *23*). GC-mediated stress effects on the dopaminergic pathway could, alternatively, involve postsynaptic neurons bearing DA receptors. We therefore studied animals deprived of GR in dopaminoceptive neurons (*10*) ($Nr3c1^{loxP/loxP}$;TgYAC-D1aCre mice, hereafter termed GR^{D1Cre} mice). In this model, GR is absent from 87 to 88% of striatal and accumbal neurons as well as from neurons located in deep cortical layers (fig. S2, A and B). Remarkably, social avoidance was completely abolished in GR^{D1Cre} mice. Undefeated control and GR^{D1Cre} mice behaved normally during the social interaction test when presented with an unfamiliar mouse (Fig. 1B). However, defeated control mice displayed a strong social avoidance, whereas defeated GR^{D1Cre} mice socially interacted like undefeated mice (Fig. 1B). The number and duration of contacts established by undefeated controls and defeated GR^{D1Cre} mice with the box containing the target mouse were comparable (Fig. 1, C

[1]Molecular Genetics, Neurophysiology and Behavior Group, Centre National de la Recherche Scientifique (CNRS) Unité Mixte de Recherche (UMR) 7224, 75005 Paris, France. [2]Institut National de la Santé et de la Recherche Médicale (INSERM) U952S, 75005 Paris, France. [3]Université Pierre et Marie Curie, 75005 Paris, France. [4]Laboratory of Excellence (Labex) Biological Psychiatry Laboratory, 75005 Paris, France. [5]Neurophysiology and Behavior Group, CNRS UMR7102, 75005 Paris, France. [6]Neurotransmission and Development Group, INSERM U839, 75005 Paris, France. [7]Physiopathology of Addiction and Relapse Group, CNRS UMR7224, 75005 Paris, France. [8]Molecular and Cellular Mechanisms of Cortical Development Group, INSERM U839, 75005 Paris, France.

*To whom correspondence should be addressed. E-mail: francois.tronche@upmc.fr (F.T.); jacques.barik@snv.jussieu.fr (J.B.)

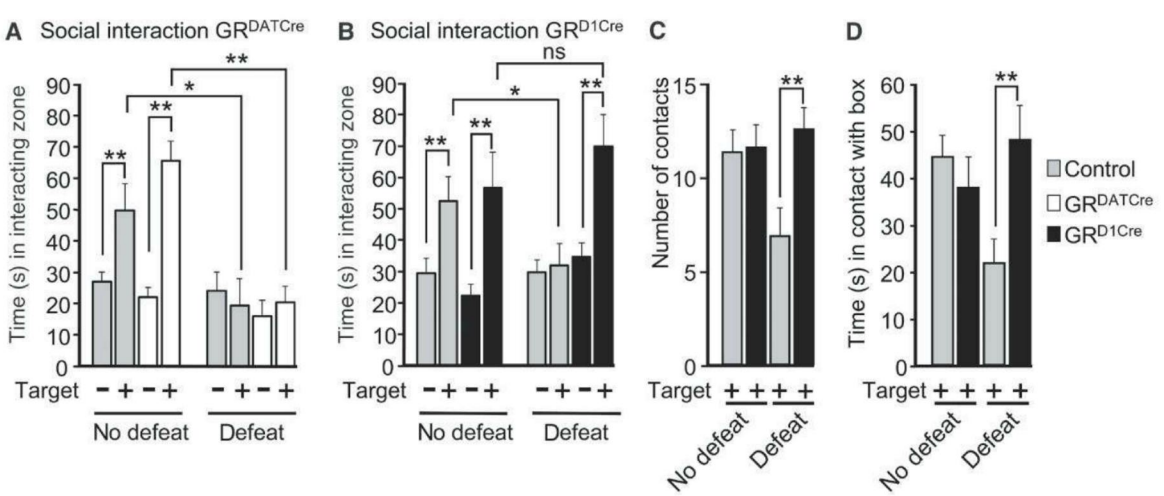

Fig. 1. GR in dopaminoceptive neurons, but not in DA neurons, selectively drives social aversion triggered by chronic social stress. (**A**) Undefeated control (gray) and GR^{DATCre} mice (white) spent more time in the virtual interacting zone when a mouse was contained in a box present in the open field (Target+) than when no mouse was introduced (Target–). In contrast, defeated control and GR^{DATCre} mice displayed social aversion (interaction defeat × target, $F_{1,44} = 19.5$, $P < 0.0001$) but no genotype effect (no interaction defeat × target × genotype, $F_{1,44} = 0.3$, $P > 0.05$). (**B**) Undefeated control (gray) and GR^{D1Cre} (black) mice displayed expected social interactions. Defeated control animals exhibited social aversion, whereas defeated GR^{D1Cre} mice exhibited social interaction (interaction defeat × target × genotype, $F_{1,44} = 9.7$, $P < 0.01$). (**C** and **D**) The numbers of contacts (C) and time spent in physical contact with the box (D) by defeated GR^{D1Cre} mice were higher than in defeated controls but similar to undefeated control mice [interaction genotype × defeat, $F_{1,44} = 4.3$, $P < 0.05$ (C); $F_{1,44} = 7.3$, $P < 0.01$ (D)]. $n = 12$ per group; $^*P < 0.05$, $^{**}P < 0.01$ (post hoc Bonferroni test).

and D). This difference in social aversion cannot be attributed to a defect in social memory, as both control and mutant mice equally performed in a social discrimination task (fig. S3A). This effect was not due to differences in circulating corticosterone levels or in HPA axis reactivity after social defeat, which were similar in GR^{D1Cre} mice and control littermates (Fig. 2A).

GRs in dopaminoceptive neurons are essential for adapting to a chronic social stress and translating this experience-dependent social behavior into a learned prediction of a recurrent danger. The absence of GR from dopaminoceptive neurons specifically affected social avoidance without modifying other behavioral changes induced by repeated defeats, such as induced anxiety-like behaviors (Fig. 2B and fig. S3B) and induced hyporeactivity to a novel environment (fig. S3C). Nor were despair behaviors affected either (fig. S3D). The lack of social aversion of defeated GR^{D1Cre} mice could result from early GR gene inactivation due to early developmental Cre expression (*24*). This is probably not the case, because chronic GR blockade (using RU486) before each daily aggression prevented social aversion, hence mimicking the dopaminoceptive-targeted GR gene inactivation (fig. S3E). Furthermore, stress triggered physiological adaptations, such as impoverishment of fur state, decreased body and thymus weights, and adrenal hypertrophy in both genotypes (fig. S4, A to D).

The change in social avoidance observed in GR^{D1Cre} mice could result from a general deficit in fear memory trace formation. To evaluate changes in learned fear, we subjected animals to classical fear conditioning training with three consecutive inescapable footshocks. The day after training, animals were reexposed to the same context and the conditional freezing response was quantified. GR^{D1Cre} mice and control littermates exhibited similar levels of emotional reactivity to learned aversive stimuli, ruling out the possibility that the lack of social avoidance could reflect an altered fear response (Fig. 2C).

To gain insight into the putative circuitry underpinning this failure of social avoidance, we measured DA release in the NAc after aggression by in vivo microdialysis in freely moving mice. Social defeat triggered a robust release of DA in control animals, whereas this effect was markedly diminished in GR^{D1Cre} littermates (Fig. 3A). The defective stress-elicited DA release in GR^{D1Cre} mice suggests that DA neuro-

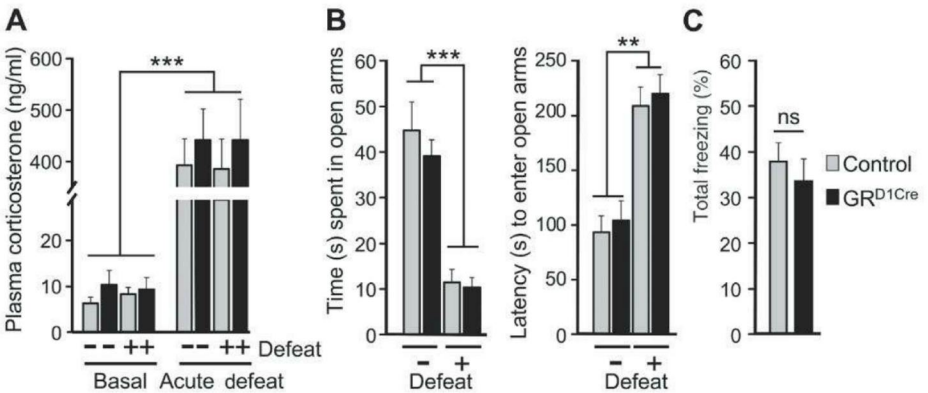

Fig. 2. GR in dopaminoceptive neurons is dispensable for emotional behavior and HPA axis reactivity subsequent to chronic social stress. (**A**) Levels of plasma corticosterone differed neither in naïve nor in chronically defeated control and GR^{D1Cre} mice under basal conditions or after an additional acute social defeat episode. Effect of acute stress ($F_{1,36}$ = 314.9, P < 0.0001) with no genotype ($F_{1,36}$ = 1.3, P > 0.05) or defeat ($F_{1,36}$ = 0.14, P > 0.05) effect. Circulating GC levels in control and defeated GR^{D1Cre} mice (black) and control littermates (gray) are shown under basal conditions or after an acute defeat. (**B**) Anxiety was measured within an elevated zero-maze in undefeated and defeated animals. After chronic defeat stress in control and GR^{D1Cre} mice, the latency to enter (right panel) and the time spent (left panel) in the open arms was equally increased and decreased, respectively. Effect of defeat (time in open arms $F_{1,44}$ = 63.3, P < 0.001; latency $F_{1,44}$ = 43.3, P < 0.001), no effect of genotype (time in open arms $F_{1,44}$ = 0.8, P > 0.05; latency $F_{1,44}$ = 0.5, P > 0.05). (**C**) Quantification of freezing behavior in control and GR^{D1Cre} mice reexposed to the conditioning context 24 hours after conditioning with footshocks (unpaired t test, P > 0.05). n = 5 to 7 mice per group (A), n = 12 mice per group [(B) and (C)]; **P < 0.01, ***P < 0.001 (post hoc Bonferroni test).

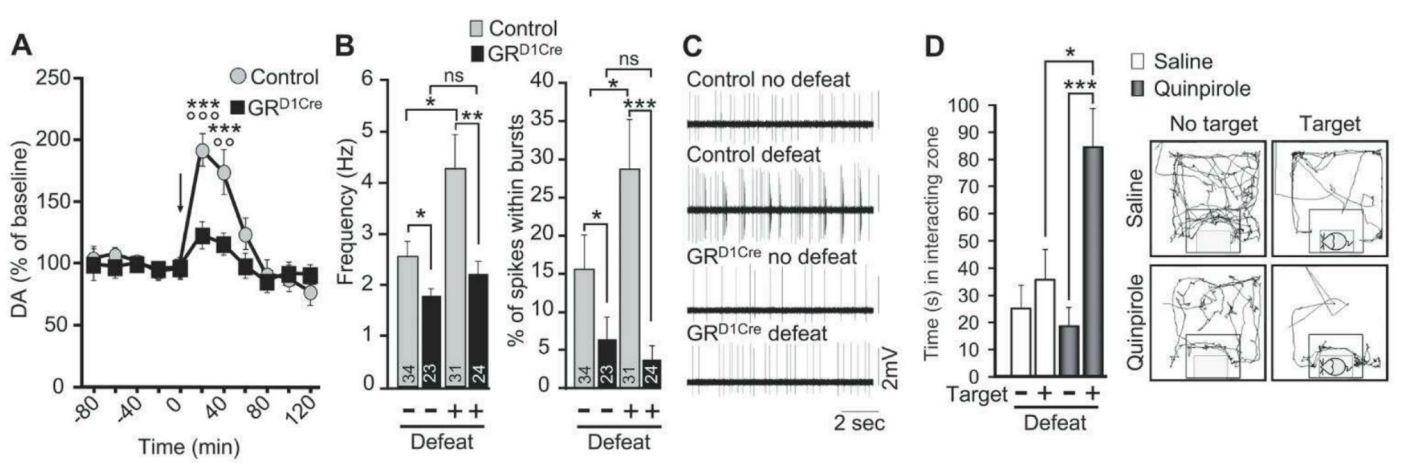

Fig. 3. Increase of in vivo firing of VTA neurons is required for the expression of social aversion. (**A**) An acute social defeat stress (arrow) fails to induce significant DA overflow, as measured by microdialysis, in the NAc of GR^{D1Cre} mice relative to control littermates (interaction defeat × genotype $F_{10,130}$ = 4.7, P < 0.0001). Stress versus respective baseline: ***P < 0.001. Control versus mutant: °°P < 0.01, °°°P < 0.0001. n = 7 to 8 mice per group. (**B**) Firing rate (left panel) and percentage of spikes within bursts (right panel) of VTA DA cells in undefeated or defeated control and GR^{D1Cre} mice in vivo. Numbers indicate the number of DA cells in corresponding groups; n = 24 to 34 neurons from 6 to 8 mice per group. (**C**) Representative recordings obtained from control and GR^{D1Cre} mice after repeated social defeat. (**D**) An acute quinpirole injection to defeated control mice prior to the social interaction test reverses social aversion, whereas saline fails to do so. Left panel: Quantification of the time spent in the interacting zone by defeated mice injected with saline (white bars) or quinpirole (0.03mg/kg, black shaded bars) in the presence of an empty box (Target–) or containing a mouse (Target+). Right panel: Representative trackings of defeated mice after either saline or quinpirole administration (interaction target × treatment $F_{1,38}$ = 7.4, P < 0.01). n = 10 to 11 mice per group. *P < 0.05, **P < 0.01, ***P < 0.001 (post hoc Bonferroni test).

transmission is a primary component of social stress–induced neuroadaptations. To further support this observation, we examined the electrophysiological properties of VTA DA neurons in vivo. These cells exhibit two discernible patterns of activity—slow, single-spike firing and fast-bursting activity—with the possibility of switching among these modes (*25*, *26*). This mode switching allows flexibility within the circuitry. It has been associated with reward-related behaviors (*27*) and has been suggested to promote alertness in cases of threatening situations (*28*). The frequency and the number of bursting events of DA neurons from defeated control mice was significantly increased relative to those of undefeated controls (Fig. 3, B and C, and fig. S5, A to D) (*29*). In contrast, DA neurons of defeated GR^{D1Cre} mice, although still expressing the GR gene, failed to demonstrate any significant electrophysiological adaptations, hence mirroring the lack of social avoidance (Fig. 3, B and C).

We further investigated this non–cell-autonomous effect of GR gene inactivation on dopamine-releasing neurons. Although VTA DA neurons of GR^{D1Cre} mice already exhibit a diminished basal activity, as we previously observed (*10*), their functioning is not completely abolished. Indeed, eticlopride [a DA D2 receptor (D2-R) antagonist] comparably increased VTA DA neuron electrophysiological activity in both control and mutant mice (fig. S5E). Moreover, these DA neurons are capable of sustaining a prolonged DA release in awake GR^{D1Cre} mice acutely challenged with morphine (*30*), indicating that these cells can be physiologically active under certain circumstances. The lack of electrophysiological adaptations observed in GR^{D1Cre} mice further supports the existence of a positive feedback loop that regulates VTA firing, and that is essential for adapting to threatening situations. We next asked whether this increase in DA neurons firing is a prerequisite for social avoidance or a subsequent neuroadaptation to stress. Just before the social interaction test, defeated and undefeated control mice received an acute injection of saline or quinpirole, a DA D2-R agonist that, when administered at low doses, primarily stimulates somatodendritic D2 autoreceptors and consequently suppresses DA neuron activity (*31*, *32*). Social interaction was similar in undefeated mice acutely challenged with saline or quinpirole (fig. S5F). However, whereas saline-injected defeated mice exhibited the expected social avoidance, quinpirole efficiently restored social interaction (Fig. 3D).

Our results show that in dopaminoceptive neurons, GR, a transcription factor induced by stress response, promotes social aversion but not other anxiety-like behaviors also induced after repeated aggression. This effect is likely to occur via a positive feedback loop from the NAc to the VTA. Our findings also suggest the existence of a discrete specification of neuronal circuits underlying behavioral outcomes of social stress. Our demonstration that a pharmacological intervention can restore social interaction suggests the possibility of normalizing specific negative outcomes of traumatic events.

References and Notes

1. K. L. Huhman, *Horm. Behav.* **50**, 640 (2006).
2. I. Kelleher *et al.*, *Br. J. Psychiatry* **193**, 378 (2008).
3. E. R. de Kloet, I. E. de Jong, M. S. Oitzl, *Eur. J. Pharmacol.* **585**, 473 (2008).
4. E. R. de Kloet, M. Joëls, F. Holsboer, *Nat. Rev. Neurosci.* **6**, 463 (2005).
5. B. S. McEwen, *Ann. N.Y. Acad. Sci.* **1032**, 1 (2004).
6. R. M. Sapolsky, *Science* **308**, 648 (2005).
7. F. L. Groeneweg, H. Karst, E. R. de Kloet, M. Joëls, *J. Endocrinol.* **209**, 153 (2011).
8. F. Tronche *et al.*, *Nat. Genet.* **23**, 99 (1999).
9. Q. Wei *et al.*, *Proc. Natl. Acad. Sci. U.S.A.* **101**, 11851 (2004).
10. F. Ambroggi *et al.*, *Nat. Neurosci.* **12**, 247 (2009).
11. J. Haller, M. R. Kruk, *Neurosci. Biobehav. Rev.* **30**, 292 (2006).
12. J. Haller, S. Millar, J. van de Schraaf, R. E. de Kloet, M. R. Kruk, *J. Neuroendocrinol.* **12**, 431 (2000).
13. D. I. Beiderbeck *et al.*, *Psychoneuroendocrinology* **37**, 1969 (2012).
14. A. H. Veenema, O. C. Meijer, E. R. de Kloet, J. M. Koolhaas, B. G. Bohus, *Horm. Behav.* **43**, 197 (2003).
15. V. Krishnan, E. J. Nestler, *Nature* **455**, 894 (2008).
16. M. Marinelli, in *Stress and Addiction*, M. Al'Absi, Ed. (Academic Press/Elsevier, Burlington, MA, 2007), pp. 41–83.
17. M. Marinelli, C. N. Rudick, X. T. Hu, F. J. White, *CNS Neurol. Disord. Drug Targets* **5**, 79 (2006).
18. O. Valenti, D. J. Lodge, A. A. Grace, *J. Neurosci.* **31**, 4280 (2011).
19. J. W. Dalley, B. J. Everitt, *Semin. Cell Dev. Biol.* **20**, 403 (2009).
20. O. Berton *et al.*, *Science* **311**, 864 (2006).
21. L. S. Zweifel *et al.*, *Nat. Neurosci.* **14**, 620 (2011).
22. Y. Xia *et al.*, *J. Neurosci.* **31**, 7811 (2011).
23. N. Omelchenko, S. R. Sesack, *Synapse* **63**, 895 (2009).
24. T. Lemberger *et al.*, *BMC Neurosci.* **8**, 4 (2007).
25. A. A. Grace, B. S. Bunney, *J. Neurosci.* **4**, 2877 (1984).
26. A. A. Grace, B. S. Bunney, *J. Neurosci.* **4**, 2866 (1984).
27. J. Mirenowicz, W. Schultz, *Nature* **379**, 449 (1996).
28. V. Krishnan *et al.*, *Cell* **131**, 391 (2007).
29. J. L. Cao *et al.*, *J. Neurosci.* **30**, 16453 (2010).
30. J. Barik *et al.*, *Biol. Psychiatry* **68**, 231 (2010).
31. A. Usiello *et al.*, *Nature* **408**, 199 (2000).
32. A. Anzalone *et al.*, *J. Neurosci.* **32**, 9023 (2012).

Acknowledgments: We thank S. Wonnacott for critical reading of the manuscript, and staff from the IFR83 animal facility for assistance. This work was funded by CNRS, INSERM, the Agence Nationale de la Recherche (TIMMS grants), the UPMC (Emergence program), the Région Île-de-France (NeRF), the European Union (FP7 STREPs PheComp and NovelTune), the Bettencourt Schueller Foundation, and the Mission Interministérielle de Lutte contre la Dépendance et la Toxicomanie. J.B. has been supported by the Fondation pour la Recherche Médicale. The authors declare no competing financial interests.

Supplementary Materials

www.sciencemag.org/cgi/content/full/339/6117/332/DC1
Materials and Methods
Figs. S1 to S5
References (*33*–*39*)

2 July 2012; accepted 21 November 2012
10.1126/science.1226767

Adolescent Stress–Induced Epigenetic Control of Dopaminergic Neurons via Glucocorticoids

Minae Niwa,[1,2,3] Hanna Jaaro-Peled,[2] Stephanie Tankou,[2] Saurav Seshadri,[2] Takatoshi Hikida,[2,4] Yurie Matsumoto,[1,3] Nicola G. Cascella,[2] Shin-ichi Kano,[2] Norio Ozaki,[3] Toshitaka Nabeshima,[1,5,6]* Akira Sawa[2]*

Environmental stressors during childhood and adolescence influence postnatal brain maturation and human behavioral patterns in adulthood. Accordingly, excess stressors result in adult-onset neuropsychiatric disorders. We describe an underlying mechanism in which glucocorticoids link adolescent stressors to epigenetic controls in neurons. In a mouse model of this phenomenon, a mild isolation stress affects the mesocortical projection of dopaminergic neurons in which DNA hypermethylation of the tyrosine hydroxylase gene is elicited, but only when combined with a relevant genetic risk for neuropsychiatric disorders. These molecular changes are associated with several neurochemical and behavioral deficits that occur in this mouse model, all of which are blocked by a glucocorticoid receptor antagonist. The biology and phenotypes of the mouse models resemble those of psychotic depression, a common and debilitating psychiatric disease.

Human behavior in adulthood is greatly influenced by various environmental conditions during childhood and adolescence (*1*–*3*). Although these environmental factors can interact with each other (*4*), individual responses vary, mainly because of different genetic predispositions among individuals (*5*). These gene-environment interactions may also underlie a variety of neuropsychiatric disorders (*6*). The development of means to intervene in such disorders, including prophylactic environmental readjustment (*7*), would be made easier if more were known about the underlying mechanisms and mediators of such interactions. Studies of dopamine responsiveness in conjunction with the effect of stress hormones in genetically selected rats were among the pioneering efforts in this field (*8*).

Maintaining mice in individual cages for 5 weeks during postnatal brain maturation, which may mimic separation from parents and family

members and social isolation in humans (*9*), critically affects their adult behavioral patterns relative to those of mice raised in normal group housing (*10*). We asked whether such "suboptimal" levels of exposure (e.g., shorter duration of exposure) to the environmental stressor during adolescence might serve as a risk factor for adult behavioral deficits when combined with one or more appropriate genetic risks. We therefore exposed a newly generated transgenic mouse model with a putative dominant-negative DISC1 (disrupted in schizophrenia 1) under expression control of the prion protein promoter (DISC1-DN-Tg-PrP; see fig. S1 for characterization of this genetic model) to 3-week isolation stress. We studied four groups of mice: wild-type mice without isolation (control, CTL); wild-type mice with 3-week isolation (environmental stressor, E); DISC1-DN-Tg-PrP without isolation (genetic factor, G); and DISC1-DN-Tg-PrP with 3-week isolation (combination of genetic factor and environmental stressor, which we designate GXE) (fig. S2A).

When examining prepulse inhibition (PPI), immobility time in a forced swim test, and locomotor activity just after puberty, we did not observe any changes in behavior among CTL, E, and G mice. In contrast, GXE mice showed robust deficits in all of these behavioral paradigms (Fig. 1 and fig. S3A), which suggests that the combination of genetic factor and environmental stressor during adolescence (from 5 to 8 weeks of age) could lead to synergistic effects in the phenotypes. These behavioral deficits are unlikely to reflect major physical changes, because there were no differences in body weight among the groups (fig. S4). The trend in the behavioral changes in GXE mice was preserved in both sexes (fig. S5; see fig. S3, B and C, for data on locomotion over time).

What is the underlying mechanism of behavioral changes in GXE mice? No change in the volume of the lateral ventricles was observed between CTL and G groups (fig. S6A). At the histological level, Nissl staining showed no robust change in the frontal cortex (Fc) of GXE mice relative to the other groups (fig. S6B). There was no change in immunostaining for glial fibrillary acidic protein (GFAP), indicating no evidence of robust gliosis (fig. S6, C and D). Thus, we hypothesized that a functional alteration in neurotransmission without anatomical and histological changes might occur in this model. The total and extracellular levels of dopamine in the Fc were significantly decreased in GXE mice (Fig. 2, A and B, and fig. S7) relative to levels in the other groups. Dopaminergic change in the GXE model may have specific pathological importance, as no alterations in levels of norepinephrine and serotonin were observed (Fig. 2A). This dopaminergic change may be more specific to the projections originating from the ventral tegmental area (VTA), because there was no change in the total levels of dopamine in the caudate putamen (CPu) (Fig. 2C). In accordance with the changes in dopamine in the GXE model, a decrease in the expression levels of tyrosine hydroxylase (TH) was observed in the Fc (Fig. 2D) but not in the nucleus accumbens (NAc) (Fig. 2E). Expression of the dopamine D1 receptor (D1R) was unchanged, whereas expression of D2R was elevated in the Fc but not in the NAc (fig. S8). The GXE model displayed an augmented elevation in the levels of dopamine upon methamphetamine (METH) challenge in the NAc but not in the Fc (Fig. 2, F and G); this suggests that these neurochemical changes could consistently underlie augmented locomotor activity observed in the GXE model. Two distinct dopaminergic projections (mesocortical and mesolimbic) originating from the VTA may therefore be differentially affected in the GXE model.

Which upstream mediator(s) may influence dopaminergic neurotransmission, and perhaps also adulthood behavioral patterns, in the GXE model? We initially addressed this question by measuring plasma corticosterone in mice after they had completed several behavioral tests, because an increase in levels of plasma corticosterone under stress conditions is frequently reported (*11*). There was no relative difference in the levels of plasma corticosterone among CTL, G, and E mice; only GXE mice showed significantly elevated levels of corticosterone (Fig. 3A). To determine whether this elevated corticosterone could underlie the dopaminergic changes, we administered the glucocorticoid receptor (GR) antagonist RU38486 (mifepristone, 20 mg/kg subcutaneously; unexpected side effects were not observed at this dose) (*12*) (fig. S2B). RU38486 successfully normalized all the dopamine-related abnormalities studied in the GXE model, including levels of basal and METH-induced extracellular dopamine, TH, and D2R (Fig. 3, B and C, and fig. S9). RU38486 also significantly ameliorated the impaired performance in PPI, forced swim test, and locomotor activity upon METH challenge in the GXE model (Fig. 3, D to F, and fig. S3D).

These results indicate that two major dopaminergic projections from the VTA are differently affected by elevated glucocorticoids in the GXE model. Do glucocorticoids primarily affect two distinct projections in a different manner? Or do they primarily affect one projection, which results in the changes in the other projection?

[1]Department of Chemical Pharmacology, Meijo University Graduate School of Pharmaceutical Sciences, Nagoya 468-8503, Japan. [2]Department of Psychiatry and Behavioral Sciences, Johns Hopkins University School of Medicine, Baltimore, MD 21287, USA. [3]Department of Psychiatry, Nagoya University Graduate School of Medicine, Nagoya 464-8601, Japan. [4]Medical Innovation Center, Kyoto University Graduate School of Medicine, Kyoto 606-8501, Japan. [5]Academic Frontier Project for Private University, Comparative Cognitive Science Institution, Meijo University, Nagoya 468-8503, Japan. [6]Department of Regional Pharmaceutical Care and Science, Meijo University, Nagoya 468-8503, Japan.

*To whom correspondence should be addressed. E-mail: asawa1@jhmi.edu (A.S.); tnabeshi@meijo-u.ac.jp (T.N.)

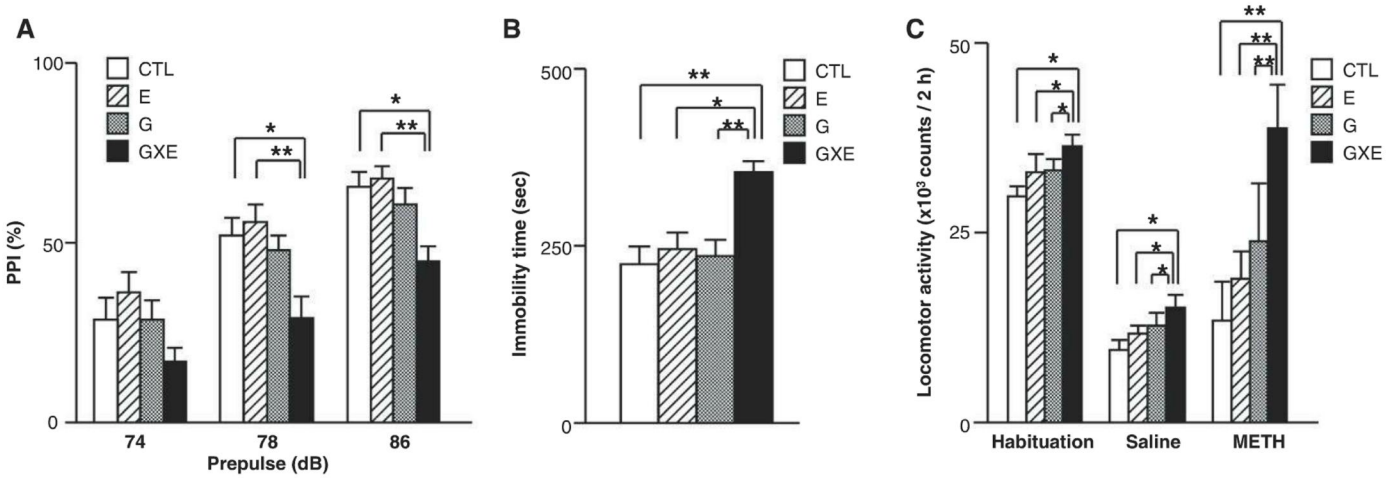

Fig. 1. The GXE mouse model: Behavioral abnormalities in DISC1-DN-Tg-PrP after exposure to adolescent isolation stress for 3 weeks. (**A**) Deficits in PPI. (**B**) Impaired performance in the forced swim test. (**C**) Aberrant locomotor activity. CTL, wild type without isolation; E, wild type with isolation; G, DISC1-DN-Tg-PrP without isolation; GXE, DISC1-DN-Tg-PrP with isolation. Values are means ± SE; $^{**}P < 0.01$, $^{*}P < 0.05$. Numbers of animals and statistical information are described in tables S1 and S2.

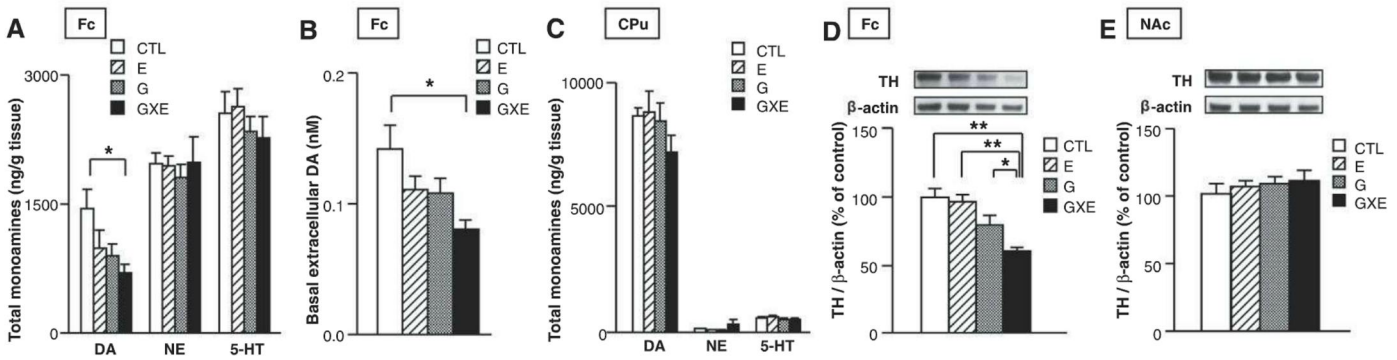

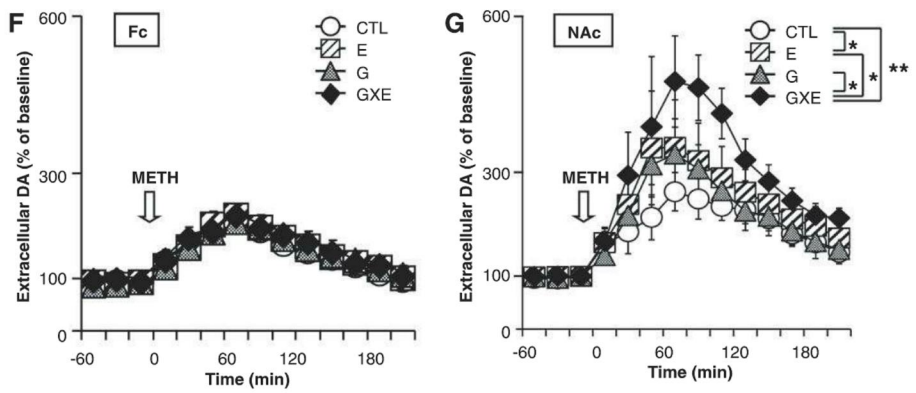

Fig. 2. Dopaminergic disturbances in the GXE model. (**A**) Levels of total content of monoamines [dopamine (DA), norepinephrine (NE), and serotonin (5-HT)]. (**B**) Levels of extracellular basal DA in the Fc. (**C**) Levels of total content of monoamines in the CPu. (**D**) Levels of TH in the Fc. (**E**) Levels of TH in the NAc. (**F**) Extracellular DA levels upon METH challenge in the Fc. (**G**) Extracellular DA levels upon METH challenge in the NAc. Total and extracellular levels of neurotransmitters were measured by high-performance liquid chromatography and in vivo microdialysis, respectively. Values are means ± SE; $^{**}P < 0.01$, $^{*}P < 0.05$.

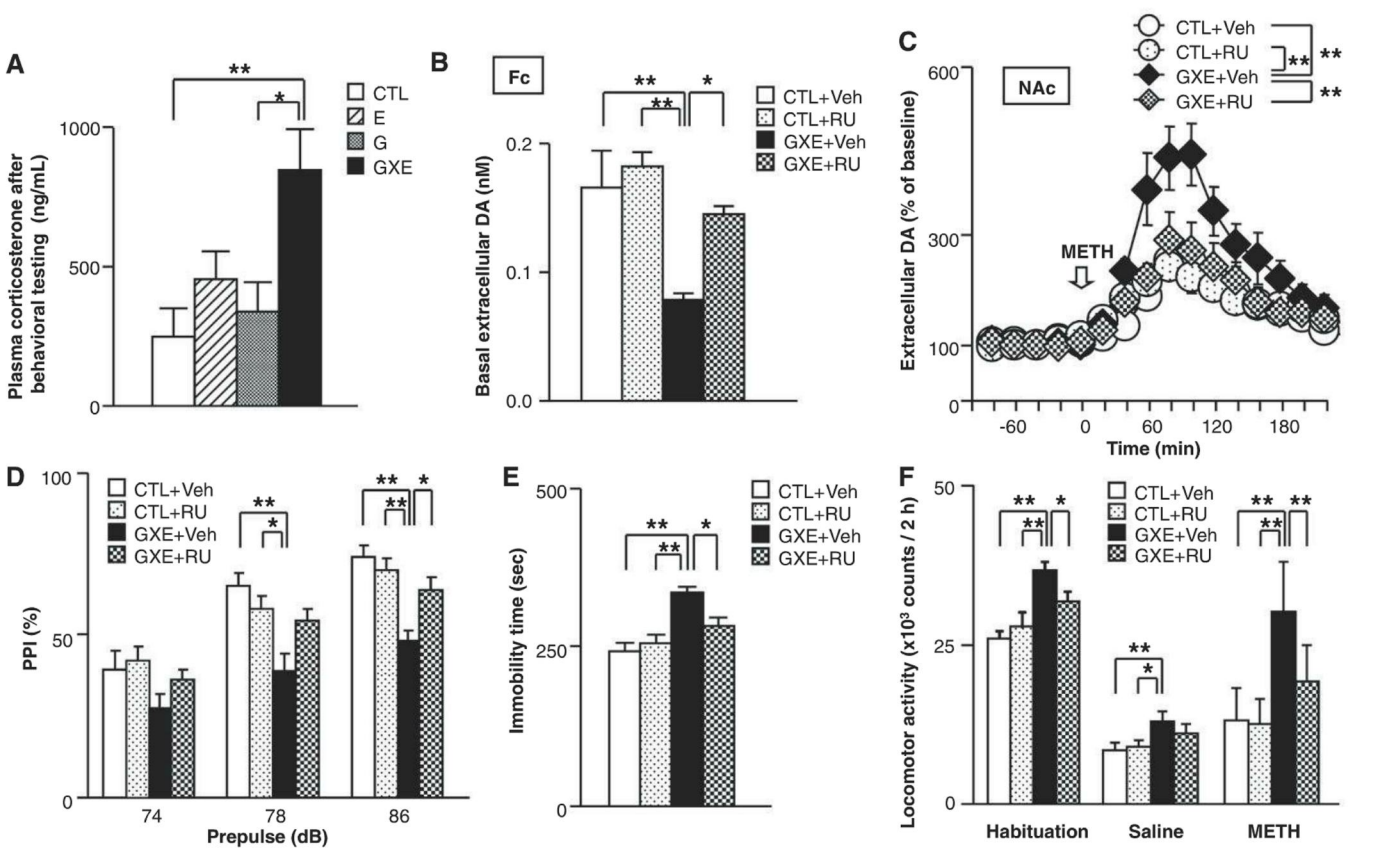

Fig. 3. Influence of glucocorticoids on neurochemical and behavioral abnormalities in the GXE model. (**A**) Levels of plasma corticosterone after behavioral tests. (**B**) Effects of the GR antagonist RU38486 on levels of extracellular basal DA in the Fc. (**C**) Effects of RU38486 on levels of extracellular DA upon METH challenge in the NAc. (**D** to **F**) Effects of RU38486 on performance of PPI (D), forced swim test (E), and locomotor activity (F). Veh, treated with vehicle; RU, treated with RU38486. Values are means ± SE; $^{**}P < 0.01$, $^{*}P < 0.05$.

Given that a decrease in TH expression can account for all other molecular changes (decrease in dopamine, compensatory increase in D2R) in the Fc of GXE mice, we first examined the effects of elevated glucocorticoids on the regulation of *Th* gene expression. The mouse *Th* gene contains a glucocorticoid response element (GRE)–like sequence (GGCACAGTGTGGTCT) located in the 5′ flanking DNA between positions –2435 and –2421 from the transcription start site (*13*). Glucocorticoids have been reported to influence DNA methylation and resultant mRNA expression in the genes containing GRE(s), such as the one that encodes FK506 binding protein 5 (FKBP5) (*14*). Thus, we hypothesized that glucocorticoids might affect DNA methylation of the *Th* gene differentially between two distinct dopaminergic projections, which would underlie neurochem-

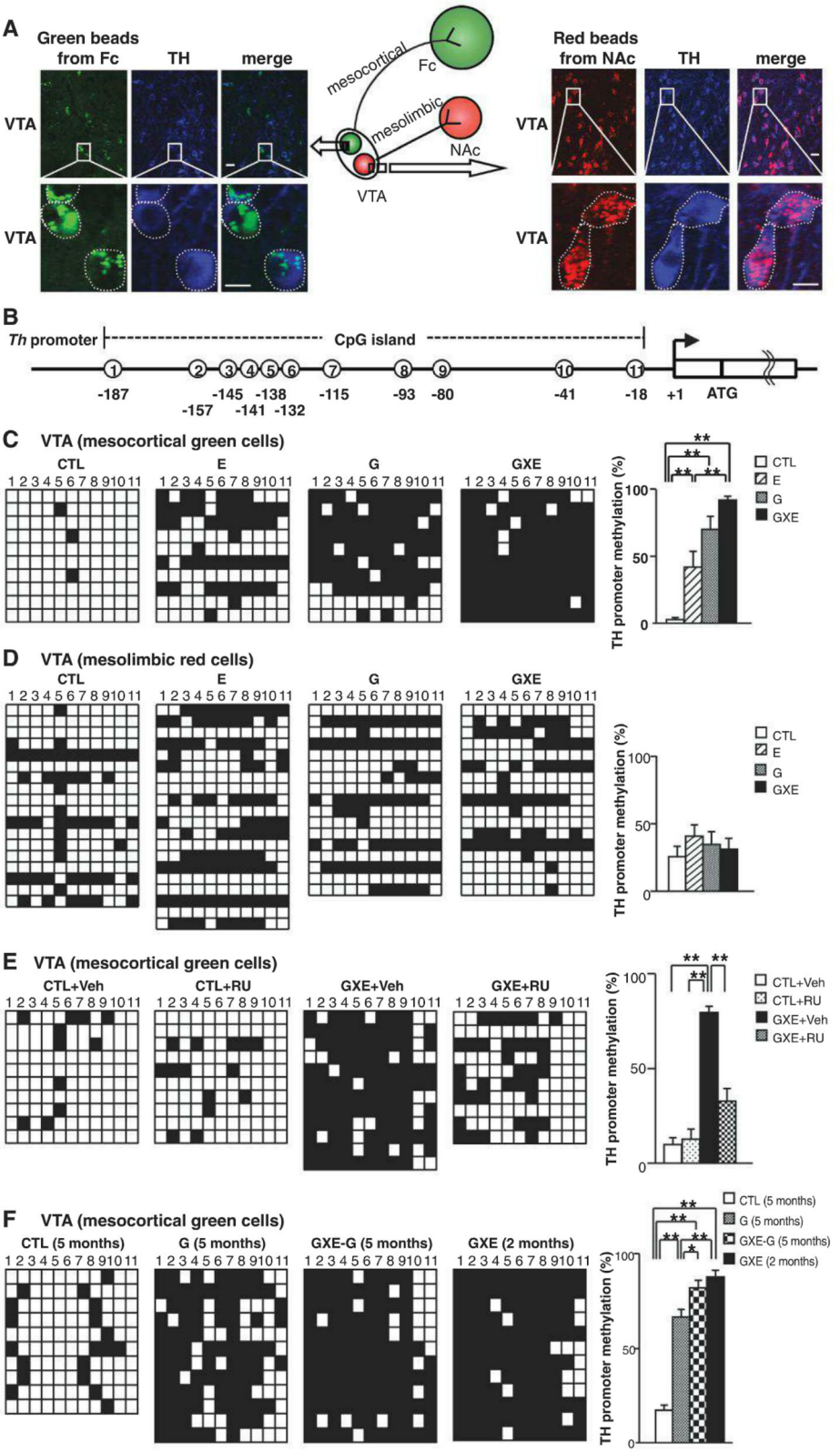

Fig. 4. Distinct influence of glucocorticoids on epigenetic modification of the *Th* genes between mesocortical and mesolimbic dopaminergic projections in the GXE model. (**A**) Confocal images of TH-immunopositive cells in the VTA (blue), which are also labeled with retrogradely transported beads in mesocortical neurons (green) and those in mesolimbic neurons (red), respectively. Scale bars, 20 and 10 μm for upper and lower panels, respectively. (**B**) Graphic representation of the bisulfite-sequenced region in the promoter of the *Th* gene. The 11 CpG sites inside the island are indicated by open circles. The transcription start site (arrow), first exon (white box), and translation start site (ATG) are shown. (**C**) DNA methylation pattern of the *Th* promoter in the VTA neurons projected to the Fc. (**D**) DNA methylation pattern of the *Th* promoter in the VTA neurons projected to the NAc. (**E**) Effects of RU38486 on increased DNA methylation of the *Th* promoter in the VTA neurons projected to the Fc. (**F**) Long-lasting change in the DNA methylation of the *Th* promoter in the VTA neurons projected to the Fc. GXE-G, GXE returned to group housing from 8 to 20 weeks. The columns and rows represent the 11 CpG sites and the sequenced clones, respectively. Black and white squares indicate methylated and unmethylated CpG sites, respectively. Results were obtained from at least three independent experiments. In right panels of (C) to (F), values are means ± SE; $^{**}P < 0.01$, $^{*}P < 0.05$.

ical and behavioral changes in GXE mice. We used green and red beads that could be retrogradely transported from projected areas back to the nucleus; green beads were injected into Fc and red beads into NAc. In the VTA, most of the TH-positive neurons contained either green or red beads, representing mesocortical and mesolimbic dopaminergic projections, respectively (Fig. 4A). Therefore, we dissected the VTA, separated and purified the green and red cells by fluorescence-activated cell sorting (FACS), and examined DNA methylation of these cells by bisulfite sequencing.

When we compared the DNA methylation levels and patterns in the *Th* gene in cells projected from the VTA to the Fc (green cells) among CTL, G, E, and GXE models, GXE showed a significant increase in DNA methylation (Fig. 4, B and C). In contrast, there was no difference in DNA methylation in cells projected from the VTA to the NAc (red cells) among these four animal groups (Fig. 4D). These results are compatible with TH expression in the Fc and NAc (Fig. 2, D and E). Might excess glucocorticoid signaling in the GXE model mediate this change in DNA methylation in the cells of the mesocortical projection? The GR antagonist RU38486 normalized methylation in the GXE model (Fig. 4E). These results demonstrate glucocorticoid-induced, projection-specific epigenetic modifications in the dopamine neurons.

A key question in epigenetics is how long such chemical modifications elicited by the primary stimulus can be maintained—that is, whether this adolescent stress leads to a long-lasting change in adulthood. The genetic model was isolated once from 5 to 8 weeks (i.e., for 3 weeks, the same condition as in the GXE model) and then returned to group housing after adolescence (from 8 to 20 weeks); we designate these mice as GXE-G (fig. S2C). At 20 weeks of age, we examined DNA methylation in the *Th* gene among GXE-G, G, and CTL mice. We then compared these results at 20 weeks of age with those from the GXE model at 8 weeks (immediately after isolation). The significantly high levels of the methylation in the GXE model at 8 weeks were maintained in the GXE-G model at 20 weeks (Fig. 4F). When we compared the epigenetic status of the genetic model without adolescent isolation (G) and that with isolation (GXE-G) at 20 weeks, we also observed significant differences as a result of isolation from 5 to 8 weeks (Fig. 4F).

Our results suggest that an environmental stressor—isolation stress during adolescence—can elicit molecular, neurochemical, and behavioral deficits only when combined with an appropriate genetic risk (in this case, dominant-negative DISC1 in the GXE mice). We observed projection-specific alterations, especially those in epigenetic modifications, in VTA-originated dopaminergic neurons of the GXE model. Under this condition, molecular changes in dopaminergic projections from the VTA and associated behavioral alterations were blocked by administration of the GR antagonist RU38486. These data are compatible with a previous report that chronic administration of corticosterone alters a potassium-induced elevation of extracellular dopamine (*15*). In the present model, the epigenetic alterations were evident in adult animals even if they were maintained in normal group housing several weeks after the transient adolescent isolation.

A key question in neurobiology is how mesocortical and mesolimbic projections are functionally related yet regulated by different means (*16*). These dopaminergic projections are involved in many important brain functions, including reward-associated behavior, motivation, and cognition, which are strongly affected by environmental stressors (*17*). Nonetheless, the link of stressors to dopaminergic projections at the molecular level has remained elusive. Our results show that glucocorticoids influence VTA-originated dopaminergic neurons in a projection-specific manner that involves, at least in part, an epigenetic mechanism. Adult human deviant behavior possibly mediated by the dopaminergic system is long-lasting and associated with stress events in childhood and adolescence (*18*). These selective changes may be accounted for directly by projection-specific molecular dispositions of GRs and downstream cascades in dopamine neurons. It is also conceivable that elevated glucocorticoids may affect neurons in the hippocampus and other areas (*19*), which in turn regulate the epigenetic status in a projection-specific manner.

DISC1 is a risk factor for many psychiatric disorders, including schizophrenia and mood disorders (*20*). DISC1 is expressed in many regions in the brain, but most of the functional studies on DISC1 have been made exclusively in the cerebral cortex and hippocampus. Previously published transgenic models from multiple laboratories have made use of the α–calcium/calmodulin-dependent protein kinase II (αCaMKII) promoter that preferentially expresses DN-DISC1 in the cortex and hippocampus after birth (DISC1-DN-Tg-CaMKII) (fig. S1, D to F) (*20*). In contrast, the present DISC1-DN-Tg-PrP model that shows the effect of gene-environment interactions expresses DN-DISC1 widely in the brain, including the hypothalamus. This evidence may open an avenue to pursue a role for DISC1 in the hypothalamic-pituitary-adrenal (HPA) axis.

Major depression with psychotic features (psychotic depression) is a common and debilitating psychiatric illness with a 0.4% prevalence in the general population in the United States and Europe (*21*), affecting up to 25% of depressed patients admitted to psychiatric hospitals (*22*). Mifepristone (RU38486) is uniquely beneficial in psychotic depression by directly blocking GRs and indirectly modulating functional interaction of cortisol and mineralocorticoid receptors (MRs) (*23*). However, no preclinical model representing this serious medical condition has been available. Given the behavioral abnormalities relevant to the endophenotypes of simultaneous psychosis and depression, as well as the pharmacological responses, the GXE mouse may be a promising model for psychotic depression. The availability of a preclinical model would allow us to study underlying pathological mechanisms, including those in the premorbid and prodromal stages, and explore novel therapeutic strategies. Such a model could provide a good template not only for screening compounds with better efficacy and fewer side effects but also for prophylactic environmental readjustment, which is crucially important in clinical psychiatry.

References and Notes

1. S. J. Blakemore, *Nat. Rev. Neurosci.* **9**, 267 (2008).
2. A. Caspi, B. W. Roberts, R. L. Shiner, *Annu. Rev. Psychol.* **56**, 453 (2005).
3. M. Gunnar, K. Quevedo, *Annu. Rev. Psychol.* **58**, 145 (2007).
4. M. J. Meaney, *Child Dev.* **81**, 41 (2010).
5. T. E. Moffitt, A. Caspi, M. Rutter, *Arch. Gen. Psychiatry* **62**, 473 (2005).
6. J. van Os, G. Kenis, B. P. Rutten, *Nature* **468**, 203 (2010).
7. E. R. de Kloet, M. Joëls, F. Holsboer, *Nat. Rev. Neurosci.* **6**, 463 (2005).
8. E. R. de Kloet, N. Y. Rots, A. R. Cools, *Cell. Mol. Neurobiol.* **16**, 345 (1996).
9. C. Morgan, M. Charalambides, G. Hutchinson, R. M. Murray, *Schizophr. Bull.* **36**, 655 (2010).
10. M. Niwa, Y. Matsumoto, A. Mouri, N. Ozaki, T. Nabeshima, *Int. J. Neuropsychopharmacol.* **14**, 459 (2011).
11. M. Fleshner *et al.*, *Endocrinology* **136**, 5336 (1995).
12. D. Saal, Y. Dong, A. Bonci, R. C. Malenka, *Neuron* **37**, 577 (2003).
13. T. Hagerty *et al.*, *J. Neurochem.* **78**, 1379 (2001).
14. R. S. Lee *et al.*, *Psychopharmacology* **218**, 303 (2011).
15. Y. Ago *et al.*, *Neuropharmacology* **55**, 1355 (2008).
16. S. Lammel *et al.*, *Neuron* **57**, 760 (2008).
17. R. Adolphs, *Nat. Rev. Neurosci.* **4**, 165 (2003).
18. R. M. Murray, P. D. Morrison, C. Henquet, M. Di Forti, *Nat. Rev. Neurosci.* **8**, 885 (2007).
19. M. Popoli, Z. Yan, B. S. McEwen, G. Sanacora, *Nat. Rev. Neurosci.* **13**, 22 (2012).
20. N. J. Brandon, A. Sawa, *Nat. Rev. Neurosci.* **12**, 707 (2011).
21. M. M. Ohayon, A. F. Schatzberg, *Am. J. Psychiatry* **159**, 1855 (2002).
22. W. Coryell, B. Pfohl, M. Zimmerman, *J. Nerv. Ment. Dis.* **172**, 521 (1984).
23. B. H. Flores, H. Kenna, J. Keller, H. B. Solvason, A. F. Schatzberg, *Neuropsychopharmacology* **31**, 628 (2006).

Acknowledgments: We thank P. Talalay, J. Roeper, M. A. Landek-Salgado, and Y. Lema for helpful advice. Supported by Stanley, RUSK, S-R, NARSAD, the Maryland Stem Cell Research Fund, and NIH grants MH-084018, MH-094268, MH-069853, MH-085226, MH-088753, and MH-092443 (A.S.); by JSPS-Korea and the Ministry of Education, Culture, Sports, Science and Technology/Ministry of Health, Labour and Welfare of Japan (MEXT/MHLW) and JSPS grants 22248033, 20390073, and 22659213 (T.N.); by Strategic Research Program for Brain Sciences and MEXT/MHLW (N.O.); and by NARSAD, NIH grant K99MH-094408, and JSPS grants 20007152 and 23-639 (M.N.).

Supplementary Materials

www.sciencemag.org/cgi/content/full/339/6117/335/DC1
Materials and Methods
Figs. S1 to S9
Tables S1 and S2
References (*24*–*40*)

4 July 2012; accepted 21 November 2012
10.1126/science.1226931

AAAS 2013 ANNUAL MEETING
14-18 FEBRUARY • BOSTON

THE BEAUTY AND BENEFITS OF SCIENCE

HYNES CONVENTION CENTER

Join Us in Boston

Participate in seminars on the biology and evolution of human language, global fisheries and food supply, the brain's plasticity, and communicating science as well as 150 symposia across 14 tracks that cover the breadth of science, engineering, education, and policy.

- Share ideas with leaders in science and technology.
- Learn about recent developments in education and policy.
- Network with colleagues and make new connections.

View full program and register at
www.aaas.org/meetings

Follow us on Twitter
www.twitter.com/AAASMeetings
#AAASmtg

Reporters: The EurekAlert! website hosts the AAAS Meeting Newsroom. Reporters can obtain details and register at
www.eurekalert.org/newsroom

AAAS
ADVANCING SCIENCE, SERVING SOCIETY

AAAS presents the

2013 AAAS ANNUAL MEETING

THE BEAUTY AND BENEFITS OF SCIENCE

WIlliam H. Press
AAAS President and 2013 Program Chair

Dear Colleagues,

On behalf of the AAAS Board of Directors, it is my honor to invite you to join us in Boston for the 2013 AAAS Annual Meeting, 14-18 February. As you may know, this annual event is one of the most widely recognized global science gatherings, with hundreds of networking opportunities and broad U.S. and international media coverage.

The meeting's theme — *The Beauty and Benefits of Science* — points to the "unreasonable effectiveness" of the scientific enterprise in creating economic growth, solving societal problems, and satisfying the essential human drive to understand the world in which we live.

The phrase "unreasonable effectiveness" was coined in 1960 by physicist Eugene Wigner, who explored the duality of mathematics — both beautiful unto itself, and also eminently practical, often in unexpected ways. The scientific program will highlight the rich and complicated connections between basic and applied research, and how they bring about both practical benefits and the beauty of pure understanding.

Everyone is welcome at the AAAS Annual Meeting. Those who join us will have the opportunity to choose among a broad range of activities, including plenary and topical lectures by some of the world's leading scientists and engineers, multidisciplinary symposia, cutting-edge seminars, career development workshops, and an international exhibition. You and your family can also enjoy Family Science Days, a free event open to the general public.

The Annual Meeting reflects tremendous efforts from the AAAS sections, divisions, and committees, which I gratefully acknowledge. I also extend a personal thanks to the members of the Scientific Program Committee who selected and assembled the many excellent ideas and proposals into this outstanding meeting.

Please join us in Boston.

William H. Press
AAAS President and Program Chair;
Warren J. and Viola M. Raymer Professor in Computer Science and Integrative Biology
University of Texas at Austin

President's Address

Thursday, 14 February

William H. Press
Warren J. and Viola M. Raymer Professor in Computer Science and Integrative Biology, University of Texas at Austin

Dr. Press is a noted researcher in computer science, genomics, statistical methods, astrophysics, and international security. He is a member of the President's Council of Advisors on Science and Technology. His current research focus is bioinformatics and whole-genome genetics. He previously served as deputy laboratory director for science and technology at the Los Alamos National Laboratory and as a professor of astronomy and physics at Harvard University. He is a member of the U.S. National Academy of Sciences, a fellow of the American Academy of Arts and Sciences, and a member of the Council on Foreign Relations.

Plenary Speakers

Friday, 15 February

Sherry Turkle
Abby Rockefeller Mauzé Professor of the Social Studies of Science and Technology in the Program in Science, Technology, and Society, MIT

The Robotic Moment: What Do We Forget When We Talk to Machines?

Dr. Turkle is founder and director of the MIT Initiative on Technology and Self. She received a joint doctorate in sociology and personality psychology from Harvard University and is a licensed clinical psychologist. Her research focuses on the psychology of human relationships with technology, especially in the realm of how people relate to computational objects. She is an expert on mobile technology, social networking, and sociable robotics and a regular media commentator on the social and psychological effects of technology. Her most recent book is *Alone Together: Why We Expect More from Technology and Less from Each Other.*

Saturday, 16 February

Nathan Myhrvold
Founder and Chief Executive Officer, Intellectual Ventures

Modernist Cuisine: The Art and Science of Cooking

Dr. Myhrvold founded Intellectual Ventures after retiring as chief strategist and chief technology officer of Microsoft Corporation. At Intellectual Ventures, he is focused on a variety of business interests relating to the funding, creation, and commercialization of inventions. During his tenure at Microsoft, he was responsible for founding Microsoft Research and technology groups that resulted in many successful products. He has extensive experience linking research to product development and commercialization and holds hundreds of patents. As a postdoctoral fellow in applied mathematics and theoretical physics at Cambridge University, he worked with Stephen Hawking on research in cosmology, quantum field theory in curved space time, and quantum theories of gravitation. He earned a doctorate in theoretical and mathematical physics and a master's degree in mathematical economics from Princeton University. He also has a master's degree in geophysics and space physics and a bachelor's degree in mathematics from University of California, Los Angeles.

Sunday, 17 February

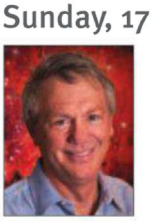

Robert Kirshner
Clowes Professor of Science, Harvard University

The Beauty of the Accelerating Universe

Dr. Kirshner is an astrophysicist studying the physics of supernovae and observational cosmology. He is a member of the High-z Supernova Search Team that used observations of extragalactic supernovae to discover the accelerating universe, which implied the existence of dark energy. Dr. Kirshner's graduate students Brian Schmidt and Adam Riess shared the 2011 Nobel Prize in Physics with Saul Perlmutter for the discovery of cosmic acceleration. He teaches a popular course for Harvard undergraduates called "The Energetic Universe" and is author of the book *The Extravagant Universe: Exploding Stars, Dark Energy, and the Accelerating Cosmos.* He is a past president of the American Astronomical Society, a member of the National Academy of Sciences, and a 2012 Guggenheim Fellow.

Monday, 18 February

Cynthia Kenyon
American Cancer Society Professor and Director of the Hillblom Center for the Biology of Aging, University of California, San Francisco

Mechanisms for Life Extension in *C. elegans*

Dr. Kenyon is a molecular biologist whose discovery with colleagues that a single-gene mutation could double the lifespan of the worm *C. elegans* sparked an intensive study of the molecular biology of aging. Her findings have since led to the discovery that an evolutionarily conserved hormone signaling system controls aging in other organisms as well, including mammals. As a doctoral student at Massachusetts Institute of Technology, she was the first to look for genes on the basis of their expression profiles, discovering that DNA damaging agents activate a battery of DNA repair genes in *E. coli.* She is a member of the U.S. National Academy of Sciences and the Institute of Medicine, a fellow of the American Academy of Arts and Sciences, and a past president of the Genetics Society of America.

AAAS 2013 ANNUAL MEETING
14-18 FEBRUARY • BOSTON

THE BEAUTY AND BENEFITS OF SCIENCE

HYNES CONVENTION CENTER

Topical Lectures

Richard Alley
Evan Pugh Professor, Department of Geosciences, and Earth and Environmental Systems Institute, Pennsylvania State University
Ice Sheets, Sea Level, and Other Surprises: Benefits of Understanding Some Beautiful Places

Karl Deisseroth
Associate Professor of Bioengineering and Psychiatry, Stanford University
Optogenetics: Development and Application

Felice Frankel
Research Scientist, Center for Materials Science and Engineering, Massachusetts Institute of Technology
More Than Pretty Pictures: How the Process of Making Science Images and Graphics Clarifies Understanding

Nina Jablonski
Distinguished Professor of Anthropology, Pennsylvania State University
The Evolution and Meanings of Human Skin Color

Chad Mirkin
Director of International Institute for Nanotechnology and George B. Rathmann Professor of Chemistry, Northwestern University
"Artificial Atoms" Formed from Nucleic Acid Nanoparticle Conjugates: The Dawn of a New Periodic Table

Peter Norvig
Director of Research, Google Inc.
Technology for Educating Everyone

GEORGE SARTON MEMORIAL LECTURE IN THE HISTORY AND PHILOSOPHY OF SCIENCE

Silvan Schweber
Emeritus Professor of Physics and Richard Koret Professor in the History of Ideas, Brandeis University
Hans Bethe and Physics in the 20th Century

JOHN P. MCGOVERN AWARD LECTURE IN THE BEHAVIORAL SCIENCES

Walter Mischel
Niven Professor of Humane Letters in Psychology, Columbia University
Demystifying Delay of Gratification

Topical Panel: European Science Policy on the Move

European science policy is as dynamic as ever. The new chief scientific advisor position to the European Commission President has been filled. National research councils are becoming more organized with the new Science Europe organization. Bottom-up research is increasingly supported at the European level. A bigger and larger EU research funding program, "Horizon 2020," will be launched next year from the European Commission. Four high-level experts will be asked to address questions about where European science policy is headed.

Moderated by: William H. Press, AAAS President and Program Chair; Warren J. and Viola M. Raymer Professor in Computer Science and Biology, University of Texas at Austin

Paul Boyle
President, Science Europe; Chief Executive, U.K. Economic and Social Research Council

Anne Glover
Chief Scientific Advisor to European Commission President, European Union

Helga Nowotny
President, European Research Council

Robert-Jan Smits
Director-General, Directorate-General for Research and Innovation, European Commission

To browse the updated program, register, and reserve hotel rooms, visit **www.aaas.org/meetings.**

Special Sessions

International Teacher-Scientist Partnership Conference
Wednesday, 13 February - Thursday, 14 February
Pre-registration required

Responsible Professional Practices in a Changing Research Environment
Thursday, 14 February
Pre-registration required

***Curiosity*'s Mission at Gale Crater, Mars**
Friday, 15 February
John Grotzinger, Fletcher Jones Professor of Geology, and Project Scientist, Mars Science Laboratory, California Institute of Technology
Open to all attendees

Seminars

Thursday, 14 February

Communicating Science

Scientific and technological issues increasingly trigger societal conflicts whenever they intersect with personal or political views. Particularly amid pressures on research and development budgets, and related concerns about transparency and accountability, today's scientists and engineers are challenged to communicate and engage with the public, reporters, and policy-makers. This seminar will share science communication expertise in working with different types of content, across a range of presentation formats, for various audiences.

Organized by: Cornelia Dean, *The New York Times;* Dennis Meredith, Science Communication Consultant

Working with Print, Broadcast, and Online Media

SPEAKERS
Juliet Eilperin, *The Washington Post*
Science Reporting at Newspapers in an Age of Tight Budgets, Constant Deadlines, Political Polarization, and Industry Upheaval

Chris Joyce, National Public Radio
Science Journalism: Alive and Kicking

Alan Boyle, NBCNews.com
Science Journalism: On Internet Time

Communicating Science to Policy-Makers

SPEAKERS
David Goldston, Natural Resources Defense Council
Why Can't They Just Do What's Right?: Misperceptions and Barriers to Science Communication

* Bill Foster, United States House of Representatives

Arthur Lupia, University of Michigan
Communicating Science in Politicized Environments

Visualizing Science

SPEAKERS
Felice Frankel, Massachusetts Institute of Technology
Tell Me What You See: Understanding Science Images

Erik Olsen, *The New York Times*
Explaining Science in Video

Yael Fitzpatrick, AAAS/*Science*
Starting with the Basics, Ending with a Bang

Engaging with Social Media

SPEAKERS
Scicurious, Neurotic Physiology
Science Blogging for Fun and Profit

Christie Wilcox, University of Hawaii
Science in a Digital Age

Dominique Brossard, University of Wisconsin, Madison
Science and the Public in New Information Environments

Friday, 15 February

The Biology and Evolution of Human Language

The human ability to learn and use language is deeply rooted in the biology of our species and processes of cultural evolution. We are biologically equipped for language in general, but inherit the specific cultural form of the languages in which we are socialized. The creation of new languages provides unique perspectives on language acquisition.

The Language Organ: The Bases of Human Language in Human Biology

Organized by: Stephen Anderson, Yale University

SPEAKERS
Stephen Anderson, Yale University
Human Language in the Broader Biological Context

Steven Pinker, Harvard University
Language as an Adaptation to the Cognitive Niche

Janet F. Werker, University of British Columbia
Infant Speech Perception: Biological Beginnings and Experiential Influences

Erich Jarvis, Duke University Medical Center
Learned Birdsong and the Neurobiology of Human Language

David Poeppel, New York University
What We Know About the Brain Bases of Language

Karen Emmorey, San Diego State University
The Generality of the Language Faculty: Biological Bases of Signed Language

Historical Syntax

Organized by: David Lightfoot, Georgetown University; Joseph Salmons, University of Wisconsin, Madison

SPEAKERS
David Lightfoot, Georgetown University
Phase Transitions in Language History

Tony Kroch, University of Pennsylvania
Studying the Diffusion of Syntactic Changes in Historical Corpora

Michel DeGraff, Massachusetts Institute of Technology
A Null Theory of Creole Formation

DISCUSSANT
Mark Liberman, University of Pennsylvania

Language Evolving: Genes and Culture in Ongoing Language Evolution

Organized by: Stephen C. Levinson, Max Planck Institute for Psycholinguistics; Karen Emmorey, San Diego State University

SPEAKERS
Simon E. Fisher, Max Planck Institute for Psycholinguistics
Language, Evolution, and the Genomics Revolution

Russell Gray, University of Auckland
Evolutionary Principles and the Diversification of Linguistic Form

Carol Padden, University of California, La Jolla
Culture Before Genes: The Case of a Village Sign Language

DISCUSSANTS
Dan Dediu, Max Planck Institute for Psycholinguistics

**Invited*

Saturday, 16 February

Brain Function and Plasticity

Early experience has a lasting impact on our ability to perceive the world. It is widely understood that the brain is initially plastic and that its connections are tuned by early experience to match the environment. Recent evidence indicates that there is also considerable residual plasticity in the adult brain, which has implications for treatment of brain injury and recovery of lost function.

The Connectome: From the Synapse to Brain Networks in Health and Disease

Organized by: David Holtzman, Washington University, St. Louis

SPEAKERS

Mark F. Bear, Massachusetts Institute of Technology
Molecules and Mechanisms Involved in Synaptic Plasticity in Health and Disease

Jeff Lichtman, Harvard University
Connectomics: Developing a Wiring Diagram for the Mammalian Brain

Steve Petersen, Washington University, St. Louis
The Human Connectome Project

Marcus E. Raichle, Washington University, St. Louis
The Brain's Dark Energy and the Default Mode Network

Nicole Calakos, Duke University
Synaptic Plasticity in the Basal Ganglia in Health and Disease

William W. Seeley, University of California, San Francisco
Brain Networks: Linking Structure and Function in Neurodegenerative Diseases

Old Dogs, New Tricks: How Plastic Is the Adult Human Brain?

Organized by: Daphne Maurer, McMaster University; Susan M. Fitzpatrick, James S. McDonnell Foundation

SPEAKERS

Daphne Maurer, McMaster University
Improving Vision After the Critical Period

Alex R. Carter, Washington University School of Medicine, St. Louis
A "New Trick" for Neuro-Rehabilitation: Treating Networks Not Spots

Arthur Kramer, University of Illinois, Urbana-Champaign
Physical Fitness Effects on Brain and Cognition

DISCUSSANT

Susan M. Fitzpatrick, James S. McDonnell Foundation

Teaching the Brain to Speak Again: New Frontiers in Trauma and Stroke Recovery

Organized by: Nan Ratner, University of Maryland; Margaret Rogers, American Speech-Language-Hearing Association

SPEAKERS

Julius Fridriksson, University of South Carolina
Real-Time Audiovisual Feedback Enables Stroke Patients to Reacquire Speech

Cynthia Thompson, Northwestern University
Neurocognitive Mechanisms of Syntactic Recovery in Agrammatism

Sheila Blumstein, Brown University
Auditory Modeling Improves Aphasic Speech Production Recovery

Sunday, 17 February

Global Fisheries and Food Supply

Ecosystem sustainability may be endangered by exploitation. As the rising world population increases demand for food production, the sustainable development of goods and services and the protection of ocean and fisheries environments will be a formidable challenge. Cooperation across scientific disciplines and international borders is crucial to securing the future ocean.

Realizing Jacques Cousteau's Vision of Aqua-Farming Replacing Hunting of the Sea

Organized by: KeShun Liu and Jeffrey Silverstein, U.S. Department of Agriculture (USDA) Agricultural Research Service

SPEAKERS

Margareth Overland, Norwegian University of Life Sciences
Sustainable Ingredient Development for Aquaculture Feed

Steven Summerfelt, The Conservation Fund Freshwater Institute
Responsible Aquaculture by Minimizing Environmental Impacts on Land and Water

Jeffrey Silverstein, USDA Agricultural Research Service
Responsible Aquaculture Development: A Holistic Approach

Moving Toward Sustainable Development of Large Marine Ecosystems

Organized by: Kenneth Sherman, National Oceanic and Atmospheric Administration (NOAA)

SPEAKERS

Hashali Hamukuaya, Benguela Current Commission
The Resilience and Robustness of the Benguela Current Large Marine Ecosystem

Yihang Jiang, United Nations Development Program/Global Environment Facility Yellow Sea Project
The Resilience and Robustness of the Yellow Sea Large Marine Ecosystem

Michael Akester, United Nations Office for Project Services
The Resilience and Robustness of the Humboldt Current Large Marine Ecosystem

Weaving the Future Ocean Web Through Collaboration: the Nereus Program

Organized by: Yoshitaka Ota and Villy Christensen, University of British Columbia

SPEAKERS

Henrik Osterblom, Stockholm University
Weaving the Future Ocean Food Web: The Nereus Diagram

Ryan Rykaczewski, Princeton University
Linkages Between the Carbon Cycle and Biota in the Global Ocean

Andre Boustany, Duke University
Habitat and Fisheries Interactions: Spatial Patterns Under Climate Change

Marc Metian, Stockholm Resilience Center
Bridging Demand and Supply of Seafood: Sustainable Aquaculture in a Changing World

Chris McOwen, United Nations Environment Program, World Conservation Monitoring Center
Linking Terrestrial Processes, Coastal Landscapes, and Marine Ecosystems

DISCUSSANTS

Claire Nouvian, BLOOM Association; Philippe Cury, Center for Mediterranean and Tropical Fisheries Research, France

Symposium Tracks

Animal, Plant, and Food Sciences

Advancing Food Safety in a Global Marketplace

Organized by Nicola J. Stagg, Dow AgroSciences; P. Michael Bolger, Retired

Alternate Paths to Food Security: Making the Right Choices While Feeding the World

Organized by Albert G. Medvitz, McCormack Sheep and Grain

Employing Cutting-Edge Plant Science To Address Global Issues that Threaten Mankind

Organized by Melvin J. Oliver, U.S. Department of Agriculture Agricultural Research Service

Fixing the Broken Tomato: What We Like and Why We Like It

Organized by Linda M. Bartoshuk and Harry J. Klee, University of Florida

How Microbes Can Help Feed the World

Organized by Ann Reid, American Academy of Microbiology

Plant Viruses: Mutualists, Modulators, and Manipulators
Organized by Ulrich Melcher, Oklahoma State University; Nilsa A. Bosque-Pérez, University of Idaho

Power of New Generation Biotechnology To Transform Global Food Security
Organized by Jenny Gu and Larry Beach, U.S. Agency for International Development

Transforming Productivity and Incomes of Poor Farm Households in the Developing World
Organized by Jerry Glover and Elizabeth Skewgar, U.S. Agency for International Development

Why a Calorie Is Not a Calorie and Why It Matters for Human Diets
Organized by Rachel N. Carmody and Richard Wrangham, Harvard University

Anthropology, Culture, and Language

Beyond Color: How Human Skin Interacts with Our World
Organized by Nina Jablonski, Pennsylvania State University; Ellen E. Quillen, Texas Biomedical Research Institute

Democratizing Science: Virtualization and Global Natural History Repositories
Organized by Herbert D.G. Maschner, Idaho Museum of Natural History; Corey D. Schou, Idaho State University

The Scars of Human Evolution
Organized by Karen Rosenberg, University of Delaware; Rachel Caspari, Central Michigan University

The Whole of Culture: Anthropology Back on Track
Organized by Dwight Read, University of California, Los Angeles; Fadwa El Guindi, Qatar University

Atmospheric, Hydrospheric, and Oceanic Sciences

Advancing the Frontiers of Understanding the Ocean and Its Role in the Earth System
Organized by Robert A. Weller, Woods Hole Oceanographic Institution

Can Oceans Help Meet the Century's Looming Food Security Challenges?
Organized by Steven Gaines, University of California, Santa Barbara

Contributions of Citizen Scientists to Climate Science
Organized by Imke Durre, NOAA

Electric Oceans: Finding the Space for Marine Renewable Energy in Crowded Waters
Organized by Jodie Toft and Mary Ruckelshaus, Natural Capital Project

Green Dreams, Blue Waves, and Shades of Gray: The Reality of Water
Organized by E. John Sadler, U.S. Department of Agriculture; Fred Vocasek, Servi-Tech Laboratories

The National Climate Assessment: Draft Findings for 2013 and Sustaining the Process
Organized by Emily Therese Cloyd, U.S. Global Change Research Program; Kathy Jacobs, Office of Science and Technology Policy, Executive Office of the U.S. President

U.S. Climate and Weather Extremes: Past, Present, and Future
Organized by Connie Woodhouse, University of Arizona; Gregory Wiles, The College of Wooster; Ester Sztein, U.S. National Academies

Biological Science and Genomics

A Decade After "Forensic Science: Oxymoron?": Will There Be Real Change?
Organized by Clifford H. Spiegelman, Texas A&M University

Confluence of Streams of Knowledge: Biotechnology and Nanotechnology
Organized by Elicia M.A. Maine, Simon Fraser University; James M. Utterback, Massachusetts Institute of Technology

Dragons of the East: China's Paleontological Riches
Organized by Richard A. Stone, AAAS/*Science*

Evolution of Giants: The Great Whales
Organized by Jere H. Lipps, Cooper Archaeological and Paleontological Center; Nicholas D. Pyenson, Smithsonian National Museum of Natural History

How Macro-Evolutionary Studies Call for an Extended Synthesis
Organized by Nathalie L. Gontier, University of Lisbon; Emanuele Serrelli, University of Milan-Bicocca

How Symbiosis, Horizontal Gene Transfer, and Virolution Call for an Extended Synthesis
Organized by Nathalie L. Gontier, University of Lisbon

Innovations in Imaging
Organized by Amy S. Gladfelter, Dartmouth College

Interfacing with the Body Using Implants and Prostheses
Organized by Erin Heath, AAAS Office of Government Relations

New Frontiers in Single Molecule Detection and Single Cell Analysis
Organized by X. Nancy Xu, Old Dominion University

Personal Genetics: An Intersection Between Science, Society, and Policy
Organized by Peter Yang, Brenna Krieger, and Kevin Bonham, Harvard University

Resurrected Ancestral Proteins: Fundamentals and Applications
Organized by Antony Dean and Romas Kazlauskas, University of Minnesota

The Architecture of the Cell Nucleus
Organized by Gary Felsenfeld, National Institute of Diabetes and Digestive and Kidney Diseases

The Invisible Revealing the Dangerously Beautiful
Organized by Isabelle Boscaro-Clarke, Diamond Light Source

The Science of Uncertainty in Genomic Medicine
Organized by Shili Lin, Ohio State University; Reed E. Pyeritz, University of Pennsylvania

Visualizing Chemistry: Seeing Another Dimension of Plants and Animals
Organized by Barbara Illman, U.S. Forest Service; Janos Kirz, Lawrence Berkeley National Laboratory

Cognitive, Neural, and Social Sciences

Advances in Brain-Machine Interfaces: Applications and Implications
Organized by Peyton West and Jennifer Wiseman, AAAS Center for Science, Policy, and Society Programs

Breakthroughs in Our Understanding of Primate Cognition and Psychopathology
Organized by Neal D. Barnard, George Washington University School of Medicine and Health Sciences

Computation, Computational Efficiency, and Cognitive Science
Organized by Robert C. Berwick, Massachusetts Institute of Technology; Anna Maria Di Sciullo, University of Quebec, Montreal

Evidence from Music, Fiction, and Visual Arts: Transfer of Learning from the Arts?
Organized by Ellen Winner, Boston College

The Economic Costs of Crime and Justice in the United States
Organized by William Alex Pridemore, Indiana University

The Elusive Common Good: What Moral Psychology and Neuroscience Now Tell Us
Organized by Robert E. Fay, Westat

Understanding Memory: The Legacy of Case H.M.
Organized by Howard Eichenbaum, Boston University

Why Is Living Healthily So Difficult?
Organized by Benedikt Herrmann and Geraldine Barry, Joint Research Center, European Commission

Communication and Public Programs

A New Social (Media) Contract for Science
Organized by Elizabeth Neeley, COMPASS

Artful Science
Organized by John R. Jungck, Beloit College

Creative and Participatory Methods in Climate Communication
Organized by Eli Kintisch, AAAS/*Science*; Juliette N. Rooney-Varga, University of Massachusetts, Lowell

Engaging Lay Publics in Museums on Provocative Societal Questions Related to Science
Organized by Larry Bell, Museum of Science, Boston

In the Eye of the Beholder: Engaging the Public in Societal Implications of Science
Organized by Larry Bell and David Sittenfeld, Museum of Science, Boston

New Tools to Engage Publics and Assess the Impact of Science Communication
Organized by David Herring, NOAA

Science Festivals: Grand Experiments in Public Outreach
Organized by Ben Wiehe, MIT Museum

Scientists' Understanding of the Public
Organized by John C. Besley, Michigan State University

Synthetic Biology and Public Perceptions: Communication and Engagement
Organized by Peyton West, AAAS Center for Science, Policy, and Society Programs; Tiffany Lohwater, AAAS Office of Public Programs

The Beauty and Benefits of Escaping the Ivory Tower
Organized by Dawn J. Wright, Environmental Systems Research Institute; Elizabeth Hadly, Stanford University

Wild Weather, Climate Change, and Media: Communicating Science, Uncertainty, and Impact
Organized by Cristine Russell and James McCarthy, Harvard University

Writing About Science for the Public
Organized by Daniel Levitin, McGill University

Education and Human Resources

Accelerating School Readiness and Cumulative Academic Performance: Birth to Age 10
Organized by David L. Featherman, University of Michigan

Animals on Exhibit
Organized by Joe Zammit-Lucia, Artist and Independent Scholar; Linda Kalof, Michigan State University

Benefits Beyond Beauty: Integration of Art and Design into STEM Education and Research
Organized by Rieko Yajima, AAAS Center of Science, Policy, and Society Programs; Gunalan Nadarajan, Maryland Institute College of Art

Creating Interdisciplinary Competency-Based Curricula for Undergraduate Students
Organized by Dee U. Silverthorn, University of Texas, Austin; William R. Galey, Howard Hughes Medical Institute

Engaging Students in Complex Science Learning via Games and Simulations
Organized by Susannah Gordon-Messer, Massachusetts Institute of Technology; Jody Clarke Midura, Harvard Graduate School of Education

For Scientists and Society: A New Vision of Chemistry Graduate Education
Organized by Bassam Shakhashiri, University of Wisconsin

How K-12 Curriculum Reform Can and Will Affect University Studies
Organized by Arthur Eisenkraft, University of Massachusetts, Boston

Increasing Diversity in Science: Learning from Successful Program Models
Organized by Rebecca L. Smith, University of California, San Francisco

Overcoming Dualisms and Promoting Minority Inclusion in Science Networks and Pipelines
Organized by Roberta Spalter-Roth, American Sociological Association

Preparing Our Future Scientific Work Force to Ensure the Success of Science
Organized by Cynthia N. Fuhrmann, University of Massachusetts Medical School; Bill Lindstaedt, University of California, San Francisco; Bruce M. Alberts, AAAS/*Science*

Science After School: Scientists Inspire the Next Generation Outside of the Classroom
Organized by Carol M. Tang, Coalition for Science After School; Elizabeth Stage, University of California, Berkeley

The 25th Anniversary of the First Collection in the History of Women in Science
Organized by Pnina G. Abir-Am, Brandeis University; Joy Harvey, Independent Scholar

Undergraduate Science Education at a Crossroad: Responding to Research Findings
Organized by Jay B. Labov, U.S. National Academy of Sciences; Susan Singer, Carleton College; Martin Storksdieck, National Research Council

Where and How Are Research and Innovation Fostering Job Creation?
Organized by Florent Bernard, European Commission

Environment and Ecology

A 50 Year Legacy: Why does Rachel Carson Matter?
Organized by Gregg Zachary and Jane Maienschein, Arizona State University

A Science and Art Interface: Geographic Information Systems and Remotely Sensed Images
Organized by Daniel Griffith, University of Texas, Richardson; Ren Vasiliev, State University of New York, Geneseo

Building Resilience of Coastal Communities to Environmental and Institutional Shocks
Organized by Richard Pollnac, University of Rhode Island; Joshua E. Cinner, James Cook University

Converging on Climate Change: From Middens to Models, the Savannah to Snæfellsjökull
Organized by Samantha Christey, European Research Council

Dynamics of Disasters: Harnessing the Science of Networks To Save Lives
Organized by Anna Nagurney, University of Massachusetts, Amherst

Environmental Challenges and Adaptation in Cities
Organized by Matthias Ruth, University of Maryland

Finding the Fault: Sampling the Source of the M9.0 Tohoku Earthquake
Organized by Charna Meth, Consortium for Ocean Leadership

Indigenous and Western Science: Collaborating for Better Research and Education
Organized by Patricia B. Campbell, Campbell-Kibler Associates

New Dimensions of Biodiversity Science and Application
Organized by Julia K. Parrish, University of Washington; Sandy J. Andelman, Conservation International

Partners for the Earth: Scientists and Religious Groups Working for the Environment
Organized by Jennifer Wiseman and Peyton West, AAAS Center for Science, Policy, and Society Programs

Spatially Distributed Environmental Factors and Health Effects
Organized by Katherine B. Ensor, Rice University

The Toxicological Impact of the Gulf of Mexico Oil Spill on Human and Wildlife Health
Organized by John Pierce Wise, University of Southern Maine; R. Joseph Griffitt, University of Southern Mississippi

Global Perspectives and Issues

A Tale of Two Networks: Connecting the African Drylands, Rio de Janeiro, and Women
Organized by Marcelo Vinces, AAAS Science and Technology Policy Fellow, National Science Foundation; Riju Srimal, AAAS Science and Technology Policy Fellow, National Institutes of Health; Gillian Bowser, Colorado State University

Bridging the Gap Between Global Environmental Change Research and Development
Organized by Timothy L. Killeen, National Science Foundation; Erika von Schneidemesser, AAAS Science and Technology Policy Fellow, National Science Foundation

Future Earth: International Coordination of Research for Global Sustainability
Organized by Roberta Quadrelli, Julie DeMeester, and Anne-Sophie Stevance, International Council for Science

Global Food Security in Relation to Climate, Population, Technology, and Earth Changes
Organized by Alfred M. Powell and Felix Kogan, NOAA

Lead: The Global Poison — Humans, Animals, and the Environment
Organized by Mark A. Pokras, Tufts University; Ronnie Levin, U.S. Environmental Protection Agency

Measurement of Economic and Social Impacts of Science and Technology Investments
Organized by Yuko Ito and Aska Takeshiro, National Institute of Science and Technology Policy

Networks of Discovery: Delivering Unsurpassed Insight into Changing Global Ecosystems
Organized by Kristen Milligan and Joe A. Tyburczy, Oregon State University

Science from the International Space Station
Organized by Julie A. Robinson, NASA Johnson Space Center; Christopher L. Martin, Oberlin College

Smart Phones, Smart Devices, Social Networks, and Smart Health Care
Organized by Vinton Cerf, Google Inc.; Ram Sriram, National Institute of Standards and Technology

The Invisible Beauty: How Security Research Helped in Real Life, but Nobody Noticed
Organized by Stephan Lechner, Joint Research Center, European Commission

The Role of Higher Education in Science Diplomacy: Possibilities and Potential Pitfalls
Organized by Elizabeth E. Lyons, U.S. Department of State

Unreasonable Usefulness of Test-Ban Verification for Disaster Warning and Science
Organized by Annika Thunborg, Preparatory Commission for the Comprehensive Nuclear-Test-Ban Treaty Organization

Health and Pharmaceutical Science

Clinical Trial and Error: Beauty and the Beast
Organized by Aidan Gilligan, SciCom–Making Sense of Science; Thomas Hartung, Johns Hopkins University

Control Engineering of Brain in Health and Disease
Organized by Steven J. Schiff, Mauricio Terrones, and Alok Sinha, Pennsylvania State University

Cultivating the Science and Scientists for 21st Century Drug Discovery and Development
Organized by Alice Clark, University of Mississippi

Engineering the Nervous System: Solutions to Restore Sight, Hearing, and Mobility
Organized by Sanna Fowler, Ecole Polytechnique Fédérale de Lausanne

Monitoring and Assuring the Quality of Essential Medicines
Organized by Gaurvika Nayyar and Joel Breman, National Institutes of Health

Multi-Scale Study of Cancer
Organized by Mark Alber, University of Notre Dame; Jill P. Mesirov, Broad Institute of Massachusetts Institute of Technology and Harvard University

Pathways to Health Equity for Aboriginal Peoples
Organized by Danièle St-Jean, Canadian Institutes of Health Research

Scientific Advances and New Strategies for Reconstruction of Oral and Facial Tissues
Organized by Paul Krebsbach, University of Michigan; Barbara D. Boyan, Georgia Institute of Technology

Stem Cell–Based Bioartificial Tissues and Organs
Organized by Sabina Bossi, Karolinska Institute

Stroke Research: New Concepts and Innovative Solutions
Organized by Ruxandra Draghia-Akli and Virginija Dambrauskaite, European Commission

The Benefits of Randomized Experiments for Science and Society
Organized by Daniel McCaffrey, RAND Corp.

Materials Science and Chemistry

Attosecond Science in Chemical, Molecular Imaging, Spintronics, and Energy Science
Organized by Andre D. Bandrauk, University of Sherbrooke; Margaret M. Murnane, University of Colorado

Nucleic Acid Nanotechnology
Organized by Andrew D. Ellington, University of Texas

Quantum Sensors: Toward the Ultimate Limits
Organized by Martin Laforest, University of Waterloo

Remembering Galileo: Lithium Ion Batteries, Atomic Clocks, and Other Stories
Organized by Carlos Saraiva Martins, European Commission

Surprises at the Frontier of the Periodic Table: Novel Paradigms in Actinide Science
Organized by Geraldine Barry and Roberto Caciuffo, Joint Research Center, European Commission

Translation of Mussel Adhesion to Beneficial New Concepts and Materials
Organized by Herbert Waite and Alison Butler, University of California, Santa Barbara

Watching Atoms Move: From Structures to Dynamics to Mesoscale Processes
Organized by Eric Stach, Brookhaven National Laboratory; Donald Baer, Pacific Northwest National Laboratory

Physical Sciences

Compressive Sensing: Sensing Sparse Phenomena in Theory and Practice
Organized by Mark Davenport, Georgia Institute of Technology; Emmanuel Candès, Stanford University

Exploring Other Worlds and Seeing Our Own Anew
Organized by Samuel P. Kounaves, Tufts University

How Fundamental Computing Research Touches Everyday Lives
Organized by Andrew Bernat and Erwin P. Gianchandani, Computing Research Association

Is Beauty Truth? Mathematics in Physics from Dirac to the Higgs Boson and Beyond
Organized by Thomas J. Kelleher, Basic Books

Mathematics of Tipping Points: Framework, Applications, and Prediction
Organized by Mary Silber, Northwestern University; Mary Lou Zeeman, Bowdoin College

Neutrinos: Nature's Smallest Surprises
Organized by Janet Conrad, Massachusetts Institute of Technology

Predictability: From Physical to Data Sciences
Organized by Albert-Laszlo Barabasi, Northeastern University

Predictive Model of the Internal Combustion Engine
Organized by Ahren Jasper and Nils Hansen, Sandia National Laboratories

The Beauty and Utility of Scientific Images
Organized by Kartik Sheth, National Radio Astronomy Observatory; Margaret Meixner, Space Telescope Science Institute

The Dark Matter of the Universe, Supersymmetry and Beyond
Organized by Maria Spiropulu, California Institute of Technology

The Higgs Boson: Past, Present, and Future
Organized by James Gillies, European Organization for Nuclear Research (CERN)

The Mirror World of Antiatoms and Antimolecules
Organized by Charles W. Clark, Joint Quantum Institute; Michael J. Brunger, Flinders University

Tiny But Mighty: Neutrinos and the New Frontiers of Science
Organized by Katie Yurkewicz, Fermi National Accelerator Laboratory

Understanding the Universe Through Images of the Cosmic Microwave Background
Organized by Asantha Cooray, University of California

What's Hot in Cold
Organized by Charles W. Clark, Joint Quantum Institute

Worldwide Progress Toward Fusion Energy
Organized by Ned R. Sauthoff, Oak Ridge National Laboratory

Public Policy

Advanced Manufacturing: Today, Tomorrow, and Beyond
Organized by Stephanie Shipp, Science and Technology Policy Institute

Can Exposure Science Quell the Furor over Environmental Endocrine Disruption?
Organized by Justin G. Teeguarden, Pacific Northwest National Laboratory

Capturing "Complicated Duality": Evaluating the Outcomes and Impacts of Science
Organized by Julia E. Melkers, Georgia Institute of Technology

Coal, Communities, Commerce, and China: A Nexus for the Sciences and Public Policy
Organized by Donna Gerardi Riordan, DGR Strategies

Convergence of Physical, Engineering, and Life Sciences: Next Innovation Economy
Organized by Larry A. Nagahara, National Cancer Institute

Effective Science for Community Adaptation to Climate Change
Organized by Thomas Webler, Social and Environmental Research Institute

Getting What We Pay For: Incentives, Peer Review, and Conservatism in Science
Organized by P. Kyle Stanford, University of California, Irvine

Predicting Major Events and Planning for Hazards: An Art or Science?
Organized by Julia Wilson, Sense About Science; Albert Yuan, *San Lian Life Weekly*

Promoting Collaborative, Policy-Relevant Science: Learning from Fulbright
Organized by Patrick Feng, University of Calgary; Walter E. Baethgen, Columbia University

Role of Science in the American Democracy: Roots, Tensions, and Paths Forward
Organized by Peter Frumhoff and Pallavi Phartiyal, Union of Concerned Scientists; James McCarthy, Harvard University

Tales of the Unexpected: How Science Advisers Manage Uncertainty
Organized by Geraldine Barry, Joint Research Center, European Commission

The Beauty, Benefits, and Challenges of Transformative Research
Organized by Bhavya Lal, Science and Technology Policy Institute; Edward J. Hackett, Arizona State University

The Science of Politics
Organized by Barbara Jasny, AAAS/*Science*; David Lazer, Northeastern University

Toward Bridging the Duality of Science: Seed-Push, Issue-Driven, or "Encounter"?
Organized by Tateo Arimoto, National Graduate School for Policy Studies, Japan; Chikako Maeda, Japan Science and Technology Agency; Yuko Harayama, Organization for Economic Cooperation and Development

Understanding and Communicating Uncertainty in Climate Change Science
Organized by Richard L. Smith, University of North Carolina

Sustainability and Resource Management

From Promise to Proof: How Ecosystem Service Science Is Transforming Real Decisions
Organized by Karen L. McLeod and Erica Goldman, COMPASS; Heather Tallis, The Natural Capital Project

Getting to Global Ecological Sustainability: Climate and Small-Planet Ethics
Organized by Kai Ming A. Chan and Paige Olmsted, University of British Columbia

Global Health and Environmental Impacts of E-Waste Recycling
Organized by Erica L. Dahl, SafeBridge Consultants Inc.; Bruce A. Fowler, ICF International

Is the Future of Conservation at a Crossroads?
Organized by Jennifer Howard, AAAS Science and Technology Policy Fellow, NOAA; Colin F. Quinn, NOAA

Socio-Hydrology: Co-Evolution and Future of Human-Water Resource Systems
Organized by Veena Srinivasan, Pacific Institute

Sustainable Chemical Manufacturing in a Resource-Limited World
Organized by Susannah Scott, University of California, Santa Barbara

Water Purification and Monitoring Under Minimal Resource Setting
Organized by Sushanta Mitra and Thomas Thundat, University of Alberta, Edmonton; Ni-Bin Chang, University of Central Florida

What Are the Roles of Knowledge Institutions in Sustainability?
Organized by David D. Hart, University of Maine; Lewis Gilbert, University of Minnesota, Saint Paul; Margaret A. Palmer, National Socio-Environmental Synthesis Center

What Is Science's Role in Developing Aquaculture as a Sustainable Use of the Ocean?
Organized by Paul A. Sandifer, NOAA; Barry Costa-Pierce, University of New England; Michael Rust, NOAA

AAAS 2013 ANNUAL MEETING

14-18 FEBRUARY • BOSTON

THE BEAUTY AND BENEFITS OF SCIENCE

HYNES CONVENTION CENTER

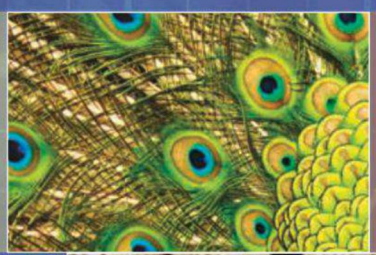
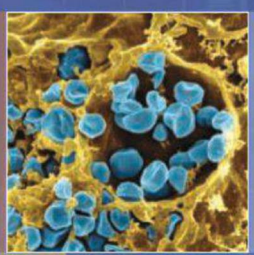


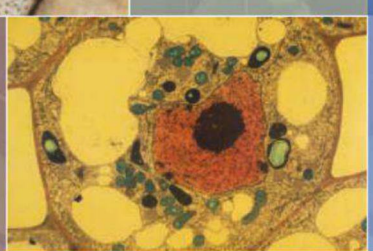
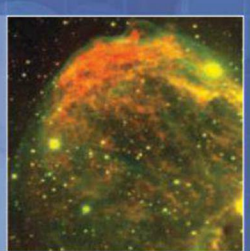

Connect with Us

www.aaas.org/meetings

@AAASMeetings, #AAASmtg

facebook.com/AAAS.Science

AAAS, publisher of *Science*, thanks the sponsors and supporters of the 2013 Annual Meeting

SUBARU

NSF

European Commission

ACS Chemistry for Life®
American Chemical Society

HELMHOLTZ ASSOCIATION

Canada

janssen
PHARMACEUTICAL COMPANIES OF Johnson & Johnson

AAAS thanks

THE KAVLI FOUNDATION

for its generous support of the Science Journalism Awards

This is Your Brain: Mapping the Connectome

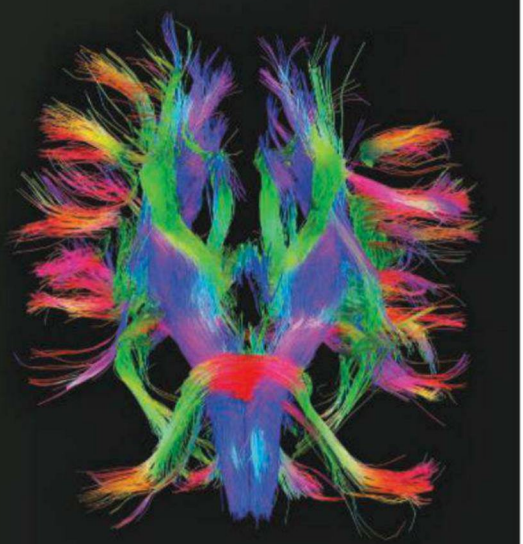

It's been 20 years since Francis Crick and Edward Jones, in the midst of the so-called Decade of the Brain, lamented science's lack of even a basic understanding of human neuroanatomy. "Clearly what is needed for a modern human brain anatomy is the introduction of some radically new techniques," the pair wrote in 1993. Clearly, researchers were listening. Today, they are using novel technologies and automation to map neural circuitry with unparalleled resolution and completeness. The NIH has dedicated nearly $40 million to chart the wiring of the human brain, and the Allen Brain Institute has poured in millions more to map the mouse brain. The data will take years to compile, and even longer to understand. But the results may reveal nothing less than the nature of human individuality. As MIT neuroscientist Sebastian Seung writes, "You are more than your genes. You are your connectome."

By Jeffrey M. Perkel

When Seung says in *Connectome: How the Brain's Wiring Makes Us Who We Are*, "You are your connectome," what he means is that neural connectivity is like a fingerprint. Each person has their own unique blend of genetics, environmental influences, and life experience. Those factors influence the detailed circuitry of the brain, such that even identical twins likely differ at the level of neural connectivity.

By mapping those connections, researchers hope to understand the normal variability of human connectomes and how they change and rewrite themselves as humans learn, mature, and age. They can begin to probe how connectomes become dysfunctional in traumatic brain injury or neurodegenerative disorders, or in patients with, say, schizophrenia or autism—conditions that Seung terms "connectopathies."

Yet the very scale of the problem is daunting. Only one connectome has been mapped to completion, and that was the roundworm, *Caenorhabditis elegans*. *C. elegans* contains just 300 neurons joined by 7,000 connections, yet charting its neural connectivity took more than a decade to complete. "Your connectome is 100 billion times larger [than *C. elegans*], with a million times more connections than your genome has letters," Seung writes. "Genomes are child's play compared with connectomes."

Nevertheless, researchers are making a stab at the problem. From the so-called macroscale of magnetic resonance imaging, to the microscale of electron microscopy, the connectome is slowly coming into focus, one synapse at a time.

The Human Connectome Project

When thinking about the connectome, says Hongkui Zeng, senior director of research science at the **Allen Institute for Brain Science,** think Google Maps. Neuroscientists would like to navigate the brain in virtual space as modern travelers do on the Internet: by zooming in and out and panning at will, from entire brain regions down to individual cells and synapses. In this metaphor, says Zeng, macroscopic MRI efforts reveal only neural superhighways. Still, she says, that can be useful, providing "an overview of the global sense of how regions are connected to each other, and how the world is organized."

That goal lies at the heart of the **Human Connectome Project** (HCP), a $40 million NIH effort launched in September 2010 to map the wiring of the live human brain. Two research consortia were funded under the HCP, with $30 million going to Washington University in St. Louis and the University of Minnesota, and $8.5 million to Massachusetts General Hospital (MGH) and the University of California, Los Angeles (UCLA).

While both teams are pursuing technology development, the WashU/Minnesota team also focuses on production, pushing 1,200

"You are more than your genes. You are your connectome."

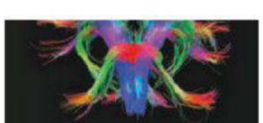

Upcoming Features

Genomics—February 15
Proteomics—March 1
Fluorescence Multiplexing—April 12

CREDIT: IMAGE PROVIDED COURTESY OF THE LABORATORY OF NEURO IMAGING AT UCLA, ARTHUR W TOGA, DIRECTOR; RENDERING BY CARLOS MENA. www.humanconnectomeproject.org

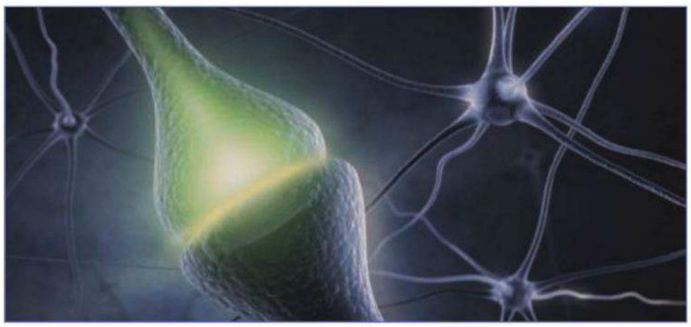

normal adults—400 sets of twins and their non-twin siblings—through a series of behavioral, genetic, and imaging scans to produce a reference against which other connectomes may be compared.

Both consortia employ magnetic resonance imaging of one form or another. At WashU, subjects are scanned for anatomic features and functional connectivity (i.e., regions linked by common purpose). To map physical connections, the consortia use diffusion MRI, a form of imaging that tracks the motion of water molecules as a marker of axonal fiber orientation. "Water molecules move more rapidly parallel to fibers than perpendicular to fibers," explains Van Wedeen, who heads the MGH team.

Wedeen invented and uses one form of diffusion MRI, called diffusion spectrum imaging (DSI); the WashU and Minnesota teams use HARDI, or high-angular resolution diffusion imaging. In both cases, the idea is to divide the brain into thousands of volumetric pixels, or "voxels," each about one cubic millimeter in size, and calculate for each one the different directions in which water diffuses. Then, in a process called "tractography," or track tracing, those vectors are connected to produce brilliant multicolor images of cables, or "fiber tracks," snaking their way through the brain's white matter.

The result is a map not of individual axons but rather thousands of axons in aggregate. "These are just numerical integrals of differential equations," says Wedeen. "These are not microscopic images of fibers." Nevertheless, collecting even those relatively low-resolution data requires some souped-up hardware. A standard clinical MRI, Wedeen says, has a magnetic field strength of 3 Tesla (T) and a gradient strength of 40 mT/m. The WashU/Minnesota group is using a specially made **Siemens** 3T scanner with a gradient strength of 100 mT/m, while the MGH/UCLA team's "Connectome Scanner" sports a 300 mT/m gradient.

That increased gradient strength offers two benefits for connectivity mapping, Wedeen says. "You get both more signal and better signal," he says, just as a telescope with a larger mirror can peer deeper into space.

Kamil Ugurbil, director of the **Center for Magnetic Resonance Research at the University of Minnesota** and co-PI of the WashU/Minnesota consortium, says his team has seen "significant technological gains" with their new scanner—resolution has been increased two- to three-fold and some 30 subjects have already been scanned, each over a two-day period.

But Ugurbil is no longer working with the 100 mT/m 3T scanner, which was shipped to WashU for the project's "production" mode. He has taken possession of a new 7T scanner, also from Siemens, which should provide even sharper images, and is awaiting shipment of an even larger $10 million, 10.5T instrument. At the moment, though, that latter magnet is sitting untested on the floor of a factory, he says, thanks to a "worldwide shortage of liquid helium."

"To cool this huge magnet we need something like 40,000 L of liquid helium, and we can't get it."

Mapping Mesoscale Connections

The Allen Institute is mapping the mouse connectome at what Zeng calls the "mesoscopic" scale—a mapping strategy first articulated by **Cold Spring Harbor Laboratory** neuroscientist Partha Mitra and colleagues in 2009. To build that map, Zeng's team uses "serial two-photon tomography."

Mice are injected in discrete brain regions with a recombinant adeno-associated virus (AAV, supplied by **University of Pennsylvania Vector Core**) that expresses a fluorescent protein. The mice are subsequently sacrificed and their brains fixed and embedded in agarose. That block is then mounted inside a two-photon fluorescent microscope tricked out with an ultrafine cutting apparatus, or vibratome—a system that has been commercialized by **TissueVision.**

> **"To really show that there's a connection, I'd have to show you there is a synapse and there are neurotransmitters crossing that synapse."**

In this configuration, the top face of the block is fluorescently imaged at 0.35 μm lateral resolution, revealing the neuronal "arbors" traced out by the cells in whatever region was injected. Then the vibratome slices off the top 100 μm to reveal the next surface, and the process repeats.

"You image, cut, image, cut, image, cut," Zeng says. The entire process is automated, she explains, producing about 750 gigabytes of raw image data in about 18 hours—*per brain*. A complete dataset comprises approximately 500 injection points, and thus at least 500 brains, all of which must then be integrated and registered onto a three-dimensional template for comparison and navigation and to generate a detailed, brain-wide connectivity matrix.

Technically, says Zeng, the Allen Institute is not collecting a "connectome." Their virus is nonreplicative, meaning it can only infect cells once. It also cannot cross neural synapses. Therefore, she says, what her project is really imaging is a "projectome."

According to Zeng, data for most brain regions has already been collected, and some has been publicly released. (These data are freely navigable using the Institute's Brain Explorer software and freely downloadable via the Allen Connectivity Atlas data portal, www.brain-map.org.) Now she is going back and repeating the process with viruses that are specific to individual neural subtypes, to understand, for instance, how projectomes of excitatory and inhibitory neurons differ.

At the Cold Spring Harbor Laboratory, Mitra is pursuing a similar strategy. He injects each of 262 grid points on each mouse brain, but does so using four tracers—two "anterograde" and two "retrograde." That's about 1,000 mouse brains per dataset.

Anterograde tracers, like AAV and biotinylated dextran (obtained from **Life Technologies**), penetrate the cell body and then "piggyback on anterograde transport mechanisms that carry molecules away from the [cell body] along the axon to the [synaptic] terminals," Mitra explains. Retrograde tracers like cholera toxin (obtained from continued>

Featured Participants

Allen Institute for Brain Science
www.alleninstitute.org

Carl Zeiss International
www.zeiss.com

Center for Magnetic Resonance Research, UMinn
www.cmrr.umn.edu/index.shtml

Cold Spring Harbor Laboratory
www.cshl.edu

FEI
www.fei.com

Gatan
www.gatan.com

Hamamatsu
www.hamamatsu.com

Human Connectome Project
www.humanconnectomeproject.org

Human Connectome Project (WashU/UMinn)
humanconnectome.org

JEOL
www.jeol.com

Life Technologies
www.lifetechnologies.com

List Biological Laboratories
www.listlabs.com

Siemens
www.medical.siemens.com

TissueVision
www.tissuevision.com

University of Pennsylvania Vector Core
www.med.upenn.edu/gtp/vectorcore

List Biological Laboratories) and rabies viruses (Duke University Viral Vector Core), enter cells via synapses, travel up axonal arbors to the cell body, and do actually provide some long-range connectivity information, Mitra says.

Mitra images each mouse brain (manually cryosectioned into 20 µm sections spaced 40 µm apart) on a **Hamamatsu** Nanozoomer 2.0 automated slide scanning fluorescence microscope. When reconstructed, the resulting dataset contains a trillion voxels measuring half a micron on a side. Those are just one-billionth the size of a diffusion MRI voxel. At one terabyte per injection site, he says, his lab has collected nearly a petabyte of information, some of which was released in June (www.brainarchitecture.org).

To The Microscale

Dense as mesoscale information is, it doesn't actually reveal synaptic connections. "If one is going to be a purist about this, we are not mapping connections per se," says Mitra. "To really show that there's a connection, I'd have to show you there is a synapse and there are neurotransmitters crossing that synapse."

Such information certainly isn't available on the mesoscale. But it is at least partially observable on the microscale. In Zeng's Google Maps analogy, this is like viewing the driveways and walkways leading into individual houses. The tool for seeing those details is electron microscopy.

At Harvard University, for instance, neuroscientist Jeff Lichtman embeds pieces of thalamus measuring just 400 x 400 x 250 µm in plastic ("That's not even one fMRI voxel," he notes), and sections them into 9,000 ultrathin slices on a home-built instrument, basically a deli-slicer, called an automatic tape-collecting ultramicrotome. Each slice is attached to a moving strip of tape as it emerges from the blockface, producing something like an old movie film reel of brain slices. That tape is then fed into a scanning electron microscope (Lichtman has instruments from Zeiss, **FEI,** and **JEOL**), which images each section one by one like a movie projector.

According to Lichtman, sections are imaged at 4 nm resolution in 16 tiles of 25,000 x 25,000 pixels each, collected at 20 megapixels per second. The process generates a terabyte of image data per day, 24/7, for 100 days, Lichtman says.

The goal, he says, is to map the organization of retinal ganglion cells in the thalamus. "We will get a good sense of the way that first stage of central processing of retinal information is organized from this dataset."

Lichtman recently acquired a new EM that collects data at twice the current speed, 40 megapixels per second. Yet even at that rate it is wholly impractical to map an entire human brain at this nanoscale resolution, both for reasons of data management—a single cubic millimeter is about 1,000 terabytes—and of time; even at 40 megapixels per second, it would still take years to image just a cubic millimeter.

A next generation instrument, though, could help. **Zeiss** is developing a new automated EM, Lichtman says, that will image sections with 61 electron beams at once (current machines use only one), speeding data acquisition up some 60-fold; he hopes to receive a prototype of this new device within a few years.

But collecting the data is only half the battle, says Moritz Helmstaedter of the **Max-Planck Institute of Neurobiology** in Martinsried, Germany; data analysis is the other.

As a postdoc, Helmstaedter worked with Winfried Denk at the Max-Planck Institute in Heidelberg. There Helmstaedter, with postdoc Kevin Briggman, used serial blockface electron microscopy (SBEM)—in which a piece of plastic-embedded brain is imaged and cut, imaged and cut, much as the Allen Institute does but on a nanometer scale—to image a piece of retinal tissue comprising about 1,000 neurons.

According to Helmstaedter, the SBEM-enabled scanning EM ran continuously for some eight weeks straight, collecting 13,000 images, each 2.5 gigapixels in size. (Both Zeiss and FEI EMs were used with a custom microtome; a complete system called 3View is now available from **Gatan**.) But it took more than two years to reconstruct the resulting neuronal circuits.

Helmstaedter's solution to that problem borrows from the crowd-sourced protein-folding game, FoldIt. His team trains computers to assemble the images to trace neurites. But to ensure accuracy, they have hired some 200 undergraduates, at $10/hour, to sit in front of a computer and navigate through the computed neurite forest by essentially "flying through the data" as if with a flight simulator. These students helped validate much of a 900-neuron retinal connectome, Helmstaedter says.

Now Helmstaedter is upping the ante with a piece of neocortex 500 µm on a side, containing some 10,000 neurons. For that, they'll need an even wider hive-mind, which they hope to tap using an in-development game version of their application for use on mobile devices.

In connectomics, says Helmstaedter, the bottleneck is network reconstruction. "We have to take these extreme measures to get it done."

Radical new techniques, indeed.

Jeffrey M. Perkel is a freelance science writer based in Pocatello, Idaho.

DOI: 10.1126/science.opms.p1300071

FLUORESCENCE MICROSCOPY SOFTWARE

The powerful research microscopy software LAS AF 3 (Leica Application Suite Advanced Fluorescence) sets new standards for intuitive operation. It covers the whole spectrum of fluorescence applications from routine work to sophisticated tasks in biomedical research, such as deep imaging of thicker tissue or interactive time lapse experiments. A key feature of the LAS AF 3 is its modern user interface, optimized for fluorescence imaging. It reduces stray light from the computer screen disturbing light-sensitive experiments. The wizard-based interface guides users safely and intuitively through data recording and evaluation. LAS AF 3 offers full control over the microscope hardware while minimizing user interaction through intelligent automation. The wide range of tools for image processing, deconvolution, and 3-D visualization enables the user to capture and process all the important details of the sample without the need for additional software.

LEICA MICROSYSTEMS
For info: 800-248-0123 | www.leica-microsystems.com

FLUORESCENCE SLIDE SCANNING

Olympus VS120 Slide Scanning System has advanced technology that creates a "virtual slide," a high-resolution image of the complete specimen that can be electronically stored on a central server, at a range of magnifications. Exhibiting unsurpassed performance in fluorescence microscopy, combined with precise color rendition and scanning accuracy, the Olympus VS120 is the perfect system for all pathology and life science research applications requiring slide scanning and data archiving. Color fidelity and precision are of paramount importance for all pathology and life-science applications where analysis may depend on both structural and color interpretation. Resolving maximum detail when scanning at high resolution depends on precision scanning to capture multiple images with the upmost positional accuracy, combined with advanced software algorithms to 'stitch' the images together to form a reliable panorama. The VS120 excels at this aspect of hardware and software interaction, scanning without distortion at high resolution, while faithfully interpreting the color standard.

OLYMPUS
For info: +49-40-23773-5913 | www.microscopy.olympus.eu

NEURON ISOLATION KIT

The Neuron Isolation Kit, mouse, depletes all non-neuronal cells so that "untouched neurons" remain. The Neuron Isolation Kit, mouse, is an indirect magnetic labeling system for the isolation of untouched neurons from cell suspensions of mouse neural tissue. Non-neuronal cells—including astrocytes, oligodendrocytes, microglia, endothelial cells, and fibroblasts (except erythrocytes)—are indirectly magnetically labeled using biotin-conjugated antibodies specific for non-neuronal cells in combination with Anti-Biotin MicroBeads. Isolation of highly pure unlabeled neuronal cells is achieved by depletion of the magnetically labeled cells. The cell number and composition of the neuronal cell fraction differs according to the mouse age and the brain region used for cell isolation.

MILTENYI BIOTEC
For info: 617-218-0030 | www.miltenyibiotec.com

NEURONAL MORPHOLOGY SOFTWARE

Version 2.5 of the MetaMorph NX Software includes modules for the study of neuronal morphology and fiber structures, support for targeted illumination devices, and a high-speed image acquisition mode. The Neurite Tracing Application Module simplifies the challenging, meticulous tasks associated with neuron research, while the FiberTracing Application Module quickly makes sense of complex, interwoven fiber structures. Moreover, added support for targeted illumination devices enables fast synchronization with regions of interest or an exact position in the image, and the new high-speed image acquisition mode allows researchers to record unlimited numbers of rapid changes in cellular function and behavior. The new software provides a single tool for researchers to use images of any size to rapidly produce quantitative and comparative descriptions of neuronal anatomy. The built-in Sholl Analysis, dendritic spine measurements, and nuclei detection features further add to the ability to conduct a thorough investigation of neurites.

MOLECULAR DEVICES
For info: 800-635-5577 | www.moleculardevices.com

NEURITE OUTGROWTH STAINING KIT

The Molecular Probes Neurite Outgrowth Staining Kit allows for quick and simple measurement of neurite outgrowth and cell viability in the same sample. It includes three fluorescent dyes: a cell viability indicator, a cell membrane stain, and a background suppression reagent. The Neurite Outgrowth Staining Kit saves time and steps relative to immunostaining. A typical workflow using this kit takes 15–30 minutes and involves only two media-exchange steps prior to taking a measurement. In contrast, immunostaining involves multiple block, wash, and antibody incubation steps that require several hours to complete. The Neurite Outgrowth Staining Kit distinguishes between compound effects on cell viability and neurite outgrowth by providing dual color readout. The fluorescence signals generated with the Neurite Outgrowth Staining Kit can be measured with a fluorescence microplate reader, microscope, or HCS instrument for compatibility with your existing workflow.

LIFETECHNOLOGIES
For info: 800-955-6288 | www.lifetechnologies.com

Science Careers Advertising

For full advertising details, go to ScienceCareers.org and click For Employers, or call one of our representatives.

Tracy Holmes
Worldwide Associate Director
Science Careers
Phone: +44 (0) 1223 326525

THE AMERICAS

E-mail: advertise@sciencecareers.org
Fax: 202-289-6742

Tina Burks
East Coast/West Coast/South America
Phone: 202-326-6577

Allyson Rosen
Midwest/Canada/Corporate
Phone: 202-326-6578

Marci Gallun
Sales Administrator
Phone: 202-326-6582

Online Job Posting Questions
Phone: 202-312-6375

EUROPE & REST OF WORLD

E-mail: ads@science-int.co.uk
Fax: +44 (0) 1223 326532

Lucy Nelson
Phone: +44 (0)1223 326527

Kelly Grace
Phone: +44 (0) 1223 326528

JAPAN

Yuri Kobayashi
Phone: +81-50-3696-5100
E-mail: ykobayas@aaas.org

CHINA & TAIWAN

Ruolei Wu
Phone: +86-1367-1015-294
E-mail: rwu@aaas.org

STANFORD
MATERIALS SCIENCE AND ENGINEERING

The Department of Materials Science and Engineering (MSE) at Stanford University invites applications for a tenure-track position at the Assistant Professor level. Under special circumstances involving exceptional academic merit, candidates at the untenured Associate Professor level may be considered. We seek applicants with significant accomplishments in materials research in its broadest sense that may include materials characterization involving structure characterization, characterization through property measurement (e.g. nano-mechanics, nano-electronics), theoretical modeling, etc. Stanford University has excellent facilities in these areas as represented by the Stanford Nanocharacterization Laboratory (SNL), the Molecular Imaging Program at Stanford (MIPS), the Stanford Nano Center (SNC), the Stanford Nanofabrication Facility (SNF), the Center for Biomedical Imaging at Stanford (CBIS) and the X-ray facilities at the Stanford Linear Accelerator Center (SLAC). The successful candidate is expected to play a major role at one of these facilities.

The successful candidate is also expected to make major contributions to large scale multidisciplinary research and to contribute significantly to leadership in Stanford's nanoscience and technology efforts which span several Departments and Schools, including faculty in the Schools of Engineering, Medicine, and Humanities and Sciences. We are looking for a motivated individual who is committed to excellence in teaching and to the mentoring of students in multidisciplinary materials research applied to energy and the environment, biomedical research and imaging, nano-mechanical or nano-electronic properties and devices, etc.

Applicants should include a summary of their educational and professional backgrounds, a current list of published work, and the names of at least three referees who may be consulted by the search committee. An indication of how the candidate's experience matches the position described above should also be given. Applicants are encouraged to write brief descriptions of their plans for future research and how those plans might be realized in a Stanford setting, as well as to submit similar statements on teaching, focusing especially on their vision of teaching to students in the Department of Materials Science and Engineering. The appointment is expected to be made during the forthcoming academic year. Please apply online at: **http://mse.stanford.edu/faculty/faculty_search.html**. Applications should be submitted by **March 31, 2013**. Questions should be directed to, **Search Committee Chair, c/o Carol Scott**, via electronic mail to **msesearch@stanford.edu**. **Professor Robert Sinclair, Chair, Department of Materials Science and Engineering, Stanford University, Stanford, CA 94305-4034; Phone: (650) 723-1102; Fax: (650) 725-4034; Email: msesearch@stanford.edu**.

Stanford University is an Equal Opportunity Employer and is committed to increasing the diversity of its faculty. It welcomes nominations of and applications from women and members of minority groups, as well as from others who would bring additional dimensions to the university's research and teaching missions.

WASHINGTON STATE UNIVERSITY

Assistant/Associate/Full Professor of Neuroscience
Two positions available

In a strategic effort to enhance existing research in drug abuse/addiction, the Department of Integrative Physiology and Neuroscience (formerly VCAPP) at Washington State University on the Pullman campus seeks to fill two (2) full-time, tenure-track faculty positions in neuroscience at the rank of Assistant/Associate/Full Professor to begin July 2013. The positions are permanent 75% state funded 12-month appointments with summer funding available for the first two years. Required: Applicants must have one of the following degrees: a PhD in neuroscience or the biological science field, MD, or DVM degree and at least 2 years post-doctoral research experience before the date of hire.

Applicants for associate or full professor positions must provide evidence of an established independent research program (peer-reviewed publications and active extramural funding). The successful applicant will be expected to maintain an innovative, extramurally funded research program with a focus on the biological basis of drug addiction. This applicant is expected to provide academic leadership in the community of addiction/drug abuse researchers at WSU, which includes the Alcohol and Drug Abuse Research Program (ADARP) and the Translational Addiction Research Center (TARC).

Applicants for an assistant professor position should demonstrate potential to establish and maintain an externally-funded research program (peer-reviewed publications and developed research agenda). The successful applicant will be a molecular/cellular neurobiologist with an interest in addiction/drugs of abuse.

Teaching duties will include classroom instruction in the Neuroscience Program. The ability to support and mentor graduate students and serve on student, departmental, and college committees is expected.

Salary and rank are dependent upon qualifications. Generous start-up packages are available. Laboratory space will be assigned in a newly-built (completion March 2013) state-of-the-art research building specifically designed for neuroscience research. Ongoing departmental research interests include drug addiction, feeding and energy homeostasis, sleep and circadian rhythms, synaptic plasticity, neurodegenerative disease, and affective neuroscience.

Washington State University has a vibrant neuroscience community and is located in a region having a high quality of life for those who enjoy the outdoors, the arts, and the collegiality of diverse neighbors.

Screening of applications will begin **February 18, 2013**. The application **must** include the following: a cover letter which states what rank is being applied for, curriculum vitae, description of teaching experience and philosophy, summary of research interests and goals, and names and contact information (including email addresses) for three references. Applicants for Associate/Full Professor position should also include their leadership philosophy in managing a campus-wide research program. Applicants for **Associate/Full Professor** please follow this link: **www.wsujobs.com/applicants/Central?quickFind=57944**. Applicants for **Assistant Professor** please follow this link: **www.wsujobs.com/applicants/Central?quickFind=57943**. No paper submissions accepted. Direct questions to **kinslow@vetmed.wsu.edu**, **http://www.vetmed.wsu.edu/neuroscience/**. *EEO/AA*

60th Anniversary
DNA Double Helix
CSH Cold Spring Harbor Laboratory

From Base Pair to Body Plan

Thursday, February 28 to Sunday, March 3, 2013

Celebrating the 60th Anniversary of the Discovery of the DNA Structure

Organized by:

Alex Gann & Rob Martienssen
Cold Spring Harbor Laboratory

Speakers

Stephen Baylin
Helen Blau
Caroline Dean
John Doebley
Denis Duboule
Michael Elowitz
Elaine Fuchs
John Gurdon
Gregory Hannon
Edith Heard
Oliver Hobert
Brigid Hogan
Steven Jacobsen
Alexander Johnson
Robert Kingston
Ruth Lehmann
Michael Levine
Craig Mello
Christiane Nusslein-Volhard
Elaine Ostrander
Olivier Pourquie
Mark Ptashne
Gary Ruvkun
Ali Shilatifard
Robert Tjian
Richard Young
Kenneth Zaret

Special Guests

Michael Ashburner
Sydney Brenner
Wally Gilbert
Thomas Maniatis
Matthew Meselson
Walter Schaffner
Phillip Sharp
James Watson

Registration, abstract submission
and further information:
http://www.cshl.edu/meetings
email: meetings@cshl.edu
phone: 516-367-8346 fax: 516-367-8845

Image: *Tribal Flower* by Paulo Zerbato http://paulo-zerbato.artistwebsites.com

Poster Design: Catherine Dougherty

CEDARS-SINAI MEDICAL CENTER

Barbra Streisand Women's Heart Center – Endowed Chairs in Translational Biomedical Science

Cedars-Sinai Medical Center (CSMC), one of the nation's premier academic healthcare institutions, is seeking highly qualified Senior Scientists to join our Heart Institute faculty in the Barbra Streisand Women's Heart Center for our two newly Endowed Chairs:

1. Basic Translational Biomedical Science
2. Clinical Trials/Epidemiology/Outcomes Translational Biomedical Science

The successful candidates will have an exciting opportunity to work with a nationally recognized multi-disciplinary team focused on investigating women's heart disease, including sex and gender differences in basic, translational and clinical trials /epidemiology/outcomes research. A competitive research funding portfolio and strategic plan for existing and future internal and external funding is developed.

The successful candidate will be responsible for leading her/his own research laboratory, mentoring young scientists, contributing to the graduate program, and integrating research results into the larger clinical and basic science efforts focused around women's cardiovascular disease. There are many diverse research opportunities throughout the institution. These include expertise in animal models of atherosclerosis, proteomics and genomics, nanodrug delivery, animal and human imaging, stem cell therapy, secondary prevention, health services research and clinical trials. Because CSMC has the largest cardiovascular and heart transplant clinical volume on the west coast and is recognized for strong extramural funding, this position represents a unique opportunity for partnership between clinician-scientists and basic scientists. CSMC has a very collaborative research environment, outstanding research core facilities, and a commitment to mentoring junior basic science and clinical faculty.

Position requirements include:

- A Doctorate (PhD, MD or both) with a successful history as Principal Investigator of federal research grants in basic, translational, or clinical cardiovascular research.
- Associate or Professor level qualifications at an academic medical institution
- A research focus on cutting edge questions in basic, translational, epidemiology, clinical trials or outcomes research that preferably includes investigation of sex and gender differences relative to cardiovascular disease.
- Cedars-Sinai Medical Center is committed to excellence in compassionate patient care, medical education, research, and community programs. Competitive salary based on academic rank and experience. Relocation support will be provided.

Qualified candidates should send their CV's as well as names of three references to:
Dr. Noel Bairey Merz, c/o Academic.Recruiting@cshs.org

Cedars-Sinai Medical Center encourages and welcomes diversity in the workplace AA/EOE

MULTIPLE FACULTY POSITIONS AT THE SENIOR OR JUNIOR LEVEL

CENTER FOR COGNITION & SOCIALITY

ibs Institute for Basic Science

Center for Cognition & Sociality at the Institute for Basic Science, Daejeon, Korea, invites applications from outstanding candidates for multiple positions for tenured or tenure-track faculty.

Applicants for senior positions are expected to have established a strong research program on neural mechanisms of cognition and sociality in the mouse or primate system. Scientists utilizing integrative approaches will be appreciated with particular emphasis on mouse genetics, physiology, or computational neuroscience. Senior faculty may form and lead a research group that includes junior faculty.

Applicants for junior positions should show a proven record of outstanding research accomplishments in neuroscience. They are expected to develop a strong research program to connect the molecule to circuit to behavior.

The faculty will be provided with full funding of their research program, including full salary support, generous start-up funds and compensation package. Excellent opportunities are available for collaborative research as well as graduate student teaching under a collaborative program between IBS and the neighboring university, KAIST, the leading university in science and engineering.

Applications should be submitted by **February 28th, 2013**, and should include curriculum vitae, a statement of research accomplishments and future plans, and a list of potential referees. These materials should be sent to: <**jihye@ibs.re.kr**>

Hee-Sup Shin, Director
Center for Cognition & Sociality
Institute for Basic Science
Daejeon, Korea
http://brain.ibs.re.kr

SOOCHOW UNIVERSITY

Research Positions at Institute for Cardiovascular Science

The Institute of Cardiovascular Science at Soochow University in Suzhou, Jiangsu, China is seeking outstanding PIs in the field of basic and application research of cardiovascular diseases, including but not limited to, stem cells, transplantation immunity, genetics of cardiovascular diseases and cardiac electrophysiology. The newly established Institute has 5 research divisions and 2 centers with combined resources of cardiovascular surgery and medicine.

The candidates should have Doctoral degrees from well-known universities with at least 3 years' post-doctoral experience in related fields. The candidates are expected to have published influential papers in top international journals. Senior candidates should have successful track records with established research programs, outstanding achievements and external research funding. All candidates are expected to have a good command of oral and written English.

Successful applicants will be offered a package including sufficient lab space, start-up funding, relocation aid and competitive salaries commensurate with experience and achievements, in addition to other employee benefits.

Applicants should submit (i) a curriculum vitae with current research projects and future plans, (ii) 3 to 5 representative papers or book chapters, (iii) names and contact details of three referees to: **Mr. Weimin Yin, Institute for Cardiovascular Science of Soochow University, No. 1 Building, the South Campus of the 1st Affiliated Hospital of Soochow University, 708 Ren Ming Road, Suzhou 215000, China, Tel: +86 512-67780947. Email: ywm@suda.edu.cn**

Cold Spring Harbor Laboratory 2013 Meetings & Courses

Meetings

Meeting dates / abstracts due

From Base Pair to Body Plan – Celebrating 60 Years of DNA
February 28 - March 3 / December 14, 2012

Single Cell Analyses
March 6 - March 9 / January 4

Systems Biology: Networks
March 13 - March 16 / January 11

Computational Cell Biology: The Interplay between Models & Experimentation
March 19 - March 22 / January 11

RNA & Oligonucleotide Therapeutics
April 10 - April 13 / January 25

Synapses: From Molecules to Circuits & Behavior
April 16 - April 20 / February 1

Cancer Biology & Therapeutics
April 23 - April 27 / February 8

Telomeres & Telomerase
April 30 - May 4 / February 15

The Biology of Genomes
May 7 - May 11 / February 22

The Ubiquitin Family
May 14 - May 18 / March 1

Retroviruses
May 20 - May 25 / March 8

78th Symposium: Immunity & Tolerance
May 29 - June 3 / March 15

Wiring the Brain
July 18 - July 22 / May 3

Metabolic Signaling & Disease: From Cell to Organism
August 13 - August 17 / May 31

Eukaryotic mRNA Processing
August 20 - August 24 / June 7

Mechanisms of Eukaryotic Transcription
August 27 - August 31 / June 14

Behavior & Neurogenetics of Nonhuman Primates
September 6 - September 9 / June 21

Eukaryotic DNA Replication & Genome Maintenance
September 9 - September 13 / June 28

Microbial Pathogenesis & Host Response
September 17 - September 21 / July 8

Stem Cell Biology
September 24 - September 28 / July 12

Neurobiology of Drosophila
October 1 - October 5 / July 19

Cell Death
October 8 - October 12 / July 26

Genome Informatics
October 30 - November 2 / August 16

Cell Biology of Yeasts
November 5 - November 9 / August 23

Precision Medicine: Personal Genomes & Pharmacogenomics
November 13 - November 16 / August 30

Harnessing Immunity to Prevent & Treat Disease
November 20 - November 23 / September 6

Plant Genomes & Biotechnology: From Genes to Networks
December 4 - December 7 / September 20

Rat Genomics & Models
December 11 - December 14 / September 27

Courses

Course dates / applications due

Workshop on Leadership in Bioscience
February 22 - February 25 / January 11

Protein Purification & Characterization
April 3 - April 16 / January 31

Quantitative Imaging: From Cells to Molecules
April 3 - April 16 / January 31

Cell & Developmental Biology of Xenopus
April 5 - April 16 / January 31

Workshop on Autism Spectrum Disorders
June 5 - June 11 / March 15

Single Cell Analysis
June 5 - June 18 / March 15

Advanced Bacterial Genetics
June 5 - June 25 / March 15

Ion Channels & Synaptic Transmission
June 5 - June 25 / March 15

Mouse Development, Stem Cells & Cancer
June 5 - June 25 / March 15

Vision: A Platform for Linking Circuits, Perception & Behavior
June 12 - June 25 / March 15

Statistical Methods for Functional Genomics
June 21 - July 3 / March 15

Workshop on Pancreatic Cancer
June 26 - July 2 / March 15

Drosophila Neurobiology: Genes, Circuits & Behavior
June 28 - July 16 / March 15

Frontiers & Techniques in Plant Science
June 28 - July 18 / March 15

Advanced Techniques in Molecular Neuroscience
July 2 - July 18 / March 15

Proteomics
July 9 - July 24 / March 15

Biology & Disorders of Learning & Memory
July 20 - August 2 / March 15

Computational Cell Biology
July 23 - August 12 / March 15

Eukaryotic Gene Expression
July 23 - August 12 / March 15

Yeast Genetics & Genomics
July 23 - August 12 / March 15

Imaging Structure & Function in the Nervous System
July 24 - August 13 / March 15

Synthetic Biology
July 30 - August 12 / March 15

Cellular Biology of Addiction
August 6 - August 12 / April 15

Programming for Biology
October 14 - October 29 / July 15

X-Ray Methods in Structural Biology
October 14 - October 29 / June 15

Computational & Comparative Genomics
November 6 - November 12 / July 15

Antibody Engineering & Phage Display
November 6 - November 19 / July 15

Advanced Sequencing Technologies & Applications
November 12 - November 24 / July 15

The Genome Access Course
April 21-23, July 18-20, November 17-19

Cold Spring Harbor Laboratory
Meetings & Courses Program
1 Bungtown Road
Cold Spring Harbor, New York 11724
Phone: 516-367-8346
www.cshl.edu/meetings
meetings@cshl.edu

CSHL course on an evening sail.

NIH National Institute of Environmental Health Sciences

Staff Scientist in Molecular Genetics
Research Triangle Park, North Carolina

The Laboratory of Molecular Carcinogenesis of the Division of Intramural Research is seeking a Staff Scientist in the Mammalian Genome Group to join a state-of-the-art molecular genetics research laboratory focused on studying the genetics and epigenetics associated with environmental exposures. The group utilizes next-gen whole-genome experimental approaches, including massively parallel genome/exon sequencing, RNA-seq, and ChIP-seq approaches, to better understand the molecular basis of complex traits.

Qualifications of the ideal candidate will include a PhD, MD, MD/PhD or equivalent with at least 5 years of experience (post doctorate) successfully conducting basic research in a cutting-edge molecular genetics laboratory with a demonstrated track record of productivity through publication in the peer-reviewed literature. Promising candidates with less experience will also be considered. The successful candidate will have good personnel management skills and be supportive of collaborative research. Expertise with a broad range of techniques in molecular and stem cell biology would be highly desirable, including massively parallel DNA sequencing, transcriptome analysis, genomic and cDNA molecular cloning and characterization, and culturing/characterization of ES/iPS cells. Specific knowledge and experience with the Collaborative Cross/Diversity Outcross or similar resources would be beneficial.

To apply, submit a Curriculum Vitae, brief statement of research experience and interests, and the names and addresses (including e-mail addresses and phone numbers) of three references to dir-appls@niehs.nih.gov or the below mailing address **by March 15, 2013**. Review of applications will begin immediately and continue until the position is filled. Salary is commensurate with level of experience. For additional information about this position, contact Dr. Rick Woychik, Deputy Director, NIEHS (rick.woychik@nih.gov).

Ms. Emily Starnes (Vacancy Number DIR 13-02)
Intramural Program Specialist
National Institutes of Health
National Institute of Environmental Health Sciences
P.O. Box 12233, Maildrop A2-06
Research Triangle Park, NC 27709
Email: dir-appls@niehs.nih.gov

DHHS and NIH are Equal Opportunity Employers
We are dedicated to building a diverse community in our training and employment programs.

LSUHealth Shreveport

PROFESSOR AND CHAIR DEPARTMENT OF BIOCHEMISTRY AND MOLECULAR BIOLOGY

A search for a new Chair of the Department of Biochemistry and Molecular Biology at the LSU Health Sciences Center in Shreveport is underway. We are seeking a candidate of international stature (Ph.D., M.D., or M.D./Ph.D.) interested in leading an outstanding basic science department, and contributing to the scientific direction of the Feist-Weiller Cancer Center (**http://www.feistweiller.org**) or a proposed Center of Excellence in Cardiovascular Diseases and Sciences.

Applicants must possess a distinguished record of scientific research, extramural funding, administrative and leadership skills, and a commitment to education and academic excellence. The selected individual will have the opportunity to recruit faculty and shape the research focus of the department. Current areas of research interests of faculty within the Department of Biochemistry (**http://www.shrevebiochem.com**) and the Feist-Weiller Cancer Center fall into the traditional areas of transcription and translation, DNA repair, cell biology, genetics, enzymology, and protein chemistry with a focus on solving major problems related to human disease including cancer, neuroscience and diabetes. Current areas of research interests of faculty within the proposed Center of Excellence in Cardiovascular Diseases and Sciences include cerebrovascular, heart, and/or peripheral vascular diseases, including risk factors that may contribute to these diseases. The administrative responsibilities include the oversight of faculty recruitment, development, evaluation, promotion and retention; finance and budget; strategic planning; development and support of educational programs; and resource allocation.

The LSU Health Sciences Center in Shreveport is committed to providing the new Chair with major resources to support the highest level of research. We are looking for an individual that would excel in a challenging and rewarding leadership position, while maintaining a dynamic research program.

Interested individuals should e-mail their curriculum vitae, names and contact information of three references, and a two page narrative to address their qualifications to: **ShvFacultyRecruitment@lsuhsc.edu**. Review of applications will begin immediately and will continue until the position is filled.

LSU Health Shreveport respects diversity in the workplace and is an Equal Opportunity Employer.

TEXAS TECH UNIVERSITY

Structural Biology: Biological NMR Spectroscopy

The Department of Chemistry and Biochemistry invites applications for a faculty member (open rank) in the area of **Biological NMR Spectroscopy**. We are especially interested in applicants whose research programs will complement existing areas of strength at TTU, such as structure, function and dynamics of membrane proteins, biomolecules involved in cancer, and plant proteins. However, all qualified candidates are encouraged to apply. The successful candidate for this position will be part of a major new **Structural Biology** initiative at TTU that includes a commitment to the acquisition of 600 MHz and 800 MHz NMR instruments and hiring two additional biological NMR spectroscopy faculty. Evidence of generating (junior rank) or maintaining (senior rank) a well-funded research program and a demonstrated commitment to excellence in teaching and service are essential. The Department of Chemistry and Biochemistry is among the top academic units at Texas Tech University, in terms of research funding, publications and graduate education. Texas Tech University is classified as a doctoral research-extensive university by the Carnegie Foundation; it has an enrollment of more than 32,000 students, and is one of the major, state-supported, multidisciplinary universities of the Southwest. A School of Medicine is located on the main campus in Lubbock.

All applications must be submitted online. Online faculty application for **requisition number 85807** can be found at **http://jobs.texastech.edu**. Applications must include a curriculum vitae, statement of proposed research and teaching philosophy. Applicants at the Assistant or Associate Professor level must also arrange to have three confidential letters of recommendation sent on their behalf to the chair of the search committee, **Dr. Joachim Weber, Department of Chemistry and Biochemistry, Texas Tech University, Box 41061, Lubbock, TX 79409-1061 (joachim.weber@ttu.edu)**. Evaluation of applications will start on **February 1, 2013**, and continue until the position is filled.

Texas Tech University is an Affirmative Action/Equal Opportunity Employer, committed to excellence through diversity. Texas Tech welcomes applications from minorities, women, veterans, persons with disabilities, dual-career couples, and all qualified persons.

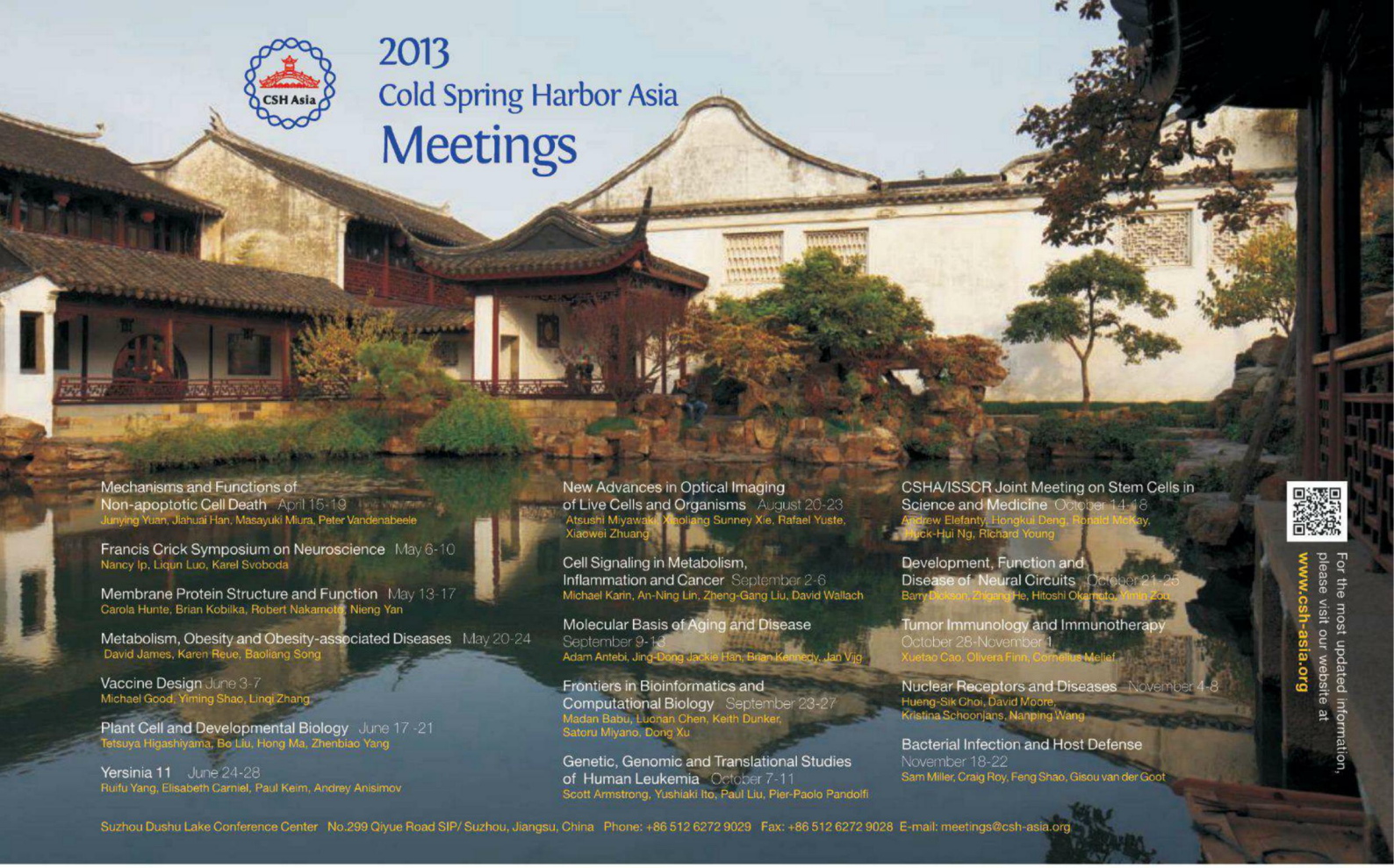

AWARDS

Fundación BBVA

The **BBVA Foundation Frontiers of Knowledge Awards** recognize and encourage fundamental advances in basic and applied research, as materialized in models and theories for understanding the natural and social worlds, technological innovations of broad impact and salient contributions to the creation, performance and conducting of the classical music of our time. Honors also go to outstanding contributions that advance understanding or deliver material progress with regard to two key challenges of the global society of the 21st century, climate change and development cooperation.

The **BBVA Foundation Frontiers of Knowledge Awards** are undertaken in collaboration with the **Spanish National Research Council (CSIC)**.

BBVA Foundation

Plaza de San Nicolás, 4
48005 Bilbao, Spain

Paseo de Recoletos, 10
28001 Madrid, Spain

www.fbbva.es

With the collaboration of

CSIC
CONSEJO SUPERIOR DE INVESTIGACIONES CIENTÍFICAS

Categories

- Basic Sciences (Physics, Chemistry, Mathematics)
- Biomedicine
- Ecology and Conservation Biology
- Climate Change
- Information and Communication Technologies
- Economics, Finance and Management
- Development Cooperation
- Contemporary Music

Nominations

Nominations are invited from scientific and artistic societies, R&D centers, university and hospital departments, conservatories of music, orchestras, public agencies, and organizations working in the climate change and development areas, as well as other organizations and natural persons specified in the award conditions.

Deadline for submission

Nominations are open from January 1 through to July 1, 2013 at 23:00 GMT.

For more details and full entry conditions: www.fbbva.es/awards · awards-info@fbbva.es

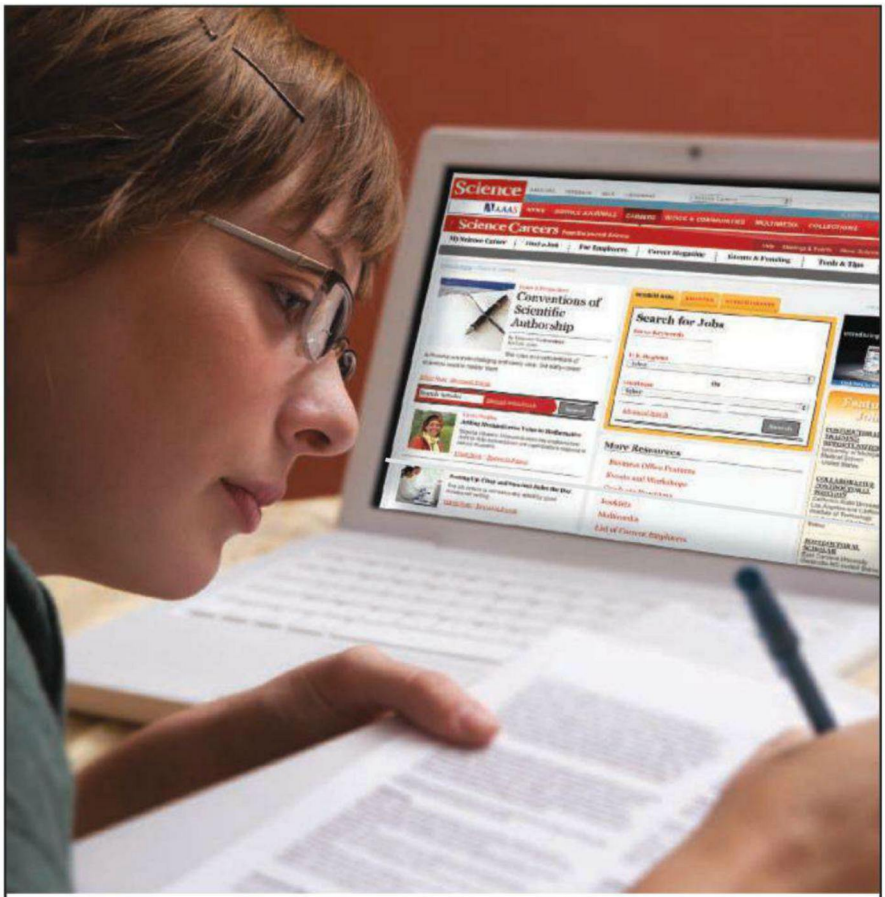

AAAS is here –
helping scientists achieve career success.

Every month, over 400,000 students and scientists visit ScienceCareers.org in search of the information, advice, and opportunities they need to take the next step in their careers.

A complete career resource, free to the public, *Science* Careers offers a suite of tools and services developed specifically for scientists. With hundreds of career development articles, webinars and downloadable booklets filled with practical advice, a community forum providing answers to career questions, and thousands of job listings in academia, government, and industry, *Science* Careers has helped countless individuals prepare themselves for successful careers.

As a AAAS member, your dues help AAAS make this service freely available to the scientific community. If you're not a member, join us. Together we can make a difference.

To learn more, visit
aaas.org/plusyou/sciencecareers

AAAS + U = Δ

Columbia University Medical Center
College of Physicians and Surgeons

Child Neurologist

The Department of Neurology at Columbia University and New York-Presbyterian Hospital announce the recruitment of a board certified Child Neurologist to help expand outpatient clinical activities and develop a Child Headache practice in the Division of Child Neurology. Protected research time and appropriate resource support will be provided.

M.D. and board certified in Neurology. Faculty rank is expected to be at the Assistant, Associate or Professor level, commensurate with experience and achievement. External research funding is preferred.

Qualified candidates should submit a letter of interest and curriculum vitae via the following link:

https://academicjobs.columbia.edu /applicants/Central?quickFind=57228

Columbia University is an affirmative action/equal opportuniaty employer.

CAREER TRENDS Running Your Lab

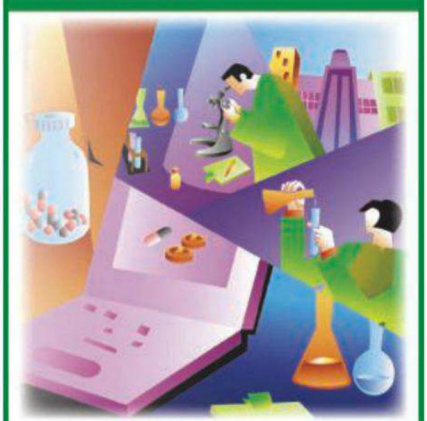

Download your free copy today at ScienceCareers.org/booklets

Science Careers
From the journal *Science* AAAS

Brought to you by the AAAS/*Science* Business Office

SANTA FE INSTITUTE
Resident Faculty Search
Call for Nominations and Applications

The **Santa Fe Institute** (SFI) seeks nominations and applications for resident faculty positions at all academic levels. Full-time appointments are of highest priority. We are also seeking sabbatical visitors.

SFI is a unique, internationally renowned research environment dedicated to investigating fundamental scientific questions that transcend traditional disciplinary boundaries. Much SFI research involves the science of complex adaptive systems. As such, we are open to applicants with an interdisciplinary focus from all scientific fields, with a preference for quantitative approaches.

The Institute serves as a research hub populated by 20-50 researchers in residence, including faculty, postdoctoral fellows, graduate students, and visitors, closely integrated with a large off-campus network of external faculty, researchers, and corporate affiliates.

We seek individuals with outstanding academic credentials in their own fields, who are also broad thinkers, are creative, catalytic, and risk-taking, and who are looking to break new ground in addressing some of science and society's most challenging problems.

Resident faculty positions at SFI are based on 5-year terms, with the potential for one renewal. SFI does not have laboratory space, although faculty are welcome to collaborate with researchers at other institutions with such facilities. Positions involve no formal teaching and come with funds for travel, visitors, meetings, and non-laboratory equipment. Participation in proposal development and Institute activities is expected.

Candidates should have a Ph.D. with a strong record of excellence, both in depth and breadth. Applications are welcome from candidates in any country. Successful foreign applicants must acquire an acceptable visa as a condition of employment. The Santa Fe Institute is an equal opportunity employer. Women and members of underrepresented groups are especially encouraged to apply.

APPLICATION REQUIREMENT: The closing date for this call is 3/15/2013. All application materials should be submitted electronically according to the instructions on the SFI Website: **www.santafe.edu/about/jobs/**

For further information *or assistance*, e-mail:
residentfacultysearch@santafe.edu

SANTA FE INSTITUTE

MANCHESTER 1824
The University of Manchester

Faculty of Life Sciences

The Healing Foundation Centre

Chair in Skin Repair and Regeneration

Salary will be commensurate with experience on the Professorial Salary Scale **Ref: LSX-02209**

The University of Manchester seeks to appoint an internationally renowned clinical translational scientist as Chair in Skin Repair and Regeneration within The Healing Foundation Centre for Tissue Regeneration. The post will be held within the Faculty of Life Sciences (FLS), with strong translational links with the Faculty of Medical and Human Sciences (FMHS). This appointment is an unrivalled opportunity to build on the outstanding potential in Manchester to translate basic discoveries towards skin regeneration, and to make a real difference to regenerative medicine and to delivering improved healthcare.

The successful individual, who is likely to be clinically and scientifically qualified, will lead the clinical translational activities of The Healing Foundation Centre for Tissue Regeneration within FLS. You will direct your own world class research programme in the area of wound healing and skin repair, develop cross-Faculty collaborations with scientists and clinicians, build on Manchester's internationally leading strengths in developmental, cell-extracellular matrix, stem/progenitor cell and inflammation biology, and provide leadership in wound repair and its translation into clinical medicine.

Informal enquiries can be made to Professor Cay Kielty. Email Cay.Kielty@manchester.ac.uk

For further information and to apply, please visit our website.

If you are unable to apply online, please request an application form by emailing hrrecruitment@manchester.ac.uk

Closing date: 20 February 2013.
Please quote reference number.

The University of Manchester values a diverse workforce and welcomes applications from all sections of the community

www.manchester.ac.uk/jobs

POSITIONS OPEN

Wake Forest™ School of Medicine

The Department of Neurobiology and Anatomy at Wake Forest Medical School Announces Open Positions for POSTDOCTORAL TRAINING in Multisensory Processes

We seek strong candidates for postdoctoral training funded by an NIH T32 Training Grant. The training program provides a rich collaborative research environment that fosters interdisciplinary approaches to understanding how the brain integrates information from multiple senses to produce perception and adaptive behavior. Candidates with direct experience as well as those in related fields are encouraged to apply. Trainees will have access to any of 10 laboratories using human subjects and/or a variety of animal models (rodents-primates) with approaches spanning molecular/cellular to perceptual/behavioral. Fellowships are awarded on a competitive basis.

Applications including a current curriculum vitae or nominations should be sent to the Training Grant Director **Dr. Barry E. Stein** (**e-mail: bestein@wakehealth.edu**), or to its co-directors: **Dr. Terrence R. Stanford** (**e-mail: stanford@wakehealth.edu**) and **Dr. Dwayne Godwin** (**e-mail: dgodwin@wakehealth.edu**). A description of the faculty and the program can be accessed via the **website: http://graduate.wfu.edu/admissions/training_ms.html.**

Wake Forest School of Medicine is an Affirmative Action/Equal Opportunity Employer and especially encourages applications from women and minority candidates.

NMR SPECTROSCOPIST

Indiana University is seeking qualified candidates for a position of NMR Spectroscopist. The rank of this position will be commensurate with qualifications and experience. This individual will assist the NMR Facility Director to oversee the function and maintenance of all instrumentation and equipment in the NMR Facility (seven NMR spectrometers from 200 to 800 MHz; **website: http://nmr.chem.indiana.edu**). Major responsibilities include providing support and training on the operation of NMR instrumentation to users, regular services and troubleshooting of NMR spectrometers, as well as maintenance of the Facility's website. The successful candidate will have a M.S. with four years of experience in NMR or a Ph.D. with specialization in NMR spectroscopy, comprehensive knowledge of NMR hardware and software, and excellent communication skills. Demonstrated experience with the operation and maintenance of high-resolution NMR spectrometers and the use of Unix/Linux operating system is required. Solid-state NMR experience is desirable but not required. Experience in Unix/Linux administration and scripting language programming is also desirable. Applicants should submit a curriculum vitae, and arrange for three letters of recommendation to be sent to: **Professor David Giedroc, Chair, Department of Chemistry, Indiana University, 800 E. Kirkwood Avenue, Bloomington, IN 47405; e-mail: chemchair@indiana.edu.** Review of application will begin February 15, 2013, and continue until the position is filled. *Indiana University is an Equal Opportunity/Affirmative Action Employer.*

POSTDOCTORAL POSITION in Structural Biology Yale University

A postdoctoral position is immediately available to study membrane protein structures. Ideal candidate should have strong background in either membrane protein biochemistry or X-ray crystallography. Please send curriculum vitae and names of three references to: **Dr. Ya Ha, 333 Cedar Street, New Haven, CT 06520. E-mail: ya.ha@yale.edu.**

POSITIONS OPEN

Weill Cornell Medical College

FACULTY POSITION in Proteomics/Metabolomics

The Department of Biochemistry and the Weill Cornell Cancer Center seek to hire a tenured/tenure-track faculty member with research interests in proteomics and metabolomics. All faculty ranks will be considered, based on the applicant's qualifications. In addition to carrying out independent research, the appointee will provide faculty oversight for a newly formed well-equipped core facility for proteomics and metabolomics.

The new appointee will have a faculty appointment in the Department of Biochemistry (**website: http://www.cornellbiochem.org/**) and will be a member of the Weill Cornell Cancer Center, which has the goal to better understand the basic biology of cancer and to develop treatments. The appointee will teach medical students and participate in the Graduate School of Medical Sciences.

Interested applicants should forward electronic versions of (1) a cover letter; (2) a curriculum vitae; (3) a brief overview of current and future research interests; and (4) the names and contact information of at least three referees. (Confidential inquiries can be considered without initial contact of referees.) Material should be sent to **Frederick Maxfield** and **Lew Cantley,** co-chairs of the Search Committee, at **e-mail: biochemsearch@med.cornell.edu.** Evaluation of applications will begin immediately and continue until the position is filled.

Equal Opportunity Employer for Minorities/Females/Persons with Disabilities/Veterans.

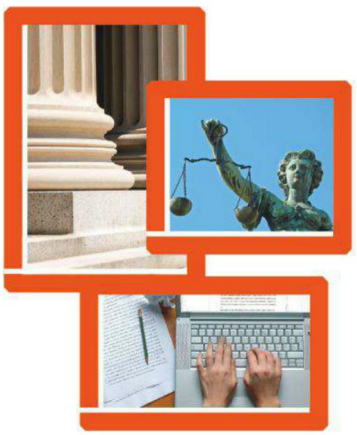

WEBINAR

Between Thought and Therapy:
Translating Neurobiology Research into Treatments

WEDNESDAY, FEBRUARY 13, 2013
12 noon ET, 9 a.m. PT, 5 p.m. GMT, 6 p.m. CET

This webinar will explore how translational neurobiology research is being conducted in the Intramural Research Program of the National Institutes of Health in disorders as diverse as depression, age-related macular degeneration, and Gaucher's disease. Our panelists all conduct translational research across the full bench-to-bedside continuum, with the ultimate goal of developing novel paradigms for the treatment of a range of diseases and improving the quality of life for patients.

Our expert panel will:

- Share their experiences of applying basic research at the bedside
- Discuss the best environments for conducting translational research
- Provide advice on working in new experimental systems, such as stem cells
- Answer questions submitted by you!

SPEAKERS

Carlos A. Zarate, M.D.
National Institute of Mental Health, NIH
Bethesda, MD

Anand Swaroop, Ph.D.
National Eye Institute, NIH
Bethesda, MD

Ellen Sidransky, M.D.
National Human Genome Research Institute, NIH
Bethesda, MD

REGISTER NOW!
webinar.sciencemag.org

Webinar sponsored by

NIH Intramural Research Program
Our Research Changes Lives

Brought to you by the *Science*/AAAS Custom Publishing Office

Science
AAAS

Illuminate Cancer Biology

The complexity of cancer systems biology requires innovative tools for interrogating the signaling pathways responsible for oncological transformation. Promega's integrated tools for reporter gene analysis assure biologically relevant results in cancer research.

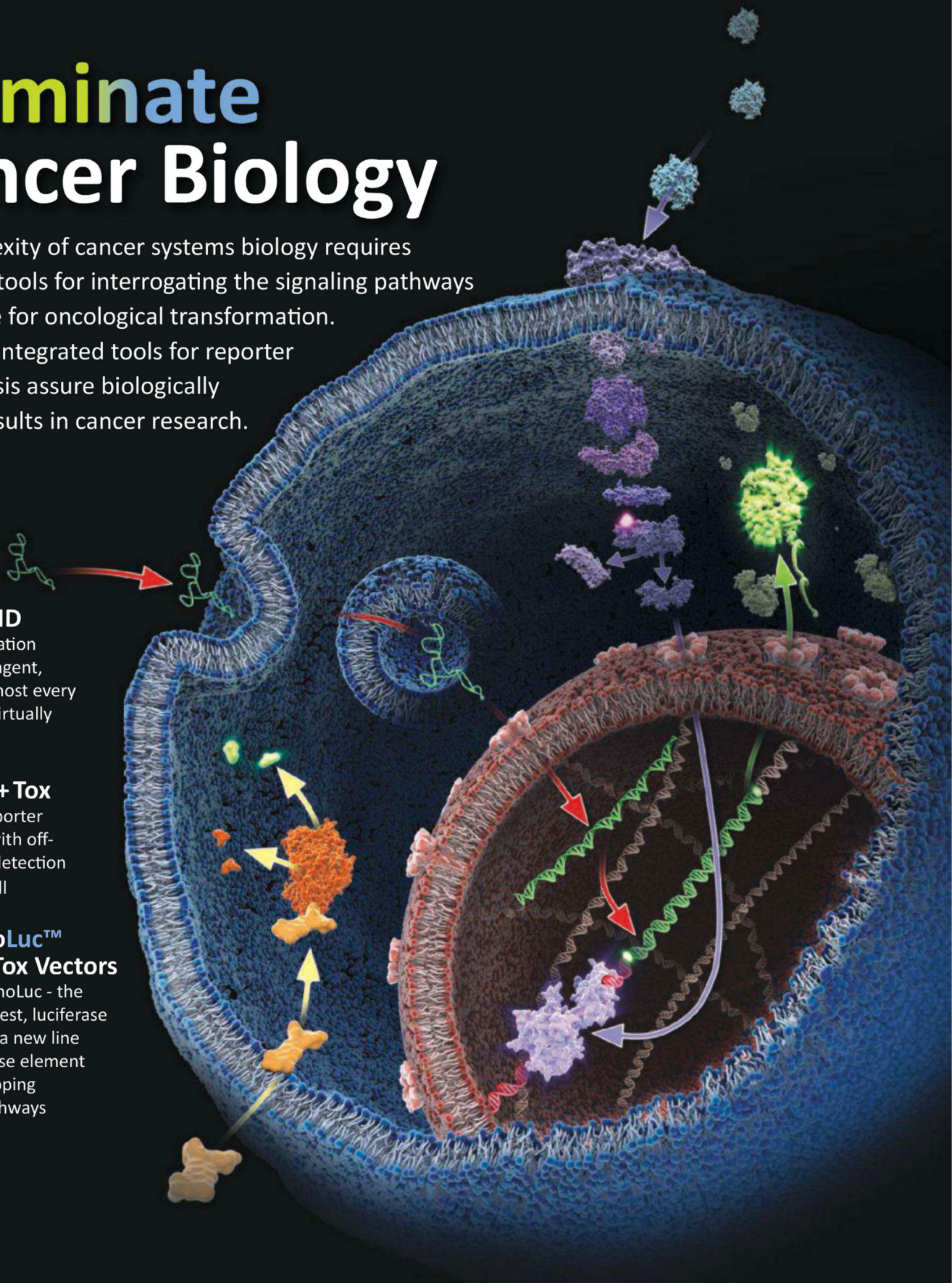

FuGENE® HD
The next generation transfection reagent, effective on almost every cell type with virtually no cell toxicity

ONE-Glo™ + Tox
Multiplexed reporter gene analysis with off-target toxicity detection in the same well

New! NanoLuc™ and pGL4 Tox Vectors
Introducing NanoLuc - the brightest, smallest, luciferase available - plus a new line of pGL4 response element vectors for mapping oncological pathways

Promega

To get a FREE sample of any one of these reagents, visit:

www.promega.com/pathwaybiology